UNIVERSIDAD
DE GRANADA

PROGRAMA DE DOCTORADO EN FÍSICA Y CIENCIAS DEL ESPACIO

DOCTORAL THESIS

Water vapor distribution in the Martian atmosphere from solar occultation measurements by the spectrometer NOMAD / Trace Gas Orbiter

---

Author:
Adrián Brines Montoro

Supervisor:
Dr. M. A. López Valverde

A Thesis submitted in fulfillment of the requirements
for the degree of Doctor of Philosophy

Instituto de Astrofísica de Andalucía - Consejo Superior de Investigaciones Científicas
(IAA-CSIC)

Group of Terrestrial Planetary Atmospheres
Solar System Department

INSTITUTO DE
ASTROFÍSICA DE
ANDALUCÍA

EXCELENCIA
SEVERO
OCHOA

CSIC

June 2024

Editor: Universidad de Granada. Tesis Doctorales
Autor: Adrián Brines Montoro
ISBN: 978-84-1195-591-1
URI: https://hdl.handle.net/10481/97597

A mi familia, amigos y quienes han estado a mi lado a lo largo de este camino.

"There is a way out of every box, a solution to every puzzle; it's just a matter of finding it."

Jean-Luc Picard

"When you have eliminated all which is impossible, then whatever remains, however improbable, must be the truth."

Sherlock Holmes

"Any sufficiently advanced technology is indistinguishable from magic."

Arthur C. Clarke

Abstract

In the Martian atmosphere, water vapor is crucial in most of the chemical and radiative processes, playing a significant role in the planet's current climate despite being a trace gas which represents about 0.03% of the total atmospheric composition. A new paradigm regarding the coupling between the lower and upper atmosphere on Mars and the evolution of this planet is emerging recently, based on data from the missions form the last 15 years. On one hand, recent observations of water vapor indicate that currently, during dust storms, the amount of this gas increases in the upper regions of the atmosphere. This novel result confirms an old suspicion that dust plays a fundamental role in the Martian water cycle. This increase in water abundances at high altitudes could imply a greater escape of H_2O to space during periods of increased dust activity. Isotopic studies on H_2O and HDO show a clear enrichment of the Martian atmosphere in deuterium, which is explained considering the escape processes that have taken place on the planet throughout history. These studies indicate a wet past for the planet, which could have had about 20% of its surface covered by water. However, considering the fact that dust may have been very variable and acting as a 'catalyst' in atmospheric escape, these estimates are likely not entirely accurate, and Mars may have been much richer in water in its early history than previously thought. On the other hand, the amounts of water vapor in the atmosphere recently observed during different seasons, vary from one hemisphere of the planet to the other, not only on column densities but also on its vertical structure, with the southern hemisphere showing a more extended vertical distribution during the local summer. This differences could indicate that the water cycle on Mars is not in equilibrium, with a net flow of water transferred from one hemisphere to the other. Despite its importance on the current climate and the planet's past, the knowledge about the vertical distribution of this species was limited, relying mostly on models and column density measurements. With the Solar Occultation (SO) observation technique, it is now possible to study not only the geographic but also the vertical distribution of water vapor.

Recently in April 2018, The ExoMars-Trace Gas Orbiter (TGO) started its science operations. This mission designed with the objective of finding methane on Mars and possible signs of life has not provided any positive detection of this species as of today. However the high sensitivity of the instruments onboard TGO proved to be excellent assets for the detection and characterization of many other trace species present in the Martian atmosphere, such as water vapor and multiple studies have revealed valuable information about the vertical structure and variability of the Martian atmosphere since the beginning of the mission.

For this Thesis we have processed and analyzed over 7000 observations performed with the Solar Occultation (SO) channel of the Nadir and Occultation for MArs Discovery (NOMAD) instrument, onboard TGO. NOMAD is an infrared spectrometer

working in the spectral range between 0.2 to 4.3 μm. It has two IR spectral channels (SO and LNO) and one operating in the UV-visible spectral range (UVIS; 200-650 nm). The SO channel covers the range between 2.3 and 4.3 μm (2320-4350 cm^{-1}) and uses an Echelle grating with a density of ∼4 lines/mm and a spectral resolution of $\lambda/\Delta\lambda \sim 20000$. The sampling time of this channel is ∼1 s allowing a vertical sampling in the observations of ∼1 km. An Acousto-Optical Tunable Filter (AOTF) is used to select different spectral windows of a width of ∼30 cm^{-1} corresponding to the different diffraction orders that can be selected during the observation. The AOTF quick change from one diffraction order to another allows to observe the atmosphere at a given altitude through 6 different spectral ranges within 1 second.

Here we present vertical profiles of water vapor obtained from NOMAD diffraction orders 134, 136, 168 and 169, analyzing: (i) the water vertical structure, (ii) its seasonal variability, (iii) its latitudinal distribution, (iv) local time variations, (v) the effects of dust storms, (vi) the saturation state of the atmosphere, and (vii) the role of the perihelion season on the escape of hydrogen to space. In order to perform those studies we developed a series of tools devoted to the correction of calibration issues present in the NOMAD Level 1.0 transmittance such as spectral shifts and bendings in the baseline of the spectra (continuum). We performed, in addition, a detailed characterization of the random component measurement noise. During those pre-processing steps, we used the line-by-line Karlsruhe Optimized and Precise Radiative transfer Algorithm, which provided precise simulated transmittances taking into account similar atmospheric conditions as those present during the NOMAD measurements, and all the instrumental features introduced into the spectra such as the NOMAD AOTF and the instrumental line shape (ILS), which was extensively studied as part of this work. For the water vapor inversions, we used the Institut fur Meteorologie und Klimaforschung (IMK) Retrieval Control Program (RCP) assuming the densities and temperature-pressure profiles derived from the Mars Planetary Climate Model (PCM) as a priori atmosphere. During the inversion, using a first order Thikonov regularization, we combined pairs of different diffraction orders at different altitude ranges, one for the lower atmosphere (typically below 60 km) and the other for the upper atmosphere (above 60 km), in order to avoid optically thick regions where the strongest absorption lines saturate and produce biases in the results.

An extensive error analysis and several sensitivity tests allowed us to determine an optimal regularization for each diffraction order used in the retrievals, and demonstrated the reliability and precision of our processing setup. Analysis of the 2018 Global Dust Storm (GDS) revealed significant variations in water vapor abundances and vertical transport, influenced by the large dust loading during the storm. Detailed observations during the perihelion showed strong vertical water vapor transport, particularly in the southern hemisphere, repeated every Martian year

(MY) although with some interannual variability due to the long term effects of the GDS. We also present an extensive water vapor climatology collecting observations during four consecutive MYs, highlighting strong seasonal and interhemispheric variations. The large extension of the data set permitted a statistical insight using cluster analysis, through which we identified six distinct atmospheric conditions throughout all four MYs. Finally, we provide comparisons with result obtained from other similar instruments revealing a good overall agreement within the expected uncertainties, validating the results reported in this Thesis. In addition, this work involved collaborations at the University of Tokyo and NASA Goddard Space Flight Center over 3.5 months of stay abroad in which a comparison of the forward models used by different teams within the NOMAD consortium was performed, proving the correct implementation of the instrumental characterization.

Resumen

En la atmósfera marciana, el vapor de agua es crucial en la mayoría de los procesos químicos y radiativos, jugando un papel significativo en el clima actual del planeta a pesar de ser un gas traza que representa aproximadamente el 0,03% de la composición atmosférica total. Un nuevo paradigma sobre el acoplamiento entre la baja y alta atmósfera en Marte y sobre la evolución de este planeta está emergiendo recientemente, a raíz de los datos de las misiones espaciales en los últimos 15 años. Por un lado, observaciones recientes del vapor de agua indican que actualmente, durante las tormentas de polvo, la cantidad de este gas aumenta en las regiones superiores de la atmósfera. Este resultado novedoso confirma una antigua sospecha de que el polvo juega un papel fundamental en el ciclo del agua marciano. Este aumento en las abundancias de agua en altitudes elevadas podría implicar un mayor escape de H_2O al espacio durante los periodos de mayor actividad de polvo. Estudios isotópicos sobre H_2O y HDO muestran un claro enriquecimiento de la atmósfera marciana en deuterio, lo cual se explica teniendo en cuenta los procesos de escape que han tenido lugar en el planeta a lo largo de su historia. Estos estudios indican un pasado húmedo para el planeta, el cual pudo haber tenido alrededor del 20% de su superficie cubierta por agua. Sin embargo, considerando el hecho de que el polvo haya sido muy variable y pueda actuar como un ’catalizador’ en el escape atmosférico, estas estimaciones probablemente no sean del todo precisas, y Marte podría haber sido mucho más rico en agua en su historia temprana de lo que se pensaba anteriormente. Por otro lado, las cantidades de vapor de agua en la atmósfera observadas recientemente durante diferentes estaciones varían de un hemisferio a otro del planeta, no solo en densidades de columna sino también en su estructura vertical, con el hemisferio sur mostrando una distribución vertical más extendida durante el verano local. Estas diferencias podrían indicar que el ciclo del agua en Marte no está en equilibrio, con un flujo neto o transferencia de agua de un hemisferio al otro. A pesar de su importancia sobre el clima actual y el pasado del planeta, el conocimiento sobre la distribución vertical de esta especie era limitado, dependiendo principalmente de modelos y mediciones de densidad de columna. Con la técnica de observación de ocultación solar, ahora es posible estudiar no solo la distribución geográfica sino también la distribución vertical del vapor de agua.

Recientemente, en Abril de 2018, el Orbitador de Gases Traza (TGO) de la misión ExoMars comenzó sus operaciones científicas. Esta misión, diseñada con el objetivo de encontrar metano en Marte y posibles signos de vida, no ha proporcionado ninguna detección positiva de esta especie hasta la fecha. Sin embargo, gracias a la alta sensibilidad de los instrumentos a bordo de TGO, han demostrado ser excelentes activos para la detección y caracterización de muchas otras especies traza presentes en la atmósfera marciana, como el vapor de agua, y múltiples estudios han revelado información valiosa sobre la estructura vertical y la variabilidad de la atmósfera

marciana desde el inicio de la misión.

Para esta Tesis, hemos procesado y analizado más de 7000 observaciones realizadas con el canal de Ocultación Solar (SO) del instrumento NOMAD (*Nadir and Occultation for MArs Discovery*) a bordo de TGO. NOMAD es un espectrómetro infrarrojo que trabaja en el rango espectral entre 0.2 y 4.3 μm. Tiene dos canales espectrales en el infrarrojo (SO y LNO) y uno que opera en el rango espectral UV-visible (UVIS; 200-650 nm). El canal SO cubre el rango entre 2.3 y 4.3 μm (2320-4350 cm^{-1}) y utiliza una rejilla Echelle con una densidad de $\sim$4 líneas/mm y tiene una resolución espectral de $\lambda/\Delta\lambda \sim 20000$. El tiempo de integración de este canal es de $\sim$1 s, permitiendo un muestreo vertical en las observaciones de $\sim$1 km. NOMAD SO utiliza un Filtro Acusto-Óptico Sintonizable (AOTF) para seleccionar diferentes ventanas espectrales de un ancho de $\sim$30 cm^{-1} correspondientes a los órdenes de difracción disponibles para ser utilizados durante la observación. El cambio del AOTF de un orden de difracción a otro es rápido, lo que permite observar la atmósfera a una altitud dada a través de 6 intervalos espectrales diferentes en 1 segundo.

Aquí presentamos perfiles verticales de vapor de agua obtenidos de los órdenes de difracción 134, 136, 168 y 169 de NOMAD, con los que analizamos: (i) la estructura vertical del agua, (ii) su variabilidad estacional, (iii) su distribución latitudinal, (iv) variaciones con la hora local, (v) los efectos de las tormentas de polvo, (vi) el estado de saturación de la atmósfera, y (vii) el papel del perihelio en el escape de hidrógeno al espacio. Para realizar esos estudios, hemos desarrollado una serie de herramientas dedicadas a la corrección de problemas de calibración presentes en las transmitancias del Nivel 1.0 de NOMAD, tales como desplazamientos espectrales y curvaturas en la línea base del espectro (continuo). Además, hemos realizado una caracterización detallada del ruido aleatorio en las mediciones. Durante esos pasos de preprocesamiento, utilizamos el Algoritmo de Transferencia Radiativa Optimizado y Preciso de Karlsruhe (KOPRA), que proporcionó transmitancias simuladas precisas teniendo en cuenta condiciones atmosféricas similares a las presentes durante las mediciones de NOMAD, y todas las características instrumentales introducidas en los espectros, tales como el AOTF de NOMAD y la forma de línea instrumental (ILS), que fue extensamente estudiada como parte de este trabajo. Para las inversiones de vapor de agua, hemos utilizado el Programa de Control de Recuperación (RCP) del Instituto de Meteorología y Climatología (IMK), asumiendo las densidades y los perfiles de temperatura-presión derivados del Modelo Climático Planetario de Marte (PCM) como atmósfera a priori. Durante la inversión, utilizando una regularización de primer orden de Thikonov, ideamos un esquema para combinar pares de diferentes órdenes de difracción en diferentes intervalos de altura, uno para la atmósfera inferior (típicamente por debajo de 60 km) y el otro para la atmósfera superior (por encima de 60 km), para evitar regiones ópticamente densas donde las líneas de absorción más fuertes se saturan y producen resultados erroneos.

Un extenso análisis de errores y numerosas pruebas de sensibilidad nos han permitido determinar una regularización óptima para cada orden de difracción utilizado en las inversiones, y han demostrado la alta fiabilidad y precisión de nuestro método de procesamiento. El análisis de la Tormenta Global de Polvo (GDS) de 2018 reveló variaciones significativas en las abundancias de vapor de agua y el transporte vertical, influenciadas por la gran carga de polvo durante la tormenta. Observaciones detalladas durante el perihelio mostraron un fuerte transporte vertical de vapor de agua, particularmente en el hemisferio sur, repetido cada año marciano (MY), aunque con cierta variabilidad interanual debido a los efectos a largo plazo de la GDS. También presentamos una extensa climatología del vapor de agua recopilando observaciones durante cuatro años marcianos, destacando fuertes variaciones estacionales e interhemisféricas. La gran extensión del conjunto de datos ha permitido un análisis estadístico de agrupación (*cluster analysis*) de grupos, a través del cual identificamos seis condiciones atmosféricas claramente distintas a lo largo de los cuatro años marcianos analizados. Finalmente, hemos proporcionado comparaciones con resultados obtenidos de otros instrumentos similares, revelando un buen acuerdo dentro de las incertidumbres esperadas, validando así los resultados presentados en esta Tesis. Este trabajo ha involucrado colaboraciones en la Universidad de Tokio y el Centro de Vuelo Espacial Goddard de la NASA durante 3.5 meses de estancia en el extranjero, durante los cuales se realizó una comparación de los modelos de transferencia radiativa utilizados por diferentes equipos dentro del consorcio NOMAD, demostrando la correcta implementación de la caracterización instrumental en los mismos.

Agradecimientos / Acknowledgements

Desde pequeño siempre me ha fascinado el Universo. Ese interés y curiosidad por los planetas y estrellas me ha llevado hasta donde me encuentro hoy, desde ese primer telescopio que me regalaron mis padres hasta el desarrollo de esta Tesis doctoral centrada en el mismísimo planeta Marte, quien me lo iba a decir. Y aunque pueda haber parecido un camino arduo y difícil (mentiría si dijese que no lo ha sido), la clave ha sido aprovechar el tiempo, junto una serie de decisiones (y una pizca de suerte), algunas mas acertadas que otras, tomadas gracias al apoyo de toda la gente que siempre ha estado a mi lado. Y es que, citando a un archiconocido mago, "lo único que tenemos que decidir es qué hacer con el tiempo que se nos ha dado". Un tiempo en esta etapa inicial en la investigación en la que he podido conocer a personas excepcionales y visitar lugares increíbles.

De entre esas personas, para empezar, gracias Miguel. No encuentro las palabras para expresar mi gratitud a tu paciencia durante estos cuatro años, sobre todo durante este último en el que mis visitas a tu despacho eran casi diarias. Quiero agradecerte también todo el apoyo y motivación que me has dado para no solo terminar este proyecto, sino para animarme a continuar en el mundo de la investigación. Por mi parte, espero haber adquirido al menos una fracción de tu amplia experiencia no solo sobre Marte, sino en el ámbito científico en general. Por supuesto, no puedo dejar pasar la oportunidad de derte las gracias también, Francisco. Sin tu ayuda, tanto en las famosas *runs* del GCM como a la hora de interpretar mis resultados, no podría haber llegado ni a la mitad del camino. Bernd, no quiero olvidarme de ti tampoco. Aguantando mis dudas sobre los retrievals y resolviendo los múltiples errores que me he ido encontrando en KOPRA y RCP todo este tiempo.

I also want to thank you, Aurélien and Ashim, for the excellent experience of working by your side. I greatly appreciate the support you have given me. Beyond our group, thank you, Shohei. You made my stay in Tokyo memorable, something I will fondly remember from this stage of my life, and I hope it happens again soon. The same goes for you Gerónimo and Sara, thank you from the bottom of my heart for all the help and support you gave me in Washington. Thanks also to all of the NOMAD team. Sharing discussions, coffee breaks, and even beers from time to time, has been a wonderful experience. Nao, Zach, I'm glad to have made friends like you along the way.

Ya para terminar, no podía faltar daros las gracias a vosotros, papá y mamá. Gracias por todo vuestro ánimo y apoyo, y por aguantarme todos estos años. También a ti, Sofía, que pese a que ya sabes que no suelo expresarlo muy a menudo, no podría haber pedido una hermana mejor que tú (aunque a veces hay que saber aguantarte a ti también ...). Gracias también a mis amigos por soportar mis penurias. A los que estáis en Valencia y con los que he compartido experiencias desde que íbamos al colegio: Alex, Ariel, Fran, Javi, Juan, María, Pablo, Rafa y Rodrigo. Y por supuesto, a los que os tengo más cerca en Granada: Elisa, Julio, Natalie, Rocío, Víctor y Zaira.

A. Brines acknowledges financial support from the grant PRE2019-088355 funded by MCIN/AEI/10.13039/501100011033 and by 'ESF Investing in your future'.

Contents

List of Figures

List of Tables

List of Abbreviations

ACS	**A**tmospheric **C**hemistry **S**uite
ACB	**A**phelion **C**loud **B**elt
AOTF	**A**cousto-**O**ptical **T**unable **F**ilter
ASIMUT	**A**tmospheric **S**pectra **I**nversion **M**odular **U**tility **T**ools
AvK	**Av**eraging **K**ernel
BIRA	**R**oyal **B**elgian **I**nstitute for space **A**eronomy
CaSSIS	**C**olour **a**nd **S**tereo **S**urface **I**maging **S**ystem
CRISM	**C**ompact **R**econnaissance **I**maging **S**pectrometer for **M**ars
CSIC	**C**onsejo **S**uperior de **I**nvestigaciones **C**ientíficas
DA	**D**ata **A**ssimilation
DBSCAN	**D**ensity-**B**ased **S**patial **C**lustering of **A**pplications with **N**oise
EMCD	**E**uropean **M**artian **C**limate **D**atabase
EMIRS	**E**mirates **M**ars **I**nf**R**ared **S**pectrometer
ESA	**E**uropean **S**pace **A**gency
EscaPADE	**Esca**pe and **P**lasma **A**cceleration and **D**ynamics **E**xplorers
FM	**F**orward **M**odel
FOV	**F**ield **O**f **V**iew
FREND	**F**ine **R**esolution **E**pithermal **N**eutron **D**etector
FSR	**F**ree **S**pectral **R**ange
GEM-Mars	**G**lobal **E**nvironmental **M**ultiscale model for **Mars**
GCM	**G**lobal **C**irculation **M**odel
GDS	**G**lobal **D**ust **S**torm
HITRAN	**HI**gh-resolution **TRAN**smission molecular absorption database
HWHM	**H**alf **W**idth at **H**alf **M**aximum
IAA	**I**nstituto de **A**strofísica de **A**ndalucía
ILS	**I**nstrumental **L**ine **S**hape
IMK	**I**nstitut für **M**eteorologie und **K**limaforschung
IR	**I**nfra**R**ed
IRIS	**I**nfra**R**ed **I**nterferometer **S**pectrometer
KOPRA	**K**arlsruhe **O**ptimized and **P**recise **R**adiative transfer **A**lgorithm
LMD	**L**aboratoire de **M**étéorologie **D**ynamique
LOS	**L**ine **O**f **S**ight
LNO	**L**imb **N**adir and **O**ccultation
LST	**L**ocal **S**olar **T**ime
LTE	**L**ocal **T**hermodynamic **E**quilibrium

MAVEN	**M**ars **A**tmosphere and **V**olatile **E**volutio**N**
MAWD	**M**ars **A**tmospheric **W**ater **D**etector
MEX	**M**ars **Ex**press
MGS	**M**ars **G**lobal **S**urveyor
MIR	**M**iddle-**I**nfra**R**ed
MIPAS	**M**ichelson **I**nterferometer for **P**assive **A**tmospheric **S**ounding
MMX	**M**ars **M**oon e**X**ploration
MMR	**M**ass **M**ixing **R**atio
MOLA	**M**ars **O**rbiter **L**aser **A**ltimeter
MRO	**M**ars **R**econnaissance **O**rbiter
MW	**M**icro **W**indow
MY	**M**artian **Y**ear
NASA	**N**ational **A**eronautics and **S**pace **A**dministration
NIR	**N**ear-**I**nfra**R**ed
NOMAD	**N**adir and **O**ccultation for **MA**rs **D**iscovery
NPH	**N**orth **P**olar **H**ood
OMEGA	**O**bservatoire pour la **M**inéralogie, l'**E**au, les **G**laces et l'**A**ctivité
OpenMARS	**Open** access to **M**ars **A**ssimilated **R**emote **S**oundings
PFS	**P**lanetary **F**ourier **S**pectrometer
PCM	**P**lanetary **C**limate **M**odel
PP	**P**re-**P**rocessing
PSG	**P**lanetary **S**pectrum **G**enerator
RCP	**R**etrieval **C**ontrol **P**rogram
RTT	**R**adiative **T**ransfer **T**heory
SAM	**S**ample **A**nalysis at **M**ars
SNR	**S**ignal to **N**oise **R**atio
SO	**S**olar **O**ccultation
SOIR	**S**olar **O**ccultations in the **I**nfra**R**ed
SPH	**S**outh **P**olar **H**ood
SPICAM	**Sp**ectroscopy for the **I**nvestigation of the **C**haracteristics of the **A**tmosphere of **M**ars
SPICE	**S**pacecraft, **P**lanets, **I**nstrument, **C**-matrix, **E**vents
SPR	**S**outhern **P**olar **R**egion
STD	**ST**andard **D**eviation
TES	**T**hermal **E**mission **S**pectrometer
TGO	**T**race **G**as **O**rbiter
TIRVIM	**T**hermal **I**nfra**R**ed channel in honor of **V**assily **I**vanovich **M**oroz
TOA	**T**op **O**f the **A**tmosphere
UTokyo	**U**niversity of **Tokyo**
UV	**U**ltra**V**iolet
UVIS	**U**ltraviolet and **VI**sibile **S**pectrometer
VMR	**V**olume **M**ixing **R**atio

Chapter 1

Introduction

1.1 Mars

1.1.1 From mythology to space exploration

Captivating humans since the beginning of our history and leaving an imprint on numerous cultures around the world, when visible at nights Mars stands out from the dark sky as a red bright point, easily visible to the naked eye. Also known as the Red Planet, its reddish hue, similar to the color of blood often led to its association with war or fire. Greeks named this planet in honor of the god of war Ares, the Egyptians refereed to this astronomical body as "*Her Desher*", translated as "*the red one*", Asian cultures often refer to it as the "*fire star*", and adopted from the Greeks, the Romans used their analog god to name this celestial body, hence its current name Mars.

The early observations of Mars were crucial for the development of the firsts heliocentric Solar System models and its relatively large orbital eccentricity helped Johannes Keppler to formulate his first two laws of planetary motion in 1609. The invention of the telescope in the early 17th century marked the beginning of detailed observations of Mars. In 1609, Galileo Galilei observed this planet through the telescope for the first time, noting its extensive rather than punctual shape and suggesting that Mars was in fact another world. Some decades later, in the mid 17th century the astronomer Christiaan Huygens registered the observation of several surface marking which allowed him to study the rotation of the planet. He came to the conclusion that Mars had a rotation period like the one on Earth, and that its size was about 60% of the size of the Earth, both estimations not far from the reality. By that time, the observation and study of surface features began to gain popularity. Many astronomers reported the presence of dark patches on Mars and in 1666 Giovani Domenico Cassini registered the first observation of what it looked like a southern polar cap. This observation was complemented a few years later by Huygens, who reported the presence of a northern polar cap. In 1781 William Herschel studied the variability of those polar caps, which showed changes in their sizes suggesting a relation with the planet's season. The presence of polar caps suggested the presence of an atmosphere, needed to avoid the sublimation of the ice, and these discoveries quickly led to speculation. Using the Earth for reference, by the late 17th and early 18th centuries, the idea of the observed dark surface patches being forests and oceans was widely spread within the scientific community, suggesting the presence of life on Mars. With the improvement of observation techniques and advances in the manufacture of telescope optics, astronomers began to map the Martian surface, noticing apparent changes in shapes, colors and sizes of structures. In 1877, Giovanni Schiaparelli described linear features he called "canali". This term was mistranslated into English as "canals," leading to widespread speculation about intelligent life constructing these structures. Percival Lowell, an American astronomer, added more to this idea in the late 1800s, hypothesizing that an advanced Martian civilization built the canals to transport water from the poles. This hypothesis was subject of debate and controversy during the whole 19th century, although observations with larger and more powerful telescopes during the early 20th century revealed that those canals were in reality a mixture of smaller features. The mid-20th century marked a significant shift from speculation to direct exploration. In the 1960s, the first spacecraft were sent to Mars, initiating an era of robotic exploration that would revolutionize our understanding of the planet.

After several attempts and failures, the first spacecraft to reach Mars and to perform a flyby was NASA's Mariner 4 in 1965. This probe was actually the first human object to conduct a successful planetary encounter. Following the design of its predecessors in the same series, this probe carried several scientific instruments onboard such as a magnetometer, micrometeorite detector and radiation detectors. In addition a TV camera was mounted in the spacecraft, allowing to obtain for the first time detailed images of the Martian surface. The images sent back to Earth showed a Lunar-like terrain and measures of the atmospheric pressure and temperature revealed an extremely thin and cold atmosphere exposed to the solar and cosmic radiation without the protection of a magnetic field. These results confirmed the absence of "canals", and the hazardous environment suggested by the atmospheric measurements vanished the expectations to find any complex lifeforms in the planet. Improving the design and performance, and focused only to planetary data acquisition, NASA's spacecrafts Mariner 6 and 7 performed again a flyby over Mars in 1969. Those spacecrafts provided more images with higher resolution and covered approximately the 20% of the planet's surface, revealing a CO_2 ice south polar cap. Mariner 6 and 7 probes also performed more atmospheric measurements, estimating the surface pressure at between 6-7 mbar. After the success of flyby mission, the efforts on the exploration of Mars focused on orbiting and landing on the planet. The first mission to enter the Martian orbit (and the first human made orbiter around other planet) was Mariner 9 in 1971. It achieved a surface mapping of about 70% of the entire planet, discovering tectonic structures, volcanoes and valleys. The spacecraft also observed the two Martian moons Phobos and Deimos and gathered data on the atmospheric composition and variability of the planet, providing information on global dust storm events. After the success of the United States on the Mariner program and in the context of the Cold War, Soviet Union doubled efforts in order to overtake the United States on the Martian space exploration. Within the Soviet Mars Program, a series of identical spacecrafts were launched between 1971-1973. The goal was not only to orbit but also to land on the planet. Although the orbiters succeeded revealing day-night temperature variations, clouds and a 40 km altitude ozone layer, the landers failed before or during the atmospheric entry. In 1975, the US developed the Viking Program, composed by the spacecrafts Viking 1 and 2, each consisted of an orbiter to perform imaging, atmospheric water vapor and temperature mapping, and a lander. In 1976, the lander separated from the orbiter and landed successfully on Mars, being the first instrument operating from the surface of Mars . These missions provided high-resolution images, extensive atmospheric data, and conducted experiments to detect signs of life. Although no definitive evidence of life was found, they offered geological and meteorological information, providing a comprehensive view of Mars and revealing features like volcanoes, lava plains, canyons, craters, and apparent evidence of surface water in the past. After these missions, the interest of the space agencies on Mars waned, taking more than a decade for the next mission to the Red Planet. In 1988 the URSS developed the Phobos Project consisting in two probes, Phobos 1 and 2 with the ambitious goal of orbiting Mars and deploying a lander on the moon Phobos. These missions were developed in cooperation with non-URSS countries and although the first failed enroute to Mars and the second was lost during the final approach to Phobos, they settled the bases for the internationalization of the space exploration. In 1997, after some failures US managed to insert the Mars Global Surveyor (MGS) into a Martian polar orbit for a complete planetary coverage every 7 days. Besides its scientific achievements such as the detailed mapping of the surface, the analysis of the magnetic field or the discovery of water ice clouds and the temperature seasonal variations, MGS acted as a communications relay for many following missions. Within the same Mars Exploration Program the lander Mars Pathfinder successfully deployed for the first time a rover on Mars. Although it was more a technological demonstration than a scientific experiment, it revived again the public interest in Mars.

During the beginning of the 21st century a new era of orbiters and landers/rovers began, with many countries around the world getting involved in the development of more powerful space launch vehicles and more complex and advanced spacecrafts. Most of the probes launched since then are still in orbit and operational, making Mars the planet despite the Earth with the largest spacecraft fleet in the Solar System. In 2001 Mars Odyssey revealed subsurface ice near the South Pole using a high energy neutron detector. Later in 2003, the European Space Agency conducted their first planetary mission with Mars Express (MEX) consisting in an orbiter and a lander, which failed during descent. Nevertheless, the success of this mission left no doubt.

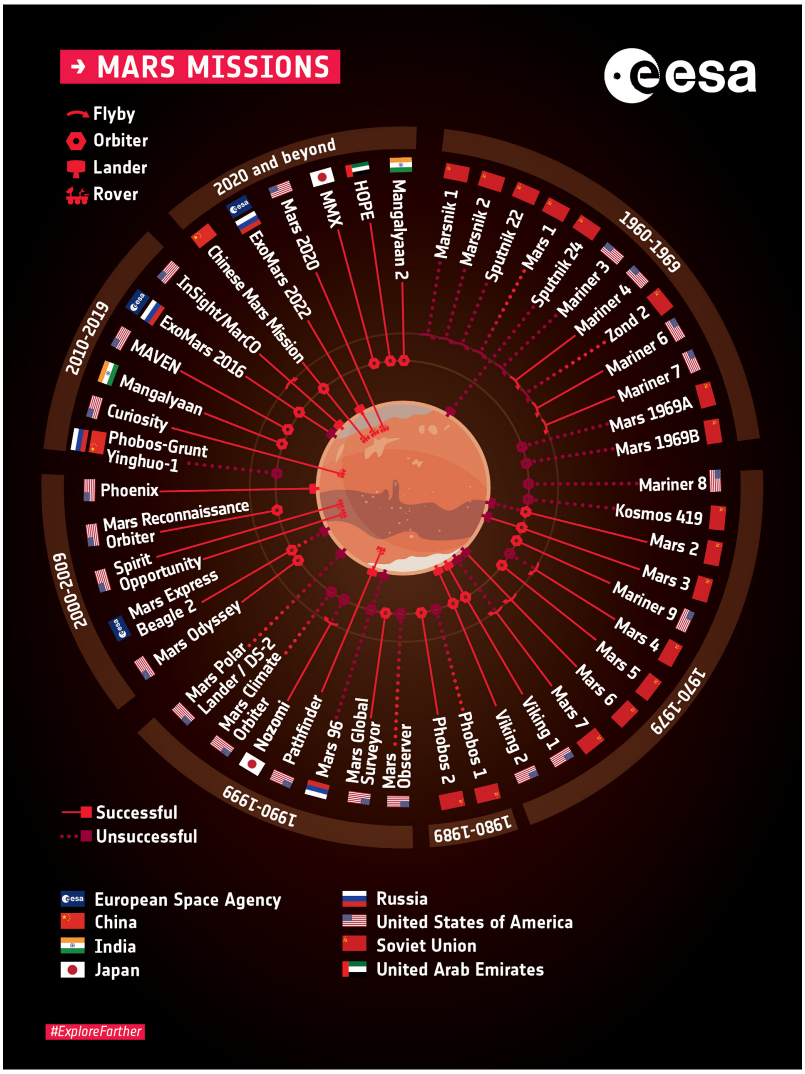

FIGURE 1.1: History of Mars exploration since 1960's to the 2020's, categorizing the missions into flybys, orbiters, landers and rovers. Credit: ESA.

Still operating and with support planned until 2026, the list of discoveries made by MEX such as the presence of water ice in the polar caps, subglacial lakes below the southern polar cap, the tentative detection of methane in the atmosphere, the detection of an aurora similar to that on Earth, or the high resolution near-complete topographical map of Mars' surface, allowed us to extend our knowledge about this planet. In 2006, the NASA's Mars Reconnaissance Orbiter (MRO) arrived to the Martian orbit carrying onboard a high resolution camera that allowed the identification of geological features compatible with the presence of liquid water flowing on the surface in past, confirming the presence of ancient river deltas and lakebeds. In 2014 the Mars Atmosphere and Volatile EvolutioN (MAVEN) arrived Mars in order to study the upper atmosphere and ionosphere, providing valuable information about the interaction of the solar wind with Mars, closely related to the loss of volatile species to space. More recently in 2016, the Trace Gas Orbiter (TGO) and the lander Schiaparelli were launched as part of the ExoMars 2016 mission, a collaboration between ESA and the Russian space agency Roscosmos. Although the lander crashed after the atmospheric entry, TGO resulted to be a success allowing the systematic search and monitoring of trace species present in the Martian atmosphere using a very sensitive solar occultation observational geometry. In 2020 China and United Arab Emirates began their contribution to the exploration of Mars with the Emirates Mars Mission and the Tainwen-1 probe. Now, in addition to these, new missions to the Red Planet are under development such as the Escape and Plasma Acceleration and Dynamics Explorers (EscaPADE) estimated for its launch in October 2024, the Mars Moon eXploration (MMX) led by Japan and planned for 2026 to explore the two moons of Mars, or the Mars Sample Return (MSR), a NASA and ESA collaborative mission planed to bring carefully selected Martian samples to Earth. An overview of all the missions sent to Mars is shown in Figure 1.1, highlighting the efforts made since the 1960's in order to explore this planet.

All these missions, even the ones that resulted in failure, provided us with knowledge to advance in the understanding of our neighbor planet, and its exploration continues to inspire and challenge our perception of all those places in the Solar System where no one has gone before.

1.1.2 Mars. An overview

Since the 1960's, the information we have about Mars has been increasing steadily thanks to the numerous missions sent to the Red Planet (fig. 1.1). Although still incomplete, the view we currently have about this planet allows us to understand and describe many properties or features we have observed both on the surface and in the atmosphere.

Being the fourth planet orbiting the Sun, it is the second smallest planet in the Solar System after Mercury with an equatorial radius of 3396 km. Mars has a mass of about 0.64×10^{24} kg with a mean surface gravity of 3.73 m/s^2, about 38% of the Earth's gravity. While a Martian Year (MY) lasts 687 Earth days, almost twice as long as a year on Earth, it completes a full rotation every 24.6 hours, just slightly longer than Earth days. Similar to that on Earth, Mars' rotation axis is currently titled about 25°, therefore allowing for cyclical seasons shaping the Martian weather during the year. Without a "Martian Calendar", the way marking the time in order to refer to different seasons is done using Solar Longitude (L_S) defined to be 0° at the vernal equinox, 90° at summer solstice, 180° at autumnal equinox, and 270° at winter solstice (all seasons referred to the Northern hemisphere). The first definition of the Mars year was arbitrarily suggested by Clancy et al., 2000, adopting $L_S = 0°$ during April 11, 1955 as the beginning of year 1. More recently, Piqueux et al., 2015 updated the enumeration of Mars years defining the beginning of MY 0 in May 24, 1953 and denoting with "-" any previous years. The duration of the seasons on Earth is similar due to its nearly circular orbit, resulting in a constant orbital velocity. However, the eccentricity of the Martian orbit is larger, about 5.6 times that of the Earth. Mars reaches its farthest point from the Sun (aphelion) at 249 million kilometers and moves most slowly around $L_S = 71^\circ$. The closest approach to the Sun (perihelion) occurs around $L_S = 251^\circ$, period when Mars moves fastest. As a result, seasonal changes are less dramatic in the northern hemisphere than in the southern, the last showing long and cold winters and hot and shorter summers. A schematic of the Martian orbit is shown in Figure 1.2.

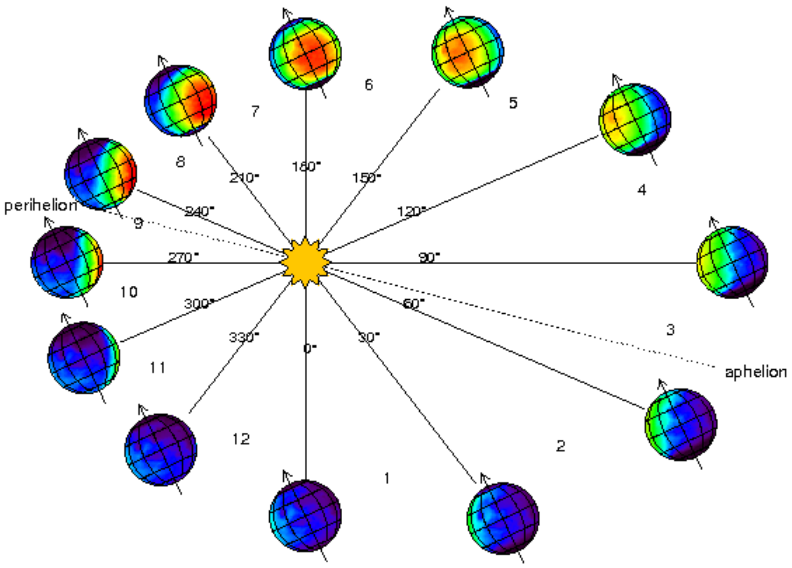

FIGURE 1.2: Schematic of the Martian orbit indicating the Solar longitude, perihelion and aphelion. Credit: The Mars Climate Database

Regarding its surface, iron materials within rocks and dust oxidizes giving to the planet its characteristic reddish hue. Vast geographical features are scattered across the planet such as the Olympus Mons or the Valles Marineris, being the largest volcano (about 22 km height) and the longest valley (4000 km long) respectively, in the entire Solar System. The lack of oceans in Mars complicates the election of the zero-elevation surface, which has been defined from the areoid as an analogous to the geoid on Earth. This reference represents the gravitational and rotational equipotential surface. Combining radio tracking and altitude measurements from the Mars Orbiter Laser Altimeter (MOLA) onboard MGS, the areoid was defined using the mean radius of the planet at the equator. The global topographic map obtained with MOLA, shown in Figure 1.3, reveals a clear crustal dichotomy between the northern and southern hemisphere, with overall lower altitudes observed at latitudes above the equator. This interhemispheric difference was first noticed on Mariner 9 images (Hartmann, 1973) and among other factors, is responsible for the large-scale latitudinal atmospheric pressure gradients (Hourdin et al., 1993) and helps in modulating the global circulation forcing a dominant southern summer

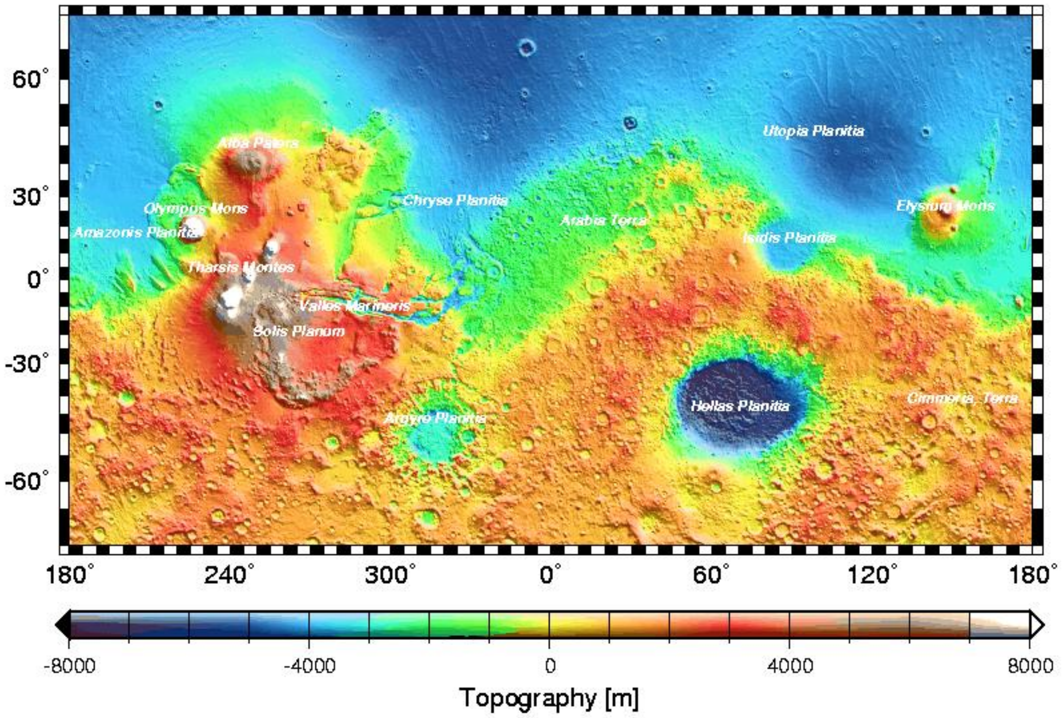

FIGURE 1.3: Global topographic map of Mars with major surface features labeled measured by MOLA onboard MGS. Credit: NASA, MOLA Science Team.

Hadley cell (Richardson & Wilson, 2002).

A summary with the main bulk and orbital parameters of Mars and the Earth are shown in Table 1.1.

1.2 The current atmosphere and climate of Mars

The existence of the Martian atmosphere was speculated since early the 18th century, and even yellowish clouds, what we know now were dust clouds, have been observed since the 1870's. However, it was Gerard Kuiper who confirmed in 1947 that in reality Mars has a extremely thin carbon dioxide (CO_2) based atmosphere (Kuiper, 1952), with a surface pressure less than one hundredth of that on Earth. Today we know that this species is present in an abundance of about $\sim$95%, with dinitrogen (N_2) and argon (Ar) the most abundant secondary components present at 2.8% and 2.1% respectively (Franz et al., 2017). In addition, several trace species have been detected in the Martian atmosphere such as oxygen (O_2), ozone (O_3), carbon monoxide (CO), water vapor (H_2O) or hydrogen chloride (HCl), all of them with abundances way below 1%. The distribution of these species through the planet depends on how the atmosphere reacts to changes in temperature, pressure, and how it interacts with the surface and the hostile conditions of the outer space.

TABLE 1.1: Bulk and orbital parameters of Mars and the Earth. Values retrieved from https://nssdc.gsfc.nasa.gov/planetary/factsheet/

Parameter	Mars	Earth	Ratio
Mass (10^{24} kg)	0.64	5.97	0.107
Equatorial radius	3396.2	6378.1	0.532
Surface gravity (m/s^2	3.73	9.82	0.380
Orbit semimajor axis (10^6 km)	227.956	149.598	1.524
Sideral orbit period (days)	686.980	365.256	1.881
Perihelion (10^6 km)	206.650	147.095	1.405
Aphelion (10^6 km)	249.261	152.100	1.639
Orbit eccentricity	0.0935	0.0167	5.599
Sideral rotation period (hrs)	24.623	23.935	1.029
Equator inclination (deg)	25.19	23.44	1.075

1.2.1 Atmospheric basic parameters

Although with a relatively thin atmosphere (compared to that on Earth), Mars exhibits a complex climate, with many atmospheric parameters varying with seasonal cycles, local times and locations. Understanding those parameters is crucial in order to understand the Martian weather we observe today. On the other hand, this planetary atmosphere represents a challenge and a unique opportunity to test and improve climate models on Earth.

Temperature

Besides its composition, temperature is one of the basic quantities that characterizes a planetary atmosphere. On Earth, the atmosphere can be "separated" into layers following the strong variations of the temperature with height. Those Earth's layers are:

- Troposphere. This layer ranges from the surface up to about 10-15 km, following a decrease of the temperature with altitude due to convection.
- Stratosphere. In this region, between 15-50 km the temperature increases with altitude due to the absorption of solar radiation by ozone. This layer is dominated by radiative transport rather than convective phenomena.
- Mesosphere. Again dominated by radiative effects, with a net cooling effect, temperature decreases between 50-85 km as the atmosphere cools down radiating heat to space.
- Thermosphere. Above about 85 km, extreme UV and X-ray absorption, mostly by oxygen, increases the temperature again.

On Mars similar regions can also be defined, although with slightly extended vertical ranges mostly due to the low pressure of its atmosphere. In addition, although present in small amounts, the absence of a thick ozone layer or any other strong absorbent makes impossible the increase of the temperature at altitudes analogous to the Earth's the stratosphere. Hence, the analogue Martian atmospheric regions are defined as "lower", "middle" and "upper" atmosphere (Smith et al., 2017). The first, corresponding to the Earth's troposphere, ranges from the surface up to about 50 km where temperatures are dominated by the surface heating decrease with height. The middle atmosphere, the analog to the Earth's mesosphere, ranges from 50 up to 100 km, with temperatures affected by thermal tides and planetary waves inducing local variations. Finally, the upper atmosphere acting as the Earth's thermosphere, shows the increase of the temperature with height as a result of the extreme UV solar radiation to which Mars is exposed. Some examples of in situ measurements of temperature profiles are shown in Figure 1.4, indicating the limits of these lower, middle and upper atmospheric regions. Throughout this Thesis, we used indistinctly the the terms low/middle/upper atmosphere and troposphere/mesosphere/thermosphere.

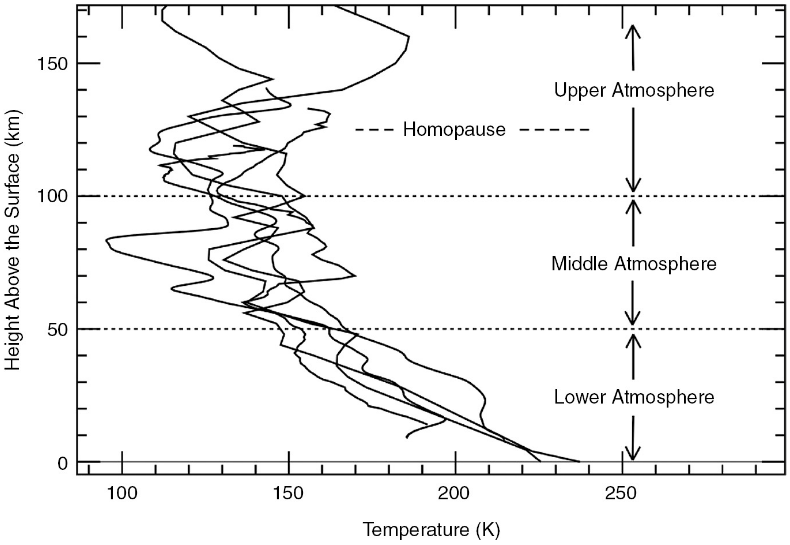

FIGURE 1.4: Temperature profiles measured during the descent phase of different landed spacecrafts. Horizontal dashed lines indicate the limits of each atmospheric layer. Credit: Smith et al., 2017

The lower atmosphere is characterized by significant seasonal and latitudinal variability, influenced by both Mars axis obliquity and orbital seasons (perihelion and aphelion), the first dominating at high latitudes and at all altitudes and the second dominating at low latitudes and close to the surface (Liu et al., 2003; Smith et al., 2001). At low altitudes, the high influence of the surface controls the thermal structure and the distribution of dust and dynamics (local winds, large scale advection, turbulence) regulates the vertical variation (Smith et al., 2017). The middle atmosphere of Mars currently remains a subject of active research. This region typically shows the coldest temperatures on Mars, down to the point of hosting CO_2 ice clouds (Liuzzi et al., 2021). In addition, nighttime temperatures within this region exhibit significant variation with height and season (Forget et al., 2009) and present particularly intense atmospheric waves and turbulences whose latitudinal distribution varies depending on the season (Nakagawa et al., 2020). The thermal structure in the upper atmosphere is affected not only by the solar radiation and its variability with the solar cycle, but also influenced indirectly by the surface and dust loading in the lower atmosphere (González-Galindo et al., 2015). The prominent topography of Mars, combined with solar illumination, produces wave structures observed even in the upper atmosphere (Keating et al., 1998) and dust storms can induce sudden increases in atmospheric densities at high altitudes (Forget et al., 2009; Kleinböhl et al., 2013). The weak greenhouse effect on Mars causes large surface temperature differences between day and night (Smith et al., 2004) and the rotation of the planet induces diurnal tides. In addition, radiative heat and absorption of aerosols (dust and water ice clouds) force tides with a period of half a day known as semidiurnal tides (Heavens et al., 2010; Kleinböhl et al., 2013; Wilson & Richardson, 2000). Recently, the systematic observations of the instruments onboard TGO allowed a detailed characterization of the thermal structure during several MYs (Belyaev et al., 2022; López-Valverde et al., 2023; Trompet et al., 2023).

Pressure

On average, the surface pressure on Mars is about 6.36 mbar, which is less than 1% of Earth's sea-level pressure. The Martian extreme topography combined with a comparatively high scale height (vertical distance over which the pressure falls by a factor e) of about 11.1 km, results in significant pressure variations across the planet much larger than those on Earth. This is, pressures falls as the elevation altitude increases. Assuming hydrostatic equilibrium, the pressure difference dp between the bottom and the top of an air parcel of width dz is equal to the the weight of the air within the parcel, this is,

$$dp = -g\rho dz \tag{1.1}$$

where g is the gravitational acceleration and ρ the density of the air. Considering the air in the parcel as an ideal gas of mean molecular weight M and temperature T, we get

$$dp = -g\frac{Mp}{k_B T}dz = -p\frac{1}{H}dz \tag{1.2}$$

where $H = k_B T/Mg$ is the scale height. Finally, for an altitude range small enough to assume g and T are constant, we obtain

$$p(z) = p_0 \exp(-z/H) \tag{1.3}$$

Since CO_2 is its main constituent, any change on the abundance of this species affects drastically the Martian atmosphere. In particular, during the winters, the cold temperatures in the polar regions allow the CO_2 to condense there whereas during summer, the polar caps sublimate releasing large amounts of this gas into the atmosphere. As a result of this CO_2 cycle, the atmospheric pressure varies by about 30% between summer and winter seasons (Smith et al., 2017). These seasonal variations, which where already detected by the Viking landers (Nier & McElroy, 1977) and are a unique phenomenon in the Solar System, have strong effects on the global atmospheric circulation.

Dust and clouds

Aerosols are one of the main components of the Martian atmosphere and two distinct types can be identified: dust and ice particles, with radiative properties that strongly influence the thermal structure of the atmosphere (Gierasch & Goody, 1972), shaping the weather and the global climate. The distribution of dust across the planet is very variable and presents strong interannual differences. However, some regularities can be seen throughout the Martian year, showing two distinct seasons. The first half of the year is characterized by a low dust abundance whereas the second half, from $L_S = 135$ to $L_S = 360$ presents a much higher dust loading. During this "dusty season", dust storms are frequent. Winds and convective vortices, known as Dust Devils, lift the dust from the surface into the atmosphere producing dust clouds or hazes (Kahre et al., 2006). Occasionally, some of these events which begin locally, expand reaching a planetary scale known as Global Dust Storms (GDS). In 2001 (MY 21), MGS performed a detailed study of one of these storms, which strongly affected the middle atmosphere increasing its temperature by 30-40 K and forced the temperature surface to drop by 20 K (Gurwell et al., 2005). Since then, several GDS where observed, with particularly intense events during MYs 28 and recently MY 34 (Stolzenbach et al., 2023). These storms alter the atmospheric circulation (Haberle et al., 1982), affecting the distribution and cycles of CO_2, water vapor and non-condesnable species such as CO (Kahre et al., 2017) and could also be possibly responsible for the variablity observed in the abundance of some trace gas species, like HCl (Aoki et al., 2021; Korablev et al., 2021).

Regarding CO_2, dust is known to affect the condensation and sublimation of this species in the polar caps, as a dust-driven circulation and thermal structure affects these processes. Also, from Viking and MGS observations it has been suggested that near solstice GDSs can lead to an increased CO_2 south polar cap sublimation (Bonev et al., 2008). Regarding water vapor, dust has a strong impact on water ice cloud formation which is more prone to occur in presence of suspended condensation nuclei (Montmessin et al., 2002). These dust-ice particles then fall to the surface producing a scavenging effect (Clancy et al., 1996; Fedorova et al., 2014), limiting the vertical extent of dust and altering its distribution and surface deposition. On the other hand, during high dust loading events, the associated increase of the atmospheric temperature due to the radiative heating by the dust particles (Neary et al., 2020) makes the formation of ice clouds to occur at higher altitudes. This, together with the enhancement of the global circulation allow for a larger vertical extension of the water vapor rich layers (Fedorova et al., 2020).

During the aphelion season, a prominent low latitude structure of condensed water ice develops at about 10 km altitude. Known as the Aphelion Cloud Belt (ACB), this recurrent feature was first identified analyzing images from the Hubble Space Telescope by James et al., 1996 and typically covers the regions between 10°S to 30°N as a result of the low aphelion temperatures coupled with the Hadley circulation vertical transport of water in the northern hemisphere (Clancy et al., 2017a). The ACB, containing about 10% of the total water atmospheric content, significantly impacts the seasonal and latitudinal distribution of water vapor, limiting the cross-equatorial transport toward southern latitudes during the northern summer (Clancy et al., 1996; Montmessin et al., 2004). In addition to the ACB, two more distinct cloud structures form during winter at polar latitudes. The North and South polar hoods (NPH and SPH respectively) show variations with season and location depending on topographic features (Hollingsworth et al., 1996) and have a direct influence on the reservoir of water available in the polar caps (Clancy et al., 2017a). Besides its similarities, due to the different surface elevation between hemispheres and different intensities of the meridional circulation during northern and southern winters, the SPH typically shows lower cloud opacities (Clancy et al., 2017a; Montmessin et al., 2004).

1.2.2 Minor species

Besides CO_2, the Martian atmosphere includes a variety of trace gases present in relatively small amounts.

- Nitrogen (N_2). Only in situ measurements of this gas are possible due to the radiatively weak transitions of this homonuclear molecule. According to data by the Curiosity rover (Mahaffy et al., 2013), the volume mixing ratio (VMR) of this species is about 0.0189 ± 0.0003.
- Argon (Ar). As a non-condensable gas, its abundance is constant throughout the Martian year, although its VMR changes as it does the amount of CO_2. With an overall VMR of about 0.0193 ± 0.0003 (Mahaffy et al., 2013), some studies claim its potential as a tracer of the atmospheric dynamics (Sprague et al., 2004; Sprague et al., 2007).
- Oxygen (O_2). The source of this species is the photolysis of CO_2 and H_2O, which produces an average abundance of about 0.0014 (Hartogh et al., 2010). Similarly to Argon, being a non-condensable gas makes it suitable as proxy of other species such as ozone, or atomic oxygen. Recently, the excellent sensitivity and coverage of the NOMAD instrument onboard TGO allowed the detection of the green line (557.7 nm) emission in the dayside atmosphere (Gérard et al., 2020),

the 630-636 nm forbidden emissions (coming not from O_2, but from atomic oxygen), and the Herzberg II band (Gérard et al., 2024).

- Carbon monoxide (CO). This species is produced in the upper atmosphere by photolysis of CO_2 and is recombined again at tropospheric altitudes by OH radicals, hence acting as an excellent tracer of the OH-catalysed chemistry. Its average VMR oscillates around 700 ppm with strong seasonal variations near the poles (Smith et al., 2009) as a result of the CO_2 ice sublimation/condensation at the polar caps. CO is non-condesable so also provides a proxy for the upper atmosphere transport. Recent observations with TGO permitted the characterization of its vertical structure (Modak et al., 2023; Olsen et al., 2021b) and the derivation of some dynamical atmospheric parameters such as eddy diffusion coefficients (Yoshida et al., 2022).

- Hydrogen (H_2). In the altitude range between 20-50 km, molecular hydrogen is produced from the combination of HO_2 radicals with atomic hydrogen, both byproducts of the photolysis of water vapor and its estimated abundance is about 15±5 ppm at low altitudes (Krasnopolsky & Feldman, 2001).

- Ozone (O_3). This species is produced by the photolysis of CO_2 and the following combination of O_2 with atomic oxygen. With an average VMR ranging between 10-350 ppb (Perrier et al., 2006), its distribution is very affected by dynamics. It shows larger abundances at polar latitudes during the winter and lower mixing ratios at all latitudes during the equinox. In addition, observations revealed local variations at high latitudes associated with the topography and oscillations in the polar vortex (Perrier et al., 2006). Many observations reported an anticorrelation with water vapor abundance, with a peak of O_3 abundance during winter when H_2O condenses and the production of OH radicals associated to the destruction of ozone reduces. This anticorrelation was recently confirmed by TGO (Olsen et al., 2022), providing a detailed characterization of its vertical distribution and seasonal variability.

- Methane (CH_4). Linked to biogenic origin on Earth, the presence or absence of this species in the Martian atmosphere is an open question and subject of an intense debate over 20 years. Recent analysis of in situ measurements using the Sample Analysis at Mars (SAM) instrument on Curiosity rover indicate background methane mixing ratio of 0.69±0.25 ppb with sporadic increases of 7.2±2.1 ppb (Webster et al., 2015). Two other relevant detections were reported, first 5.78±2.27 ppb with SAM and the following day 15.5±2.5 with the Planetary Fourier Spectrometer (PFS) onboard Mars Express after a reanalysis of previously undetected amounts. Taking into account that the lifetime of methane is about 330 years, much larger than the timescale for mixing in the Martian atmosphere, a uniform global distribution would be expected (Lefevre & Forget, 2009). If those detections are to be believed, this notable variability would require mechanisms for the destruction of this molecule which are currently unknown. In addition to the problem of these very localized detections, the high sensitivity of the instruments onboard TGO specifically designed for the detection of methane, among other trace species, has not revealed any single detection of this compound in the atmosphere to date (Escudero-Jiménez et al., n.d.; Knutsen et al., 2021; Korablev et al., 2019; Montmessin et al., 2021).

- Hydrogen Chloride (HCl). This trace species, previously considered negligible in the Martian atmosphere (Hartogh et al., 2010; Villanueva et al., 2013), has now been systematically detected by two instruments aboard TGO (Aoki et al., 2021; Korablev et al., 2021). Several works suggest that the Martian surface could be a source of chloride minerals and perchlorate salts (Glavin et al., 2013), which, through surface-atmosphere interactions, might enable chlorine photochemistry in the Martian atmosphere. On Earth, volcanic activity is a primary source of HCl (Graedel & Keene, 1995), implying that the detection of HCl on Mars may indicate active geological processes. Ongoing studies, both theoretical and experimental (accumulation of TGO data) aim to characterize the climatology of HCl on Mars, exploring potential relationships between temperature and other atmospheric components such as dust or water vapor.
- Water vapor (H_2O). Despite its relatively low abundances, water vapor is involved in multiple chemical, radiative and dynamical processes, as mentioned through this Section, positioning itself as a fundamental component of the Martian atmosphere and climate. Given its importance and being the main topic for this Thesis, we will extend its discussion in next Section.

A summary with the atmospheric parameters of Mars and the Earth are shown in Table 1.2.

1.3 Water vapor

In April 1963, Spinrad et al., 1963 using ground base spectroscopic observations detected for the first time evidences of the presence of water vapor in the Martian atmosphere. Temperature and pressure in the surface of Mars, close to the triple point, do not allow water to be stable in the form of liquid, so only gaseous and vapor phases can persist. In 1973, the ground base observations were confirmed with the InfraRed Interferometer Spectrometer (IRIS) onboard the Mariner 9. With these first spacecraft observations of water vapor, Conrath et al., 1973 reported strong seasonal variations in its distribution over the polar regions. A few years later, Farmer et al., 1977 presented the first systematic mapping of the water vapor global distribution. They used the Mars Atmospheric Water Detector (MAWD) onboard Viking orbiters to observe column densities between the northern summer solstice and the following equinox. They revealed that the maximum column abundances moved from high

TABLE 1.2: Parameters and abundances of the main components of the Martian atmosphere of Mars compared with those on Earth. Values retrieved from https://nssdc.gsfc.nasa.gov/planetary/factsheet/

Parameter	Mars	Earth
Surface pressure (mb)	6.36	1014
Surface density (kg/m^3)	0.020	1.217
Scale height (km)	11.1	8.5
Total mass (kg)	2.5×10^{16}	5.1×10^{18}
Average temperature (K)	210	288
CO_2	95.3 % (Owen et al., 1977)	420 ppm
N_2	0.019 % (Mahaffy et al., 2013)	78.08 %
Ar	0.019 % (Mahaffy et al., 2013)	9340 ppm
O_2	0.0014% (Hartogh et al., 2010)	20.95 %
CO	800 ppm (Smith et al., 2009)	100 ppb
H2O	15-1500 ppm (Smith et al., 2004)	1 %

northern latitudes to the equatorial region and that strong local time variations appear at locations with abrupt elevation topographic features. Accumulating Viking observations during more than one MY, Jakosky and Farmer, 1982 provided the first evidences of a water vapor seasonal cycle, with each hemisphere showing its maximum column abundance during the local summer suggesting the sublimation of water ice reservoir in the polar caps, although with the northern polar column abundances being significantly larger than those over southern polar regions. These observations suggested a dominating northern polar cap with a water inventory equivalent to a global layer of 22-33 m thickness (Smith et al., 1999), and an apparent net transport of water toward the southern polar cap.

By the end of the 20th and the beginning of the 21th century, the Thermal Emission Spectrometer (TES), onboard NASA's MCS, confirmed and complemented most of the Viking observations, although some differences were found at the southern hemisphere. TES observed a peak in the column densities at high southern latitudes that was not detected by MAWD due to biases related with two global dust storm occurring during the Viking observations (Smith, 2002). TES also revealed the difference in the condensation level between perihelion and aphelion, typically located 10-15 km during the first and at about 30 km altitude during the second. Extending the data set, Smith, 2004 was able to provide a more complete view of the water cycle from MYs 24 to 26. They reported a warmer and dustier atmosphere with lower ice cloud occurrence during the perihelion than at aphelion. The interannual variability resulted to be more relevant during the perihelion. In the case of water vapor, this larger variability was more prone to occur near the southern polar region at $L_S = 270° - 300°$.

With the arrival of new spacecrafts to Mars, new observations and studies focused on different aspects of the water cycle and distribution were possible. OMEGA (Observatoire pour la Minéralogie, l'Eau, les Glaces et l'Activité) onboard MEX allowed the mapping of the water vapor abundance over the northern polar cap during the summer, capturing the sublimation process (Encrenaz et al., 2005; Melchiorri et al., 2007) and observations above the Tharsis volcanoes revealed a water vapor VMR enrichment at their summits (Maltagliati et al., 2008). With an analysis of the first year of OMEGA data (MY 27), Maltagliati et al., 2011b stated the necessity of water vapor vertical profiles to properly analyze contributions to the water cycle such as water ice clouds and the vertical mixing of water.

The Spectroscopy for the Investigation of the Characteristics of the Atmosphere of Mars (SPICAM) on board MEX provided more data on the seasonal distribution of water vapor, which besides reporting systematically lower abundances than MAWD and TES, the seasonal patterns observed were comparable with those from previous works (Fedorova et al., 2006). Another MEX instrument, PFS, reveled that most of the water vapor remains in the northern hemisphere after the polar cap sublimation, with only about a quarter part being transported southward (Tschimmel et al., 2008).

The Compact Reconnaissance Imaging Spectrometer for Mars (CRISM) onboard MRO extended even more the number of available observations of water column densities, adding MYs 28 and 29 to the record. During southern summer of the first year, a global dust storm occurred and the column densities observed by CRISM reduced compared to observations from previous years (Smith et al., 2009).

When compared to column profiles measurements, the vertical distribution and variability of water vapor in Mars have been poorly characterized to date. SPICAM permitted for the first time the systematic monitoring of the vertical structure of the atmosphere, allowing for the characterization of CO_2, aerosols and water vapor vertical distribution from 15 to 50 km altitude (Fedorova et al., 2009). These observations showed frequent episodes of water present in excess of saturation (supersaturation) which could impact the escape of water to space (Maltagliati et al., 2011a). With time, enough SPICAM observations allowed annual surveys. A first seasonal variation of the vertical distribution of water during a complete MY was presented in Maltagliati et al., 2013, where they revealed a strong dynamism of the vertical structure during the southern spring and discrepancies with the models. These observations proved the strong bias' of the previous nadir observations to the lowermost altitudes. More studies based on SPICAM observations followed, providing more insight on the relationship of water vapor with dust storms, which produce a more vertically extended distribution of water (Fedorova et al., 2018a). More recently, Fedorova et al., 2021 presented a multiannual survey of vertical distributions of water vapor from MYs 27 to 34 in which periods with two global dust storms were included, confirming the impact of dust storms on the water vapor vertical distribution and the importance of the perihelion season on the hydrogen escape.

All these observations and studies combined with the development of progressively more sophisticated theoretical models, permitted piece by piece, to build our current understanding of the water cycle in Mars, which is extensively described in several reviews, like that of Montmessin et al., 2017. Besides some interannual differences, the same processes seem to control the global distribution of water every year. This seasonal cycle, illustrated in Figure 1.5 with results from TES and CRISM for several MYs and simplified in Figure 1.6 , can be summarized as follows (seasons are refereed to the northern hemisphere):

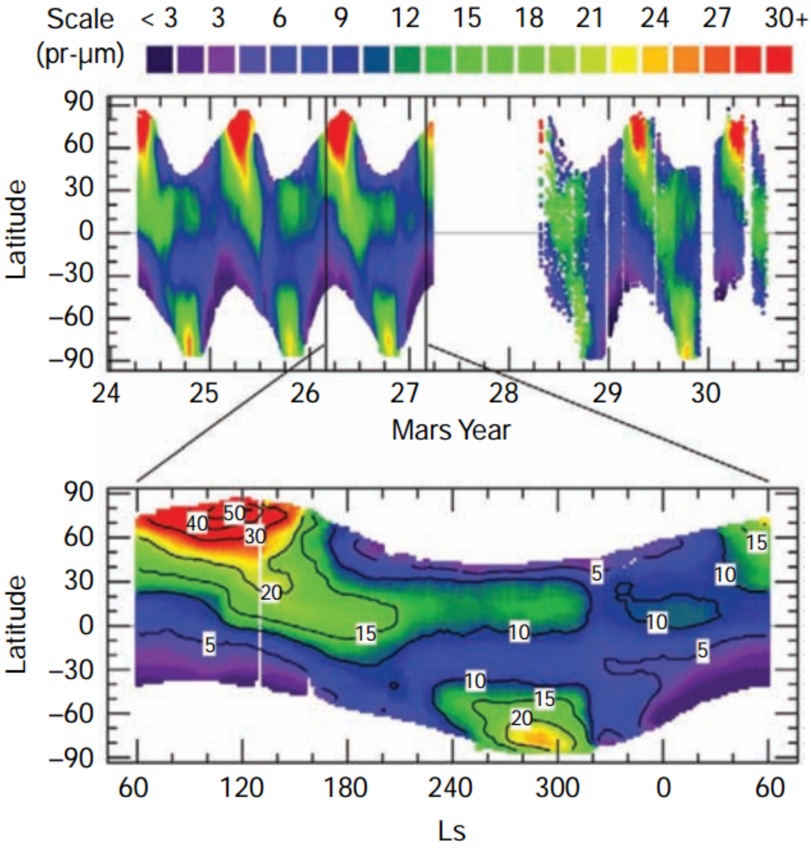

FIGURE 1.5: Annual cycle of water vapor column abundance versus season and latitude over several Matian Years from TES (MY 24-27) and CRISM (MY 28-30) observations. Credit: Montmessin et al., 2017

- Spring equinox ($L_S = 0°$). The beginning of the Martian year is characterized by a cool and dry atmosphere. The global atmospheric circulation at this solar longitude is dominated by a symmetric Hadley cell. The subsolar point at this season is located at low latitudes, so the upward branch of the cell occurs at equatorial regions. Later in this season, after $L_S = 40°$, the surface temperature in the northern hemisphere raises, and the sublimation of the polar cap leads to the water vapor progressively increasing.

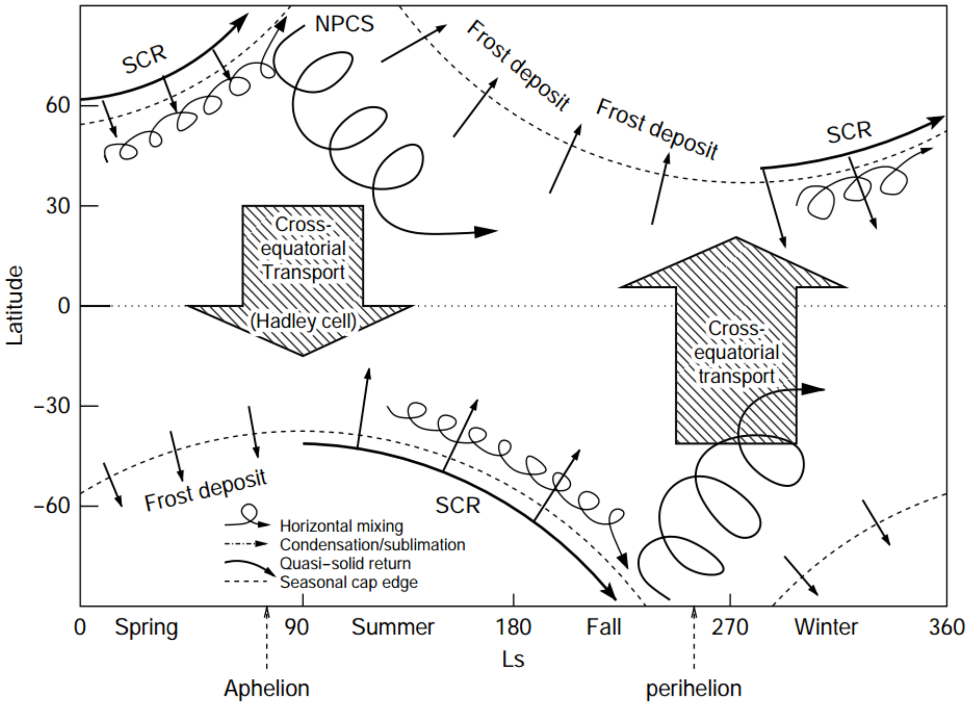

FIGURE 1.6: Schematic representation of the water cycle during a Martian Year. NPCS stands for North Polar Cap Sublimation; SCR stands for Seasonal Cap Recession. Credit: Montmessin et al., 2004

- Summer solstice ($L_S = 90°$). At high latitudes above 70°N the atmosphere shows the highest water vapor abundances, peaking near the pole at $L_S = 120°$, corresponding to the maximum sublimation of the northern polar cap, and decreasing southward. After $L_S = 130°$, water vapor levels in the north decline sharply, counteracted with a progressive increase of abundances in the south as water is transported to that hemisphere. By this time, the meridional circulation is dominated by a single Hadley cell with an upward branch located at high northern latitudes. When water enters this branch, part is transported southward and part northward, recondensing again into the polar cap. As a result the northern polar cap slowly retreats with an thicker annular structure at the edges. The peak in column abundances moves southward, showing maximum levels at 45°N by $L_S = 135°$ and at 30°N by $L_S = 150°$. Soon after, by $L_S = 170°$ a significant maximum forms between the equator and 30°N latitude.

- Autumn equinox ($L_S = 180°$). As the water vapor abundance in the northern hemisphere decreases, it gradually rises in the southern hemisphere. During the equinox, the meridional circulation is dominated by two symmetric cells with the upper branch located at equatorial latitudes, that progressively moves southward transitioning to an asymmetric single Hadley cell. By $L_S = 220°$, the larger insolation sublimates the southern polar cap, increasing the water abundances at high southern latitudes.

- Winter solstice ($L_S = 270°$). At this season the global circulation is controlled by a single asymmetric Hadley cell with the upward branch located at high southern latitudes. The peak abundances appear around $L_S = 290°$ and although the column abundances are typically lower than those in the northern analog season, recent observations of vertical profiles revealed that the water is not confined to low altitudes but vertically extended as a result of a more intense global circulation. During this season, frequent dust storms occur, affecting even more the vertical distribution of water and allowing for high abundances even higher than usual. After $L_S = 300°$ water in the southern hemisphere begins to diminish and by $L_S = 330°$ the progressively cooler temperatures lead to a drier and more water vapor is confined to very low altitudes similar to the picture during the beginning of the year.

1.4 Motivation and objectives of this Thesis

Scientific motivation and opportunity. Currently, as discussed in previous Sections, Mars is a cold and almost dry planet with a thin atmosphere composed mainly of CO_2. However, there is evidence that in the past, liquid water could have flowed on its surface, creating many of the channel-like geological structures we see today. This suggests that Mars' atmosphere has evolved from being a moist, water vapor-rich atmosphere that was possibly conducive to life, to the weak and dry atmosphere it has now. This loss of water is attributed to several factors, with atmospheric escape (Chaffin et al., 2017) being one of the most plausible explanations. The cyclical or permanent deposition of water vapor in the polar caps (Khayat et al., 2019) also plays a fundamental role in Mars' atmospheric dynamics.

Numerous space missions have been sent to the Red Planet over the past 25 years to study its surface (Pathfinder, Spirit and Opportunity rovers, Phoenix Lander, Insight, and recently Perseverance) and its atmosphere (MGS, MEX, MRO, Maven …). Except for MEX and MAVEN, all these missions have focused on studying the lower atmosphere, leaving the upper atmosphere as a still not well-characterized region of the planet, even though it is essential for understanding escape processes and large-scale climate evolution.

The recent European ExoMars 2016 Trace Gas Orbiter mission, in orbit around Mars since April 2018, aims to address numerous currently open questions about Mars and its upper atmosphere (López-Valverde et al., 2018; Vandaele et al., 2018), thanks to an extremely sensitive technique for characterizing vertical profiles of trace gases such as water vapor. This strategy is also ideal for detecting other trace gases that are even less abundant and previously unknown. The precise determination of vertical profiles, specifically of H_2O, represents an excellent opportunity to understand aspects not yet known of the water vapor, like its vertical distribution and transport, and its role on the chemistry of other species. This is also a chance to study the escape processes occurring in the Martian atmosphere (Heavens et al., 2018), and therefore could help to better understand the history of water on Mars in the past, as well as enable a better characterization and understanding of the planet's current hydrological cycle.

Last, but not least, the IAA participates actively as co-PI in the scientific exploitation of the NOMAD data, with privileged access to the measurements. All this adds another sense of opportunity to this Thesis. In the Solar System department, there is a large experience on remote sounding, atmospheric modeling and retrieval theory, which are essential tools for a proper analysis of the NOMAD data.

Objectives of this Thesis. In this context, the Nadir and Occultation for Mars Discovery (NOMAD) instrument on board the TGO orbiter allows for the systematic probing of the Martian atmosphere with unprecedented $\sim$1 km vertical resolution. This, combined with the high sensitivity of the solar occultation signal, enables the detection of gases present in very low concentrations in the atmosphere. The study of the vertical distribution of water vapor, as mentioned above, is fundamental for explaining the escape mechanisms that have led Mars to its current state. Moreover, the correct characterization of the Martian atmosphere (and climate) can be very useful in supporting upcoming robotic missions (and, in the longer term, perhaps human exploration missions) to the Red Planet. Therefore, the scientific exploitation of TGO's observations is of enormous interest and highly relevant, meaning that they can have a significant impact on the scientific community. The main objectives this Thesis aims to achieve are listed as follows:

- *The analysis of the distribution and cycle of water vapor*. It is particularly useful and ambitious to understand how water vapor is distributed with altitude, as well as its spatial and seasonal variability, and its relationship with various environmental conditions such as dust storms, thermal structure, winds, etc.
- *The characterization of the middle/upper atmosphere as a whole and its connection with lower altitudes*, with the purpose of addressing the still badly understood vertical transport and the escape processes that occur in that region. Correctly understanding the escape mechanisms in the upper atmosphere and their relation with dust and water at low altitudes is necessary for understanding why Mars is currently so dry.

During the development of this Thesis, we followed a series of programmatic steps that allowed the successful analysis of the NOMAD data, which permitted achieving the objectives discused above. Those steps can be summarized as follows:

- Familiarization with the ExoMars 2016 Trace Gas Orbiter mission and the NOMAD instrument.

- Specific training in the chemistry, dynamics, and radiation of the Martian atmosphere, with an emphasis on the dynamic and chemical processes affecting H_2O in the atmosphere and on remote sensing and atmospheric retrieval techniques.
- Conducting synthetic inversions of solar occultation data in order to identify optimal retrieval and processing parameters for the latter NOMAD data analysis. Extending the study to perform an early error analysis.
- Collecting and cleaning NOMAD infrared spectra for their evaluation and improvement of their official calibration.
- Operational application of the previous techniques and combination of spectra from complementary diffraction orders.
- Comparison with results published by other teams and with numerical simulations using global climate models.
- Physical interpretation of the results.

This manuscript summarizes in eight Chapters the work done during our research in order to accomplish the objectives proposed here. The contents are structured as follows: Chapter 2 presents a description of the TGO mission and the NOMAD instrument, focusing on the Solar Occultation channel. Chapter 3 contains a summary of radiative transfer and inversion theory fundamentals, highlighting some important aspects of the water molecular spectroscopy that are used throughout this work. In addition, the radiative transfer tools and retrieval algorithms used during this research are briefly described in this Section. Chapter 4 is devoted to the processing and analysis methodology of the NOMAD data. The main results of this Thesis are presented in Chapters 5, 6 and 7, focused on the impacts of the Global Dust Storm during MY 34, on the vertical distribution of water vapor in the upper atmosphere and on the analysis of the global distribution of water vapor during the whole ExoMars-TGO mission. Finally, Chapter 8 presents a summary of this work, highlighting the main conclusions and suggesting future extensions and improvements.

Chapter 2

ExoMars 2016 Mission: Trace Gas Orbiter

2.1 The ExoMars mission overview

During the beginning of the 21th century, several instruments reported detection of methane in the atmosphere of Mars. The Planetary Fourier Spectrometer (PFS) onboard Mars Express observed a global average methane mixing ratio of about 10±5 parts per billion by volume (ppbv) (Formisano et al., 2004). Ground-based high resolution spectrometers also detected similar abundances with variability of few ppbv (Krasnopolsky et al., 2004; Mumma et al., 2009). Since the outgasing in Mars is very low and the orbital observations of thermal emission do not reveal hot spots on the surface, theses studies discarded geological processes producing methane, and suggested that the main source of this species could be biological, produced by living organisms below the surface of the planet. This discovery motivated the space exploration community to develop a dedicated mission in order to study the atmosphere of Mars in detail in the search for methane and trace species. In 2008, the National Aeronautics and Space Administration (NASA) and the European Space Agency (ESA) started collaborating in order to elaborate a scientifically profitable mission for the 2016 launch opportunity (Zurek et al., 2011). Finally, due to budgetary problems, NASA abandoned the project and the resulting ExoMars mission ended up being a cooperation between ESA and Russia's Roscosmos State Space Corporation for the science part of the mission, with Roscosmos providing the launch vehicle (Proton rocket) and several scientific instruments. At that time, ExoMars was designed as a two parts mission planed for the launch windows on 2016 and 2018, with two main goals: (i) to achieve detection of methane and a wide variety of atmospheric trace gases characterizing their spatial and temporal variation from orbit, and (ii) to study possible signatures of life in the surface with a rover. The element responsible for the atmospheric study is the Trace Gas Orbiter, currently in orbit around Mars since 2016 and in scientific routine operations since 2018. However, the part of the mission involving the surface rover, initially planed for the first part of the mission, was delayed and replaced by the landing module demonstration vehicle Schiaparelli, launched with TGO in 2016. The second part of the mission designed to land the rover have been delayed several times since 2018, and the current launch window for is planned for no earlier than 2028.

2.2 Trace Gas Orbiter

The 2016 Trace Gas Orbiter (TGO) was launched on 14th March 2016, entering Mars orbit nine months later and releasing the Schiaparelli surface platform, which failed during the atmospheric entry and crashed into the surface. After orbital maneuvers and aerobreaking, in 2018 TGO entered into its planned orbit at 400 km altitude from the surface with a period of about 2h and an inclination of 74 degrees (Ashman et al., 2018). Since then, TGO is performing measurements regularly observing Mars in different geometries, illustrated in Figure 2.1.

- Nadir Observation: The spacecraft is pointing downwards and towards the surface, observing the reflected sunlight or surface thermal emission. The line of sight is perpendicular to the surface.
- Limb Observation: The satellite is pointing to the edge (limb) of the planet, observing emissions from the atmosphere. The line of sight is parallel to the surface.
- Solar Occultation: The spacecraft is pointing to the Sun through the atmosphere, probing the composition and properties of the atmosphere as it absorbs, and scatters sunlight. The line of sight is parallel to the surface. This geometry using the Sun as a light source provides an excellent Signal to Noise Ratio (SNR) (Thomas et al., 2016) suitable for the detection of trace species.

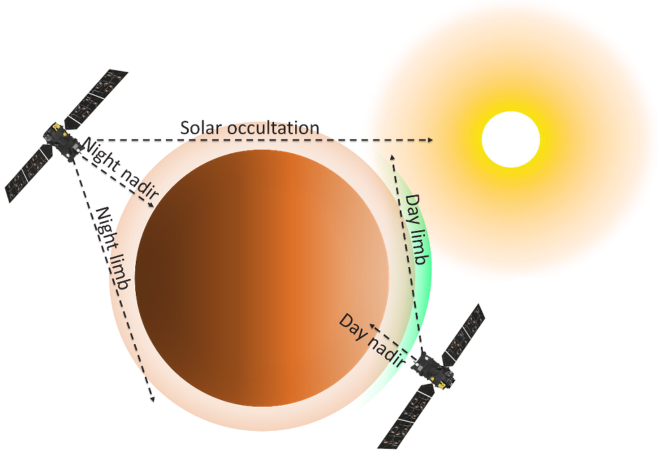

FIGURE 2.1: TGO observation modes. Credit: https://nomad.aeronomie.be/

The spacecraft carries four scientific experiments dedicated to the detection and characterization of trace gases (minor species with abundances less than 1 %), which are illustrated in the Figure 2.2.

- The Colour and Stereo Surface Imaging System (CaSSIS) (Thomas et al., 2017) is a high resolution camera (4.6 m/pixel) designed to capture color and stereoscopic images of the Martian surface. Its main objective is to monitor the surface in search of possible sources of trace gases.

- The Fine Resolution Epithermal Neutron Detector (FREND) (Mitrofanov et al., 2018) is a neutron telescope designed to map the epithermal neutron emissions on Mars. The observation of this neutron emissions allows for an indirect way of detecting the presence of Hydrogen below the surface, i.e. proxy of subsurface water deposits.
- The Atmospheric Chemistry Suite (ACS) (Korablev et al., 2018) is equipped with three distinct infrared spectrometers dedicated to the observation of the Martian atmosphere in different geometries: solar occultation, limb, and nadir.
- Finally, Nadir and Occultation for Mars Discovery (NOMAD) (Vandaele et al., 2018) is an integrated suite of three spectrometers probing the atmosphere with solar occulation and limb observation modes, similar to ACS.

The near-circular TGO orbit and its inclination, provide an excellent coverage of the Martian surface and enable opportunities for solar occultation/limb observations. This orbit also allows the spacecraft to relay data from the existing assets on the planet and future landers and rovers (Vandaele et al., 2018).

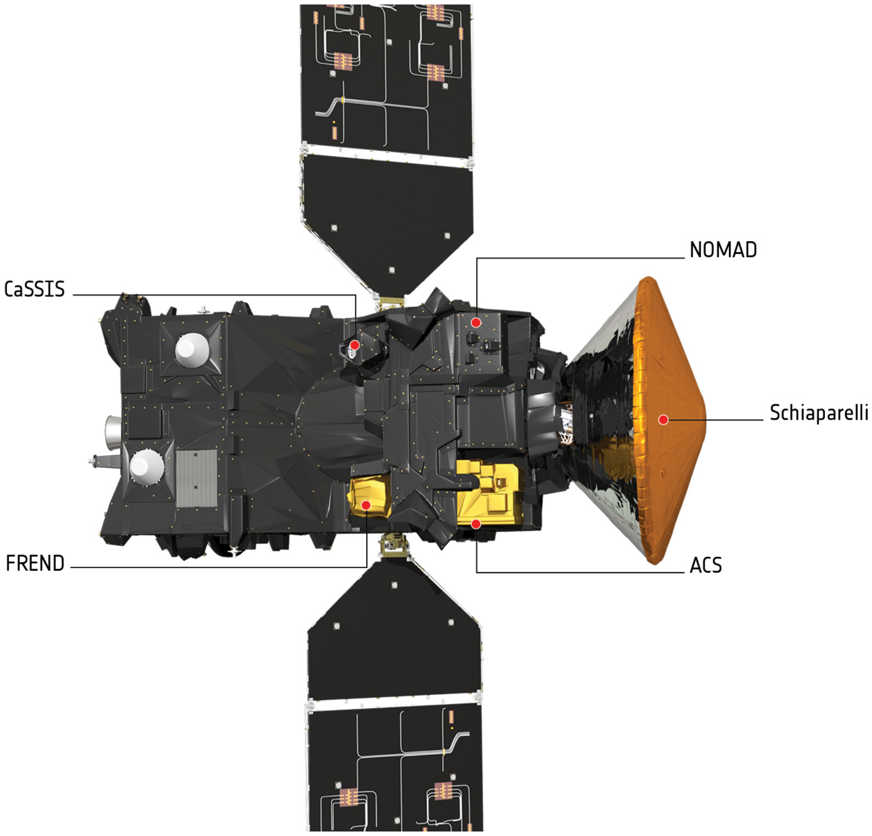

FIGURE 2.2: ExoMars 2016 Trace Gas Orbiter (TGO) and Schiaparelli, with the four scientific instruments CaSSIS, FREND, ACS and NOMAD. Credit: ESA/ATG medialab.

2.3 The NOMAD instrument

NOMAD is one of the four scientific instruments onboard TGO and key for trace gas detection and mapping on Mars. The instrument is led by the Belgian Institute for Space Aeronomy (BIRA-IASB) (Neefs et al., 2015; Patel et al., 2017; Thomas et al., 2016). Its objective is to survey the Martian atmosphere in ultraviolet (UV), visible and infrared (IR), searching for many minor species, and if not detected, improving and constraining their detection limits. In order to fulfill this goal, NOMAD is composed of three independent spectrometers and its design is based upon the Solar Occultations in the Infrared (SOIR) from the Venus Expres mission (Bertaux et al., 2007). Each one of those spectrometers, shown in the schematic of Figure 2.3, are thoroughly described in their own technical reports and in diverse papers in the literature. Here we only provide a brief comment about them:

- The Ultraviolet and VIsibile Spectrometer (UVIS) was designed to operate in both solar occultation and nadir observation modes. It is capable to probe the atmosphere in the spectral range of 200-650 nm with a spectral resolution <2nm. A detailed description of UVIS is presented in Patel et al., 2017.
- The Limb Nadir and Occultation (LNO) operates in limb and solar occultation modes in the infrared spectral range of 2.3-3.8 µm. A detailed description of UVIS is presented in Neefs et al., 2015.
- The Solar Occultation (SO) channel, building upon SOIR is designed to operate in the infrared covering the 2.3-4.3 µm spectral range. This channel, unlike the others, is devoted only to observe the atmosphere in solar occultation mode, allowing for a SNR of about 2000 (Thomas et al., 2016). An in-depth technical description of SO is presented in Neefs et al., 2015 and Thomas et al., 2022, although we provide a summary of its main features in the following Section.

2.3.1 Solar Occultation channel

The results presented in this Thesis were obtained using observations from the SO channel, hence, this Section will focus on that precise channel summarizing the main instrumental features involved during the data acquisition.

Acousto Optical Tunable Filter

SO operates in the infrared, covering a spectral range between 2.3 to 4.3 µm (2320 - 4350 cm^{-1}). As shown in the schematic of the NOMAD SO optical design 2.4, the first element the light finds along its pass through the channel's optics is the Acousto Optical Tunable Filter (AOTF). This passband filter (whose main component is a TeO_2 crystal) uses an electric radio-frequency generator to induce an oscillation of expansion and compression of the crystal which changes its the diffraction properties

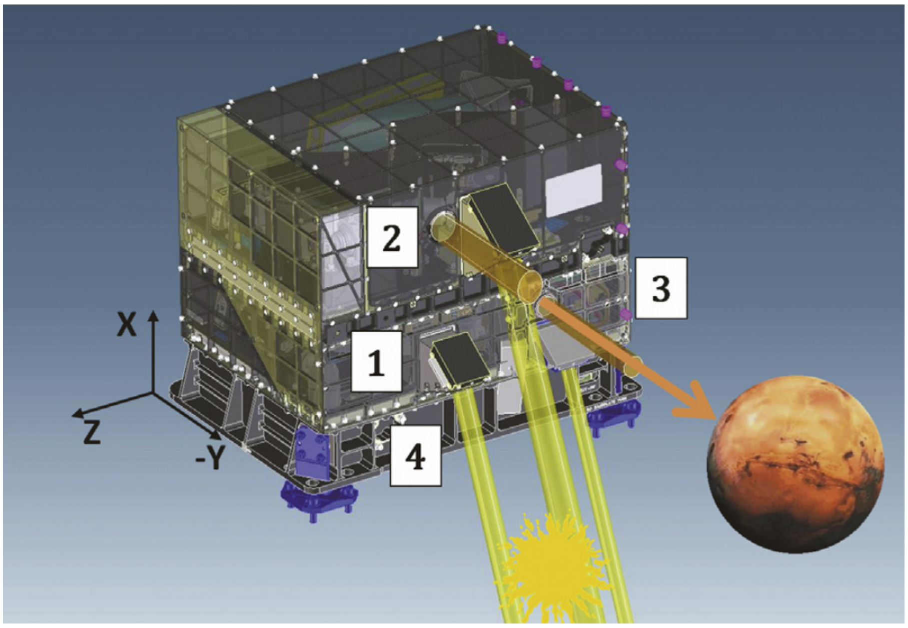

FIGURE 2.3: Schematic of the NOMAD instrument and the channels SO (1), LNO (2) and UVIS (3); and the electronics (4). Credit: Vandaele et al., 2015

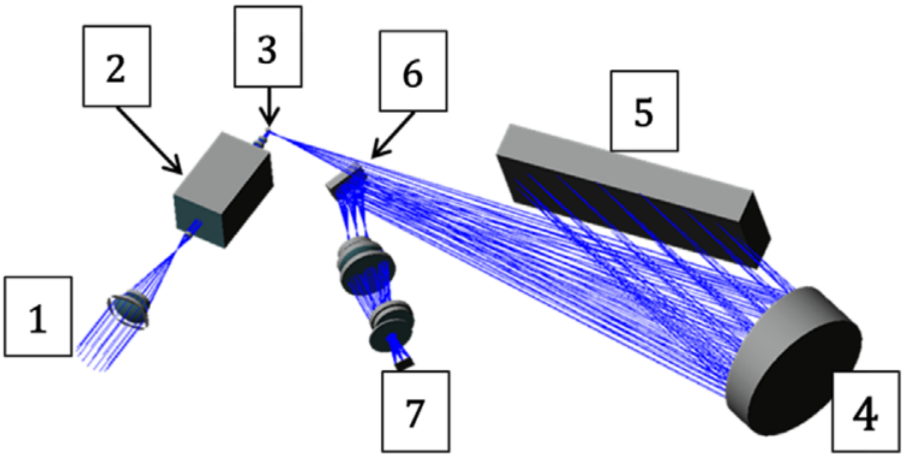

FIGURE 2.4: Optical design of the NOMAD SO channel. (1) entrance optics, (2) AOTF filter, (3) spectrometer slit, (4)parabolic mirror, (5) echelle grating, (6) folding mirror, (7) detector. Credit: Thomas et al., 2016.

(Thomas et al., 2016). As result, part of the light is refracted, and by controlling the input radio-frequency it is possible to select a specific spectral range of the incident beam to pass through the filter unaltered, hence reaching the diffraction grating as the selected main order. The AOTF introduces a sinc-squared function response to the signal and in order to maximize the output, its central wavenumber, i.e. the peak of the AOTF, should match the central wavenumber of the diffraction order to measure.

Despite the advantage of a non-moving parts mechanism and its quick order selection capability, the AOTF has some drawbacks. Due to the nature of the sinc function, the contribution of signal coming form adjacent diffraction orders is not null, therefore light from nearby spectral regions is mixed with the main order's signal. In the case of NOMAD, during extensive calibration campaigns (Liuzzi et al., 2019; Villanueva et al., 2022a) it was found that the left and right AOTF sidelobe wings, responsible of the adjacent orders contribution, are not symmetric and their ratio change as the central wavenumber does. The width of the AOTF also depends on its frequency. In order to reproduce the observed signal, a Gaussian function with a constant width but a frequency dependent intensity, needs to be added to the sinc resulting in a complex function with four parameters which have variable values across the whole NOMAD SO spectral range. The AOTF functional can be expressed as

$$f_{\mathrm{AOTF}}(\nu) = I_0(\nu) w_0^2 \frac{\left[\sin \frac{\pi(\nu-\nu_0)}{w_0}\right]^2}{\pi^2(\nu-\nu_0)^2} + I_{G,0} \exp\left[\frac{-(\nu-\nu_0)^2}{\sigma_G^2}\right] \tag{2.1}$$

$$I_0(\nu) = \left\{ \begin{array}{lr} S_0, & \nu \leq (\nu_0 - w_0) \\ 1, & (\nu_0 - w_0) \leq \nu \leq (\nu_0 + w_0) \\ S_0 A_0, & \nu \geq (\nu_0 + w_0) \end{array} \right\}$$

The AOTF is defined by its central wavenumber ν_0, width $w_0 = w(\nu_0)$, asymmetry factor $A_0 = A(\nu_0)$, sidelobe intensity $S_0 = S(\nu_0)$, Gaussian width $\sigma_G = 50\ \mathrm{cm}^{-1}$ and Gaussian intensity $I_{G,0} = I_G(\nu_0)$. The AOTF center, which sets the position of the peak of the AOTF sinc, is defined as a function of the radio frequency applied to the crystal filter

$$\nu_0 = G_0 + G_1 A + G_2 A^2 \tag{2.2}$$

where A is the frequency applied (Hz) and the coefficients $G_0 = 305.060$, $G_1 = 0.150$ and $G_2 = 1.341 \cdot 10^{-7}$ Liuzzi et al., 2019. In addition, this central wavenumber has a dependence on the filter's temperature T, shifting its position as

$$\nu_0' = \nu_0(1 - 6.528 \cdot^{-5} T) \tag{2.3}$$

The AOTF functional for the NOMAD SO diffraction order 168 as for its closest four adjacent orders is shown in top panel of Figure 2.5. The bottom panel shows the relative contribution to the total observed flux of each order.

This AOTF needs to be included in any Forward Model that aims to produce realistic simulations of the NOMAD SO signal. The implementation of the AOTF into the IAA processing pipeline has taken a great effort. Given its complexity and with the objective of validating its correct performance, we lead a comparison campaign involving different teams in the NOMAD consortium such as BIRA-IASB, The University of Tokyo and NASA Goddard Space Flight Center. A summary of the results of this extensive comparison are presented in Chapter 6 and in Appendix A.

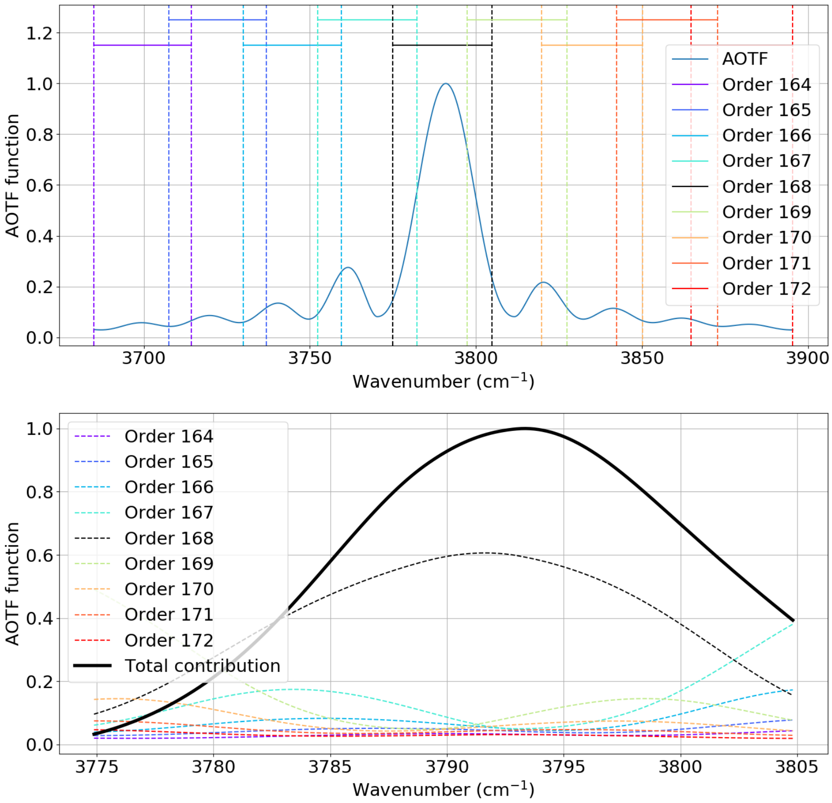

FIGURE 2.5: Top panel: Simulated AOTF for the NOMAD diffraction order 168 using the parameters from the nominal characterization (Villanueva et al., 2022a). Four adjacent orders have been considered. Bottom panel: Relative contribution of the adjacent orders to the main diffraction order. Note that the spectral range is different in both panels.

For this Thesis, we adopted the latest AOTF characterization provided by Villanueva et al., 2022a, for which the AOTF parameters as function of the wavenumber ν are defined as

$$w(\nu) = 20.173 + 7.476 \cdot 10^{-4}\nu + -1.664 \cdot 10 - 7\nu^2 \tag{2.4}$$

$$S(\nu) = 4.088 + -3.302 \cdot 10^{-3}\nu + 8.107 \cdot^{-7} \nu^2 \tag{2.5}$$

$$A(\nu) = -1.249 + 1.290 \cdot 10^{-3}\nu + -1.545 \cdot^{-7} \nu^2 \tag{2.6}$$

$$I_G(\nu) = 1.601 + -9.638 \cdot 10^{-4}\nu + 1.493 \cdot 10^{-7}\nu^2 \tag{2.7}$$

for the AOTF width, sidelobe ratio, asymmetry factor and Gaussian offset respectively. These parameters are illustrated in Figure 2.6.

Echelle grating

After the AOTF, the slit and the mirrors, the next element in the optical path is the the echelle grating. In order to obtain the spectra, the SO channel uses an echelle grating in a near Littrow configuration, i.e, the angle of the incidence beam α is almost equal

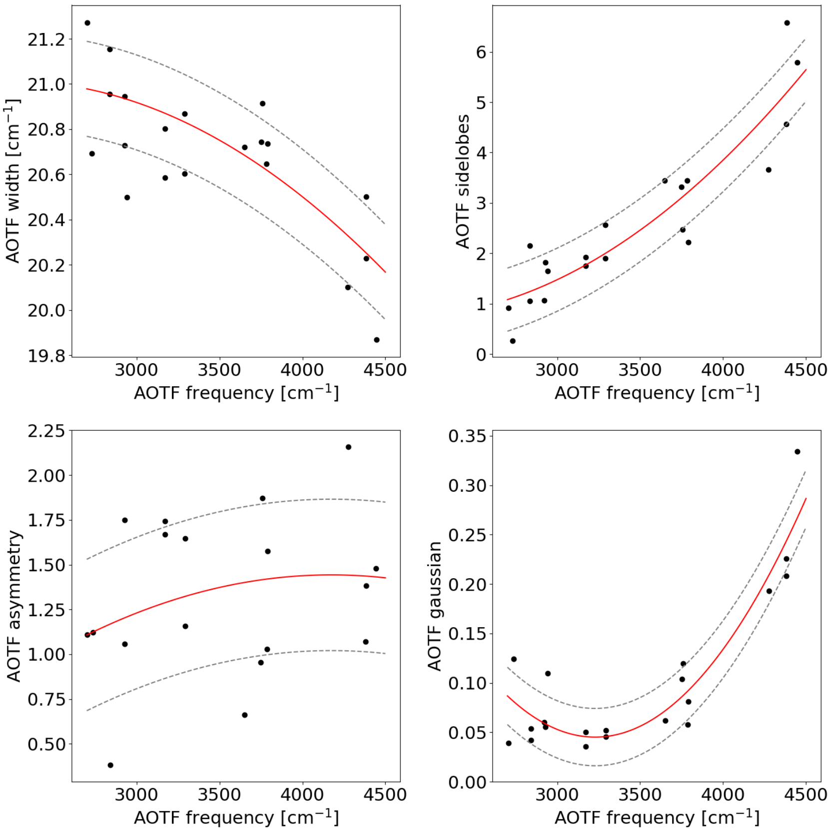

FIGURE 2.6: AOTF recipe from Villanueva et al., 2022a.

to the angle of the diffracted beam β, both separated by an angle γ. In addition, the incidence angle is slightly tilted by i from the blaze angle θ_B in the plane normal to the grating surface. Therefore, the grating equation for this conditions can be written as

$$\frac{\nu_c}{m} = \frac{g}{2\sin(\theta_B)\cos(i)\cos(\gamma)} \tag{2.8}$$

where ν_c is the central wavenumber of the diffraction order m and g the grating density (lines/mm). From this equation we can define the spectral range where adjacent orders do not overlap with the main order m, i.e. the Free Spectral Range (FSR), which is simply

$$\text{FSR} = \frac{\nu_c}{m} \tag{2.9}$$

Ideally, none of the terms in equations 2.8 and 2.9 should change, following the constant FSR set for the SO channel during the ground calibrations to 22.56 cm−1 (Neefs et al., 2015). In addition, the SO optics were designed in such a way that the central wavenumber of the order ν_c coincides with the center of the detector, this is, pixel number 160 out of 320. However, subsequent in-flight calibrations (Liuzzi et al., 2019) and recent specific observations devoted for a calibration campaign (Villanueva et al., 2022a), showed that the actual FSR varies with the diffraction order and with the instrument's temperature. For each pixel p, it was found that the FSR can be described very well with a second order polynomial

$$\mathrm{FSR}_p = F_0 + F_1 p + F_2 p^2 \tag{2.10}$$

with coefficients $F_0 = 22.473$, $F_1 = 5.560 \cdot 10^{-4}$ and $F_2 = 1.751 \cdot 10^{-8}$ (Liuzzi et al., 2019) which provide the pixel-wavenumber calibration. Then, the shift produced by variations in temperature T is

$$\mathrm{FSR}' = \mathrm{FSR}[1 + K(T)] \tag{2.11}$$

where the temperature function $K(T)$ was determined to be

$$K(T) = K_0 + K_1 T + K_2 T^2 \tag{2.12}$$

with coefficients $K_0 = -1.900 \cdot 10^{-4}$, $K_1 = -1.307 \cdot 10^{-5}$ and $K_2 = -2.444 \cdot 10^{-7}$ (Villanueva et al., 2022a). Within each order, the intensity of the light reaching the detector follows a wavenumber-dependent function known as blaze function, being the result of the wavelength dependency of the diffracted angle (Thomas et al., 2016). This function can be approximated with a squared-sinc function (Liuzzi et al., 2019)

$$f_{\text{blaze}}(\nu, \nu_0, w_b) = \left[w_b \frac{\sin \frac{\pi(\nu - \nu_b)}{w_b}}{\pi\,(\nu - \nu_b)} \right]^2 \tag{2.13}$$

where ν_b is the blaze center and w_b is the width of the blaze, which is equal to the FSR. As mentioned above, an anomaly in the optics of the SO channel displaces the center of the blaze, which is approximately following a third order polynomial function depending on the diffraction order m. In terms of the AOTF central wavenumber ν_0, the blaze center can be defined as

$$\nu_b = \left[22.586 + 9.793 \cdot 10^{-6} \overline{\nu}_0 - 7.206 \cdot 10^{-9} \overline{\nu}_0^2 - 1.002 \cdot 10^{-11} \overline{\nu}_0^3 \right] \cdot m \tag{2.14}$$

where $\overline{\nu}_0 = \nu_0 - 3700\ \mathrm{cm}^{-1}$.

This description of the grating's FSR and blaze are assumed by all NOMAD teams, and is incorporated into the IAA Forward Model.

Instrumental Line Shape

Ideally, the spectral features captured by the detector should resemble to Dirac deltas, this is, narrow and strong absorption lines. However, in addition to the AOTF, the dispersion and diffraction effects of the light throughout the whole optical system affect the signal reaching the detector, and the extended width of the slit (not being infinitesimally narrow) introduce an instrumental effect to the spectral lines. Typically, the Instrumental Line Shape (ILS) can be modeled convolving a monochromatic

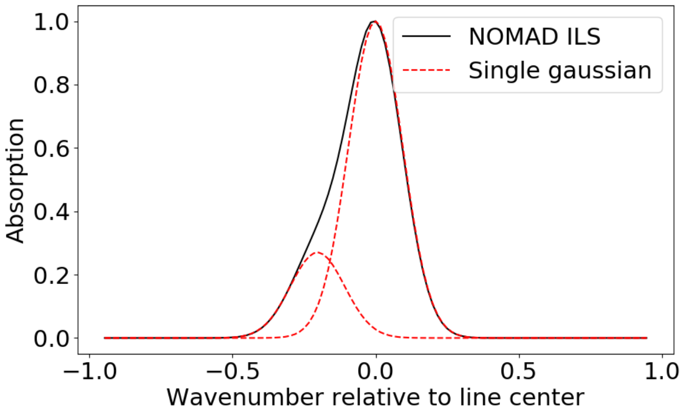

FIGURE 2.7: ILS double Gaussian model.

spectrum with a Gaussian kernel. However, the NOMAD data shows asymmetric lines with an extended left wing of the Gaussian. This feature can be reproduced with a double Gaussian whose separation varies with frequency and diffraction order (Thomas et al., 2022) as illustrated in Figure 2.7.

$$f_{\mathrm{ILS}}(\nu, p) = \exp\left[\frac{(\nu-\nu_p)^2}{2c^2}\right] + a\exp\left[\frac{[(\nu-b_p)-\nu_p]^2}{2c^2}\right] \tag{2.15}$$

where the parameters reported in Villanueva et al., 2022a are:

- $a = 0.27$ the intensity of the second Gaussian.
- c the width equivalent to the instrumental resolving power $RP = \lambda/\Delta\lambda = 17000$ defined as $c = \nu_c/2RP\sqrt{2\ln 2}$ for the central wavenumber ν_c of the order.
- ν_p the wavenumber at pixel p.
- $b_p = b(p)$ the separation of the two Gaussians defined by the central wavenumber of the diffraction order (ν_c) as

$$b(p) = \left[-1.367\cdot 10^{-3} + 1.716\cdot 10^{-3}p - 3.067\cdot 10^{-6}p^2\right]\left(\frac{\nu_c}{3700}\right) \tag{2.16}$$

As part of the collective efforts made within the NOMAD consortium in order to provide a precise and reliable instrumental calibration recipe (Villanueva et al., 2022a), at the IAA-CSIC we performed an exhaustive study of the ILS. We analyzed more than 60 occultations taken during the first year of NOMAD SO observations. For a set of diffraction orders from 121 to 190, after correcting for some residual calibration issues such as a spectral shift in the line positions and a residual bending in the transmittance baseline (see Chapter 4 for more details), we merged the spectra of all of the observations at each order within a predefined altitude range, carefully selected for each spectral line. In order to avoid optically thick conditions at low

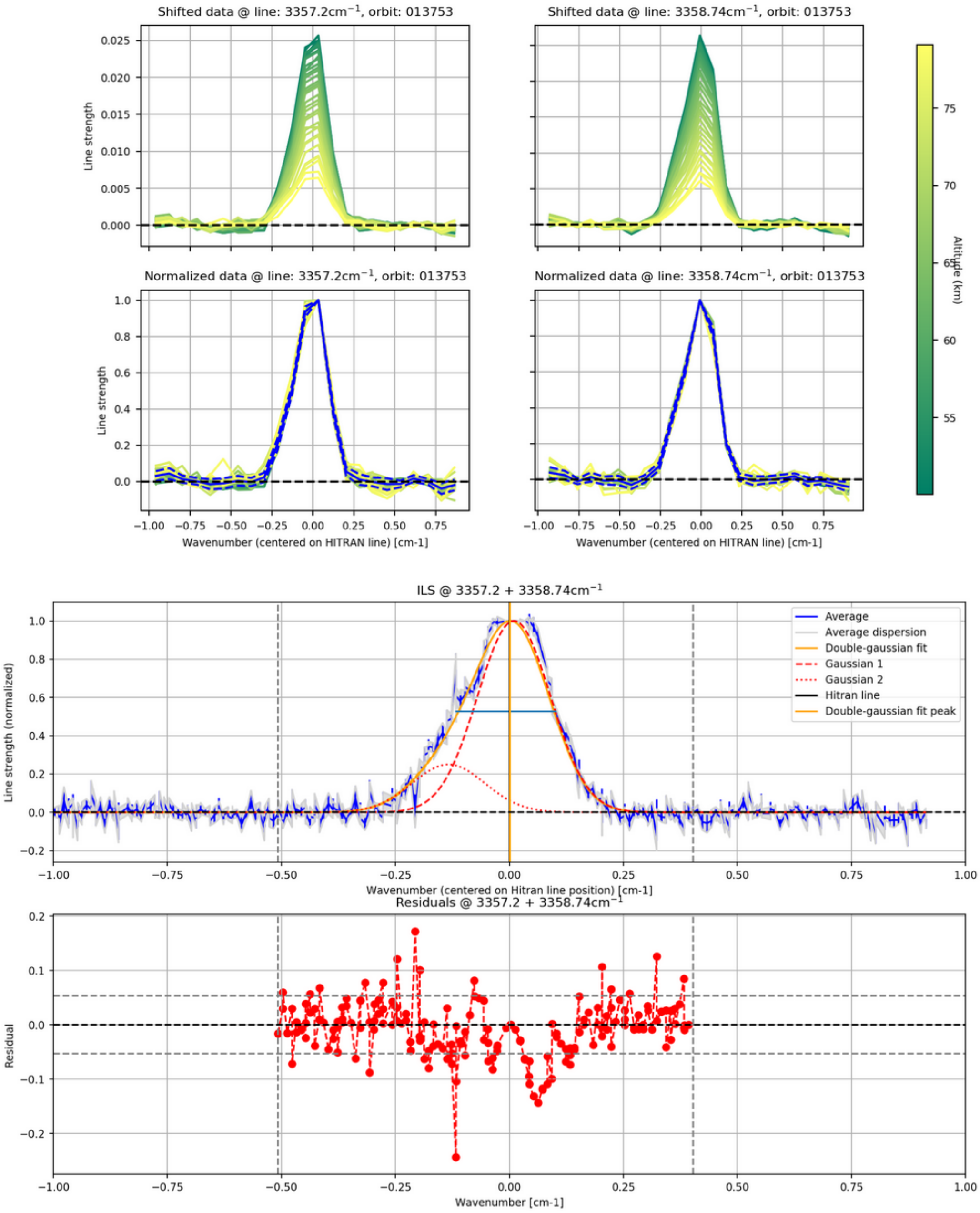

FIGURE 2.8: Characterization of the instrumental line shape at order 149. Top four panels show the merged lines at 3357 (a1) and 3358 (b1) cm^{-1} from 8 NOMAD SO observations between 50 and 80 km and their normalization (a2 and b2 respectively). Blue lines indicate the average. Bottom panels show the fitting (c) of a double Gaussian (orange line) after combining both lines and the residuals of the fitting (d).

altitudes, which could alter the line shapes and taking into account that absorption lines at high altitudes are noisy due to the very low densities, we decided to focus the analysis between 50-100 km and 15-50 km altitude for orders with strong and weak absorption lines respectively. Then, we normalized the merged lines and fitted a double Gaussian to each one of them combining two adjacent lines in order to increase the sample size for the line characterization. During the process, we realized that both the ratio of the two gaussians intensity and the width were approximately constant across the diffraction orders, so we decided to fix those parameters during the fitting. With this approximation we focused our fitting on the separation between the main and the second Gaussian, which showed a systematic increase towards the right hand side of the diffraction order (equation 2.16). An example of the line merging, normalization and fitting process for the CO_2 line at 3357.2 cm^{-1} order 149 is shown in Figure 2.8. The results obtained are similar to those obtained by other two teams (BIRA-IASB and NASA Goddard) with different methodologies. The three were combined to provide the recommended ILS for the NOMAD SO channel (Villanueva et al., 2022a).

2.3.2 Sampling and data coverage

Two of the main characteristics of the SO channel are its spectral resolution and field of view (FOV), and both are strongly linked to a key parameter of every remote sensing instrument: its vertical resolution. With a 2×30 arcmin width slit, the spectrometer achieves a nominal resolving power of $\lambda/\Delta\lambda \sim 17000$ (according with the latest calibration from Villanueva et al., 2022a). On the other hand, tipically the SO channel samples the atmosphere with a vertical step of about 1 km. Typically, there are two occultations, each per 2-hour orbit (TGO's orbit), of $\sim 4 - 17$ minutes preceded by a cooling time of the detector of about 10 minutes Vandaele et al., 2018. During the mission, different types of solar occultations are performed:

- Ingress/Egress: These are the nominal and more frequent type of orbits. NOMAD measures spectra from top/bottom to the bottom/top of the atmosphere with enough time to pre-cool the detector between both phases.
- Merged: This type of orbits occur when the time difference between the ingress and egress is less than the required cooling time of the detector. In these cases, the detector does not stop even when the line of sight is below the surface, measuring the ingress and egress phase during one single observation.
- Graze: When the angle between the TGO orbital plane and the Mars-Sun vector (β-angle) is larger than 63.5°, TGO is not able to sample down to the surface. This occultations are measured up β-angle of 67°.

Both merged and graze occultations are much less frequent than the regular ingress/egress orbits. In addition, due their geometry and large latitudinal drift (larger β-angles imply longer solar occultaitons), the observed atmospheric profile is not vertical (or quasi vertical, as is the case of the regular ingress/egress occultations) but tilted, making the data particularly difficult for interpretation. Hence, for this Thesis we analyzed nominal (ingress/egress) orbits exclusively.

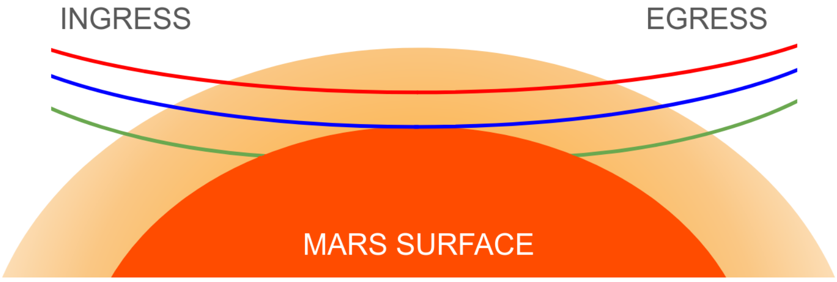

FIGURE 2.9: Schematic of the NOMAD SO orbit types. Ingress/Egress, merged and grace orbits are shown with green, blue and red solid lines respectively.

Despite its complexity and difficulties in calibration and characterization (Liuzzi et al., 2019; Villanueva et al., 2022a), the AOTF has advantages, as it is designed with the capability to change its frequency quasi-instantaneously (Thomas et al., 2022), which allows NOMAD to measure up to 6 diffraction orders per second simultaneously during the full atmospheric scan. During the measurement of the solar radiance, typically, when the light reaches the detector only 16 rows in the spatial direction out of 256 are illuminated, although the 320 pixels in the spectral direction are fully illuminated. This limitation in the illuminated rows is imposed by the projected size of the slit in the detector and the apparent size of the solar disk. Those 16 rows are then grouped in "bins" in order to produce 4 independent spectra. As these are independent, they could be combined to gain vertical sampling for specific studies. For this work we used only the spectra from bin #1.

The orbital configuration of TGO provides NOMAD (an its companion instrument ACS) with the capability to sample the Martian atmosphere at various latitudes, longitudes, and local times, offering enough data for a comprehensive understanding of atmospheric composition and dynamics. However, certain limitations exist due to the specific orbit parameters of TGO, which may impose restrictions on the coverage and timing of the NOMAD observations. Most of the occultations take place at mid/high latitudes around ± 50° - 60° with scarce data measured at equatorial regions. This is illustrated in Figure 2.10, where we show the latitude of all of the solar occultations available since the beginning of the mission as a function of solar longitude. In addition, the atmosphere is always observed at the terminator (morning/evening), limiting the sampling to Local Solar Time (LST) of ∼6 am/pm, as shown in Figure 2.11.

2.4 Summary

The detection of methane on Mars, although controversial, has led to a collaborative effort between space agencies to develop the ExoMars mission. Since 2016, the Trace Gas Orbiter, as part of this mission, probes the Martian atmospheres with different instruments and observation geometries. One of those instruments, the Nadir and

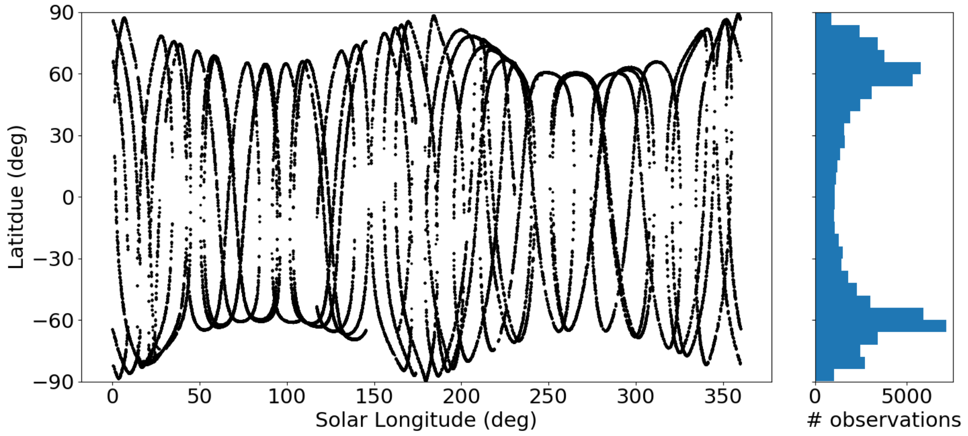

FIGURE 2.10: Latitude-Solar Longitude distribution of the NOMAD SO observations from May 2018 to April 2024. Histogram shows the number of observations within 0.5 hour bins.

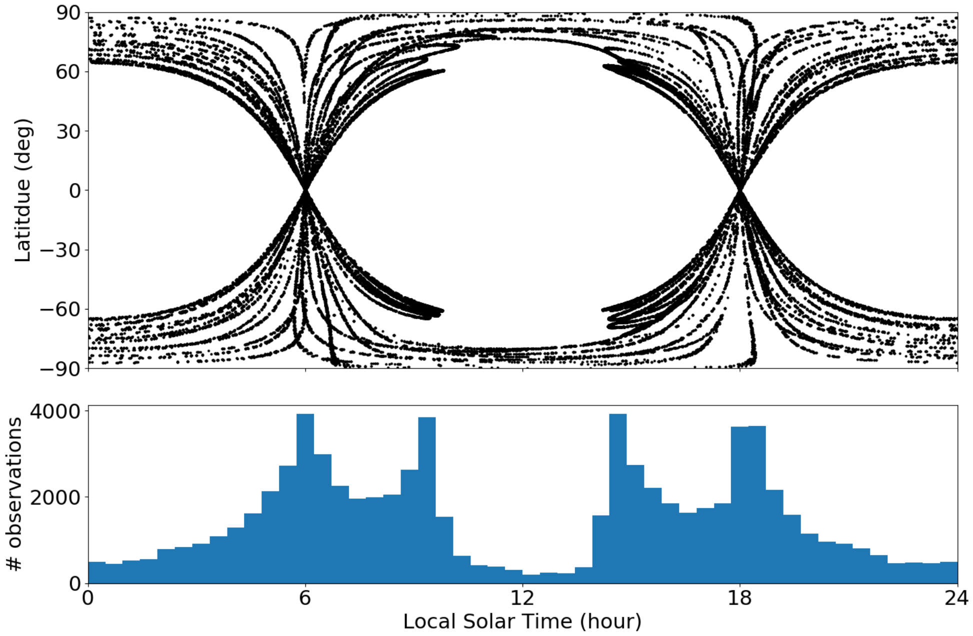

FIGURE 2.11: Latitude-Local Time distribution of the NOMAD SO observations from May 2018 to April 2024. Histogram shows the number of observations within 4° latitude bins.

Occultation for Mars Discovery (NOMAD) with its Solar Occultation channel allows for the systematic search of trace species and its vertical distribution in the Martian atmosphere. The solar occultation technique is the key to detection capabilities, and NOMAD offers for the first time its systematic application on other planet besides Earth. The SO channel, based on the design of the SOIR spectrometer onboard Venus Express, uses an echelle grating in Litrow geometry with an Acousto-Optical Tunable Filter (AOTF) to separate diffraction orders. This configuration allows NOMAD SO to probe the atmosphere with different diffraction orders quasi simultaneously with a vertical sampling of about 1 km. The AOTF, which can be described with an asymmetric sync-squared function and the instrumental line shape (ILS) described by a double Gaussian, have been recently characterize in a collaborative effort by different teams within the NOMAD consortium. This characterization has provided the best description of the parameters involved in the AOTF and ILS up to date. Here, we have summarized the results of those efforts, highlighting my participation within the IAA-CSIC team in the characterization of the ILS as part of the work o this Thesis.

Chapter 3

Radiative Transfer and Inversion Theory for Solar Occultations

3.1 Introduction

Radiative transfer is a fundamental concept in fields like astrophysics or atmospheric sciences, and concerns the propagation of radiation through a medium and radiation-matter interactions. It describes how energy in the form of electromagnetic radiation is absorbed, emitted or scattered by particles and gases in the medium, playing a key role in shaping the thermal structure of planetary atmospheres via the control of the radiative energy balance. Although many studies about photometry and light propagation were conducted during the 18th century, it was not until 1887 when the concept of radiative transfer first appeared (Lommel, 1887). Beginning as purely empirical, the radiative transfer theory (RTT) has been evolving since then, implementing the progressively an increasing number of theories about the nature of light such as the Maxwell equation or quantum electrodynamics, and describing how light interacts with atoms and molecules within a medium. In this Chapter we focused on the basic concepts of RTT and spectroscopy, providing a comprehensive background of the physical principles underneath the observational data analyzed during this Thesis. In addition, we describe the fundamentals of the inverse problem and how the RTT equation can be solved in order to obtain the maximum information about atmospheric properties from remote measurements such as solar radiances going through the atmospheric limb. Finally we summarize the basics of the computational algorithms used during our inversion process.

3.2 Radiative transfer for solar occultation

NOMAD SO measures the solar radiance as it passes through the Martian atmosphere, hence, we need to understand the processes affecting the radiation throughout its path from the light source to the detector. The basics about RTT in planetary atmospheres are thoroughly described in numerous textbooks like that by Goody and Yung, 1995. Here we will follow this reference, providing a brief summary focused on solar occultaitons.

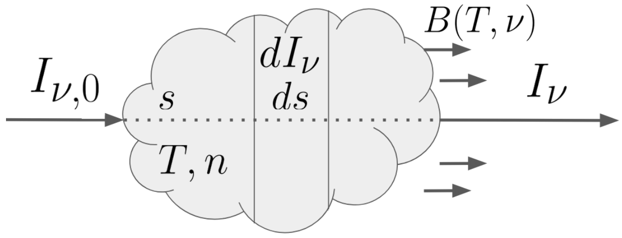

FIGURE 3.1: Representation of an air parcel absorbing solar radiation.

As illustrated in Figure 3.1, assuming that the incoming sunlight with intensity $I_{\nu,0}$ passes through a medium at temperature T with density n and thickness s, we can express the variation of the radiation intensity ignoring scattering effects and assuming local thermodynamic equilibrium (LTE), as

$$\mathrm{d}I_\nu = B(T,\nu)\mathrm{d}s - I_{\nu,0}\sigma_\nu n\mathrm{d}s \tag{3.1}$$

where $B(T,\nu)$ is the Plank's black body emission of the atmosphere and σ_ν is the absorption cross section of the medium. Here we are using the Beer-Lambert law, which assumes that the reduction of the intensity is proportional to the number of absorbers. With LTE we are also assuming that the temperature can be defined as the kinetic temperature and that the velocities of the molecules follow the Maxwell-Boltzmann distribution. Since the solar radiation is much stronger than the atmospheric thermal emission in the near infrared where NOMAD SO operates, we can ignore the first term of the equation. Then, taking into account the different i species of the atmosphere we can write

$$\mathrm{d}I_\nu = -I_{\nu,0}\sum_i \sigma_{\nu,i} n_i \mathrm{d}s \tag{3.2}$$

Defining the optical depth as

$$\tau_\nu = \sum_i \int_s \sigma_{\nu,i} n_i \mathrm{d}s \tag{3.3}$$

and integrating the equation 3.2, the radiation that finally reaches the sensor can be expressed as

$$I_\nu = I_{\nu,0}\exp^{-\tau_\nu} \tag{3.4}$$

Another way of expressing this equation is, instead of as a function of the slant path, writing the optical depth as a function of the altitude h. Applying basic trigonometry, assuming a spherical planet and neglecting refraction, we can reformulate the slant path ds as

$$ds = \frac{1}{\sqrt{1-\left(\frac{R_M+h_{\mathrm{tg}}}{R_M+h}\right)}}dh \tag{3.5}$$

where R_M is the radius of Mars and h_{tg} is the altitude from the surface to the tangent point. This is extremely convenient, taking into account that the atmospheric parameters, such as the gas density, change with altitude. Then, the optical depth can be reformulated as

$$\tau_\nu = 2\sum_i \int_{h_{\mathrm{tg}}}^{h_{\mathrm{TOA}}} \sigma_{\nu,i} n_i(h) \frac{1}{\sqrt{1-\left(\frac{R_M+h_{\mathrm{tg}}}{R_M+h}\right)}} \mathrm{d}h \tag{3.6}$$

were h_{TOA} is the altitude at the top of the atmosphere (TOA). The factor 2 appears from considering the section of the atmosphere between the Sun and the tangent point plus the section from the tangent point to the observer. At this point, we need to identify discrete symmetric atmospheric layers where we assume the atmospheric parameters (temperature, pressure, absorption coefficients...) are constant within each layer (horizontal homogeneity) and being only functions of the altitude h of the layer. Since NOMAD provides transmittances, it is convenient to express equation 3.4 relative to the solar radiance $I_{0,\nu}$ as the transmittance $\mathcal{T}_\nu$

$$\mathcal{T}_\nu = \frac{I_\nu}{I_{\nu,0}} = \exp\left(-2\sum_i \int_{z_{\mathrm{tg}}}^{z_{\mathrm{TOA}}} \sigma_{\nu,i} n_i(h) \frac{1}{\sqrt{1-\left(\frac{R_M+h}{R_M h_{tg}}\right)}} \mathrm{d}z\right) \tag{3.7}$$

The formal solution of this equation requires precise calculations and a fine discretization of the atmospheric layers. Based on previous studies on Mars limb observations Jiménez-Monferrer et al., 2021, we decided to use a 2 km layering from 0 km to 200 km as trade off between numerical precision and computational performance. To do so, we used the the Karlsruhe Optimized and Precise Radiative transfer Algorithm (KOPRA), whose layering approximation methodology is briefly described in Section 3.5, to compute the gas column densities (integral from equation 3.2) and radiances/transmittances, quantities needed to resolve the inversion problem (see Section 3.4).

3.3 Molecular spectroscopy

As light travels through the atmosphere, it interacts with its constituent components. From quantum mechanics we know that molecules can only absorb photons with specific frequencies following certain selection rules. This is, molecules do not show a continuum in the spectrum but discrete lines caused by quantized energy levels (Goody & Yung, 1989). Changing the state of a molecule from one energy level to another is called a radiative transition. When a photon interacts with a molecule, different transitions can occur depending on the frequency of the incident photon: (i) electronic transition, when the frequency of the photon is large enough to change the orbit of an electron (absorption of UV-visible radiation); (ii) vibrational transition, when the incident photon changes the frequency of the oscillation of the atoms forming the molecule (absorption of mid-IR radiation); and (iii) rotational transition, when the incident photon changes the frequency of the rotation of the molecule (absorption of far IR radiation). At the typical temperatures of the terrestrial planets of the Solar System, Mars in particular, their thermal emissions occur in the IR part of the spectrum. These photons excite ro-vibrational transitions of the most common molecules, like H_2O or CO_2. The NOMAD SO spectral range has been designed to cover a sufficiently large number of absorption features not in the IR where the Solar flux is low, but in the near-IR. Here, because of the NOMAD SO channel characteristics, we will focus only on the IR spectroscopy, i.e., ro-vibrational transitions, following the fundamentals described in Banwell, 1972 and Goody and Yung, 1989.

3.3.1 Ro-vibrational transitions

Vibrational transitions

The simplest way to model a molecule is to consider that the atoms conforming it are bonded together by "springs" oscillating with a certain frequency, allowing the molecule to be stretched/compressed or bent. This harmonic oscillator approximation (ignoring higher order anharmonicity terms) has well known energy levels

$$E(v) = h\nu \left(v + \frac{1}{2} \right) \tag{3.8}$$

where h is the Plank's constant, v the vibrational quantum number, which can have integer values (0, 1, 2, ...) and ν is the vibrational wavenumber (in cm^{-1}) determined by the strength of the atomic bonds and inversely proportional to the square root of the reduced mass of the molecule μ (for diatomic molecules). In general, for non-linear geometries, molecules formed with N atoms move with a total of $3N$ degrees of freedom, 6 related to translation and rotation and the left $3N$-6 ($3N$-5 in case of linear molecules) related to vibrational modes. Then, the total vibrational energy is

$$E_{\text{v}}(v) = \sum_{k}^{3N-6} h\nu_k \left(v_k + \frac{1}{2} \right) \tag{3.9}$$

where the selection rules impose $\Delta v_k = \pm 1$. For the water molecule, 3 vibrational modes are allowed: (i) bending, (ii) asymmetric and (iii) symmetric stretching, as illustrated in Figure 3.2. The asymmetric-symmetric modes refer to the C_2 axis spliting the molecule H-O-H in half. The vibration wavenumbers (fundamental frequencies) of these fundamental modes are ν_1=3657 cm^{-1}, ν_2=1525 cm^{-1} and ν_3=3736 cm^{-1} respectively. These modes induce a change in the water molecule dipole responsible for the absorption of infrared radiation, hence making the water a IR-active molecule and influencing the rotational transitions.

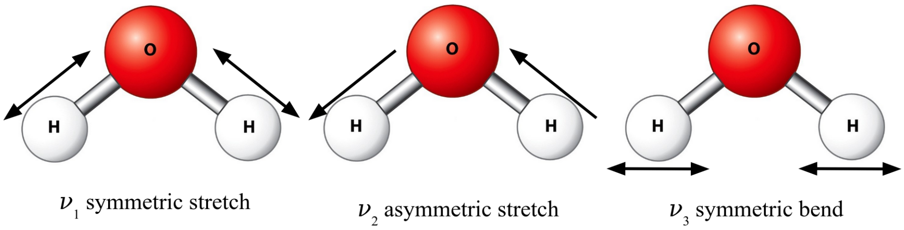

FIGURE 3.2: Vibration modes of the water molecule.

Rotational transitions

Following a similar approach as previously, we can approximate a molecule to a rigid rotor ignoring deformation effects due to the centrifugal force. In classical mechanics, the rotation energy for a frequency ω is defined as

$$E = \frac{L^2}{2I} \tag{3.10}$$

where $L = I\omega$ is the angular momentum and I is the momentum of inertia. In quantum mechanics, however, the angular momentum is discrete and defined as

$$L(J) = \frac{h}{2\pi}\sqrt{J(J+1)} \tag{3.11}$$

where J is the rotational quantum number. Then, the quantized rotational energy is

$$E_{\mathrm{r}}(J) = \frac{h^2}{8\pi^2 I}J(J+1) = hcBJ(J+1) \tag{3.12}$$

defining $B = h/(8\pi^2 Ic)$. Finally, assuming that the rotation is independent to the vibrational movements (Born-Oppenheimer approximation), we can express the total ro-vibrational energy levels ε in units of cm^{-1} (using the relation $E = hc\nu$) as a sum of both energies

$$\varepsilon(v,J) = \frac{E_{\mathrm{v}}(\nu)}{hc} + \frac{E_{\mathrm{r}}(J)}{hc} = \sum_{k}^{3N-6} \overline{\nu}_k \left(v_k + \frac{1}{2}\right) + BJ(J+1) \tag{3.13}$$

where $\overline{\nu} = \nu/c$. For each fundamental vibrational transition, variations of the rotational quantum number produce transitions known as branches. Following the selection rules, those branches are P, Q and R for transitions $\Delta J = -1$, $\Delta J = 0$, $\Delta J = +1$ respectively, with line spacing of $\sim 2B$ for P and R branches and with a narrow (almost unresolved) spacing for Q branches.

This discussion is valid for linear molecules with only one moment of inertia requiring only one quantum number. In the case of water, molecules have three different moments of inertia ($I_A \neq I_B \neq I_C$), hence, requiring three sets of quantum numbers, all of them changing simultaneously. These so called asymmetric top molecules do not have analytical expressions for their energy levels and its computation requires interpolation of energy levels derived for symmetric top molecules ($I_A \neq 0, I_B = I_C \neq 0$) using different ratios for their moments of inertia. As a result, water vapor exhibit a complex infrared spectrum, with an irregular distribution of absorption lines scattered around the fundamental vibrational bands. This is shown in Fig. 3.3, where the distinct vibrational bands (centers of ν_1, ν_2, and ν_3 marked with vertical red, blue and green lines respectively) can be observed surrounded by scattered rotation-induced lines. Water vapor has been extensively studied in laboratory, and its lines' strengths, spectral positions and collisional coefficients are well described in databases like the high-resolution transmission molecular absorption database (HITRAN, (Gordon et al., 2017, 2022)) used in this work.

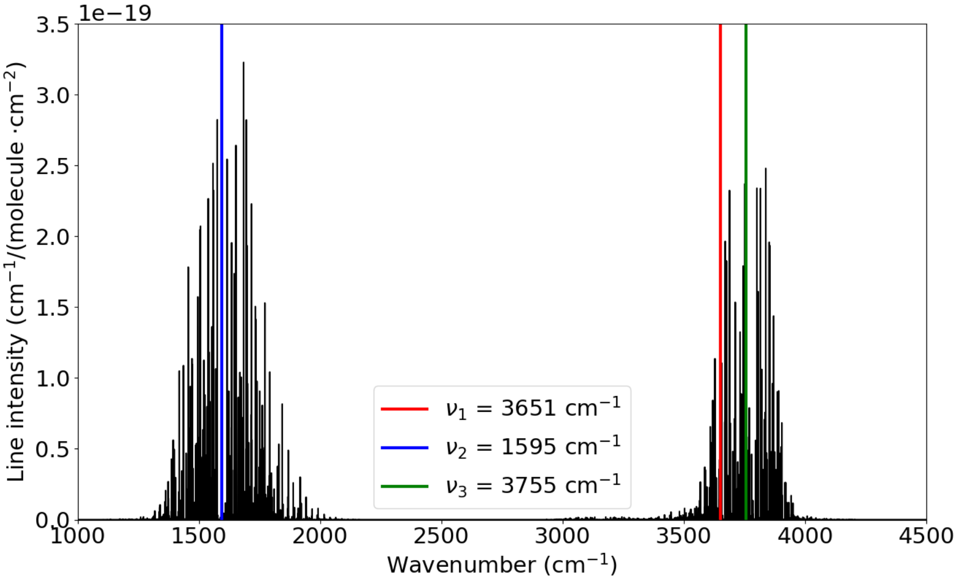

FIGURE 3.3: Infrared spectrum of the main water isotopologue ($H_2{}^{16}O$), according to the HITRAN database (Gordon et al., 2022).

3.3.2 Spectral line shape

When a transition from one energy level to an another occurs, a photon is absorbed (lower to higher energy level) or emitted (higher to lower level) producing the so called spectral lines. Ideally, those lines are Dirac deltas with an infinitesimal width and intensity S. However, because of the thermal motion and interaction between molecules, the lines are broadened. In addition, due to the Heisenberg's uncertainty principle, a natural width appears on the lines, although negligible compared with the atmospheric broadening.

Line intensity

A key parameter for deriving abundances of absorbing gases like H_2O is the strength of its absorption lines, and in particular, this parameter's dependence on temperature. The derivation of the line intensity between two ro-vibrational states have been thoroughly described in the literature (Šimečková et al., 2006). For a single molecule per unit volume, the intensity of the line resulted from a transition between the lower and upper states i and j with energy $\Delta\varepsilon = \varepsilon_i - \varepsilon_j = \nu_{ij}$, can be expressed as

$$S_{ij}(T) = I_a \frac{A_{ij}}{8\pi c \nu_{ij}^2} \frac{g' \exp(-c_2 E_i/T)(1 - \exp(-c_2 \nu_{ij}/T))}{Q(T)} \tag{3.14}$$

where A_{ij} is the Einstein coefficient for spontaneous emission, g' is the statistical weight of the upper state, E_i is the energy of the lower state, $c_2 = hc/k_B$ is the second radiation constant and $Q(T)$ is the total internal partition function defined as

$$Q(T) = \sum_k g_k \exp\left(\frac{-c_2 E_k}{T}\right) \tag{3.15}$$

This definition of the intensity, used in the HITRAN (Gordon et al., 2022), assumes that S_{ij} is weighted according to the isotopic abundances I_a of the Earth's atmosphere (table 3.1). The intensities of all the water isotopes available in HITRAN are shown in Fig. 3.4. In order to calculate the intensity for any other temperature different from the HITRAN reference temperature ($T_{ref} = 296$ K) we can use

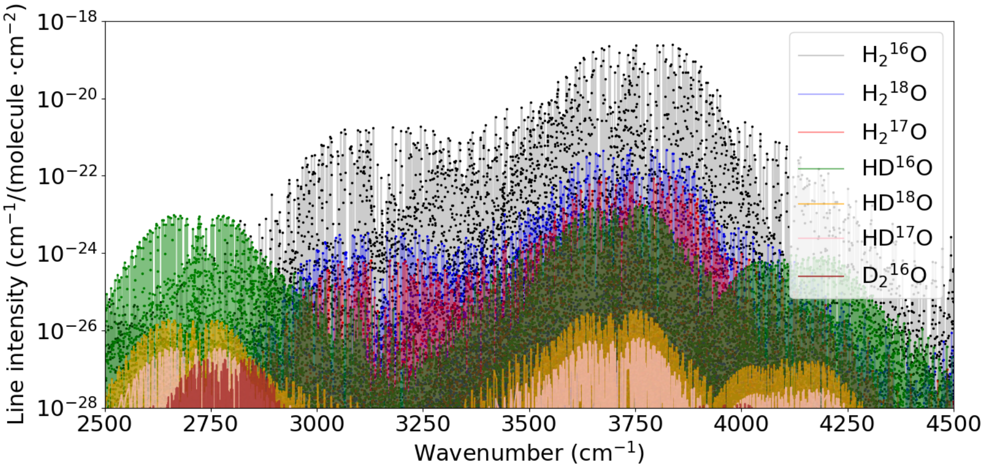

FIGURE 3.4: H2O isotopes

$$S_{ij}(T) = S_{ij}(T_{ref}) \frac{Q(T_{ref})}{Q(T)} \frac{\exp(-c_2 E_i/T)}{\exp(-c_2 E_i/T_{ref})} \frac{1 - \exp(-c_2 \nu_{ij}/T)}{1 - \exp(-c_2 \nu_{ij}/T_{ref})} \tag{3.16}$$

The partition function $Q(T)$ is well known for water vapor in the range of temperatures observed in the Martian atmosphere. Therefore, the strengths of the

TABLE 3.1: Molecular mass and abundances of the water vapor isotopologues from Gordon et al., 2022.

Molecule	Molecular mass (g/mol)	Earth Abundance
$H_2{}^{16}O$	18.010565	0.997317
$H_2{}^{18}O$	20.01481	0.002000
$H_2{}^{17}O$	19.014782	$3.718840{\cdot}10^{-4}$
$HD^{16}O$	19.016842	$3.106930{\cdot}10^{-4}$
$HD^{18}O$	21,021087	$6.230030{\cdot}10^{-7}$
$HD^{17}O$	20,021059	$1.158530{\cdot}10^{-7}$
$D_2{}^{16}O$	20,023119	$2.419740{\cdot}10^{-8}$

lines can be incorporated and handled by our forward model KOPRA with a very high degree of accuracy.

Line shape

Besides the frequency and intensity, the absorption lines are defined by their spectral width. As mentioned before, the lines do not appear as Dirac deltas but as continuous functions peaking at the frequency of the transition. This broadening is due to several reasons. Three distinct processes widen the lines. The Heisenberg's uncertainty principle, the thermal motion of the absorbing molecules and the collisions between them, which in truth depend on the ambient atmospheric pressure. Each of these produces a very distinct broadening, normally called natural, Doppler and Lorentz or pressure broadening respectively (Goody & Yung, 1989). We describe the last two below.

We can define the line profile as a function f scaling the line strength S

$$\sigma(\nu) = S(T) f(\nu - \nu_0) \tag{3.17}$$

where σ is identified as the absorption coefficient (see equation 3.2), ν_0 is the theoretical or central frequency of the transition. This way S can be expressed as

$$S = \int \sigma_\nu \mathrm{d}\nu \tag{3.18}$$

There are two main contributions to the function $f(\nu - \nu_0)$:

Doppler Broadening. Molecules are not idle but moving elements in the atmosphere following different directions. Then, the frequency at which the transition occurs for a molecule moving at speed u is different compared to the frequency of the same molecule when stationary. This Doppler shift (when $u \ll c$) can be expressed as

$$\nu = \nu_0 \left(1 + \frac{u}{c}\right) \tag{3.19}$$

Assuming thermodynamic equilibrium, we can state that the probability of a molecule with mass m to have velocity u is

$$p(u) = \sqrt{\frac{m}{2\pi k_{\mathrm{B}} T}} \exp\left(-\frac{mu^2}{2k_{\mathrm{B}}T}\right) \tag{3.20}$$

Then, combining 3.19 and 3.20, we can derive the Doppler profile

$$f_{\mathrm{D}}(\nu - \nu_0) = \frac{1}{\alpha_{\mathrm{D}}\sqrt{2\pi}} \exp -\frac{(\nu-\nu_0)^2}{2\alpha_{\mathrm{D}}^2} \tag{3.21}$$

where α_{D} is the Half Width at Half Maximum (HWHM) for the transition at frequency ν_0

$$\alpha_{\mathrm{D}}(\nu_0, T, m) = \frac{\nu_0}{c}\sqrt{\frac{k_{\mathrm{B}}T}{m}} \tag{3.22}$$

Pressure Broadening. During the process of absorbing/emitting photons, if the medium is dense enough, molecules can collide with each other. Typically this behavior is modeled assuming that the duration of the collision is much smaller than the time between collisions (impact theory approximation). Under this frame, we can interpret that the collision is causing a reduction in the life time of the transition and an instantaneous shift of the transition frequency. This effect is particularly relevant for the lower atmosphere, where the pressure is large enough to dominate over the Doppler effects mentioned above. In these cases, the line shape is close to a Gaussian and is called a Lorentz profile. For this work we provide the final expression as a function of the distance from the central wavenumber ν_0:

$$f_{\mathrm{L}}(\nu - \nu_0) = \frac{1}{\pi}\frac{\gamma_{\mathrm{C}}}{\gamma_{\mathrm{C}}^2 + (\nu-\nu_0)^2} \tag{3.23}$$

where γ_{C} is the HWHM of the line, being a function of pressure an temperature:

$$\gamma_{\mathrm{C}}(p, T) = \left(\frac{T_{\mathrm{ref}}}{T}\right)^{n_{\mathrm{air}}} \left(\gamma_{\mathrm{air}}(p - p_{\mathrm{self}}) + \gamma_{\mathrm{self}} p_{\mathrm{self}}\right) \tag{3.24}$$

Here the coefficients n_{air}, γ_{air}, γ_{self} are the temperature dependence of the air-broadened half width, the air-broadened HWHM and the self-broadened HWHM respectively, the latter two computed at a given reference temperature and pressure $T_{\mathrm{ref}} = 296$ K and $p_{\mathrm{ref}} = 1$ atm respectively. In HITRAN, these coefficients refer to the Earth's main constituents, N_2 and O_2. For the work presented in Chapters 5, 6 and 7, we used the coefficients provided by HITRAN (Gordon et al., 2017, 2022), i.e., computed for an Earth-like atmosphere. Mars, however, has a CO_2 rich atmosphere and the air-broadened coefficients differ. In Section 3.5 we show that our election of using default HITRAN parameters does not have any significant impact in our results.

Typically, in the atmosphere both broadening effects occur at the same time and there are altitudes where none of them can be neglected. In this case, the line profile usually follows the Doppler broadening in the spectral region close to the transition frequency, what is called the core of the line. Then, because of the rapid fall of the Gaussian wings, the Lorentz profile due to the collisional broadening dominates in the region away from the line center. This kind of mixed line shape can be obtained convolving both Gaussian and Lorentz profiles to form a Voigt function

$$f_{\mathrm{V}}(x,y) = f_{\mathrm{D}} * f_{\mathrm{L}} = A\frac{y}{\pi}\int_{-\infty}^{+\infty}\frac{\exp(-t^2)}{(x-t)^2+y^2}dt \tag{3.25}$$

with

$$A = \frac{S}{\alpha_{\mathrm{D}}\sqrt{\pi}}\sqrt{\ln 2} \tag{3.26}$$

$$x = \frac{\nu-\nu_0-\delta_{\mathrm{C}}}{\alpha_{\mathrm{D}}}\sqrt{\ln 2} \tag{3.27}$$

$$y = \frac{\gamma_{\mathrm{C}}}{\alpha_{\mathrm{D}}}\sqrt{\ln 2} \tag{3.28}$$

where x is the distance from the line center in Doppler halfwidth (3.22) units and y is the ratio of the Doppler halfwidth to the Lorentz halfwidth (3.24).
A comparison of the three line profiles discussed in this Section is shown in Fig. 3.5. In the case of the Martian atmosphere, previous studies showed that the transition from Lorentz to Doppler line shapes occurs around 60 km altitude, this is, in the lower mesosphere (López-Valverde & López-Puertas, 1994). A Voigt profile has to be used around those altitudes for a correct description of the radiative transfer in that atmosphere.

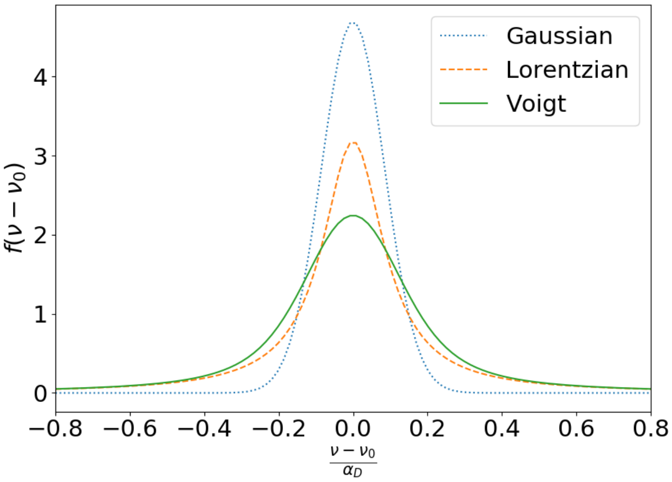

FIGURE 3.5: Doppler (dotted blue), Lorentzian (dashed orange) and Voigt (solid green) profiles. Doppler and Lorentz profile have been defined for the same intensities and widths.

3.4 Inversion theory

Remot sensing implies measuring certain quantities in a specific medium at a distant location by exploiting their interaction with the radiation field, and indirectly, inferring information and physical properties characterizing such a specific system. In particular for atmospheric sounding, the refraction, transmittance, scattering or thermal emission among others are usually measured in order to characterize parameters like the abundance of certain species, the temperature, pressure or density of the atmosphere. There are multiple observational techniques to perform remote atmospheric sensing (nadir, limb, solar occultation...) but in all of them, when the parameter space is undetermined, the goal is the same: To determine the best representation of a parameter based on certain measurements along with prior information. This issue is known as the "inversion problem". There is plenty of literature describing how to solve this problem, being Rodgers, 2000 the most usual reference for atmospheric science. In order to address this complex issue, let us define two vector spaces: (i) the "measurement space", which contains the measured quantities and is represented by a vector $\mathbf{y}$ with dimension m, and (ii) the "state space", with the quantities to be retrieved represented by another vector $\mathbf{x}$ with dimension n. In the case of NOMAD SO signal, $\mathbf{y}$ represent solar radiances measured at m different altitudes, and $\mathbf{x}$ atmospheric densities of water vapor at n distinct altitudes. For the notation in this Section, we followed the same convention as Rodgers, 2000, where vectors are written in bold letters.

Ideally the measurements can be described by physical laws, so there is always a forward function that for a given state vector reproduces the measurement. However, in reality the act of measuring involves some uncertainty and physics describing the state need to be approximated. Therefore we can describe the forward problem as

$$\mathbf{y} = \mathbf{F}(\mathbf{x}) + \epsilon \tag{3.29}$$

where ϵ is the measurement error and $\mathbf{F}(\mathbf{x})$ stands for a radiative transfer function which describes the physics underneath our problem. This function can be complex, so introducing a linearization provides an alternative way of expressing the forward model problem as a first order approximation around a reference state $\mathbf{x_0}$.

$$\mathbf{y} = \mathbf{F}(\mathbf{x_0}) + \frac{\partial \mathbf{F}(\mathbf{x})}{\partial \mathbf{x}}(\mathbf{x} - \mathbf{x_0}) + \epsilon \tag{3.30}$$

This, however, includes a practical assumption that such reference state $\mathbf{x_0}$ can be obtained before hand. We can define the Jacobian $\mathbf{K} = \partial \mathbf{F}(\mathbf{x})/\partial \mathbf{x}$. This $m \times n$ matrix represents the rate at which the output of a function changes in response to changes in its input. The number of linearly independent rows of $\mathbf{K}$ conform a subspace of the "state space" with dimension p. The relation between m, n and p provides the information required to identify if the equation 3.29 either has or not solution. If

$p < m$ then the problem is under-determined and the solution is not unique. This means that there are regions of the state space to be retrieved that are not determined by the measurements.

One of the possible ways for solving the equation 3.29 is to use the weighted least-square method. Defining the residual $\mathbf{r} = \mathbf{y} - \mathbf{F}(\mathbf{x})$, we compute the weighted sum

$$f = \parallel \mathbf{r} \parallel^2_{\mathbf{S_y}} = \mathbf{r}^{\mathrm{T}}\mathbf{S_y}^{-1}\mathbf{r} \tag{3.31}$$

where $\mathbf{S_y}$ is the covariance matrix of the measurement errors with elements

$$S_{ij} = \langle(\epsilon_i - \langle\epsilon_i\rangle)(\epsilon_j - \langle\epsilon_j\rangle)\rangle \tag{3.32}$$

where ϵ_i and ϵ_j are the errors in the measurements i and j respectively. However, due to its ill-posed nature (more than one $\mathbf{x}$ solves the equation 3.29), we need to introduce some constrains to solve the problem. This is done by adding a regularization term to the weighted sum f. There are several ways to add regularization to the problem, such as the optimal estimation or the maximum a posteriori approaches (Rodgers, 2000). In our case we followed the Tikhonov regularization approach (Honerkamp & Weese, 1990), which is useful when the a priori is not perfectly characterized (Eriksson, 2000). This approach defines the regularization matrix $\mathbf{\Gamma} = \gamma\mathbf{L}^{\mathrm{T}}\mathbf{L}$, where γ acts as smoothing parameter of the solution and $\mathbf{L}$ can typically be the identity ($\mathbf{I}$) or a differential operator depending on the order of the regularization. Introducing this regularization term into 3.31 we obtain

$$f = \parallel \mathbf{r} \parallel^2_{S_y} + \parallel \mathbf{x} - \mathbf{x_0} \parallel^2_{\Gamma} = \mathbf{r}^{\mathrm{T}}\mathbf{S_y}^{-1}\mathbf{r} + (\mathbf{x} - \mathbf{x_0})^{\mathrm{T}}\mathbf{\Gamma}(\mathbf{x} - \mathbf{x_0}) \tag{3.33}$$

which can be written as

$$f = [\mathbf{y} - \mathbf{F}(\mathbf{x}_0) - \mathbf{K}(\mathbf{x} - \mathbf{x}_0)]^{\mathrm{T}}\mathbf{S_y}^{-1}[\mathbf{y} - \mathbf{F}(\mathbf{x}_0) - \mathbf{K}(\mathbf{x} - \mathbf{x}_0)] + (\mathbf{x} - \mathbf{x}_0)^{\mathrm{T}}\mathbf{\Gamma}(\mathbf{x} - \mathbf{x}_0) \tag{3.34}$$

Then in order to minimize f we just need to solve the equation

$$\frac{\partial f}{\partial \mathbf{x}} = 0 \tag{3.35}$$

which by iterating over $\mathbf{x}$, gives the solution to the inverse problem

$$\mathbf{x}_{i+1} = \mathbf{x}_i + [\mathbf{K}^{\mathrm{T}}\mathbf{S}_y^{-1}\mathbf{K} + \mathbf{\Gamma} + \lambda\mathbf{I}]^{-1} \times \{\mathbf{K}^{\mathrm{T}}\mathbf{S_y}^{-1}[\mathbf{y} - \mathbf{F}(\mathbf{x}_i)] - \mathbf{\Gamma}(\mathbf{x}_i - \mathbf{x}_0)\} \tag{3.36}$$

Defining the gain matrix $\mathbf{G}$

$$\mathbf{G} = [\mathbf{K}^{\mathrm{T}}\mathbf{S}_y^{-1}\mathbf{K} + \mathbf{\Gamma} + \lambda\mathbf{I}]^{-1} \times \mathbf{K}^{\mathrm{T}}\mathbf{S_y}^{-1} \tag{3.37}$$

the equation 3.36 can be written as

$$\mathbf{x}_{i+1} = \mathbf{x}_i + \mathbf{G}\{[\mathbf{y} - \mathbf{F}(\mathbf{x}_i)] - \mathbf{\Gamma}(\mathbf{x}_i - \mathbf{x}_0)\} \tag{3.38}$$

Here we introduced an optional Levenberg-Marquardt damping term $\lambda\mathbf{I}$, where $\mathbf{I}$ is the identity matrix, in order to maintain the linear domain during the iterations (Levenberg, 1944; Marquardt, 1963), in other words, preventing large variations in $\mathbf{x}_i - \mathbf{x}_{i+1}$. Depending on the results we want to obtain, the most suitable regularization to use will be different. A zero order regularization, i.e. $\mathbf{L_0} = \mathbf{I}$, is useful only when the retrieval profiles are expected to be close to the a priori allowing for local variations in the magnitude of the solution. On the other hand, higher order regularizations minimize the derivatives of $\mathbf{x} - \mathbf{x_0}$ introducing smoothness to the retrieved profile, stabilizing the inversion and reducing oscillations in the retrieved profile. In our setup, we use a regularization in a way that we can scale the diagonal (zero order) and off-diagonal (first order) elements of $\mathbf{\Gamma}$, hence defining the regularization matrix as

$$\mathbf{\Gamma} = \gamma_0 \mathbf{L_0} \mathbf{L_0}^{\mathrm{T}} + \gamma_1 \mathbf{L_1} \mathbf{L_1}^{\mathrm{T}} \tag{3.39}$$

where L_0 and L_1 are the zero and first order differential operators respectively. During the inversion, we defined γ_0 and γ_1 as vectors (diagonal matrix) with a length equivalent to the length of the retrieved vector. To stabilize the inversion, we used a strong constrain by the zero order term (referred to as a diagonal constrain) only at the edges of the retrieved vector, where there are no measurements available. The elements for which there are available measurements were set to 0. On the other hand, the first order term (referred as regularization constrain) was optimized for each diffraction order, as discussed in 4.3.3.

A key diagnostic of the inversion problem is the averaging kernel matrix, which relates the retrieved profile with the real atmospheric profile and can be defined as $\mathbf{A} = \mathbf{GK}$. In the ideal case where the retrieved profile reproduces perfectly the real atmosphere, $\mathbf{A} = \mathbf{I}$. The averaging kernel matrix is often used for the diagnostic of the retrievals. Low values in the diagonal of this matrix imply that the information content from the observations is not enough to provide a robust result. In addition, the full width at half maximum of the rows of $\mathbf{A}$ represent the vertical resolution. This way, a broad row in the averaging kernel matrix produces a vertical profile where the retrieved value at each altitude depends on the values form above and below.

3.5 The forward model KOPRA

A high accuracy on the forward model calculation ($\mathbf{F}(\mathbf{x})$) is required in order to obtain precise results during the retrievals. Among others, one of the most flexible and best tested radiative transfer codes currently available is the Karlsruhe Optimized and Precise Radiative transfer Algorithm (KOPRA), developed at the Institut für

Meteorologie und Klimaforschung (IMK) in collaboration with the Instituto de Astrofísica de Andalucía (IAA-CSIC) (Stiller, 2000). The code was originally designed specifically for the analysis of the Michelson Interferometer for Passive Atmospheric Sounding (MIPAS) data (Stiller et al., 2002). This instrument devoted for the study of the Earth's atmosphere, allowed for observations in limb geometry, sampling the atmosphere down to the troposphere. The characteristics of MIPAS required for an accurate modeling of the radiative transfer physics. For that purpose, KOPRA was developed to be able to model specific geophysical conditions, precise instrumental responses, to be flexible enough for future updates and modifications, and to provide the information required during the retrieval process, such as the Jacobians (**K**). Since its original development, KOPRA has been tested and validated on multiple Earth atmosphere remote sounding projects (Glatthor et al., 1999). More recently, the usage of KOPRA has been extended and adapted to other planetary atmospheres, proving its validity even simulating low pressure atmospheres like that of Mars (Jiménez-Monferrer et al., 2021).

As a high numerical precision line-by-line and layer-by-layer forward model, KOPRA calculates the infra-red radiative transfer through the atmosphere. Unlike other algorithms using direct integration methods, it follows a Curtis-Godson approach (Curtis, 1952; Godson, 1953), integrating the radiatiave transfer equation and calculating the slant column densities (equation 3.6) for each path segment (inside one layer) along the line of sight (Stiller et al., 2002). This method involving differential displacement of the ray paths, assuming linear refractive index variation within each integration step, along with a precise geophysical modeling, allows KOPRA to take into account refraction effects along the line of sight and an ellipsoidal surface with horizontal (latitudinal or longitudinal) inhomogeneity. The line-by-line modeling uses an optimized implementation of the Humlicek's algorithm (Kuntz, 1997; Ruyten, 2004) for an accurate evaluation of the Voigt line shape function, which, as explained above in Section 3.3, consists in a convolution of Lorentz and Doppler line shapes 3.36. The main spectroscopic information containing the line parameters such as self- and air-broadening coefficients, line intensities, or pressure spectral shifts are obtained from the HITRAN database (Gordon et al., 2017, 2022). In addition, the instrumental line shape and AOTF function of NOMAD SO have been implemented in KOPRA for a correct simulation of the NOMAD spectra. This implementation is also flexible, as it allows the user to introduce any value for the function parameters, any number of adjacent diffraction orders and possible shifts in the position of the blaze function.

3.6 Inversion program RCP

In order to solve the inversion problem described in Section 3.4, and to obtain water vapor number densities and abundance for their latter scientific analysis, we used the Retrieval Control Program (RCP). RCP was developed at IMK in collaboration with the IAA-CSIC, which contributed to implement a section designed to address non local thermodynamic equilibrium (non-LTE) conditions. The main task of this retrieval processor is to iteratively solve the equation 3.36. It is very versatile, as it is able to derive information on any parameter entering the forward model, both physical magnitudes and mathematical constrains, calibration biases, etc. Furthermore, RCP can solve them simultaneously not sequentially, which is the most consistent approach to retrieve multiple multiple targets. The key components required to perform retrievals are: (i) a forward model, (ii) the appropriate measurements, and (iii) the appropriate constrains and retrieval assumptions. For the point (i), as discussed in Section 3.5, KOPRA is an optimal candidate to be used as forward model during the retrievals since it is able to provide not only simulated radiances to model the measurements, but also the derivatives for the Jacobians. Regarding the measurements (ii), we used a specific pipeline designed to clean and format the NOMAD SO transmittances into solar equivalent radiances, which are the basic magnitude used by RCP, making them suitable for the retrievals (see Section 4.2). Hence, the remaining requirements are the constrains and retrieval parameters. For the work presented in this Thesis, and in order to obtain the best possible water vapor abundance vertical profiles, we set as retrieval targets three elements: (1) the possible spectral shift of the calibrated NOMAD SO spectra, (2) the water vapor number density and (3) the continuum of the spectra, normally associated to the aerosols present in the Martian atmosphere.

3.6.1 Retrieval parameters

As we will discuss in Section 4.2, our inversion proceeds in two steps. First, we performed retrievals dedicated solely to obtain a precise characterization of the spectral shift present in the NOMAD transmittances. These inversions were done for a specific altitude range taking into account only a dozen of spectra. These altitudes were carefully selected for each diffraction order and occultation, to avoid overlapping with the Lorentz wings of nearby lines and, at the same time, maintaining significantly strong absorption (above measurement noise levels). Secondly, we computed another inversion where both the water vapor number density and the spectral continuum were retrieved simultaneously. The latter used as an empirical offset applied to the baseline of the spectra from the forward model in order to accommodate the modeled transmittances to the NOMAD data. This offset does not depend on any physical model and although it was useful to take into account the aerosol absorption at low altitudes, it was particularly needed for the top most altitudes, where the calibrated transmittance sometimes showed values slightly above 1. This effect is not physically possible and it is due solely to inaccuracies during the calibration process of the NOMAD level 1 transmittances.

Regarding the constrains, i.e. the regularization, as discussed in Section 3.4, we used a first order Thikonov regularization optimized for each diffraction order. The diagonal elements are set to zero except for those altitudes where there were no measurements available, in order to stabilize the inversion and to avoid large oscillations at the edges of the retrieved profile. The selection of the optimal regularization for each diffraction order was done during a long series of sensitivity studies, evaluating the impact of different degrees of smoothing on the retrieved water vapor profiles (see Section 4.3.3 for details). One of the lessons learned from this study is that the is some degree of arbitrariness in the strength of the regularization to use. In practice, the degree of smoothing associated to the regularization depends on the scientific focus that one desires. In this work we used a single regularization (optimized for each diffraction order) for the whole NOMAD SO data set. Specific studies in the future could use another regularization setup.

For both, the a priori state and first guess solution required to solve the inversion problem (eq. 3.36), we used water vapor profiles and atmospheric parameters derived from specific runs of the Mars Planetary Climate Model (Mars-PCM). This is, using the geophysical data from the NOMAD SO measurements, we extracted vertical profiles at the same exact latitude, longitude and time of the observations. Because the Mars-PCM output grid is relatively coarse, this requires an interpolation, which was performed with the internal procedure of teh PCM, also used for the generation and extraction of the data from the Mars Climate Database Forget et al., 1999; Millour et al., 2022. In addition to water vapor at each tangent altitude, we also used temperature and pressure profiles (total atmospheric density) from the same PCM simulation and interpolation. Although the optimal way to carry out the retrievals is using the real atmospheric structure (temperature/pressure at each altitude) or, alternatively, measured densities from NOMAD SO data Modak et al., 2023 or other instruments, these are not always available. Proved, by performing sensitivity tests (see Section 4.3.3), that the impact of the temperature/pressure structure on the water vapor is small, this approach is the simplest and fastest solution, also used by other teams in the NOMAD consortium Aoki et al., 2019, 2022.

One of the main advantages of KOPRA and RCP is that, instead of using the whole spectral range of the diffraction order, narrow spectral windows can be selected. This feature, with an optimized selection of micro windows (MW), allows speeding up the retrievals and permits filtering those spectral regions contaminated with features from other gaseous species or instrumental effects. In our processing scheme we decided to use MW covering the full orders during the cleaning process. Then only few MWs with strong water vapor absorption lines were used during the inversion. Tables 3.2,3.3, 3.4, 3.5 show the MWs used during both processes for the main orders analyzed in this Thesis.

TABLE 3.2: Micro windows (cm^{-1}) used for the orders 134 during the cleaning and the retrieval process. ($*$) denotes MWs used for the retrieval.

Order	MW1	MW2*	MW3	MW4*	MW5	MW6*	MW7	MW8*	MW9
134	3012.9 | 3014.8	3014.8 | 3016.5	3016.5 | 3021.5	3021.5 | 3023.0	3023.0 | 3024.8	3024.8 | 3026.5	3026.5 | 3029.8	3029.8 | 3032.5	3032.5 | 3034.0

TABLE 3.3: Micro windows (cm^{-1}) used for the orders 136 during the cleaning and the retrieval process. ($*$) denotes MWs used for the retrieval.

Order	MW1	MW2*	MW3	MW4*	MW5*	MW6	MW7	MW8*	MW9
136	3057.0 | 3059.0	3059.0 | 3061.0	3061.0 | 3063.5	3063.5 | 3065.5	3065.5 | 3067.5	3067.5 | 3072.0	3072.0 | 3077.0	3077.0 | 3078.5	3078.5 | 3079.5

3.7 Mars Planetary Climate Model

As discussed in previous sections, for this Thesis we used results from the Mars Planetary Climate Model as our a priori and first guess for the inversions. T‘he Mars Planetary Climate Model, formerly known as Laboratoire de Météorologie Dynamique Mars Global Circulation Model (LMD-MGCM) (Forget et al., 1999), was developed at the (LMD) in collaboration with other teams (The University of Oxford, The Open University and the IAA-CSIC) as a modification of a previous Earth GCM. These models provide numerical simulations of the temporal evolution of the planet's atmosphere from the physical and mathematical description of the atmospheric circulation. The Mars-PCM was one of the first models with the capability of a self-consistent simulation of the full atmosphere, from the ground to the exobase (González-Galindo et al., 2015) including physical processes such as CO_2 cycle and condensation (Forget et al., 1998), generation and evolution of water ice clouds (Navarro et al., 2014a), distribution and radiative properties of dust (Madeleine et al., 2011), variability of the upper atmosphere (González-Galindo et al., 2015), and many chemical and photochemical reactions taking place in the Martian atmosphere and ionosphere (González-Galindo et al., 2013).

The Mars-PCM has been thoroughly tested and validated with many available observations, including, among others:

- Surface pressures measured by the Viking landers.
- Surface and atmospheric temperatures, water vapor, water ice columns and dust optical depths from TES (Smith, 2004).
- Atmospheric temperature and dust opacity from MCS (Kleinböhl et al., 2009).

TABLE 3.4: Micro windows (cm^{-1}) used for the orders 168 during the cleaning and the retrieval process. ($*$) denotes MWs used for the retrieval.

Order	**MW1**	**MW2***	**MW3**	**MW4***	**MW5**	**MW6***	**MW7***	**MW8**	**MW9***	**MW10**
168	3777.0 | 3778.5	3778.5 | 3780.5	3780.5 | 3783.5	3783.5 | 3786.0	3786.0 | 3790.5	3790.5 | 3795.5	3795.5 | 3797.0	3797.0 | 3800.0	3800.0 | 3802.0	3802.0 | 3803.0

TABLE 3.5: Micro windows (cm^{-1}) used for the orders 169 during the cleaning and the retrieval process. ($*$) denotes MWs used for the retrieval.

Order	**MW1**	**MW2***	**MW3**	**MW4***	**MW5**	**MW6***	**MW7**	**MW8***	**MW9**
169	3799.0 | 3800.5	3800.5 | 3802.0	3802.0 | 3806.5	3806.5 | 3807.5	3807.5 | 3814.5	3814.5 | 3817.3	3817.3 | 3820.3	3820.3 | 3822.3	3822.3 | 3827.5

- Winds and pressures measured by InSight (Lange et al., 2022).
- Atmospheric temperatures, water ice columns and dust optical depths obtained by the Emirates Mars InfraRed Spectrometer (EMIRS) (Smith et al., 2022).

The comparisons of the latest version of the model with all these datasets are summarized in Forget et al., 2022, proving the Mars-PCM to be a key asset for the modeling of the martian atmosphere and climate. The Mars Climate Database, freely available through an easy-to-use web page (MCD, 2024), is derived from a set of runs of the Mars-PCM and is used nowadays by more than one hundred of space agencies, laboratories and research groups worldwide.

Elaborate and well validated climate models are essential to examine how different physical, chemical and dynamical processes affect the atmosphere and vice versa. Although the Mars-PCM model is able to precisely reproduce the observed distribution of many atmospheric species, in order to realistically simulate each Martian Year it has to assume some column dust opacity. This is because the amount and distribution of aerosols are extremely variable on Mars, and so important for the atmospheric thermal structure. For that purpose we used the dust climatology from Montabone et al., 2020, updated for MYs 34, 35 and 36 which is mostly based on observations of the dust optical depth from MCS. Another important input for the model is the UV solar flux reaching the planet, affecting the thermospheric temperatures and also, through photodissociation rates, the atmospheric composition. We used the procedures described in González-Galindo et al., 2013. For this Thesis, specific runs of the Mars-PCM for the conditions (dust load, solar activity) of MY 34 to MY 36, were performed, generating simulated vertical profiles of temperature, pressure and gas densities at the location and time of the NOMAD SO observations.

A caution is needed when extracting results from a climate model at the NOMAD precise locations. Typically, during each NOMAD observation the latitude and longitude of the observed tangent point drifts within a range of few a degrees. After several tests and taking into account the relative small impact of the a priori atmosphere in the water vapor retrievals (see Section 4.3.3), we decided to assume the coordinates of the tangent point at 50 km altitude as the location of each occultation . This is equivalent to the midpoint of the projected path of the whole occultation.

3.8 Summary

Since NOMAD measures solar radiances that have passed through the Martian atmosphere, a fundamental understanding of how this radiation interacts with matter was necessary. In this Chapter we summarized the main concepts about radiative transfer and molecular spectroscopy following the theoretical basis from well known references in the filed of radiation in planetary atmospheres (Goody & Yung, 1995) and Banwell, 1972; Goody and Yung, 1989, adapting the theory to the solar occultation technique and to the water vapor molecule. With this basic knowledge we presented an overview of the fundamentals of the inversion theory, which is the operational tool used to exploit remote sensing data. In addition, the computational algorithms used for both, the calculation of the radiative transfer equation, and for the solution of the inversion problem were presented. Finally, regarding atmospheric a priori information and as an essential part of the retrieval process, a brief description of the Mars Planetary Climate Model was provided. Hence, this Chapter collected the basic physical principles and the computational algorithms involved required during the processing of the NOMAD SO measurements analyzed in this Thesis.

Chapter 4

IAA NOMAD Retrievals of Trace Species

4.1 Introduction

Sampling the atmosphere in a solar occultation geometry implies measuring the radiant flux emitted by the Sun as it is absorbed or scattered by the gas and aerosols present at different atmospheric layers. Practically speaking, the sensor of the NOMAD Solar Occultation (SO) channel registers the number of counts produced by incident photons, which is not a physical unit to work with. Hence, when TGO sends NOMAD raw data to the Earth, several calibration steps are required prior to its scientific analysis. The Belgian Institute for Space Aeronomy (BIRA-IASB) is responsible for this task. The pipeline of this process is complex and extensively described in Thomas et al., 2022; Trompet et al., 2023, however, we provide a brief summary here listing the main calibration steps achieved, hereafter referred as "calibration Levels". First, during Level 0.1, the raw binary data is corrected from any onboard issue with the observational parameters and converted to physical units. This is stored in HDF5 structured files, with one file per diffraction order. Then, bad pixels on the detector are identified and the spectra are corrected by linearly interpolating the data form adjacent pixels. For the Level 0.2, the TGO telemetry is used to calculate the latitudes, longitudes and tangent altitudes of the observations using the SPICE (Spacecraft, Planets, Instrument, C-matrix, Events) kernels (Acton Jr, 1996). During Level 0.3, an advance process of the data is performed, characterizing the instrument temperature dependence and applying an spectral calibration in order to convert pixel units to wavenumber. Finally, for the Level 1.0, the calibrated radiances measured at tangent altitudes where atmospheric absorption is present (so called region A) are converted into transmittances using the spectra measured directly from the Sun outside the atmosphere during the beginning of the occultation (so called region S). After that, an error analysis is done, providing the nominal measurement noise of the trasmittances. The schematics of this process is presented in Figure 4.1.

As it is well known, not a single calibration scheme is ideal. This is the case of the NOMAD SO data provided with the Level 1.0, despite of the efforts and the continuous improvements, the calibrated transmittances fall short of being suitable for their analysis. In the following Sections we present the in-house tools developed

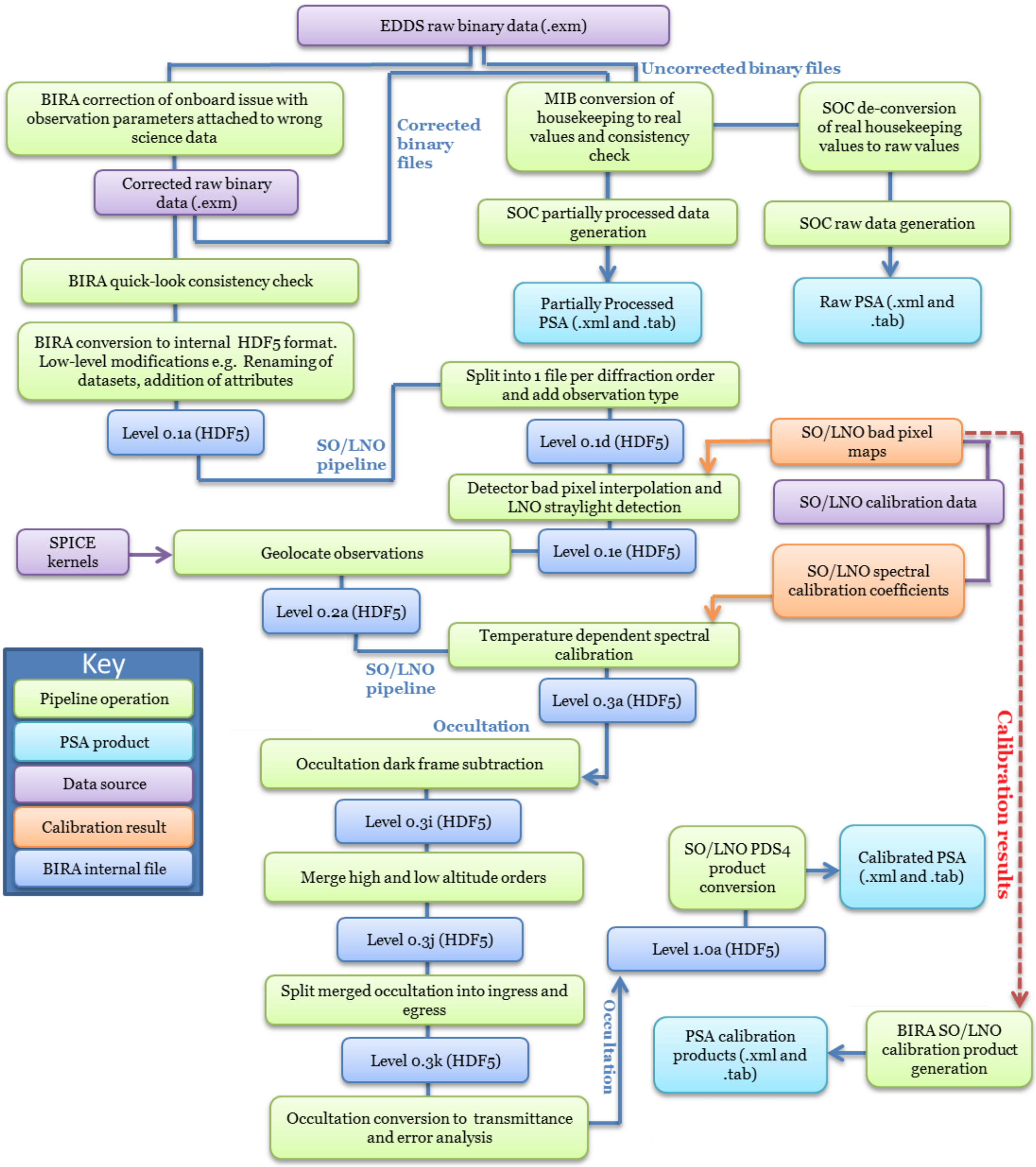

FIGURE 4.1: Calibration pipeline for the NOMAD Solar Occultation channel. Adapted from https://nomad.aeronomie.be/index.php/data/data-pipeline/hdf5-calibration-pipeline.

at Instituto de Astrofísica de Andalucía (IAA-CSIC) with the objective of correcting for some systematic issues still present in the NOMAD SO calibrated data. In addition, we provide a detailed description of an improved characterization of the transmittance uncertainty and we present the basics of a novel statistical analysis on Martian water vapor profiles based on data clustering. Most of these tools where specifically developed during and for this Thesis.

4.2 IAA Pre-Processing

When inspecting the Level 1.0 data, we observed residual inaccuracies persisting in the calibrated transmittances. First, we confirmed, as it was found by the NOMAD consortium teams, that the spectra were affected by a curvature in the continuum which varied through the diffraction order. This spectral bending changed from occultaiton to occultation, occasionally being quite significant. Another issue present in the measurements was a systematic and variable spectral shift of the center of the absorption lines in all diffraction orders. Comparing the HITRAN (experimental) frequency of the absorption lines within each diffraction order with the NOMAD SO measured lines we observed a displacement typically smaller than 0.1 cm^{-1}. At IAA-CSIC we developed the appropriate software tools to identify and correct for these issues prior to the addressing the inversion of the spectra. This IAA Pre-Processing (IAA-PP) was applied in different stages and played a key role in the IAA NOMAD SO analysis pipeline. All the Sections outlined in this Chapter were essential components of the IAA-PP pipeline, which is summarized in Figure 4.2.

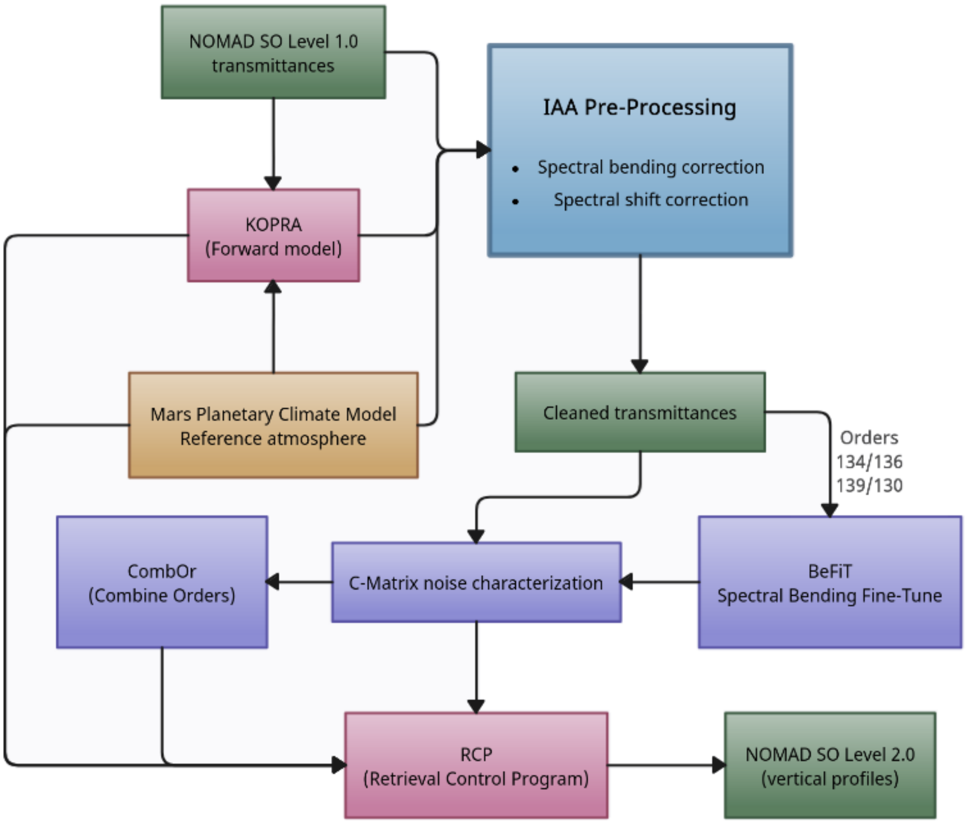

FIGURE 4.2: IAA Pre-Processing and retrieval pipeline

4.2.1 Spectral bending correction

The NOMAD SO transmittances showed an oscillation present at all altitudes and diffraction orders. However, its shape and intensity was different at every scan and order, impeding a general description. Therefore, it had to be characterized for every case independently. The simplest solution to solve this issue was to estimate the baseline of the spectra and then remove it. However, the absorption lines from the order and the contamination of adjacent orders introduced real features and variations of the continuum that should not be removed when subtracting the baseline, making this approach valid only at high altitudes where the absorption line were negligible or non existent. Thus, a more meticulous approach was required. To get around this issue we decided to use line-by-line forward model simulations computed with the Karlsruhe Optimized and Precise Radiative transfer Algorithm (KOPRA) (Stiller, 2000) which takes into account the effect of the lines and the contribution of adjacent diffraction orders to the baseline of the spectra. Considering all the main contributions to the measured transmittance along the slant path (path followed by the light from the Sun to the detector, passing through the atmosphere), one possible way to characterize the transmittance is:

$$\mathcal{T}(\lambda) = \mathcal{T}_0^k(\lambda) \times \exp^{-\tau} \times \mathcal{T}_b(\lambda) \tag{4.1}$$

where $\mathcal{T}$ is the measured transmittance at wavenumber λ at a given altitude, $\mathcal{T}_0$ is the KOPRA simulated transmittance, k is a scaling factor used to accommodate the line depths of the KOPRA simulation at every altitude, τ is the aerosol slant opacity assumed constant through each diffraction order, and $\mathcal{T}_b$ is the residual spectral bending to estimate. During the characterization of the bending, based on the visual inspection of hundreds of spectra, we assumed a fourth-degree polynomial to describe its shape, so the bending can be expressed as

$$\mathcal{T}_b(\lambda) = \frac{\mathcal{T}(\lambda)}{\mathcal{T}_0^k(\lambda) \exp^{-\tau}} = \sum_{j=0}^{j=4} a_j \lambda^j \tag{4.2}$$

where a_j are the coefficients of the polynomial. The estimation of the bending was done for a wide set of predefined values of k, τ and a large set of KOPRA simulations $\mathcal{T}_0(\lambda)$ at different altitudes. For each pair of values, we computed the ratio

$$\mathcal{S} = \frac{1 - \mathcal{T}(\lambda)}{\mathcal{T}_0^k(\lambda) \mathcal{T}_b(\lambda) \exp^{-\tau}} \tag{4.3}$$

At the end, the most suitable set of parameters that describe the measured transmittance is the one that minimizes the ratio $\mathcal{S}$. Exploring the whole parameter space of k and τ looking for the best combination is computationally expensive and time consuming. Consequently, we developed a jump-search algorithm where at first, the parameter space of k and τ was explored in "low resolution", i.e. only some

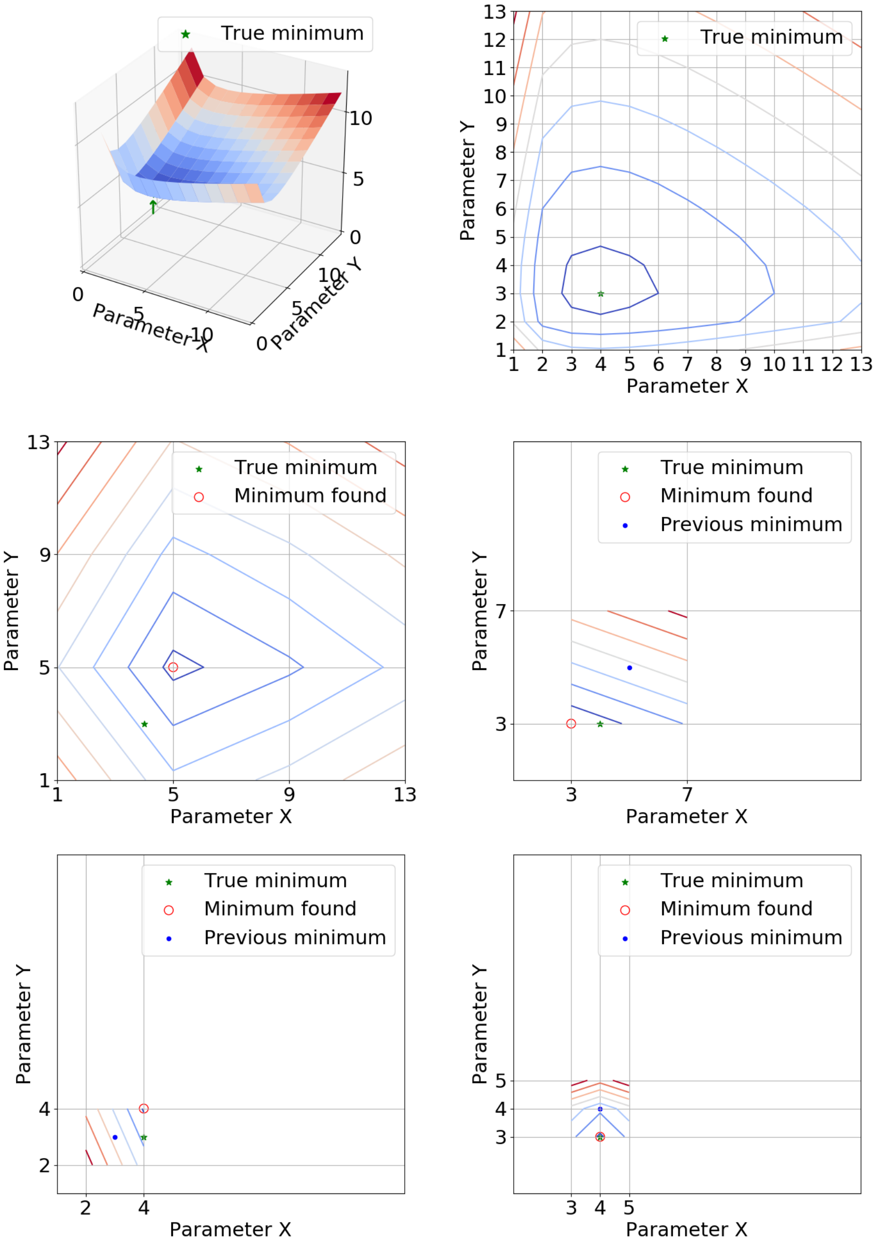

FIGURE 4.3: IAA-PP jump-search algorithm scheme

indexes were considered during the search. This first iteration provided a region where the minimum of $\mathcal{S}$ should be located. Then, the process was repeated only with the parameters close to that region increasing the resolution of the parameter space after each iteration until the true minimum was found. Finally, the polynomial $\mathcal{T}_b(\lambda)$ resulting from the best set of parameters was subtracted from the NOMAD SO measured transmittance. An example illustrating the IAA-PP jump-search algorithm is shown in Figure 4.3, where a set of 13×13 parameters is used to sample a function whose minimum is located at the coordinates (4,3). The top panels show the function and the parameter space at full resolution. Bottom panels show the adaptive process of the algorithm from the full parameter space at low resolution (left middle panel) to the local and high resolution space (right bottom panel). During the cleaning of NOMAD data, we used a grid of 40 values for k ranging from -2 to 2, 40 values for τ ranging from 6 to 10^{-10}. Aerosol opacities larger than 3 are unusual on Mars, only found in the case of heavy global dust storms, but these conditions can not be sounded with solar occultation measurements. In Figure 4.4, we show a comparison between the original NOMAD SO transmittances before (red line) and after the bending and shift correction (blue line) for a few tangent heights from the diffraction order 136. Note that during this correction for bending , a value of the aerosol opacity τ is obtained. When a spectrum is bent, this value can be fixed with some arbitrariness. In other words, the bending is "flattened" at the absorption background given by τ, and this is decided by the user. In this work we used a spectral window in the center of the order to derive a value of τ, which, for every spectra obtained during the occultation, was then applied to the whole order.

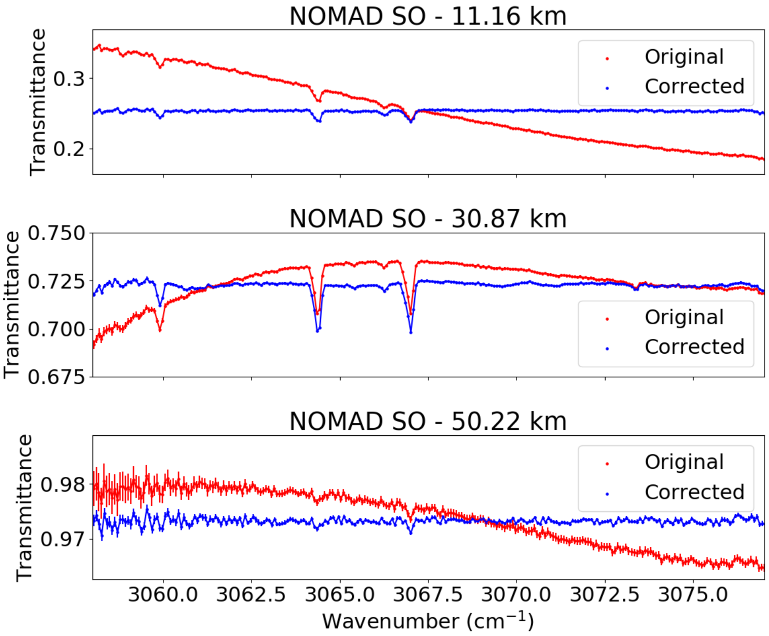

FIGURE 4.4: Bending correction for the solar occultation 20181126_045122_1p0a_SO_A_E_136.

Bending Fine Tune Correction (BeFiT)

The spectral bending observed in the measured transmittances is mainly caused by the Acousto-Optical Tunable Filter (AOTF) and its variation depends on the temperature of the SO channel detector, which varies during each atmospheric scan. Although the characterization of the bending with a fourth degree polynomial was a good approximation as shown in Figure 4.4, and this approach has been used by other NOMAD teams, in cases where the bending was large (variation in transmittance $\Delta\mathcal{T} > 0.1$), the cleaned spectra still showed a residual oscillation. The amplitude of this second order bending was small, typically $\Delta\mathcal{T}{\sim}10^{-3}$, slightly above the measurement noise. This issue can be observed in the top panel of Figure 4.5 for one arbitrary occultation in order 134, where after averaging a dozen of cleaned spectra at the top of the atmosphere (after the standard IAA-PP cleaning) a residual oscillation clearly appears. This issue was particularly relevant for those orders with weak absorption lines, where an insufficient bending correction of the full order is particularly evident. In those cases we applied a fine tuning of the bending characterization. This second cleaning examined the data at the top of the atmosphere (TOA) and computed the average of all the spectra within an altitude window of ∼20km (in the case of order 134 this means altitudes from ∼100 km to ∼120 km). The residual bending was then characterized with a running mean along the spectral dimension, providing an oscillating function with a certain amplitude. During this process we assumed the residual oscillation to be similar at all altitudes. This assumption is appropriate as it is shown in the middle panel of Figure 4.5, where the normalized transmittances at all tangent height show the same oscillation. Once this second correction function or "BeFiT", is computed at TOA, its application to lower altitudes requires some caution. For this, BeFiT was compared with the cleaned spectra at each tangent height, where an iterative variation of the scale of the BeFiT function was performed until the residuals between the TOA baseline and the spectra were minimal. This allowed for possible small variations of the amplitude of the oscillation with altitude, keeping its shape unaltered. Once the optimal baseline for each tangent height was obtained, it was subtracted from the measured transmittance. The improvements on the bending correction after this process is shown in the bottom panel of Figure 4.5. This methodology was applied only to those orders where no absorption lines were detected at those altitudes. This fine correction was designed for the analysis of trace species with extremely weak spectral features, such as HCl, which are being studied by the IAA-CSIC team. Although it does not have a significant impact on water vapor retrievals, it is part of the processing pipeline applied during the development of this Thesis, so we decided to include it here for completeness.

4.2.2 Spectral shift correction

During our pre-processing of the data, not only the bending is corrected but also any spectral shift of the absorption lines respect to their experimentally well determined central wavenumber. It was clear from the first analysis of the NOMAD SO spectra that a non-constant shift was present in all diffraction orders, which usually is equivalent to some sort of stretching of the spectral lines from their expected locations Aoki et al., 2019. For this task, again KOPRA simulations were used, taking into account the line parameters from the latest version of the High-resolution Transmission (HITRAN) molecular absorption database (Gordon et al., 2022). The characterization of the spectral shift was done in two main steps:

First, during the above mentioned bending correction, in addition to the set of parameters k and τ, a set of spectral shifts $\Delta\lambda$ was provided to the IAA-PP, adding

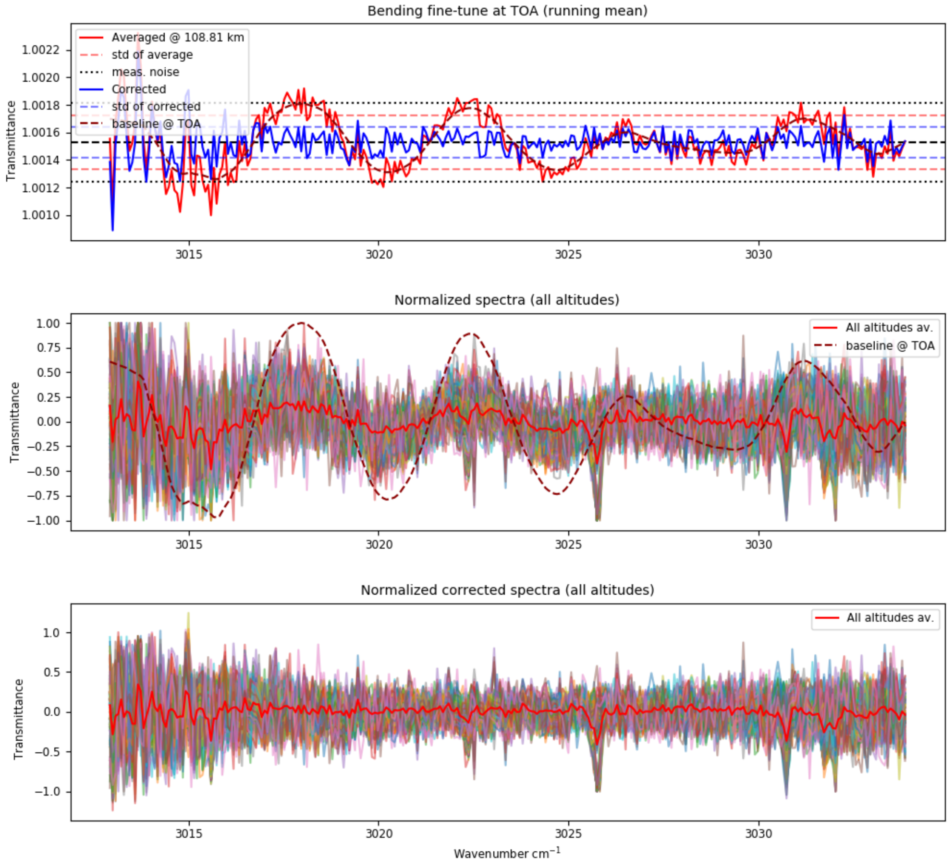

FIGURE 4.5: Bending Fine Tune correction for the order 134 during the solar occultation 20200423_164632_1p0a_SO_A_E.

a third dimension to the minimization problem described in 4.2.1. Therefore, the equation 4.3 can be expressed as

$$S = \frac{1 - \mathcal{T}(\lambda + \Delta\lambda)}{\mathcal{T}_0^k(\lambda + \Delta\lambda)\mathcal{T}_b(\lambda)\exp^{-\tau}} \tag{4.4}$$

Finding the correct $\Delta\lambda$ is complicated in a generic case. Computing the shift at spectral regions or altitudes where the lines are weak would provide wrong results, introducing biases in the cleaned transmittance. And on the contrary, when strong absorption lines are present, for example a tropospheric altitudes, shifts are far from obvious. Therefore, its estimation must be done carefully. Our approach was to consider as valid the spectral shift obtained only at some spectral ranges within the order, i.e. micro-windows (MW), where the strongest absorption lines were located. For each MW, the shift was estimated independently at every altitude. Then the altitude range where the minimum standard deviation of these shifts was located was used as "optimal" altitude for the shift estimation. For the reasons discussed above, this altitude range is usually at upper tropospheric or mesospheric altitudes, to avoid noise and overlapping of absorption lines. The mean value within that altitude range was considered as the best solution. This is shown in the top panel of Figure 4.6, where for the MW located at 3077 cm^{-1}, the best altitude range for the spectral shift characterization was found at 25 km. Then, once the spectral shift was obtained for the selected MWs, a linear fitting was done through all of them in order to estimate the variation of the shift within the full diffraction order. This is shown in the bottom panel of Figure 4.6. With this method we assumed that the spectral shift did not change with altitude and that its variation within the order was linear. During this process we used a grid of 40 values for $\Delta\lambda$ ranging from -0.1 cm^{-1} to 0.1 cm^{-1}, which means that our correction may have an accuracy close to 0.005 cm^{-1}, which is at the sub-pixel level (the typical spectral sampling of NOMAD SO is about 0.09 cm^{-1}).

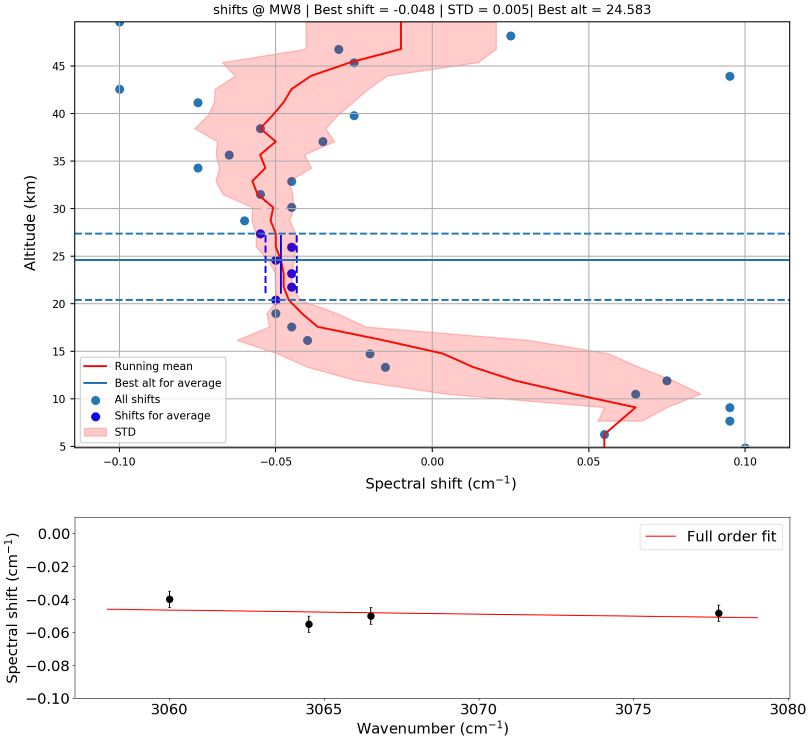

FIGURE 4.6: IAA-PP spectral shift characterization for the order 136 during the solar occultation 20190103_155621_1p0a_SO_A_I.

The second step of the shift characterization was done after the cleaning of the data, during a first inversion of our retrieval suite, as explained in Section 3.6. Using the Retrieval Control Program (RCP), which among other parameters it is able to provide spectral shifts, we performed inversions of the data only at the shift "optimal" altitude range found during the previous step. This quick inversion provided a fine tune of the spectral shift previously obtained by the IAA-PP, with more accurate values, which are used during the second and final inversion of the whole vertical profile afterwards.

4.2.3 Aerosol opacity characterization

One of the byproducts of the IAA-PP is the dust optical depth. As described in Sections 4.2.1 and 4.2.2, the correction fro the spectral shift and the continuum's characterization were done in a fast, appropriate manner by using constant grids of predefined values of the two magnitudes. This grid or limit in precision was not critical for the shift correction since the precision obtained is at sub-pixel level. In addition, the inversion after the pre-processing, prior to the water vapor retrieval, provided an even more accurate shift characterization without the grid resolution limit. However, the term referred to the continuum of the spectra in equation 4.4 has a strong dependency on the parameter τ, i.e., the aerosol slant optical depth. Hence, using a discrete grid of τ may introduce some uncertainties when characterizing the continuum. In order to avoid this situation, we performed a fine tune of the continuum in the last step of the pre-processing process. For each spectra, once the best spectral shift $\Delta\lambda$ and factor k were found, we used a third order polynomial fitting for adjustments around the best τ previously found. This method allowed us to use a continuous space rather than a discrete one for the continuum characterization.

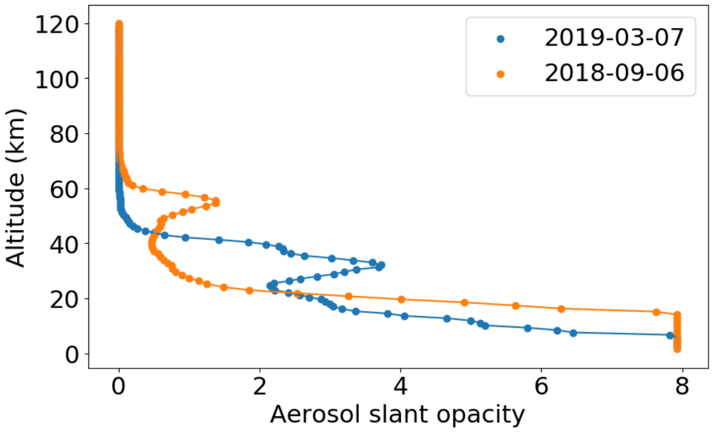

FIGURE 4.7: Aerosol slant opacity computed for two different arbitrary NOMAD solar occultations, 20190307_153209_1p0a_SO_A_I (blue) and 20180906_084740_1p0a_SO_A_E (orange).

Other aspects are important for the aerosol opacity. Figure 4.7 shows the estimation of the aerosol slant opacity for two solar occultations. These two profiles were generated for each observation and we used them in order to determine the lowermost altitude suitable for the retrievals. In particular, we used a "cloud filter" excluding those altitudes where the slant optical depth was larger than 1.5. In addition, we also imposed the criterion to reject those altitudes with a gradient in the slant opacity lager than 0.08 km^{-1}. These two values, although arbitrary, proved to be conservative enough to guarantee an adequate ratio of retrieval convergence. This is not surprising because high opacities implies hidding spectral lines by aerosols, reducing the information content of the target gases, like H_2O. Reducing these conditions did not had any significant effect on the results besides changing the altitude of the lowest layer. In contrast, relaxing this criterion led to an increased numerical instability during the inversions.

4.3 Error analysis and retrieval performance

4.3.1 Covariance Matrix

Our retrieval scheme and our code RCP are prepared to use the measurement noise as a pure uncorrelated error. The measurement noise present in the NOMAD SO data files provided by the BIRA-IASB calibration (Thomas et al., 2022) is a global uncertainty but it does not differentiate between systematic and random uncertainties. Therefore, we are interested in correcting the data for the most relevant systematics such as spectral shift and bending as discussed in Section 4.2. In order to disentangle the systematic and random components of the NOMAD SO measurement noise we used covariance matrices (C-matrix). The elements of those matrix can be defined as

$$\sigma_{jk}^2 = \frac{\sum_i^N \left(x_{ij} - \overline{x}_j\right)\left(x_{ij} - \overline{x}_k\right)}{N} \tag{4.5}$$

where N is the number of spectra (altitudes), x the transmittance and indexes j, k the spectral pixels (1 to 320) at the diffraction order of interest. The element $\overline{x}_j$ represents the average of x at pixel j for all the N altitudes. A typical study of the covariance for two different occultations and diffraction orders is presented in Figure 4.8 (order 134 in the left and order 168 in the right panels), with the top panels showing a 320x320 matrix with a clear diagonal over a random background with non-diagonal elements in the case of Figure 4.8-a1. The bottom panels of this Figure show a row of the matrix at an arbitrary pixel (pixel #250 in this case), showing a maximum at the column #250 (diagonal) in Figure 4.8-a2. From the diagonal of this matrix we obtained the variances that characterize the random noise (C-noise) of the spectra. This approach was only valid when there were no strong vertically correlated systematics in the spectra, such as absorption lines or biases from the calibration. These features introduce artifacts in the non-diagonal elements of the matrix as illustrated in Figure 4.8-b2. The artifacts produced by absorption lines can be easily avoided by computing the matrix only at those altitudes where the lines were undetected. The presence of systematics in the spectra, however, would require a re-calibration of the data. Instead of increasing even more the complexity of the pre-processing, we decided to accept as valid only those C-Matrix whose diagonal elements at pixel j were larger than the standard deviation of their row/column. This is illustrated in bottom panels of Figure 4.8. The C-Matrix of the occultations that did not fulfill this requirement, like that on Figure 4.8-b1, were rejected and the measurement noise used during the inversion was the nominal one, which is a conservative assumption of the random noise.

The pure random measurement noise obtained from the accepted C-Matrix was representative only for the upper atmosphere where the matrix was computed. However, the noise level in solar occultation measurements is known to vary slightly with altitude Thomas et al., 2016, partly because increasingly importance of the shot noise at low altitudes, where the solar signal has been severely absorbed. In order to extend this random noise characterization to all altitudes, we scaled the new uncertainties in the vertical, following a specific functional form. This function is mimicking the vertical profile of the nominal error. More precisely, the new measurement noise profile $\delta\mathcal{T}'(z)$ at any given frequency and altitude z throughout the whole solar occultation can be defined as

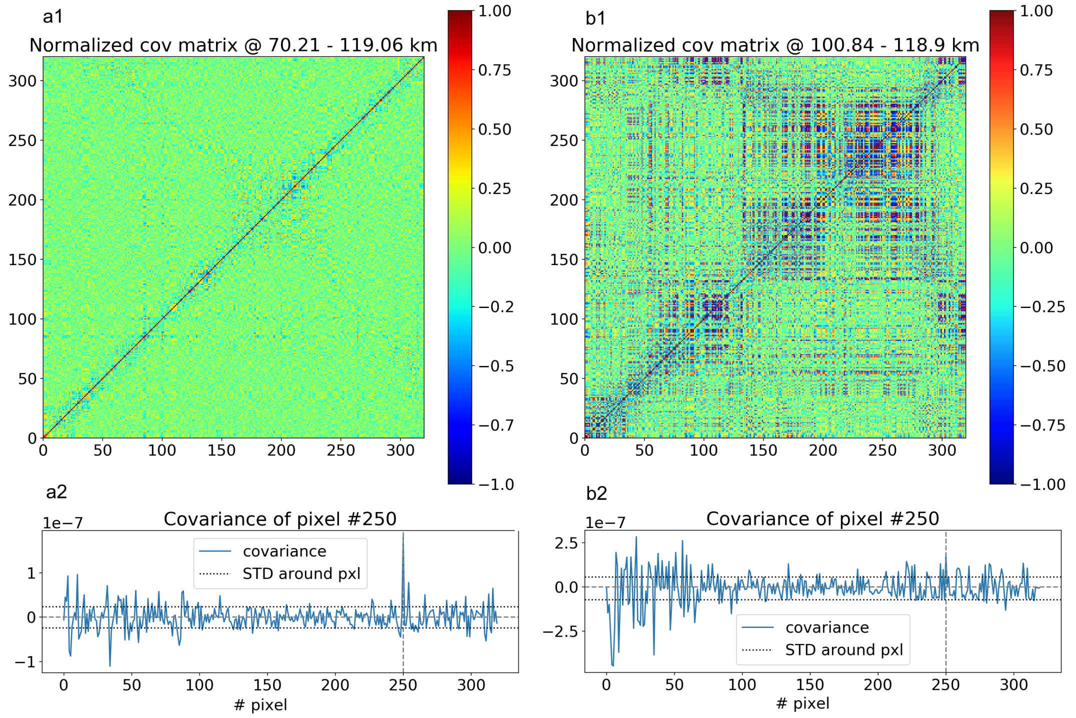

FIGURE 4.8: Normalized covariance matrices $\left(\sigma_{ij}^2/\sqrt{\sigma_{ii}^2\sigma_{jj}^2}\right)$ for the order 134 (a1) and 168 (b1) during the solar occultation 20180627_054013_1p0a_SO_A_I and 20190407_232215_1p0a_SO_A_E respectively. Bottom panels show a slice of the matrix at pixel #250.

$$\delta\mathcal{T}'(z) = \delta\mathcal{T}_0 + (\delta\mathcal{T}(z) - \delta\mathcal{T}_0)\,\frac{\delta\mathcal{T}'_{TOA} - \delta\mathcal{T}_0}{\delta\mathcal{T}_{TOA} - \delta\mathcal{T}_0} \tag{4.6}$$

where $\delta\mathcal{T}(z)$ is the nominal noise at altitude z, $\delta\mathcal{T}_0$ is the nominal noise at the lowermost altitude, $\delta\mathcal{T}_{TOA}$ is the nominal noise at the topmost altitude (top of the atmosphere) and $\delta\mathcal{T}'_{TOA}$ is the new noise at the topmost altitude obtained from the covariance matrices (C-noise) explained above. This extrapolation of the noise to low altitudes is valid when the random oscillations of the spectra, i.e. its standard deviation, decreases proportionally with the signal. Typically, the vertical profile of the nominal measurement noise is proportional to the transmittance vertical profile. This is, when the signal drops at low altitudes due to the large absorption produced by the aerosols, the measurement noise drops accordingly. However, this is not always the case. We noticed occultations with sharp decreases in the signal as the observed tangent height approached to the surface. In those scenarios, the vertical profile of the observed standard deviation (STD) did not follow the noise profile. Instead, the STD showed a lower gradient towards lower values at the altitudes where the nominal noise had the sharp decrease. This is illustrated in Figure 4.9, where we computed the standard deviation of the spectra at every altitude for an occultation and diffraction order with absorption lines below the detection limit. The Figure shows how the measured standard deviation (blue) coincides with the C-noise at the top of the atmosphere and with the nominal noise at the lowermost altitudes. However, at 50-60 km the nominal noise decreases faster than the true random oscillations in the spectra. As a result, both the nominal noise and the C-noise scaled with 4.6 were overestimating the true random uncertainty of the spectra, providing values too small compared with the STD. Hence, we decided to use the C-noise at those altitudes where the nominal noise was larger than the C-noise. Then, for the lower altitudes we simply followed a straight line from the C-noise to the value of the noise at the lowermost altitude (black solid line in Fig.4.9). We applied this method at every frequency within the diffraction order. The characterization of the C-matrix and this scaling method were only applied during the analysis presented in Chapters 6 and 7. A comparison between the new measurement noise computed with the

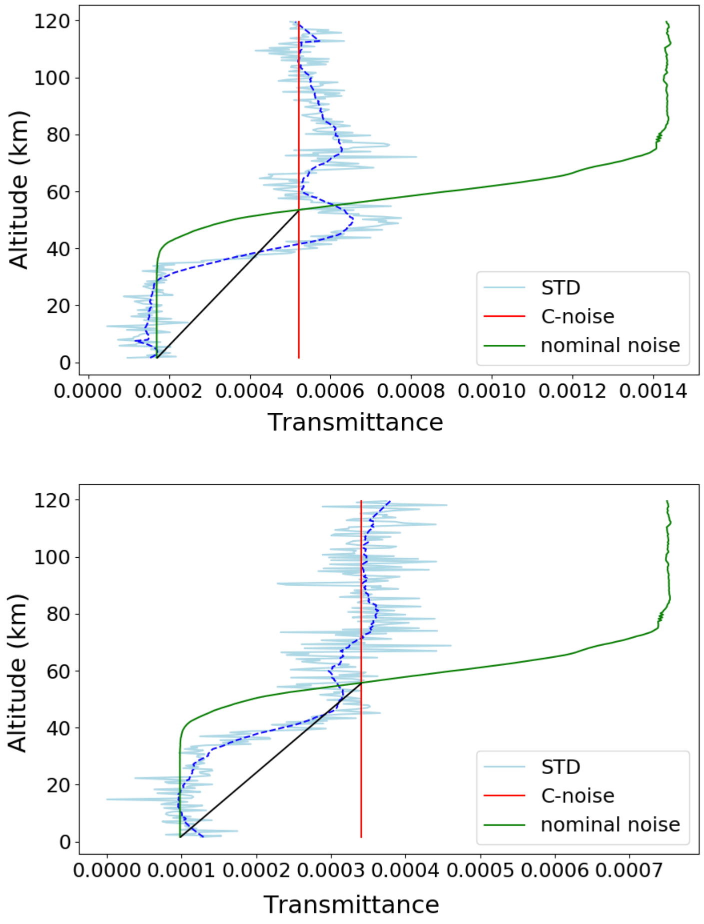

FIGURE 4.9: Measurement noise vertical profile obtained for the order 130 during solar occultaiton 20180627_054013_1p0a_SO_A_I at two different spectral MWs.

covariance matrix and the nominal NOMAD SO measurement noise is shown in 4.10. Typically, the new uncertainties at high altitudes were up to 4 times smaller than the nominal noise. This methodology of measurement noise characterization based on covariance matrices, which proved to be useful during the data analysis, has been recently implemented in the BIRA-IASB calibration pipeline.

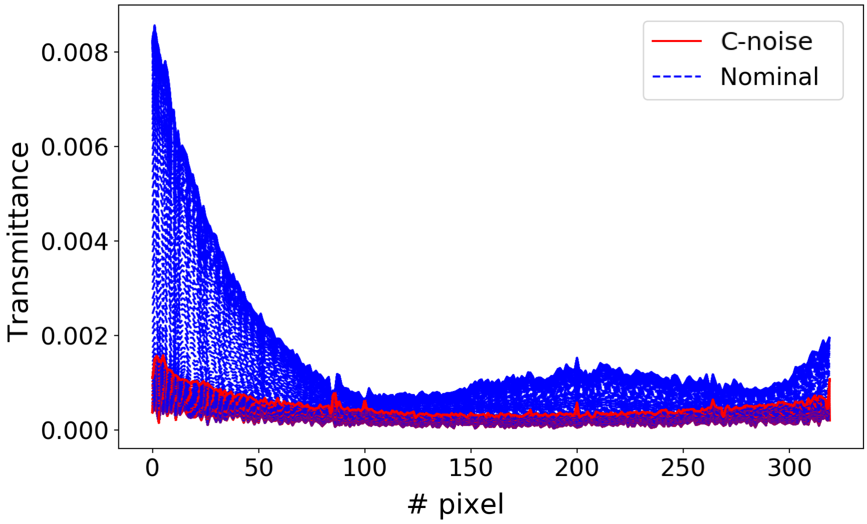

FIGURE 4.10: Comparison of the noise obtained from the Covariance Matrix (red) with the nominal NOMAD SO measurement noise (blue) for the order 130 during the solar occultation 20180627_054013_1p0a_SO_A_I. Each red/blue curve corresponds to a different altitude.

4.3.2 Typical retrieval performance

After all the calibration and pre-processing steps discussed above applied to the NOMAD data, we performed the inversion of the water vapor vertical profiles. As mentioned in Chapter 3, we used RCP to solve the inversion problem. This tool provides several byproducts and diagnostics needed for the evaluation of the retrieval performance. The typical results and set of parameters used to examine every solar occultation are presented in Figure 4.11 for an arbitrary occultation. Figure 4.11-a shows a typical water vapor vertical profile, with a relative uncertainty related to the measuremnt noise of about 2-5 % below 50 km and progressively increasing up to about 10% at 80 km altitude, as illustrated in Figure 4.11-b. This is due to several reasons: (i) the measurement noise at low altitudes is smaller, as discussed above in Section 4.3.1, (ii) the diffraction order used to retrieve the water vapor above 60 km is different to that used below, as it will be discussed in Section 4.4, and (iii) the density is decreasing with altitude and so does the sensitivity to VMR. Figure 4.11-c and 4.11-e show the vertical resolution and Averaging Kernel matrix (**A**) respectively. Again, and closely related to the previous discussion about the nose, the vertical resolution increases from 2-5 km at low altitudes to 8-10 km at higher altitudes, following the typical performance of retrievals from solar occultaiton measurements. Note that the reduction of the error and the vertical resolution in Figures 4.11-b and 4.11-d above 80 km are due to regularization effects for this particular case. Finally, Figure 4.11-d shows the absorption coefficient profile, required to adjust the continuum of the spectra during the inversion.

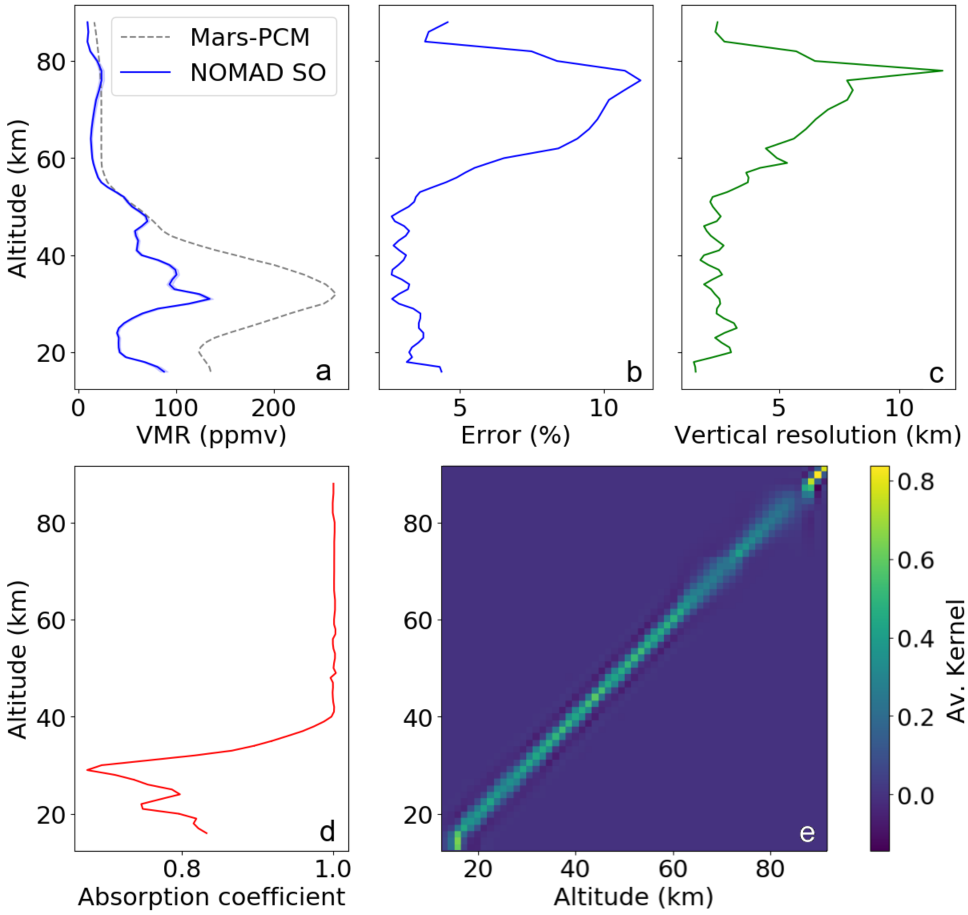

FIGURE 4.11: Example of the typical retrieval performance for the occultation 20200517_215727_1p0a_SO_A_I. Panels a, b and c show the vertical profiles of the retrieved water vapor, the propagation of the measurement noise and the vertical resolution of the profile respectively. Gray dashed line in panel a indicates the a priori water vapor profile from the Mars Planetary Climate Model (Mars-PCM). Panel d shows the continuum due to aerosols. Panel e shows the averaging kernel matrix.

Another key diagnostic essential to evaluate the good or bad performance of the inversion is the fitting of the NOMAD SO spectra with the forward model. Four spectral fittings, with their residuals, at different altitudes for four arbitrary occultations are presented in Figure 4.12 for the main diffraction orders used throughout this work. Fittings for diffraction orders 134, 136, 168 and 169 at 10, 30, 60 and 90 km are shown in Figures 4.12-a1, 4.12-b1, 4.12-c1, 4.12-d1 respectively. Their residuals are illustrated in Figures 4.12-a2, 4.12-b2, 4.12-c2, 4.12-d2 respectively. Note that the fitting is only performed at the narrow selected MWs containing the strongest water vapor lines (see Section 3.6.1 for details). In all these panels, taking into account the complexity of the NOMAD SO calibration and pre-processing, the fitting is good, within the measurement noise (illustrated with gray dotted lines in the panels showing the residuals). In order to achieve this overall good performance, a series of sensitivity tests were performed, as it will be discussed in the following Section.

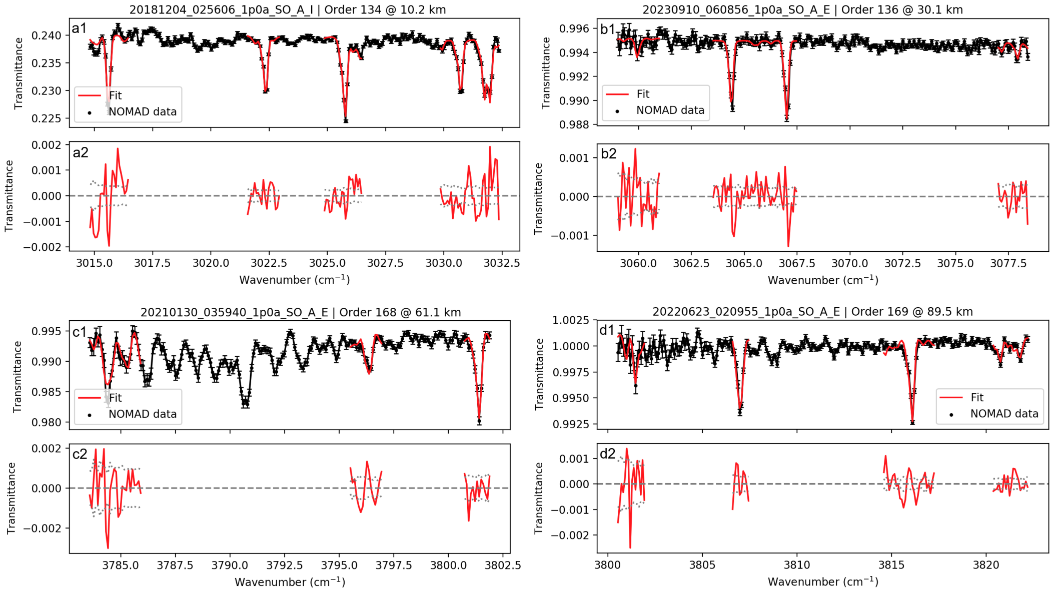

FIGURE 4.12: Fittings (red line in panels a1, b1, c1 and d1) and residuals (red line panels a2, b2, c2, d2) obtained after the inversion of four NOMAD observations with diffraction orders 134 (a), 136 (b), 168 (c) and 169 (d) at 10, 30, 60 and 90 km altitude respectively. NOMAD data is shown in black. Dotted lines in panels a2, b2, c2 and d2 indicate the NOMAD measurement noise.

4.3.3 Sensitivity studies

During the retrievals of the vertical profiles of water vapor, and other targets, from NOMAD SO spectra we did several assumptions required to solve the inversion problem. The solution to this problem was not unique, and our trace-gas retrieval scheme did only allow the gaseous species to be free parameters during the inversion. Hence, different inputs and constrains, including a reference (a priori) atmosphere close to reality, were needed. In order to quantify the impact of those assumptions to the result, we performed sensitivity tests by introducing perturbations into the input parameters, keeping the retrieval target fixed.

Regularization test

In order to constrain the inversion, as discussed in 3.4, we used a first order Tikhonov regularization. In practical terms, the degree of regularization determines the smoothing or noise filtering in our retrieved profile. Although there are several approaches for the estimation of the optimal regularization (Quémerais et al., 2006; Serio et al., 2016; Villanueva et al., 2022b), we decided to perform a series of synthetic retrievals in order to evaluate and to quantify precisely the impact of regularization with different degrees of smoothing. To do so, we used KOPRA to generate synthetic spectra for different diffraction orders from a set of well known reference atmospheres. These spectra were generated taking into account the instrumental characterization of NOMAD, including a random measurement noise, equivalent to that present in the NOMAD real data, generated with a random function with a standard deviation equivalent to the standard deviation of the NOMAD measurement uncertainty. In order to obtain a statistically meaningful result, for each reference atmosphere we generated 10 sets of spectra in which only the random noise was changed (fixing the standard deviation). Then, we performed the inversion for each set, resulting in 10 vertical profiles per order. We replicated the typical NOMAD sampling by using spectra only from 10 km to 120 km altitude. The advantage of using synthetic spectra is that we know the true vertical profile to obtain, and the signal is free from systematics (including uncertainties in the ILS and AOTF). Repeating this process for different regularizations allowed us to identify the non-physical oscillations (respect to the true profile) propagated to the vertical profiles due to the noise in the data. In Figure 4.13 we present an example of two regularizations applied to the same profile, highlighting its effects on the 40-120 km altitude range. Figures 4.13-a1 and 4.13-a2 show a case of "low" regularization, whereas Figures 4.13-b1 and 4.13-b2 show a larger regularization. These second values are closer to what we consider is the optimal value. We imposed a strong regularization at altitudes with no measurements, this is, below 10 km and above 120 km. Also, the values at the edges of the retrieved vector (0 km and 200 km for this example) were forced to the a priori using a strong diagonal constraint. As a result, the oscillations in the altitude regions outside the measurement vector were smaller and all profiles converged to the a priori. After identifying the optimal regularization, which was the one that allowed oscillations within the profile error bars, we fine-tuned its value with retrievals using real NOMAD data.

The atmospheric conditions, and as we will discuss in following Chapters, the abundance of water vapor changes drastically depending on the season and location on Mars. The optimal way to define the regularization is by examining profile by profile, selecting a specific regularization for each particular observation. However, taking into account the large size of the NOMAD data set (thousands of observations), this method would require extremely large computation times. For that reason, after repeating these tests with several observations, we decided to apply a global regularization valid for different atmospheric conditions, maximizing the convergence rate of the retrievals. A drawback of this strategy is that for some cases, the retrieved profiles were too smooth or too noisy, suggesting that the regularization used was overestimated or underestimated. Nevertheless, as shown in Chapters 5,6 and 7, with this method we managed to achieve a trade off between stability during

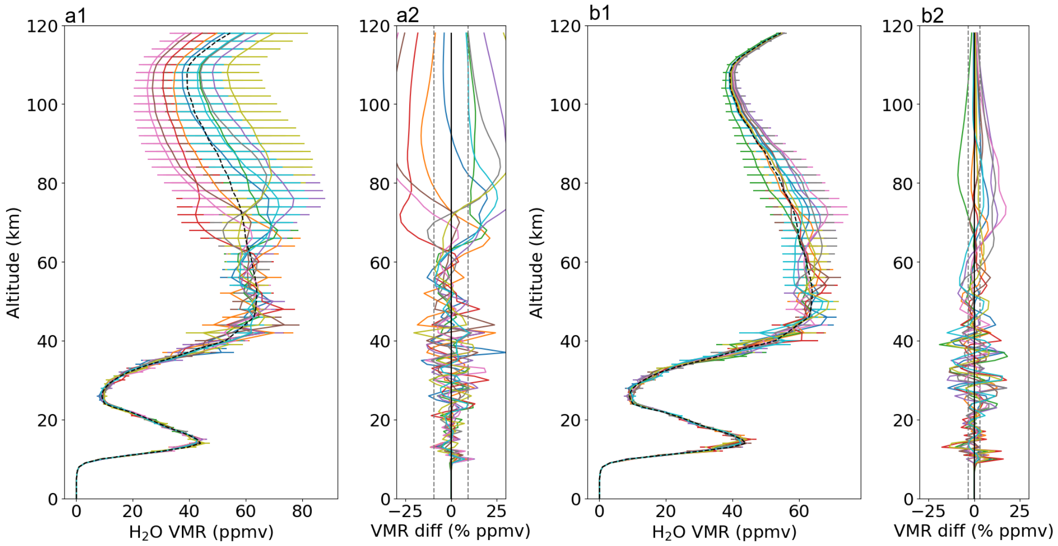

FIGURE 4.13: Retrieved water vapor vertical profiles from synthetic spectra using two different degrees of regularization (panels a1 and b1) after 10 random variations on the simulated measurement noise (indicate with colors). Black dashed line shows the true profile. Panels a2 and b2 show the relative difference to the true profile. Vertical gray dashed lines indicate the standard deviation.

the inversion and reliability of the results.

A priori and first guess on H_2O abundances test

Two of the key inputs required during the retrieval are the a priori and first guess which in our setup, the same reference atmosphere is used for both. In order to evaluate the sensitivity of the retrieved profile to those inputs, we performed again specific synthetic retrievals with two different a priori profiles of water vapor. The results are shown in Figure 4.14. Two different test were done: (i) introducing modifications in the a priori (top panels) and (ii) introducing modifications in the first guess (bottom panels). For both tests, the modifications introduced were a constant offset of factor 2 (left panels) and a wave of amplitude 80% to the original input profiles (right panels). As shown in the Figures 4.14-c1 and 4.14-d1, variations in the first guess had null impact on the inversion, as the retrieved profile in both the original and that obtained with modified inputs were extremely similar, showing differences below 0.1 % as shown in Figures 4.14-c2 and 4.14-d2. On the other hand, and as expected, the variations in the a priori did affect those altitudes with strong diagonal constraint (see Section 3.4). For this test, we introduced a diagonalization below 10 km and, progressively increasing, above 70 km altitude. As a result, the retrieved profiles between 0 and 10 km are fixed to the apriori and above 70 km, they start to diverge from the true abundance to the value of the apriori. Between 10 and 70 km altitude, all profiles overlap, showing differences below 10% as shown in Figures 4.14-a2 and Figures 4.14-b2, indicating a small impact of the regularization and of the first guess and a priori.

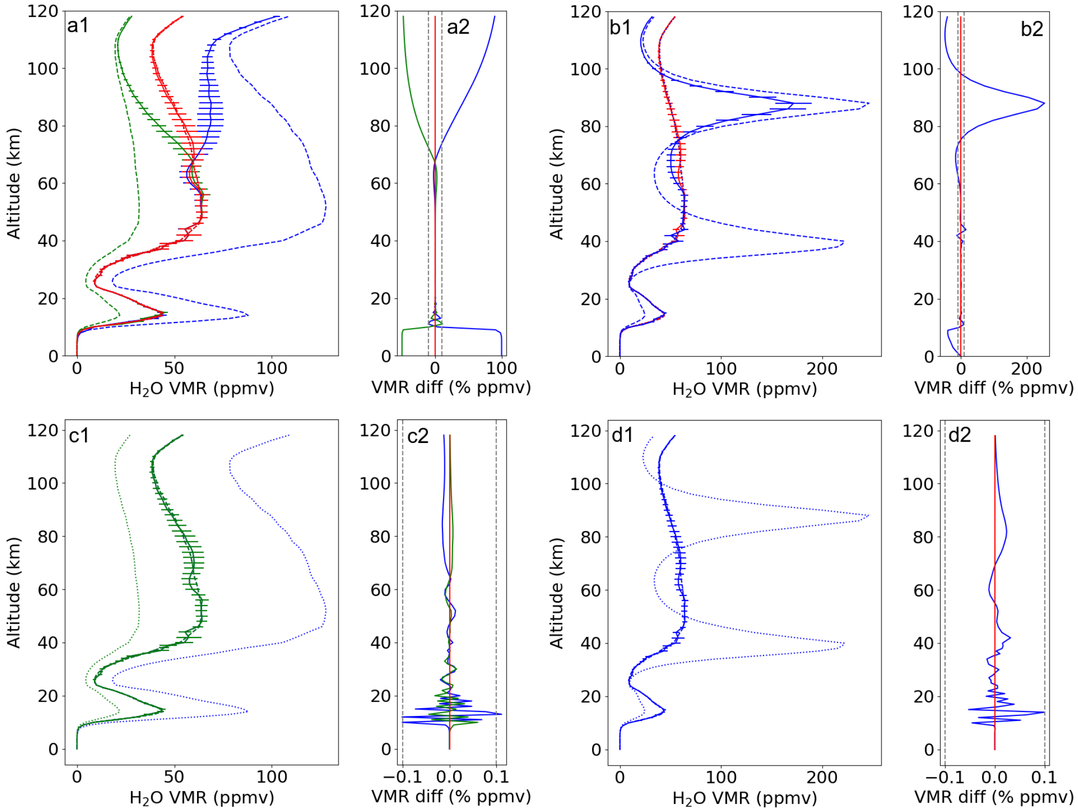

FIGURE 4.14: Water vapor vertical profiles obtained during a priori and first guess sensitivity test. Top panels show the impact of changing the a priori profiles (dashed lines) during the retrieval. Bottom panels show the tests for changes in the first guess (dotted lines) during the retrieval. Right panels (a1 and c1) show the result of introducing a constant offset in the input profiles of ×2 (blue lines) and ×1/2 (green lines). Left panels (b1 and d1) show the same for a wave function in the input profiles. True profiles (retrieved with unmodified a priori and first guess) are shown in red color. Differences between retrieved profiles using the unmodified and modified inputs are shown in panels a2, b2, c2 and d2. Vertical dashed lines indicate ±10% in panels a2 and b2, and ±0.1% in panels c2 and d2. Note that all retrieved profiles overlap on panels c1 and d1.

Pressure and temperature sensitivity test

Our retrievals did not include atmospheric densities directly derived from the NOMAD measurements, i.e. from CO_2 lines. Instead, we assumed temperature (T) and pressure (P) the from the Mars-PCM that we used as our a priori atmosphere. For a subset of observations distributed through different latitudes and seasons, we performed inversions introducing known biases in the a priori. First, we retrieved water vapor profiles using the temperature from the Mars-PCM after adding an offset of ±5 K at every altitude. As shown in Fig. 4.15, the error introduced by these changes in the temperature were negligible, below about 2%. The second test was to modify the pressure profile. For this case we introduced a wave function with a 10% amplitude to the Mars-PCM, $P'(z) = P(z)(1 + 0.1\sin(4\pi z))$. The result showed that this oscillation propagated onto the volume mixing ratio (VMR) profile. This

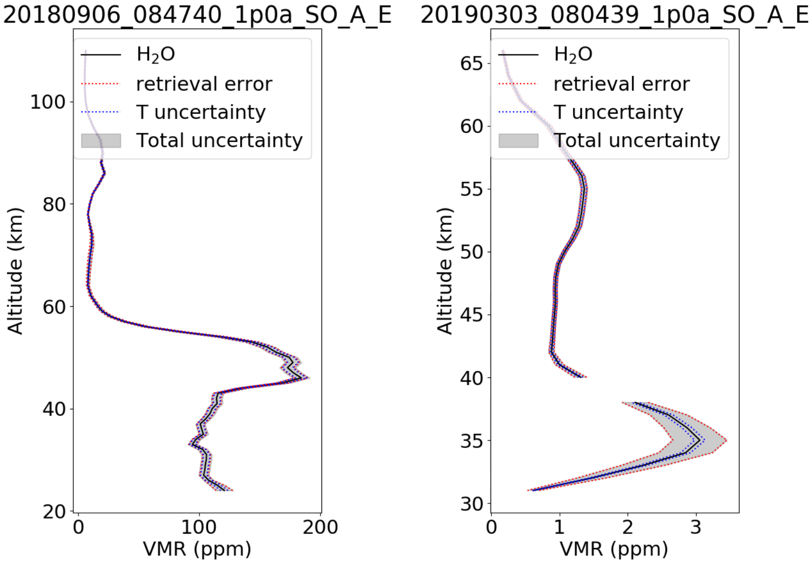

FIGURE 4.15: Temperature sensitivity tests

was expected, as the VMR is inversely proportional to the total atmospheric density. However, the impact on the true retrieved product, i.e. the water vapor number density, was again negligible, with overall differences below 2% as shown in Fig. 4.16. These tests proved to be a key aspect for our retrieval scheme, giving us a very valuable estimation of the error introduced by one of our strongest assumptions, and providing us with a greater confidence in our results.

Broadening coefficients test

The HITRAN line parameters are provided for the Earth's atmosphere, i.e., a N_2-rich atmosphere, and the broadening coefficients may differ in a CO_2-rich atmosphere, such as the one on Mars. However, due to its low pressure and temperature, this coefficient is not particularly relevant when simulating transmittances through the Martian atmosphere. In Figure 4.17 we compare the air-broadening coefficient (γ_{air} in equation 3.24) provided by Gordon et al., 2022 with the coefficient calculated for a CO_2-rich atmosphere provided by Gamache et al., 2016. For the Martian typical temperature range (150-300 K), the difference between the coefficients from both lists for the strongest absorption lines in orders 134, 136, 168 and 169 was below 10%, slightly varying from order to order. In order to test the impact of this difference on the actual transmittance, we performed KOPRA simulations for those orders with both linelists. In Figure 4.18 we show the comparison of the simulations computed with the HITRAN default line parameters (dashed orange) with that computed using the line list provided by Gamache et al., 2016. The simulations were computed at the most common sounding altitudes of each order where their absorption lines were in optically thin conditions (see Section 4.4.1). As it can be seen in the Figure, the difference between both simulations are negligible and, in most cases, almost one

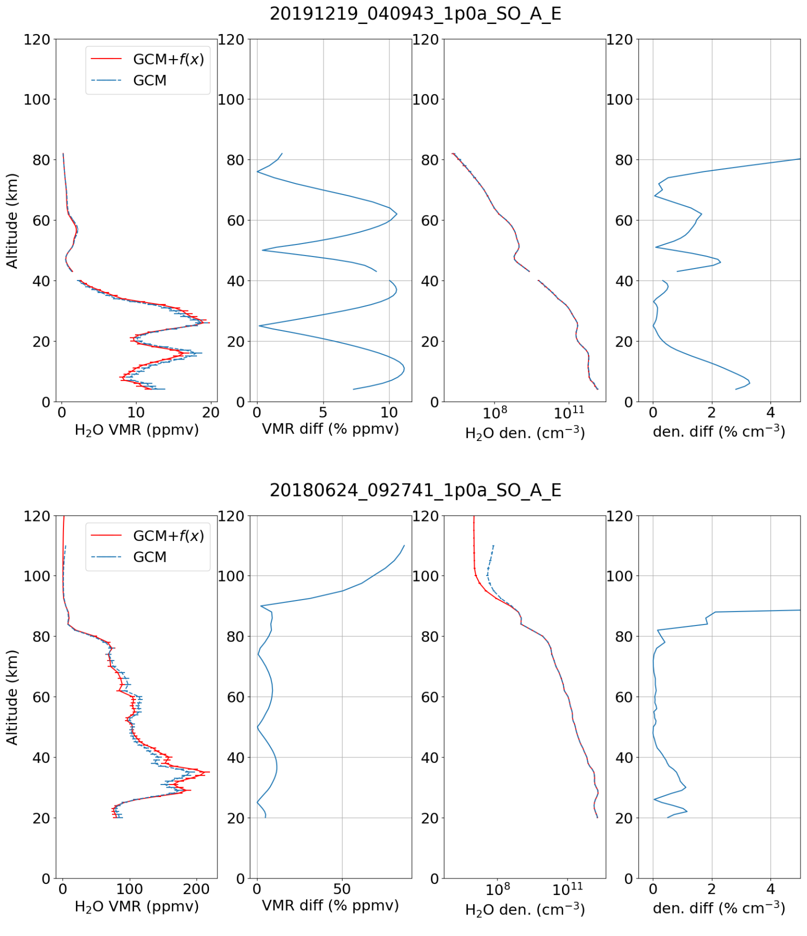

FIGURE 4.16: Pressure sensitivity tests.

order of magnitude below the typical NOMAD SO measurement noise (represented with gray dashed lines in Figure 4.18).

AOTF sensitivity test

Another crucial test for the error analysis and the characterization of the instrumental uncertainties was to quantify the impact of our uncertainty on the AOTF parameters. As shown in Figure 2.6, the AOTF recipe from Villanueva et al., 2022a provides what the NOMAD consortium considers is the optimal value for each parameter at different diffraction orders. However, due to the complexity of the method used and the difficulties to characterize these parameters, the dispersion of the different measurements was not small. During our sensitivity tests we decided to perform a set of retrievals varying each parameter separately within a range equivalent to the standard deviation of the set of measurements (gray dashed line in Figure 2.6). In this work we selected a few solar occultations and examined the four major AOTF parameters. We performed a total of 9 retrievals per occultaion as following: one retrieval using the default parameters and two inversions for each parameter (± its standard deviation). The effects on the retrieved water vapor VMR are presented

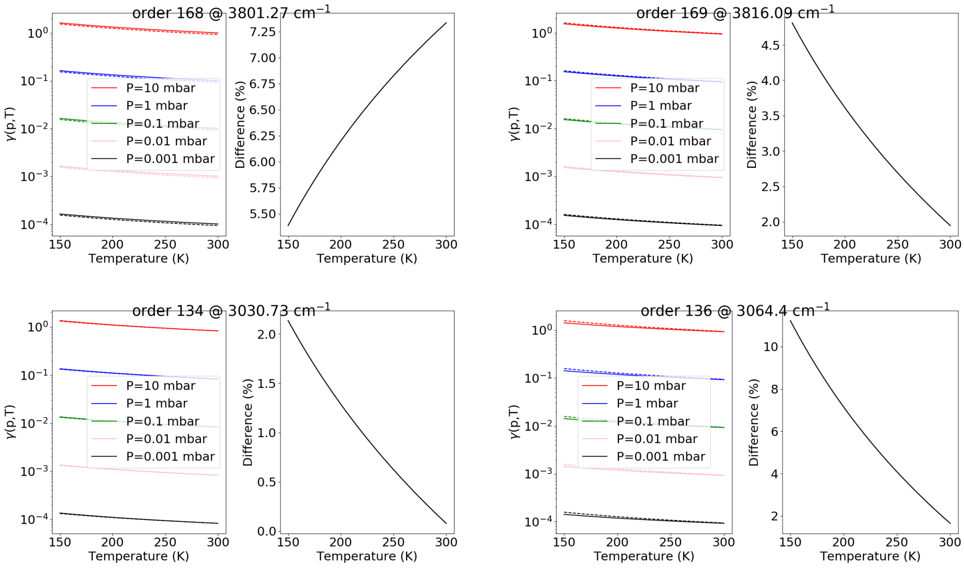

FIGURE 4.17: Comparison of the air-broadening coefficient γ_{air} from the HITRAN default line list (dashed line) and from Gamache et al., 2016 (solid line) for the strongest absorption line at the four main NOMAD SO diffraction orders used in this Thesis. Two panels are used for each absorption line: (i) left panel shows the variation of γ_{air} within a typical Martian temperature range for a wide range of pressures, and (ii) right panel shows the relative difference between both line lists (the relative difference is the same for all pressures).

in Figure 4.19 for two solar occultations, with different colors for each parameter. Applying this test to a subset of 10 solar occultations, we observed that the parameter whose uncertainty was the largest was the Gaussian offset. We can define a total AOTF uncertainty ϵ_{AOTF} by combining individual parameters' uncertainties as follows:

$$\epsilon_{\text{AOTF}} = \sqrt{\epsilon_w^2 + \epsilon_S^2 + \epsilon_A^2 + \epsilon_{I_G}^2} \tag{4.7}$$

where ϵ_w, ϵ_S, ϵ_A and ϵ_{I_G} are the uncertainties of the AOTF widht, sidelobe ratio, asymmetry factor and Gaussian offset intensity respectively. We obtained from this study that ϵ_{AOTF}~10% of the water vapor VMR obtained.

Total error budget

These tests revealed that the most important uncertainties in the retrieved water vapor profiles are due to the measuement noise and the to the AOTF, both comparable in magnitude ranging between 5% to 10%, although the latter resulted to more relevant at low altitudes, below 60 km. All these uncertainty estimations have to be taken into account when analyzing our water vapor vertical profiles, and comparisons between other data sets and results presented in Chapters 5, 6 and 7 have to be done carefully.

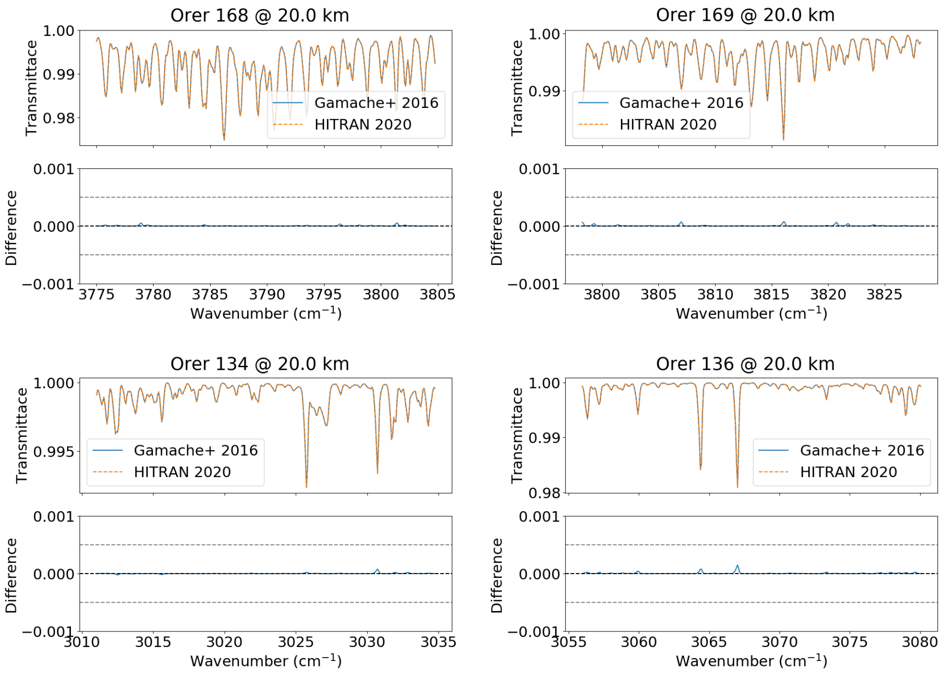

FIGURE 4.18: Comparison of KOPRA simulations using HITRAN default line parameters with KOPRA simulations using line parameters from Gamache et al., 2016.

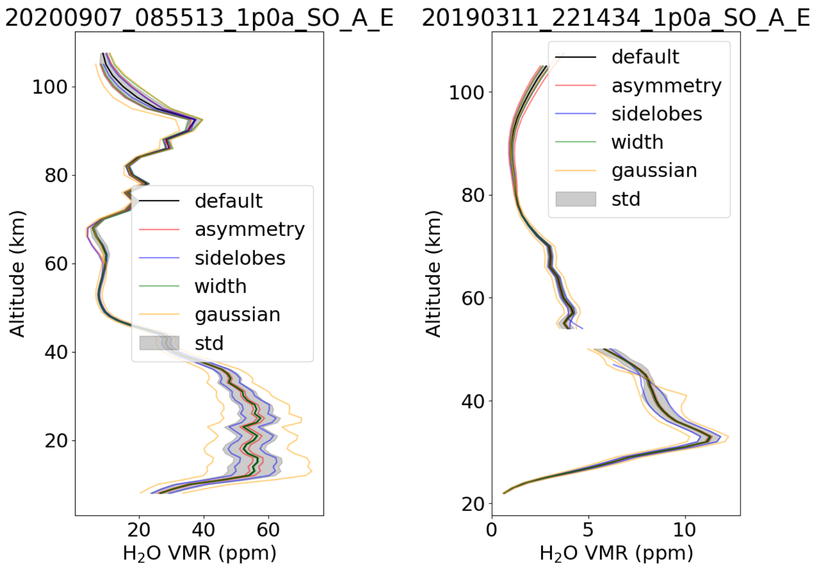

FIGURE 4.19: AOTF sensitivity tests.

4.4 Combination of diffraction orders

The intensity of the water vapor absorption lines have a strong variation through different diffraction orders. The NOMAD SO spectral range covers the region between 2300 to 4500 cm^{-1} with the strongest water vapor absorption lines located between 3500 to 4000 cm^{-1}. This region sampled with the NOMAD diffraction orders 155-180 corresponds to the ν_1 and ν_3 fundamental bands due to the O-H stretching vibrations (see Section 3.3). Those lines have intensities about 10^{-19} $\mathrm{cm^{-1}/(molecule \cdot cm^{-2})}$ (Gordon et al., 2022). Outside this spectral region, the strength of the lines fall to $\sim 10^{-21}$ $\mathrm{cm^{-1}/(molecule \cdot cm^{-2})}$. The stronger the intensity of the lines, the lower the number of absorbers required to obtain a given absorption, for example, to produce a spectral feature larger than the noise level. Therefore, strong lines can be used to sound at high tangent altitudes. This is a well known criterion in remote sounding, but caution is needed when using strong lines, which may produce a total optical depth along the line of sight larger than one. When this happens, the lines saturate, reducing the information that can be obtained from the whole slant path. This is, in optically thick conditions, the incoming light from the Sun is totally absorbed by the water vapor molecules before reaching the observer. This condition occurs in diffraction orders between 155 and 180, where some lines saturate at relatively low altitudes, as the atmosphere is denser.

The effect of saturation in absorption lines introduces uncertainties and instability in the retrievals. In order to minimize this issue, we developed a strategy to perform retrievals of the orders which have been measured only at optically thin regions, i.e., where water vapor lines are not saturated. Our strategy is to differentiate between diffraction orders at high tangent altitudes (with strong lines) and at low tangent altitudes (with weak lines). Taking advantage of the feature that allows NOMAD SO to sample the atmosphere with different orders simultaneously, it is possible to build homogeneous vertical profiles using different orders at different altitude ranges. Examples of high tangent altitude orders are 168 ad 169, whereas orders of low tangent altitudes are 134 and 136. Then, it is required to identify the appropriate transition altitude between the low and high altitude orders. To compute this altitude, we followed different approaches:

Merging retrievals. Our first approach was to set a fix transition altitude. After inspecting dozens of water vapor retrievals and sensitivity tests, we concluded that the optimal transition altitude between the low-altitude and the high-altitude orders had to be around 60 km. Then, we performed independent retrievals, first for the low-altitude and then for the high-altitude orders. The inversions of the firsts were done for the full altitude range, whereas for the second, the retrievals were done limiting the lowermost altitude during inversion to 60 km. This is because 60 km the saturation effect is so large that the results diverge and are of no use. In addition, the retrieved profiles obtained during the first inversion were used as a priori for the high-altitude order retrieval. This way, constraining the second inversion below 60 km, we obtained vertical profiles for the full altitude range merging the results from both altitude ranges. This simple approach proved to be successful, and allowed us to obtain the first NOMAD water vapor vertical profiles using the IAA-PP pipeline for the southern summer season of Martian Years (MY) 34 and 35 (Brines et al., 2023e), which are presented in Chapter 5. However, performing independent retrievals at different altitude ranges may introduce some biases and uncertainties that we decided to avoid a different and better approach.

Combining orders. Lately, instead of merging results from independent retrievals/diffraction orders, we improved our strategy by combining spectra from different diffraction orders and performing a single inversion,i.e., handling data from the two orders at once, simultaneously. We adapted our retrieval pipeline to use spectra from two diffraction orders at different altitude ranges during the global fit. With this technique, the retrieval processor RCP performs and elegant mathematical combination (global inversion) of the information content in both diffraction orders, and the error analysis is also more consistent,removing some of the ad-hoc assumptons in the transition altitude. However, a criterion to determine the transition altitude was still required, as discussed in the following section.

4.4.1 Saturation of absorption lines

On Mars, the atmospheric density shows strong latitudinal and seasonal variations Montmessin et al., 2017. For this reason, trying to fix a single, constant transition altitude for all the solar occultations is not optimal. When observing the atmosphere at high latitudes close to the polar regions, or during the winter season where the atmospheric density is lower, the expected saturation altitude for the orders within the ν_1-ν_3 bands should be lower than when observing the equatorial regions or during the summer season. Thus, we decided to use a dynamic saturation altitude of those orders, in other words, we need to determine a different transition for each solar occultation.

Method 1

The initial method we followed, was to focus on the strongest absorption lines within the orders and to study their transmittance profile at the core and the wings of the line. For every scan and for a selected set of absorption lines, we computed the ratio R_λ,

$$R_\lambda = \frac{\Delta\mathcal{T}(z)}{1-\mathcal{T}_\lambda(z)} \tag{4.8}$$

where $\Delta\mathcal{T}(z)$ is the difference between the measured transmittance at the core of the line ($\mathcal{T}_\lambda$) and the observed transmittance at the wings of the line. This allowed us to identify where the shape of the line starts to be distorted by saturation, this is, to identify the optically thick region, providing an estimate of the transition altitude to the optically thin regime.

We applied this combination method to a subset of observations during the perihelion season of MYs 34, 35 and 36, which are presented in Chapter 6. The precise spectral point at the line's wings were given by a $\Delta\lambda$ that we fixed after

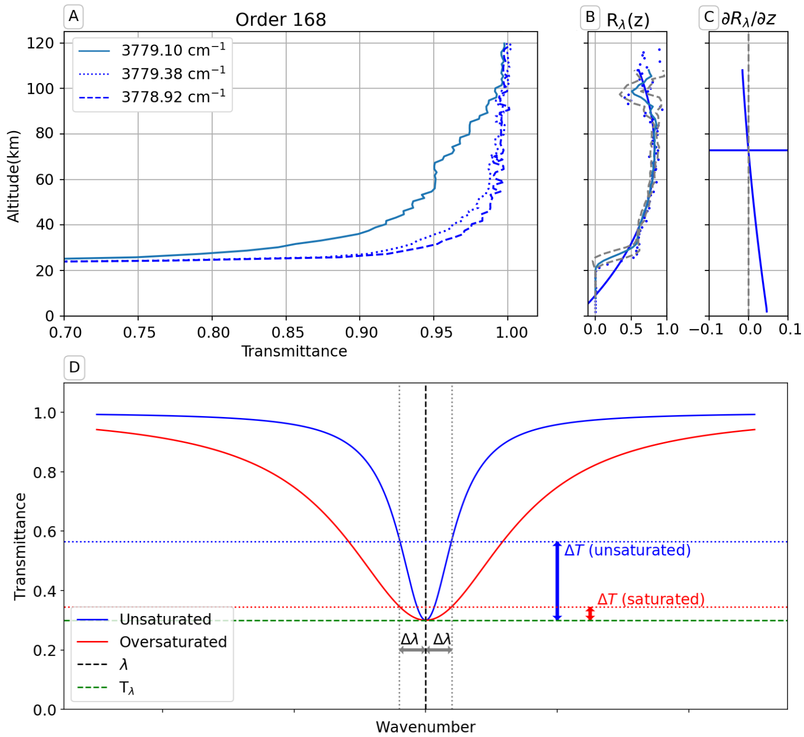

FIGURE 4.20: Study of the saturation of absorption lines and example of H_2O vertical retrieved profile. Panel A shows the transmittance vertical profile at the core of the absorption line centered at 3779.1 cm^{-1} (solid line) and at its wings (dotted and dashed lines) in the NOMAD diffraction order 168. Panels B and C show the ratio R_λ and its derivative respectively. The horizontal line in panel C shows the estimated transition altitude z^0_λ. Panel D shows the schematic of the methodology used to estimate the saturation of the absorption lines. Two curves are shown simulating unsaturated (blue) and saturated (red) absorption lines. The limit of the wings of the line is determined by $\Delta\lambda$.

some experimentation. It was set to ~0.2 cm^{-1} in order to take into account the typical width of the NOMAD double Gaussian ILS. With this method, we were able to characterize two altitude regimes (high and low altitude) separated by a "transition altitude".

- High altitude (optically thin): Transmittance at the wings is close to $\mathcal{T}_\lambda$ due to the low line depth and the measurement noise hiding the absorption line. Hence, $\Delta\mathcal{T}$~0 and R_λ~0. Typically, this analysis was done below 90-100 km, region where the core of the lines are clearly observed in the measured transmittance.
- Transition altitude: Transmittance at the wings is close to the continuum τ (ideally $\tau = 1$). Therefore $\Delta\mathcal{T} \sim \tau - \mathcal{T}_\lambda$ and R_λ gets to its maximum.
- Low altitude (optically thick): Transmittance at the wings is close to $\mathcal{T}_\lambda$ due to the apparent line broadening caused by the saturation. Then $\Delta\mathcal{T}$~0 and R_λ~0.

The application of this method to an absorption line at $\lambda = 3779.1$ cm^{-1} and the schematic definition of R_λ are presented in Figure 4.20 in panels A to C and D respectively. We applied this analysis to four absorption lines of similar line strength across the orders 168 (located around 3779 cm^{-1}, 3784 cm^{-1}, 3796 cm^{-1} 3801 cm^{-1}) and 169 (located around 3800 cm^{-1}, 3807 cm^{-1}, 3816 cm^{-1}, 3819 cm^{-1}) looking for the altitude z^0_λ where $(\partial R_\lambda/\partial)z \mid_{z^0_\lambda} = 0$. Then we averaged the four z^0_λ obtained, characterizing a transition altitude z^0 for each solar occultation. Hence, during the inversion of each specific occultation, we used spectra from orders 168 or 169 above z^0 and spectra from orders 134 or 136 below that altitude. We also defined a "transition range" around z^0 where spectra from both orders were used. To accommodate for the uncertainties during the characterization of the transition altitude and in order to guarantee a smooth transition from the low to the high altitude orders, we estimated a transition range of ±5 km. This approach allowed us to obtain water vapor vertical profiles from ∼10 km up to ∼120 km.

Method 2

Although this method represented a substantial improvement respect to Brines et al., 2023e, more recently we introduced a second improvement to the strategy mentioned above for computing the transition altitude. The ratio described in equation 4.8 was useful only when the absorption lines were strong and the water vapor lines did not show contamination from other species (like CO_2). If that was not the case, R_λ could be poorly constrained, introducing biases and variations/oscillations to the transition altitude with unexpected changes from scan to scan. In order to address this issue we examined a set of specific KOPRA simulations computed with only water vapor lines, avoiding any possible contamination from CO_2 or other species. Then, we analyzed the equivalent width W_λ of the strongest lines in the spectral region between 3770-3830 cm^{-1} (ν_3 band) as a function of the slant column density (column density along the line of sight), i.e. the curve of growth. We defined W_λ as

$$W_\lambda = \int_0^\infty \frac{\mathcal{T}_{\lambda,0} - \mathcal{T}_\lambda}{\mathcal{T}_{\lambda,0}} d\lambda \tag{4.9}$$

where $\mathcal{T}_{\lambda,0}$ is the transmittance of the line at the core and $\mathcal{T}_\lambda$ is the transmittance within the integration range. The curve of growth shows the relation of W_λ with the number of absorbents. For optically thin conditions, W_λ increases linearly with the density. When the gas becomes optically thick, the relation is no longer linear but logarithmic and eventually, the collisional broadening extends the wings of the line introducing a well known root square relationship. The top panel in Figure 4.21 shows the curve of growth of two absorption lines at 3801 and 3816 cm^{-1}. In our simulations we estimated that the optically thin regime (black dashed line) stopped for water vapor column densities, i.e., number densities integrated along the line of sight, larger than $\sim 2 \cdot 10^{16}$ cm^{-2}, equivalent to a water vapor partial pressure of about $\sim 9 \cdot 10^{-9}$ mbar at the tangent point, as shown in the bottom panel of Figure 4.21.

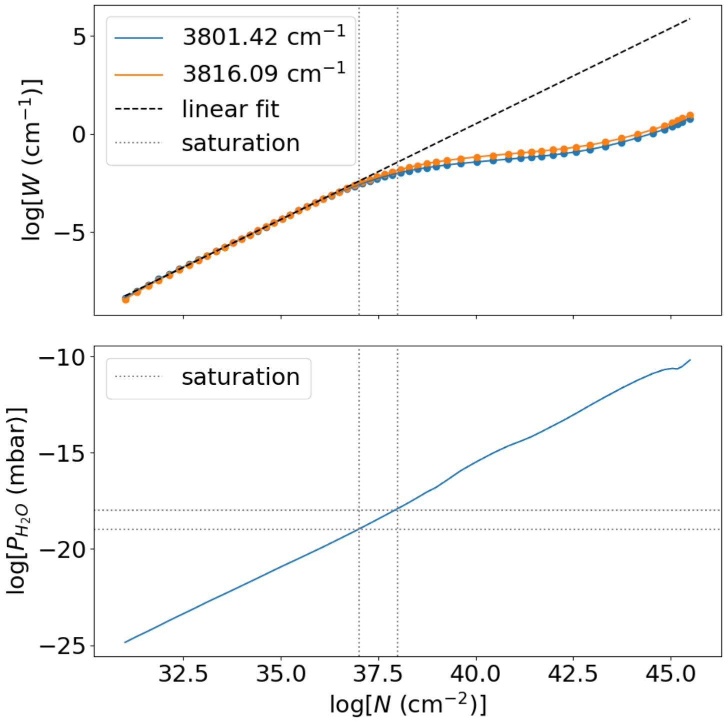

FIGURE 4.21: Top panel: Curve of growth of the strongest absorption lines simulated with KOPRA within the orders 168 and 169. Dashed black lines shows the linear fit of the region of number density between 30-37 cm^{-2}. Bottom panel: Relation between H_2O number density and H_2O partial pressure used during the simulation.

During the IAA-PP, the parameter k (from equation 4.4) used to fit the KOPRA simulations to the measured transmittances allowed us to compute a rough estimation of the expected density and water vapor VMR for each solar occultation. With that estimation and the reference atmosphere from the Mars-PCM, we were able to establish a relationship between water vapor partial pressure and tangent height, which allowed us to identify the altitude where the strongest lines within the ν_3 band (within 3770-3830 cm^{-1}) became optically thick for each observation. This method was applied during the processing and inversion of all the data presented in Chapter 7.

4.5 Clustering of NOMAD SO vertical profiles

The clustering technique, often referred to as cluster analysis, examines a collection of objects, each characterized by a range of variables. The primary objective of this method is to identify groups of objects, or "clusters," that exhibit high internal similarity while being distinct from objects in other clusters. Taking into account the inherent properties of the data, clusters emerge naturally without the need for predefined categories or prior knowledge about their properties. Building upon previous studies on the clustering of vertical temperature profiles of the Martian atmosphere (Cala Hurtado, 2016; Jiménez Monferrer, 2019; Marzo et al., 2008), we implemented a novel routine in the NOMAD SO IAA processing pipeline in order to identify representative structures on retrieved NOMAD water vapor profiles, grouping these into distinct groups. The clusters identified through this technique were crucial for several reasons. Firstly, they enabled the detection of patterns and relationships that might not be apparent through traditional physical, geographical analysis methods. By grouping similar objects, it was possible to identify common characteristics and behaviors, leading to a deeper understanding of specific climatological patterns and seasonal and latitudinal variability. Additionally, the detection of anomalies or bias might indicate the presence of unique or previously unobserved phenomena, prompting further investigation, or biases, which may require revision of pre-porcessing or retrieval methods.

There are several well known methods developed to perform cluster analysis effectively, each with its strengths and weaknesses. In all of them, the goal is to compute the distance between data points, but the way those distances are computed and interpreted might vary. It is possible to identify four main types of clustering algorithms:

- Density-based. These algorithms identify clusters as the areas of higher density of data points than the surroundings. One of the most commonly used algorithms of this type is DBSCAN (Density-Based Spatial Clustering of Applications with Noise), which is capable of finding arbitrarily shaped clusters handling noise.
- Distribution-based. These methods assume data is generated from a mixture of several distribution models, typically Gaussian distributions. These kind of algorithms produce detailed models for clusters, effectively capturing attribute correlations and dependencies. However, the required knowledge about the distribution of the data set may impose some limitations to data sets that cannot be modeled with Gaussian distributions. As a result, some density-based clusters might not be modeled using distribution-based algorithms.
- Hierarchical-based. These algorithms form clusters by connecting data points based on their proximity, meaning that data points are more closely related to nearby points rather than distant ones. These algorithms do not yield a single partitioning of the data set. Instead, they produce an extensive hierarchy of clusters that merge at specific distances.
- Centroid-based. In this technique, each cluster is defined by a representative centroid. Then, the algorithm assigns each data point to a cluster minimizing the squared distance from the point to the centroid of the cluster. The K-means algorithm is one of the most widely used centroid-based clustering methods in

data analysis. Its simplicity and computational efficiency make this technique suitable for its application to a large data sets such as the NOMAD water vapor vertical profiles data set.

Despite its widespread use, cluster analysis comes with challenges. Choosing a clustering algorithm may introduce bias into the results, as different algorithms may produce varying clusters from the same data set. In addition, many algorithms require setting parameters (e.g., the number of clusters in K-means) which do significantly impact the results and its interpretation. Not many studies of this kind have been made for the Martian atmosphere and in the case of water vapor, there are no previous references to follow. As presented in Cala Hurtado, 2016, the K-means centroid-based algorithm proved to be extremely useful to provide a simplified cluster-based temperature climatology on Mars, therefore we followed a similar path for the clustering of the NOMAD SO data.

4.5.1 Basics of the K-means method

The K-means algorithm (Arthur et al., 2007; Forgy, 1965) is a versatile and widely-used tool in cluster analysis, valued for its simplicity and efficiency, despite some limitations. This algorithm performs clustering by identifying the most representative elements of the final clusters, known as the centroids of the corresponding clusters. It begins by selecting an initial set of centroids, which can be chosen randomly or based on some prior knowledge. Each data point is then assigned to the nearest centroid, forming the initial clusters. Then, the algorithm recalculates the centroids as the mean of all points assigned to each cluster and iteratively performs a new assignation of the data points based on the new cluster's centroids. Formally speaking, the K-means algorithm is designed to select centroids that minimize the variance within clusters and maximizes the distance between them. For a number of objects N (vertical profiles) and a set of K cluster, and following Arthur et al., 2007, we define the objective function

$$J = \sum_{i}^{N} \sum_{j}^{K} \omega_{ij} \parallel x_i - \mu_j \parallel^2 \tag{4.10}$$

where μ_j is the centroid of the cluster j and $\omega_{ij} = 1$ or $\omega_{ij} = 0$ if the data point x_i does belong or not to the cluster j. The minimization of J is done in two steps. First, the data points are assigned to the closest randomly selected initial clusters, this is, fixing μ_j and choosing ω_{ij} as

$$\omega_{ij} = \begin{cases} 1 & \text{if } j = \operatorname{argmin}_l \parallel x_i - \mu_l \parallel^2 \\ 0 & \text{otherwise} \end{cases} \tag{4.11}$$

Then, the second step minimizes J for each μ_j, fixing the optimal ω_{ij} previously found,

$$\frac{\partial J}{\partial \mu_j} = \sum_{i}^{N} \sum_{j'}^{K} \omega_{ij'} \frac{\partial}{\partial \mu_j} (x_i - \mu_{j'})^T (x_i - \mu_{j'}) = \sum_{i}^{N} \omega_{ij} (-2x_i + 2\mu_j) = 0 \tag{4.12}$$

which provides a redefinition of the centroids with the new data assignment as

$$\mu_j = \frac{\sum_i^N \omega_{ij} x_i}{\sum_i^N \omega_{ij}} \tag{4.13}$$

This process of assignment and recalculation continues until the centroids no longer change significantly, indicating that the algorithm has converged to a stable set of clusters. The final centroids represent the most central points within each cluster, effectively capturing the essence of the grouped data points. One of the disadvantages of this method is that the number of clusters K must be specified in advance, which can be challenging to determine. Our final goal was to identify clusters with profiles representative of different seasons and latitudes. Once the clustering was done and based on our current knowledge of the Martian climatology, we estimated an optimal number of about 5-10 water vapor profile clusters. In order to estimate the validity of this clustering and complementary to the visual inspection, we used several quality metrics. We needed enough clusters to be able to describe seasonal/latitudinal variability, but not so many that outliers were introduced making the analysis more difficult.

4.5.2 Quality metrics

Silhouette coefficient

The Silhouette coefficient is a validation technique which provides information about how well each object has been classified in its group (Rousseeuw, 1987), this is, the intra-cluster cohesion is compared with the inter-cluster separation. Typically, this value is normalized so it ranges from -1 to 1, where a higher Silhouette Coefficient score relates to better defined clusters. The Silhouette for the cluster C_j can be defined as

$$s_j = \frac{b - a}{\max(a, b)} \tag{4.14}$$

where a is the mean distance between each data point of C_j and all the other points within C_j, and b is the mean distance between each data point of C_j and all other points in the nearest cluster.

Calinski-Harabasz index

Similarly to the silhouette method, the Calinski-Harabasz index compares the between-cluster separation with the within-cluster dispersion (Caliński & Harabasz, 1974). For a date set of N elements grouped into K clusters, we can define the within-cluster dispersion matrix W_K and the between-cluster dispersion matrix B_K as

$$W_K = \sum_{j}^{K} \sum_{x \in C_j} \| x - \mu_j \|^2 \tag{4.15}$$

$$B_K = \sum_{j}^{K} n_j \| \mu_k - \mu_N \|^2 \tag{4.16}$$

where μ_j is the centroid of cluster C_j, n_j is the number of points within cluster C_j and μ_N is the centroid of the data set. Then, we define the Calinski-Harabasz index as

$$CH = \frac{\mathrm{tr}(B_K)}{\mathrm{tr}(E_K)} \frac{N-K}{K-1} \tag{4.17}$$

The first term with the traces of W_K and B_K indicates the ratio between the separation and the cohesiveness of the clusters, whereas the second term containing the degrees of freedom of W_K (numerator) and B_K (denominator) normalizes the values, ensuring that they are comparable across varying numbers of clusters. The best clustering is achieved for the higher values of CH.

Davies–Bouldin index

This index is based on the evaluation of the similarity of clusters assuming a probability distribution, this is, the number of elements within each cluster reduces as the distance to the cluster centroid increases (Davies & Bouldin, 1979). Hence, we define cluster similarity as

$$R_{ij} = \frac{s_i + s_j}{d_{ij}} \tag{4.18}$$

where s_i is the average distance between the each element of the cluster C_i and its centroid μ_i, and d_{ij} is the distance between the centroids of clusters C_i and C_j. With this, the Davies-Bouldin index for a number of K clusters can be defined as

$$DB = \frac{1}{K} \sum_{i}^{K} \max(R_{ij}) \tag{4.19}$$

For this index, the lower DB is, the larger the separation between-cluster and the compactness within-cluster.

One of the main drawbacks of the K-means algorithm is that the first best cluster assignation requires predefined cluster's centroids. As discussed above, we used random centroids, i.e. random vertical profiles, for the fist iteration. In order to evaluate the impact of this assumption and to quantify the uncertainty in the final clustered data associated to the random initialization, we performed the data clustering 10 times for a set of clusters n_K with K clusters ranging from 2 to 20.

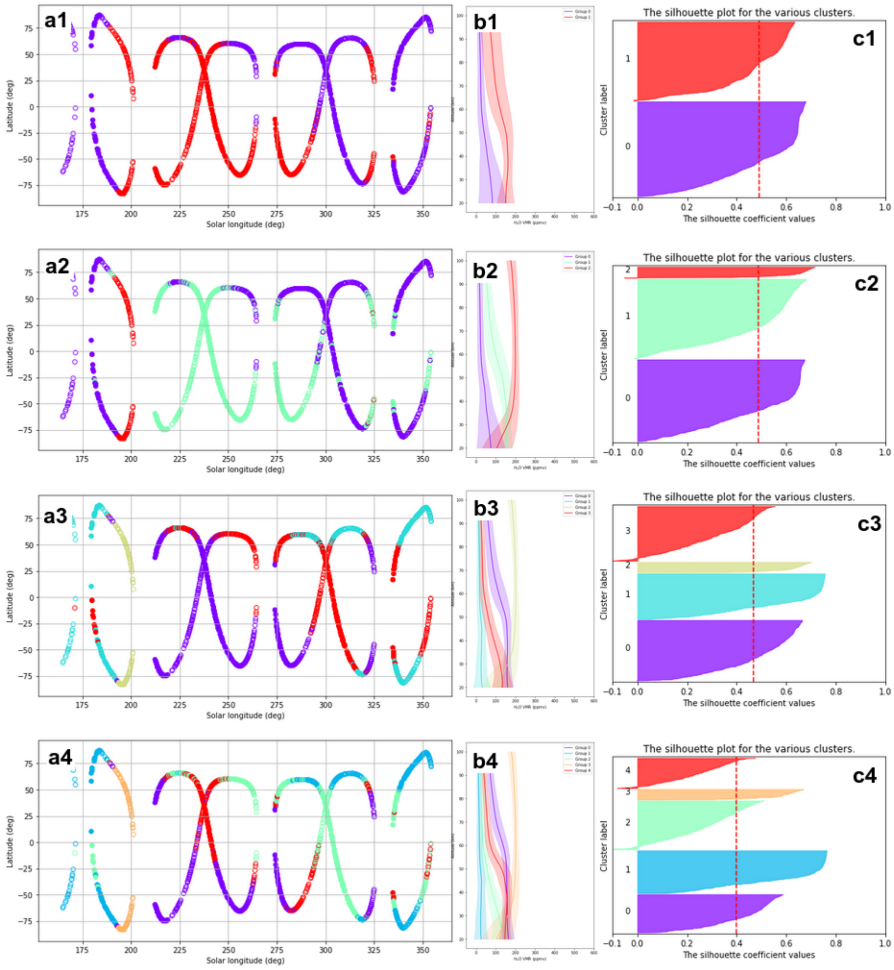

FIGURE 4.22: Clustering of Mars-PCM water vapor vertical profiles during MY 34. A total of 1500 profiles are grouped into 2, 3, 4 and 5 clusters

With the intention of reducing the computation time and the complexity of this sensitivity analysis, we applied this method to each MY separately. We did the clustering for both the retrieved water vapor profiles and the Mars-PCM climatology obtained for each solar occultation. Then, by the examination of the quality metrics we were able to evaluate the dependency of the results to the initialization, allowing us to decide the optimal number of clusters to use. In Figures 4.22 4.23, we show the data clustering obtained when using sets of clusters ranging from 2 to 9 for the Mars-PCM and in Figures 4.24, 4.25 the same but for NOMAD data sets, both during MY 34. In these Figures, panels from a1 to a8 (left) indicate the latitude and solar longitude of the observations, with the clusters represented by colors. Panels b1 to b8 show the representative profile of each cluster (centroids) and panels c1 to c9 present the silhouette analysis. These Figures (also done for MYs 35 and 36) allowed us to estimate that the number of cluster required to characterize the most relevant climatological features on Mars had to be at least larger than 4. Using fewer clusters did not allow for a complete description of the water vapor variability, as it

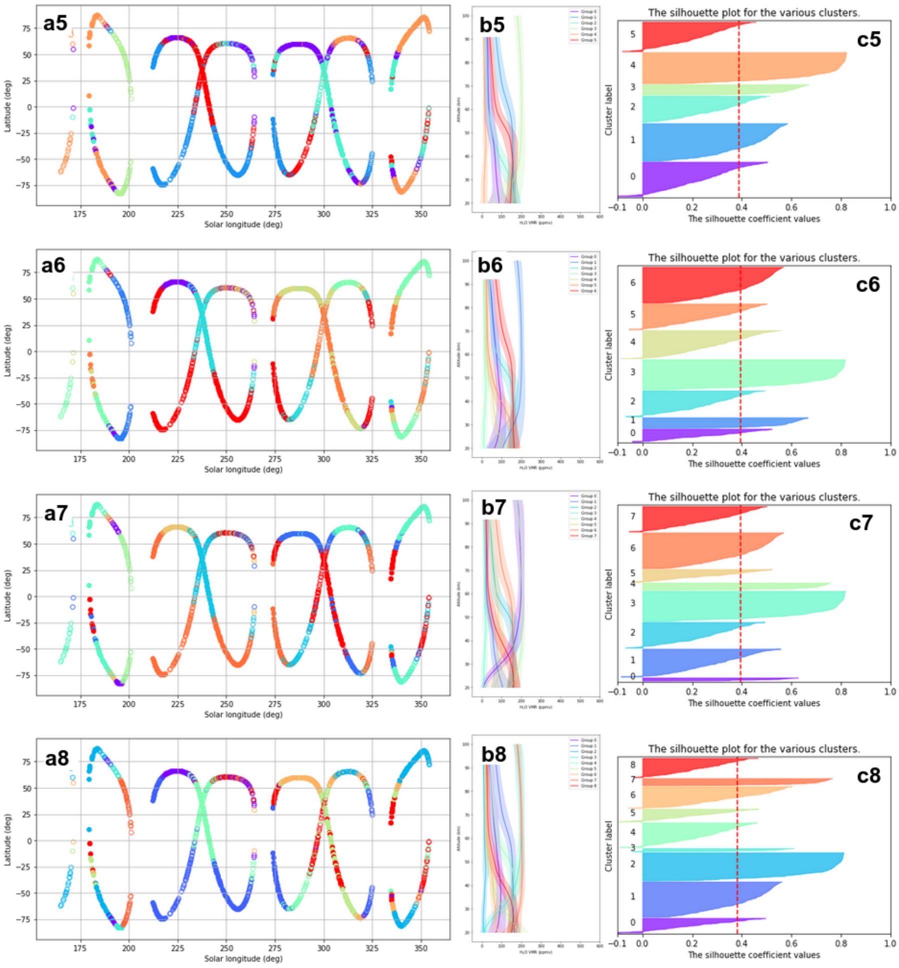

FIGURE 4.23: Same as 4.22 but for 6, 7, 8 and 9 clusters.

is understood nowadays by physical methods and models.

In Figure 4.26 we show the quality metrics obtained during 10 runs of the K-means algorithm for the MY 34 for the Mars-PCM (left column) and NOMAD (right column) datasets. The Silhouette Coefficient, Calinski-Harabasz Index and Davies–Bouldin Index against the number of groups used during the clustering are presented in top, middle and bottom panels respectively. These metrics were useful to facilitate the selection of the best number of clusters within a small set of options. This is, when using a large number of clusters such as those used in Figure 4.26, instead of looking for absolute critical points, one has to look for local maxima (local minima in the case of Davies–Bouldin Index) in order to identify the optimal clustering configuration. As shown in Figure 4.26, omitting those metrics for low number of groups (<4 based on the analysis done with Figures 4.22,4.23 and Figures 4.24,4.24), the optimal cluster configuration might be between 5-10 clusters. This number of clusters show similar metrics during the 10 runs of the K-means algorithm. However, for number of clusters larger than 10 we observed that the metrics oscillate when changing the initial cluster assignation. Although the final clusters were basically identical, some profiles ended

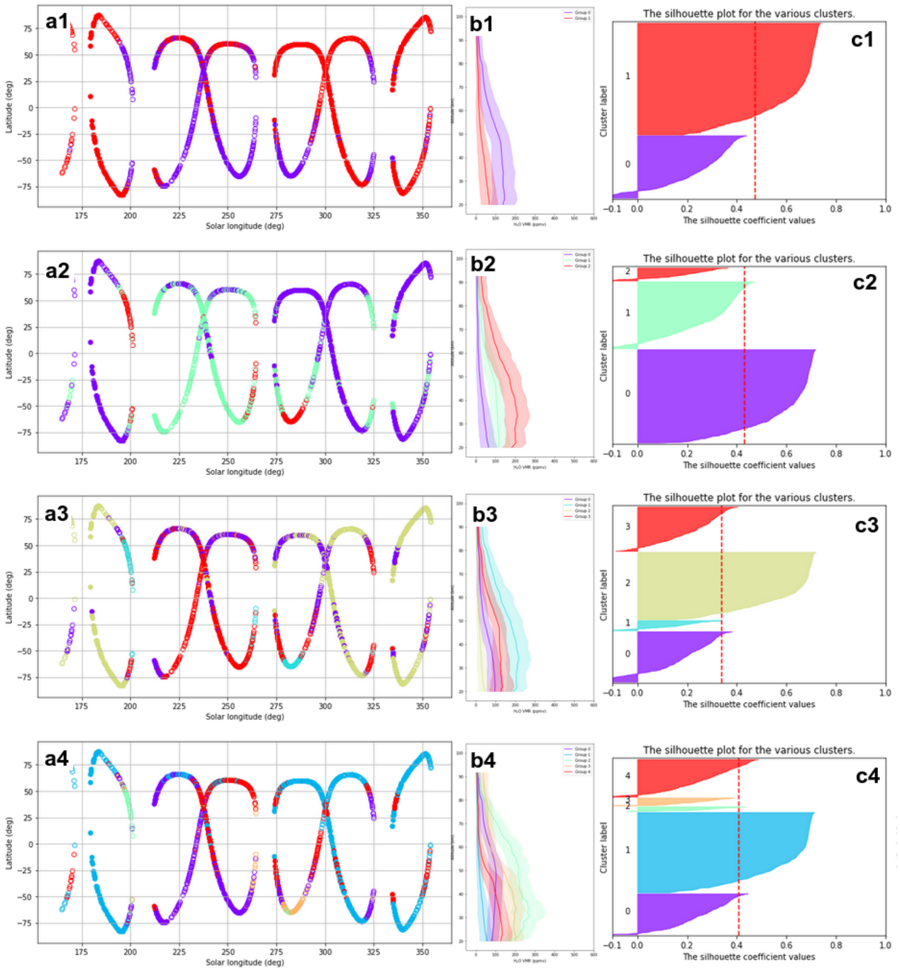

FIGURE 4.24: Clustering of NOMAD SO water vapor vertical profiles during MY 34. A total of 1500 profiles are grouped into 2, 3, 4 and 5 clusters

up being grouped in different clusters each time the algorithm was lunched, causing the observed dispersion in the metrics. Hence, in order to avoid initialization effects, we decided to use no more than 10 clusters during the analysis. The application of this method to the NOMAD data and its detailed analysis are presented in Chapter 7.7. However, the present analysis is extremely useful for internal consistency and validation purposes, as it already shows that no clusters with random location/times around the planet are observed, which might indicate anomalies or non-physically meaningful profiles. All clusters of NOMAD-SO data show latitude-L_S distributions similar to those observed in the Mars-PCM.

4.6 Summary

Starting at the Belgian Institute for Space Aeronomy (BIRA-ISAB), the NOMAD measurements go through numerous calibration processes, during which the data is geolocated, spectrally calibrated and finally converted into transmittances. Despite

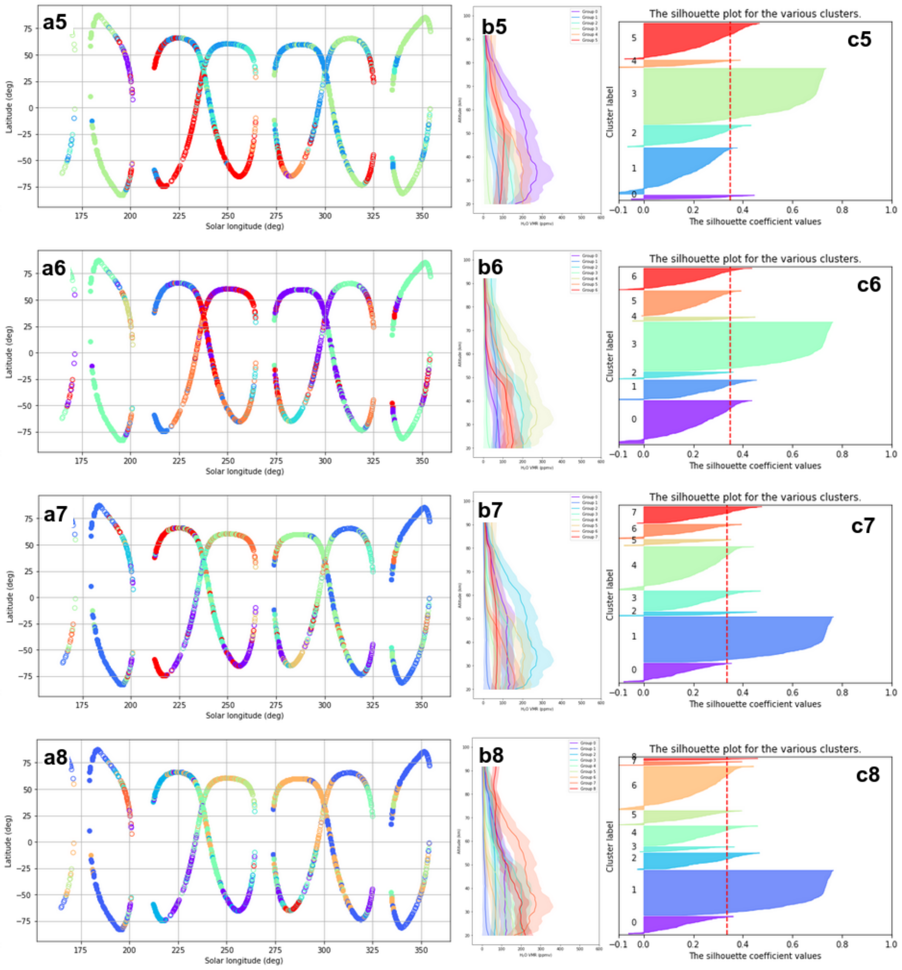

FIGURE 4.25: Same as 4.24 but for 6, 7, 8 and 9 clusters.

the efforts made at BIRA-ISAB, those calibrated transmittances still require further processing prior to their scientific analysis. From the first analysis of NOMAD SO data, and in common with other NOMAD teams, we identified two major systematics present in the spectra: (i) a bending in the continuum of the spectra, and (ii) a spectral shift moving the absorption lines from their theoretical frequency. Due to the complexity of the data, at the Instituto de Astrofísica de Andalucía we have developed specific tools designed to identify and eliminate those systematics present in the measurements. The IAA Pre-Processing (IAA-PP) uses the line-by-line Karlsruhe Optimized and Precise Radiative transfer Algorithm (KOPRA) to remove the bending using a fourth order polynomial at every tangent height followed by a precise running mean estimation of the spectral baseline at the top of the atmosphere. At the same time, the spectral shift is corrected, also utilizing KOPRA simulated transmittances. In addition to the cleaning of the data, our pipeline included a characterization of the random measurement noise computed with covariance matrices which allowed us to increase the sensitivity of the retrieval at high altitudes. Before the inversion of the vertical profiles we performed several test in order to verify the reliability of our pipeline. Those test included the generation of NOMAD-like synthetic spectra

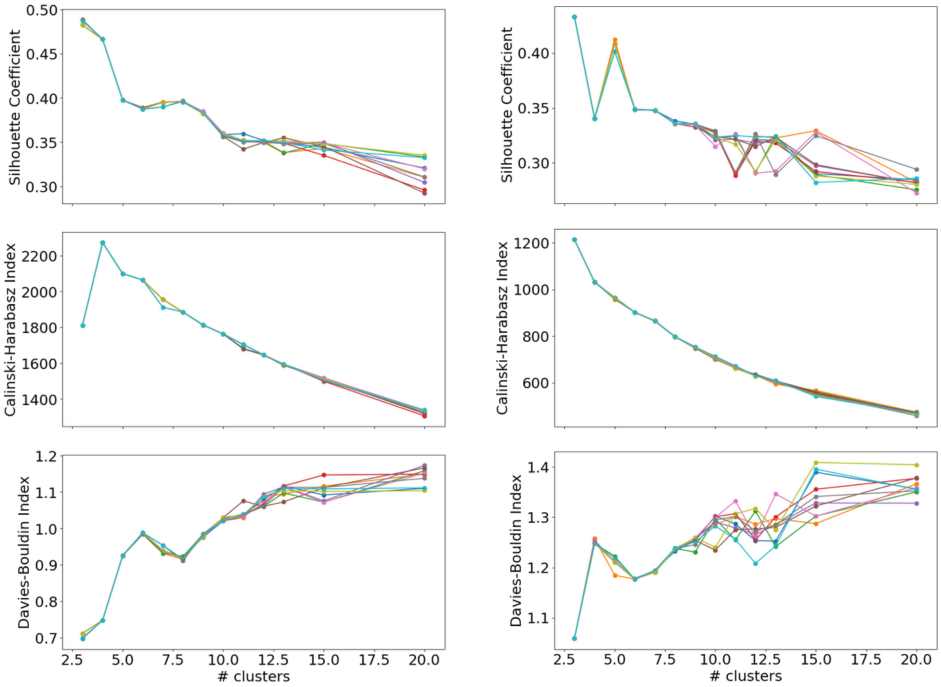

FIGURE 4.26: Clustering metrics for MY 34 for the Mars-PCM (left) and NOMAD SO (right) data sets.

used to perform inversions and testing the performance of our setup. In addition, we performed pressure and temperature sensitivity tests providing an estimation of the error introduced by assuming the Mars Planetary Climate Model (Mars-PCM) as reference atmosphere during the inversions. This error in the retrieved water vapor vertical profiles resulted to be below 2% for variations in temperature of ±5 K and variations in pressure of ±10 % at all altitudes below 120 km. We also performed an estimation of the uncertainty of the Acousto-Optical Tunable Filter (AOTF) characterization, which resulted to have an impact of about 10 % in the retrieved water vapor, comparable to the uncertainty due to the propagation of the measurement noise. Finally, we developed a strategy to use different diffraction orders at different altitude ranges during the inversions. In order to apply this technique, we had to identify where the absorption lines became optically thick by analyzing the line shape and its change with altitude, thus avoiding the use of orders at altitudes where the saturated absorption lines produce biases. The large data set provided by NOMAD permitted a statistical analysis based on data clustering. Based on previous works by our team in this field, we adopted the K-means clustering algorithm and extended its application to the retrieved NOMAD water vapor vertical profiles for the first time. This ruled out ubiquitous bizarre vertical profiles, and associated biases, which might be overlooked during the more classical analysis methods used in this Thesis.

Chapter 5

Effects of the 2018 Global Dust Storm

This Chapter is based on the publication: "Water Vapor Vertical Distribution on Mars During Perihelion Season of MY 34 and MY 35 With ExoMars-TGO/NOMAD Observations"
Published in Journal of Geophysical Research: Planets, 128 (2023)
https://doi.org/10.1029/2022JE007273

Abstract

The water vapor in the Martian atmosphere plays a significant role in the planet's climate, being crucial in most of the chemical and radiative transfer processes. Despite its importance, the vertical distribution of H_2O in the atmosphere has not still been characterized precisely enough. The recent ExoMars Trace Gas Orbiter mission, with its Nadir and Occultation for MArs Discovery instrument, has allowed us to measure the H_2O vertical distribution with unprecedented resolution. Recent studies of vertical profiles have shown that high dust concentration in the atmosphere, in particular during dust storms, induces an efficient transport of the H_2O to higher altitudes, from 40 km up to 80 km. We study the H_2O vertical distribution in a subset of solar occultations during the perihelion of two Martian years (MYs), including the 2018 Global Dust Storm (GDS), in order to compare the same Martian season under GDS and non-GDS conditions. We present our state-of-the-art retrieval scheme, and we apply it to a combination of two diffraction orders, which permits sounding up to about 100 km. We confirm recent findings of H_2O increasing at high altitudes during L_S = 190°-205° in MY 34, reaching abundances of about 150 ppmv at 80 km in both hemispheres not found during the same period of MY 35. We found a hygropause's steep rising during the GDS from 30 up to 80 km. Furthermore, strong supersaturation events have been identified at mesospheric altitudes even in presence of water ice layers retrieved by the IAA team.

5.1 Introduction

The proper characterization of the vertical distribution of water vapor on Mars is a currently ongoing research field and there are many open issues in the description of the water vapor transport and distribution (Montmessin et al., 2017). Until this last decade, the water cycle has been studied with an emphasis on column densities, being the most abundant measurements available until then (Montmessin et al., 2017; Smith, 2004), and hence with a poor insight on the actual vertical distribution.

Therefore, the General Circulation Models were the main source of information about the vertical distributions (Navarro et al., 2014b). The recent possibility of systematic solar occultation (SO) observations has opened a new path toward a better understanding of the Martian climate and the water cycle. Using this technique, water vertical profiles have been studied sporadically by the SPectroscopy for the investigation of the Characteristics of the Atmosphere of Mars (SPICAM) instrument onboard Mars Express. Water vapor observations have been performed also by the Mars Climate Sounder (MCS) and Compact Reconnaissance Imaging Spectrometer for Mars (CRISM) on board Mars Reconnaissance Orbiter (MRO). With SPICAM observations, previous works showed that during the dusty periods or dust storm events (e.g. 2007), the H_2O reached altitudes up to 100 km with volume mixing ratios higher than 100 ppmv (Fedorova et al., 2018b), highlighting the importance of the vertical distributions for a better understanding of the physical and chemical processes driving the water cycle (Maltagliati et al., 2013). Also, researches with MCS data showed that the enhancement of water vapor and the transport of water ice by deep convection to the middle atmosphere (30-90 km) affects the hydrogen escape rate enhancing it during dust storms events (Heavens et al., 2018). This same phenomena is also suggested by Chaffin et al., 2017, 2021 who presented results using combined data from three different spacecrafts (MRO, Mars Atmosphere and Volatile EvolutioN, and TGO).

More recent studies with the Atmospheric Chemistry Suite (ACS) on board ExoMars TGO (Alday et al., 2021; Belyaev et al., 2021; Fedorova et al., 2020; Holmes et al., 2021) revealed that the phenomenon of high altitude water vapor also took place during the Global Dust Storm (GDS) in MY 34 (2018), suggesting that during dust storms, the increase of dust leads to an enhancement of the atmospheric temperatures and favors the upward transport of the water to the middle atmosphere. This same event was reported from the observations made by the Nadir and Occultation for MArs Discovery (NOMAD) instrument, also on board TGO (Aoki et al., 2019; Neary et al., 2020; Villanueva et al., 2021). As a result of these findings, several recent works focused in the hydrogen escape from Mars (Alday et al., 2021; Chaffin et al., 2021; Holmes et al., 2021; Stone et al., 2020; Villanueva et al., 2021, 2022a) revealing the strong influence of dust storms in this process, proving the dust enhancement to have a direct effect on the escape of the hydrogen to space and suggesting that the potential for water to escape could be underestimated.

Two manuscripts related to studies of water vapor on Mars from the TGO/NOMAD data have been submitted to this issue. Aoki et al., 2022 provides an overview of the global distribution of water vapor vertical profiles from the measurements for 3.5 years, and Villanueva et al., 2022a reveals the distribution of D/H ratio in the water vapor vertical profiles near the polar regions. Also three companion papers have been submitted by the IAA/CSIC team to this special issue.

All of them using NOMAD SO observations, López-Valverde et al., 2023 retrieves temperature and CO_2 density profiles up to 90 km from NOMAD first year of solar occultations, (Stolzenbach et al., 2023) derives nature and composition of Martian aerosols, and (Modak et al., 2023) retrieves CO vertical profiles.

Here, we present the vertical distributions of water vapor abundances retrieved from NOMAD data during the first half of the perihelion season in two consecutive Martian years (MYs). We analyze the seasonal and latitudinal variation of the water in the atmosphere, sampling an altitude range from the surface of the planet up to the mesopause at 110 km. Following (Smith et al., 2017), we will refer to the altitudes below about 50 km as lower atmosphere and those above as middle atmosphere or mesosphere López-Valverde et al., 2023. Also, we perform tentative characterization of the hygropause and a first estimation of the saturation ratio of the atmosphere, comparing it with water ice distribution maps.

The goal of this paper is to confirm previous results on the characterization of the water abundance in the Martian atmosphere (Alday et al., 2021; Aoki et al., 2019, 2022; Belyaev et al., 2021; Fedorova et al., 2020; Villanueva et al., 2021, 2022a) but also to add new insights using a wider data set than those in Aoki et al., 2019 and Fedorova et al., 2020, including observations during MY 35, processing a larger altitude range than that presented in Aoki et al., 2022 and applying the latest instrument calibration. The analyzed period covers the GDS event in 2018, when large dust opacities were present in both hemispheres, in particular in the southern hemisphere (Montabone et al., 2020). This same period during MY 35 clearly showed lower dust opacities compared to MY 34 (Olsen et al., 2021a) giving us the possibility of a direct comparison of the same season with different dusty conditions: GDS and non-GDS conditions. However, after the GDS event and for the rest of the dusty season the column dust opacities in both MYs are similar (Montabone et al., 2020; Olsen et al., 2021a).

This study is focused on the perihelion period from $L_S = 180^\circ$ to $L_S = 270^\circ$ in two consecutive Martian years, MY 34 and MY 35. The paper is structured as follows: The description of the NOMAD instrument and the data set is presented in Section 5.2, the analysis of the data and the methodology used are described in Section 5.3, the description and discussion of the results are presented in Section 5.4. Finally we present a summary and conclusions in Section 5.5.

5.2 NOMAD-SO measurements

5.2.1 NOMAD instrument

NOMAD is an infrared spectrometer covering the spectral range between 0.2 to 4.3 µm. The instrument has three spectral channels in order to observe the Martian atmosphere in nadir, limb, or SO geometries at different wavelengths: Two IR spectrometers, SO, operating in the range between 2.3 and 4.3 µm (2320-4350 cm^{-1}) and the Limb Nadir Occultation channel, operating between 2.3 and 3.8 µm (2630-4550 cm^{-1}), and a third channel operating in the UV-visible (200-650 nm) capable of both nadir and occultation observations (Vandaele et al., 2015, 2018)

The SO channel design is based on the Solar Occultation in the Infrared instrument, onboard Venus Express. It uses an echelle grating with a density of ∼4 lines/mm in a Litrow configuration. An Acousto-Optical Tunable Filter (AOTF) is used to select different spectral windows (with a width that varies from 20 to 35 cm^{-1}). Each window corresponds to the desired diffraction order to be used during the atmospheric scan. The spectral resolution of the SO channel is $\lambda/\Delta\lambda \simeq$ 20,000. The sampling time of this channel is approximately 1 s, allowing a vertical sampling of ∼1 km. Also, the AOTF permits a quick change from one diffraction order to another. As a result, the SO channel is able to probe the atmosphere at a given altitude through 6 different diffraction orders quasi-simultaneously (within 1 second).

5.2.2 Data set selected for this work

NOMAD science operations began in April 2018 and up to this date, almost daily observations have been performed since the middle of MY 34 (March 2018–March 2019). For this study, we have selected two subsets of measurements taken by the NOMAD SO channel covering the same Solar Longitude period $L_S = 180 - 270^\circ$ in two different Martian years: MY 34 (during the period from 22 May to 8 October 2018) and MY 35 (during the period from 18 April to 29 August 2020). Water vapor spectral absorption lines are present over a wide range of the IR spectrum. Since CO_2 is the dominant gas in the Martian atmosphere, we have to select a spectral range free of CO_2 lines in order to be able to detect the H_2O lines. For that reason we have decided to analyze observations taken at the NOMAD SO diffraction order 134 (3011-3035 cm^{-1}) and order 168 (3775-3805 cm^{-1}). Order 134 has absorption H_2O lines with a moderate intensity ($I \sim 10^{-21}$ $cm^{-1}/(\text{molecule} \cdot cm^{-2})$) allowing the study of the lower atmosphere where lines are not heavily spectrally saturated Aoki et al., 2022, while order 168 has stronger lines ($I \sim 10^{-19}$ $cm^{-1}/(\text{molecule} \cdot cm^{-2})$) allowing the sounding at higher altitudes. By spectral saturation, we refer to how the absorption lines penetrate into the continuum of the spectrum. In optically thin conditions, the line depth increases proportionally with the gas density. When in saturated conditions, the line core stops growing and the overall absorption does not follow the gas density anymore. As a consequence of this limitation, each order has an optimal altitude range to be used: order 134 for the lower atmosphere and order 168 for the upper atmosphere. The data set has been selected including simultaneous observation of both diffraction orders. With these two subsets, a total of 962 occultations have been analyzed, including observations in both hemispheres at different latitudes. Latitudinal coverage over solar longitude of the occultations is shown in Figure 5.1, also indicating the Local Solar Time of the observations, each point representing one single occultation.

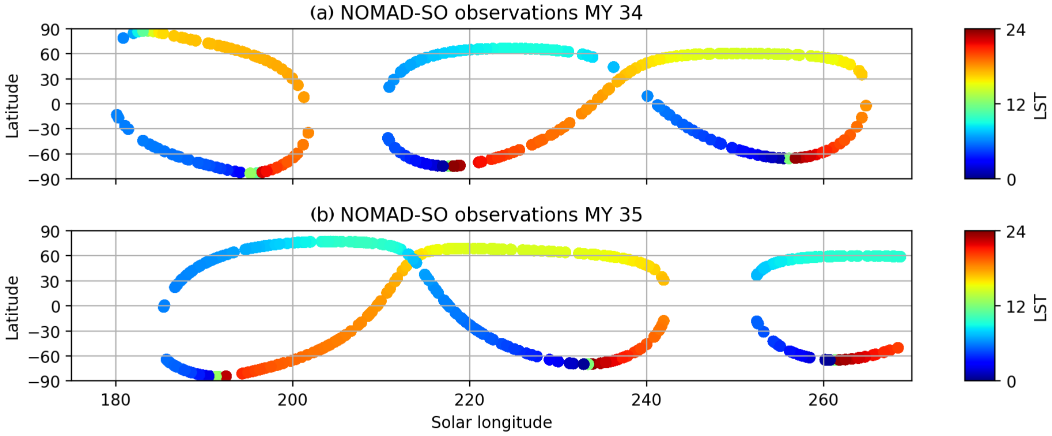

FIGURE 5.1: Latitude of the analyzed Nadir and Occultation for MArs Discovery (NOMAD) Solar Occultation (SO) observations over solar longitude for (a) MY 34 and (b) MY 35. Color indicates local solar time of the measurements.

5.3 Data analysis

5.3.1 Data cleaning and preprocessing

In this work, we used Level 1 SO data (i.e., calibrated transmittances) from the NOMAD SO channel. Although a lot of effort has been devoted to their spectral calibration (Thomas et al., 2022; Trompet et al., 2023; Villanueva et al., 2022a), there are still some inaccuracies which can affect the performance and quality of the retrievals. The most relevant to take into account are the spectral calibration uncertainty, a residual bending in the spectral dimension, and the effects of the AOTF and the instrumental line shape (ILS). Last two affecting the forward model calculation are described in Section 5.3.2. At IAA, we have developed preprocessing tools to identify and eliminate the residual bending and to do a first estimation and correction of the spectral shift using the line by-line radiative transfer algorithm KOPRA (Karlsruhe Optimized and Precise Radiative transfer Algorithm) (Stiller, 2000) developed at IAA and IMK (Institut für Meteorologie und Klimaforschung) in Karlsruhe, Germany. The preprocessing is described in some detail in a companion paper in this special issue (López-Valverde et al., 2023) but a summary is included. It proceeds in several steps, separating different components of the measured transmittance. Also the preprocessing computes the aerosol slant optical depth, which is used later to retrieve extinctions at the tangent point Stolzenbach et al., 2023. These values are used during gas retrievals, like H_2O, CO_2 (López-Valverde et al., 2023), or CO Modak et al., 2023 following a sequential retrieval chain. This preprocessing works considering the measured transmittances ($\mathcal{T}$) corrected for spectral shift ($\Delta\lambda$) as a proportional combination of the forward model ($\mathcal{T}_0$) scaled by a factor (k), the residual bending ($\mathcal{T}_b$), and the aerosol slant opacity (τ). These transmittances are combined with the instrumental response in a precise line-by-line calculation using the KOPRA forward model. One of the possible ways to express the measured transmittance is the following one, which is useful to correct for the spectral bending:

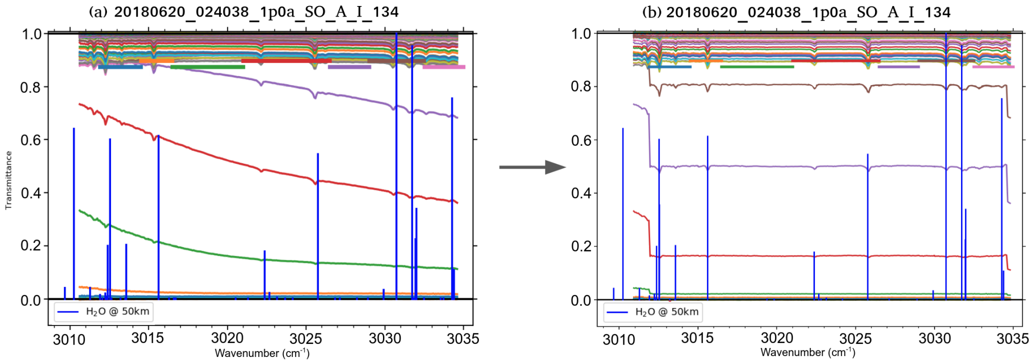

FIGURE 5.2: Examples of Nadir and Occultation for MArs Discovery Solar Occultation (SO) transmittances from diffraction order 134 before the cleaning process (a) and after the first correction of the spectral shift and the bending (b). Each color indicates a different tangent altitude (left and right panel do not share the same color scheme). The vertical blue lines indicate the positions of the H_2O absorption lines from HITRAN 2016 and their relative line intensity to a normalization of the strongest line in the measured spectral range.

$$\mathcal{T}(\lambda + \Delta\lambda) = \mathcal{T}_0^k(\lambda)\;\mathcal{T}_b(\lambda)\;\mathrm{e}^{-\tau} \tag{5.1}$$

Then, using an optimized brute force method, we compute an extensive set of simulated spectra for each measured spectrum using a radiative transfer line-by-line calculation. In principle, this set of simulations shall cover a large grid of the three cleaning parameters (scale factor, bending, and aerosol slant opacity), however, we have implemented a jump search algorithm in order to reduce the number of simulations speeding up the convergence. The goal is to select the optimal combination of parameters, that is, that which gives the lowest variance when compared to the data. Afterward, by adjusting the position of the CO_2 and H_2O absorption lines to the position from HITRAN 2016 database (Gordon et al., 2017), we perform a first correction of the spectral shift. Figure 5.2 shows an example of the cleaning process applied to order 134. Left panel shows the spectra before cleaning, where large bending can be observed at some altitudes. This bending is caused by the instrument and is larger than the expected bending due to water ice scattering. Right panel in Figure 5.2 shows the spectra after the cleaning process, where the different baseline levels observed are due to aerosol attenuation. We have excluded the edges of the spectra from any cleaning and inversion process due the large level of noise in those regions. Based on the estimated aerosol opacity, we apply a cloud filter to the data excluding the observations close to the surface where the slant opacity estimated to be greater than 2.0 and selecting the minimum altitude where the gradient in the slant opacity is smaller than 0.08 km^{-1}.

5.3.2 Retrieval scheme

A priori climatology

The a priori temperature and density profiles needed by the forward model are obtained in this work from the Mars Planetary Climate Model developed at the Laboratoire de Météorologie Dynamique (LMD Mars PCM) (Forget et al., 1999), using the latest implementations of the dust and water cycles described in Navarro et al., 2014b and a new comprehensive photochemical scheme (Lefèvre et al., 2021) covering all atmospheric layers from the surface to the exobase. Simulations with the dust scenarios appropriate for MY 34 and MY 35 (Montabone et al., 2015; Montabone et al., 2020) were conducted. For each observational profile, we extract the modeling results interpolating at the exact location (latitude, longitude) and time (L_S, local time) of the observation, provided by the navigated NOMAD data at 50 km altitude. Ideally, when the signal is sufficient, the retrieval results are basically independent of the a priori. Hence, using a climatological model is appropriate for creating this a priori climatology.

Forward model

For both the cleaning of the data and the water vapor inversions, we simulate the spectra with KOPRA. As a line-by-line and layer-by-layer code, KOPRA was designed to calculate the infrared radiative transfer through the atmosphere. An extensive description of this line-by-line radiative transfer algorithm can be found in Stiller, 2000. Originally developed for the Earth, KOPRA was recently adapted to limb emissions on Mars (Jiménez-Monferrer et al., 2021) and for this work it has been adapted to SO data on Mars for the first time. Some modifications have been made in order to make the code suitable for the analysis of the NOMAD data. Because of the AOTF, the NOMAD SO spectra of a certain diffraction order also includes the signal from several adjacent orders. That is, the data to be analyzed is a combination of several diffraction orders Neefs et al., 2015. Therefore, understanding and characterizing the AOTF and ILS is mandatory to accurately simulate the instrumental effects in the measured data. A first attempt to characterize these instrumental effects was performed during in-flight calibrations, summarized in Liuzzi et al., 2019 and Thomas et al., 2022. More recently, a revision by several teams within the NOMAD consortium improved the AOTF and ILS descriptions (López-Valverde et al., 2023; Villanueva et al., 2022a). It was found that the AOTF transfer function can be described with an asymmetric Sinc function added to a Gaussian offset. The parameters that describe the AOTF are order dependent. Also, as shown in Thomas et al., 2022, it was found that the ILS can be described by two Gaussian functions with a separation and a scaling ratio between them that varies across the diffraction orders. A large amount of effort has been devoted in the last year within the NOMAD consortium to identify the key parameters and to characterize those variations with a proper parameterization. This is described in detail in Villanueva et al., 2022a. In this work, we have adopted the nominal parameters for the ILS and AOTF parameterization proposed by Villanueva et al., 2022a. The new AOTF and ILS significantly improved the convergence of the fittings in our H_2O retrievals and the agreement between different diffraction orders.

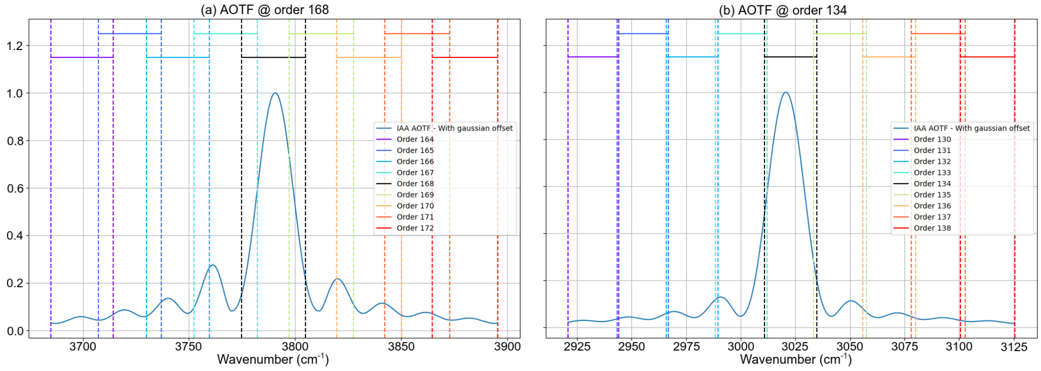

FIGURE 5.3: Nadir and Occultation for MArs Discovery Solar Occultation Acousto-Optical Tunable Filter (AOTF) functional for orders 134 (a) and 168 (b). Vertical dashed lines indicate the limits of the diffraction orders. Only ±4 adjacent orders are represented.

In Figure 5.3, we show the AOTF normalized functionals used for orders 134 and 168. For the analyzed diffraction orders, the simulated spectra is calculated taken into account the flux contribution of ±4 adjacent orders (i.e., orders 164 to 172 for the order 168 and orders 129 to 138 for the order 134) since the contributions of further orders starts to be less relevant as the number of adjacent order increases. In Figure 5.4a, we show reference KOPRA radiances for order 168 calculated considering 0, 1, 2, 3, and 4 adjacent orders (e.g., the radiance calculated considering 4 adjacent orders has been obtained taking into account orders 164, 165, . . ., 168, . . ., 171, and 172).In Figure 5.3, colors denote NOMAD orders while in Figure 5.4, they indicate the number of adjacent orders included during the radiance simulations. Figure 5.4b shows the relative difference between each radiance referred to the radiance computed with four adjacent orders, highlighting the main contribution comes from the first ±1 adjacent orders and no more than a 5% contribution comes from the pm3rd adjacent orders. Also, increasing the number of adjacent orders has a direct impact in the calculation time of the forward model, so a balance between performance optimization and accuracy has to be taken into account.

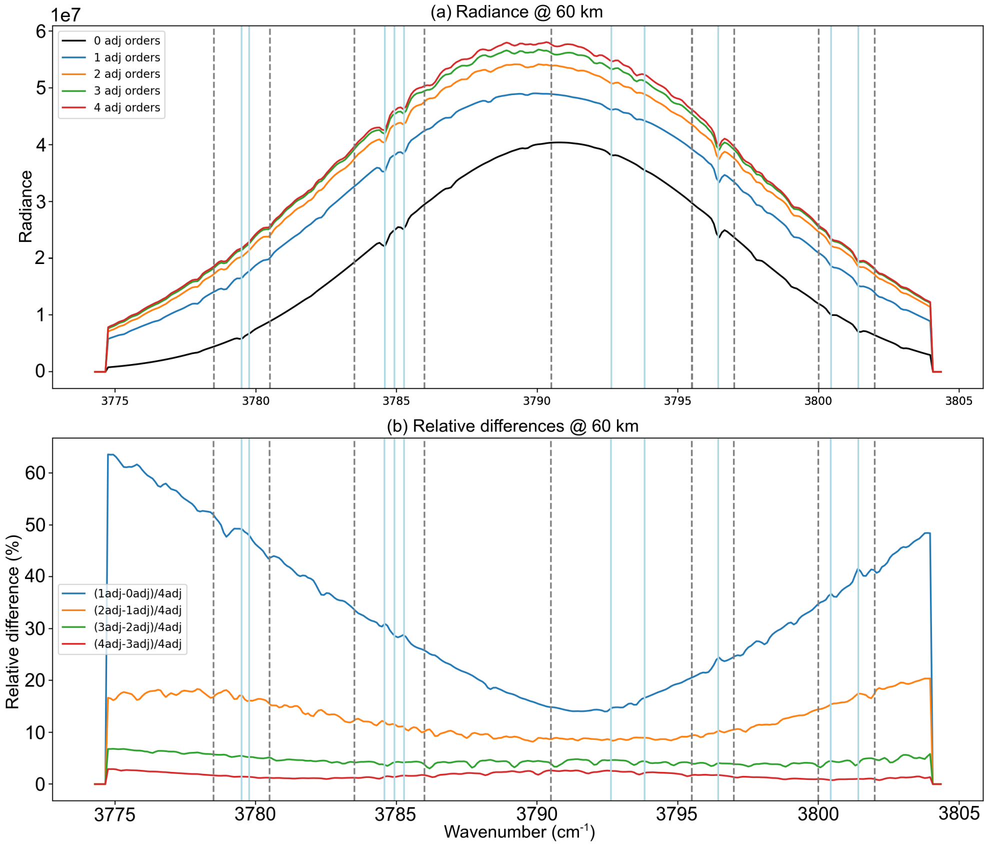

FIGURE 5.4: Examples of radiances computed with Karlsruhe Optimized and Precise Radiative transfer Algorithm for the order 168 considering a different number of adjacent orders. Panel (a) shows the radiances calculated with 0, ±1 (167-169), ±2 (166-170), ±3 (165-171), and ±4 (164-172) adjacent orders. Panel (b) shows the relative differences between them refereed to the radiance calculated with four adjacent orders, where the relative individual contribution of the adjacent orders can be seen. Vertical solid lines indicate the positions of the strongest H_2O absorption lines. Vertical dashed lines indicate the limits of the microwindows used for the retrievals.

An example demonstrating the NOMAD-specific KOPRA forward modeling applied to a monochromatic transmittance spectrum is summarized in Figure 5.5. First, the monochromatic spectrum (a) is convolved with the ILS (b). Then, the AOTF filter is applied (c) and the contributions from adjacent orders are shifted to the central order and added (d) to generate the final spectrum to use during the retrievals (e).

Inversion and convergence criteria

For the H_2O inversion we use the Retrieval Control Program (RCP) developed at IMK, which incorporates the KOPRA forward model. After providing an a priori, a first-guess and the measured spectra, RCP solves the inversion problem iteratively until the convergence of the solution. The IMK-IAA level-2 processor relies on multi-parameter nonlinear least squares fitting of measured and modeled spectra (von Clarmann et al., 2003a). Further information about RCP and the inversion problem

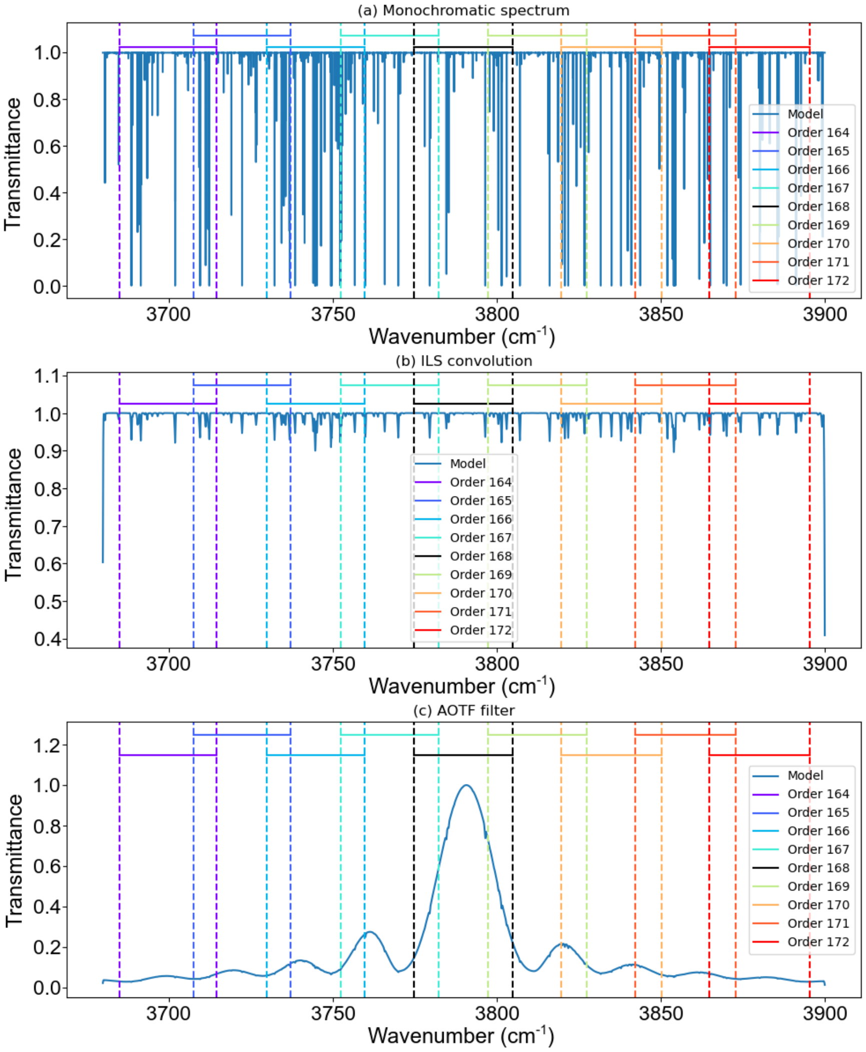

FIGURE 5.5: Example of the Nadir and Occultation for MArs Discovery-specific forward modeling steps applied to monochromatic spectrum (a): instrumental line shape (ILS) convolution (b), Acousto-Optical Tunable Filter (AOTF) transfer function application (c), adjacent orders addition (d), and final spectrum used for the retrieval (e). Panels (d and e) cover a smaller spectral range than panels (a-c).

can be found in Jurado Navarro et al., 2016. We use a first order Tikhonov-type regularization optimized for each diffraction order. Also, we apply a strong diagonal constrain at the lowermost altitudes (below 1 km) and at high altitudes where no information form the spectra is expected (above 95 km in order 134 and above 110 km in order 168). For this study, we are considering the measurement errors in the data provided by Thomas et al., 2022 as pure uncorrelated random errors, giving as a result a diagonal measurement noise covariance matrix whose elements are defined as follows:

$$S_{ij} = \langle (\epsilon_i - \langle \epsilon_i \rangle)(\epsilon_k - \langle \epsilon_j \rangle) \rangle \ , \tag{5.2}$$

where $S_{ij} = 0$ when $i \neq j$.

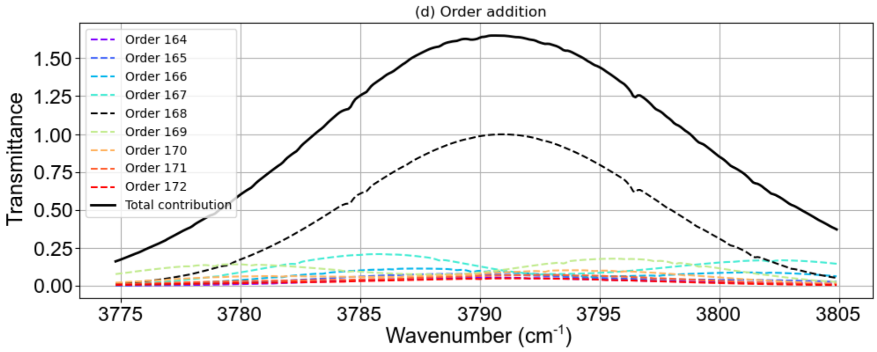
(d) Order addition

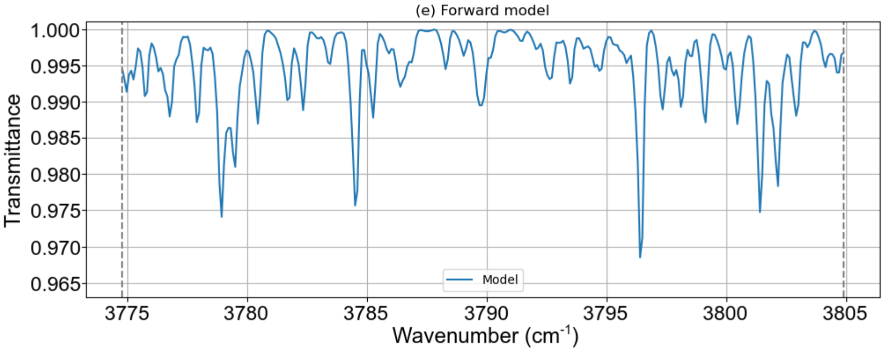
(e) Forward model

FIGURE 5.5: (continued)

After the convergence of the retrieval, RCP generates the vertical profiles of the targeted species, the noise error covariance matrix in the retrieval parameter domain, the averaging kernels, and the vertical resolution. A sample of those products obtained for orders 134 and 168 are shown in Figure 5.6.

Previous to the analysis of the data set presented here, we have performed several tests with synthetic spectra mimicking the NOMAD SO instrument (AOTF, ILS and instrumental random noise) and the Martian atmosphere (realistic aerosol vertical distribution profiles) in order to prove the stability and performance of our cleaning and retrieval setup. Also, in order to check for the independence of the retrieved profiles to the used climatology, we have performed synthetic retrievals modifying the a priori and first-guess inputs like H_2O volume mixing ratio (VMR) or temperature. Regarding this last one, and in contrast to other retrieval targets that our team has also delivered (temperature, CO abundances), the assumed temperature is of minor importance for H_2O.

Discrete spectral ranges (i.e., micro-windows, MWs) can be selected in order to optimize the retrieval. For each diffraction order, we have selected different MWs corresponding to those regions where strong absorption lines are present. Here, we differentiate two sets of micro-windows: Cleaning-MWs and Retrieval-MWs. MWs selected for this work are described in tables 3.2 and 3.4. The first set corresponds to the spectral ranges used during the cleaning process and cover almost the full order (just excluding the edges). The second set, included in first one, corresponds to

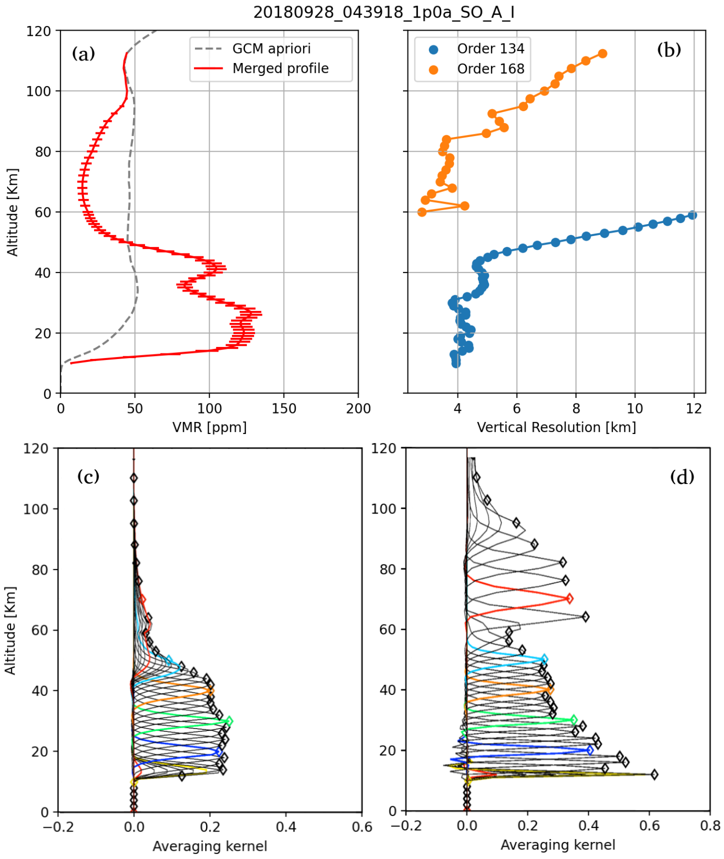

FIGURE 5.6: Performance of the retrieval of the data taken at the observation 20180928_043918_1p0a_SO_A_I. Panel (a) shows the retrieved water vapor, panel (b) shows the vertical resolution obtained for the order 134 (blue) and 168 (orange). Bottom panels show the the averaging kernels of the retrievals for orders 134 (c) and 168 (d)

those MWs used for the retrieval, and only those with strong absorption lines are considered.

To obtain the water vapor vertical profiles, we follow a sequential retrieval scheme. First we retrieve a spectral shift correction from the cleaned data within a confined altitude range of just 10-20 km where the absorption lines are clearly visible. In order to have a proper characterization and stability, water vapor also is retrieved but the result is not considered in this first stage. After that, we retrieve the water vapor vertical profile in the full altitude range for each order (except the lowermost altitude range excluded by the cloud filtering). Along with the water vapor, a spectrally constant transmittance level is adjusted to account for the impact continuum absorption by aerosols. A full aerosol optical depth retrieval is done by Stolzenbach et al., 2023 and its results about the water ice particles characterization are used in this work. Finally, when orders 134 and 168 are measured during the same atmospheric scan, we merge both profiles using the result from order 134 for the lower atmosphere and the result from order 168 for the upper atmosphere.

Merging of diffraction orders 134 and 168

The performance and confidence on the retrievals from orders 134 and 168 can be obtained after a statistically large number of occultations. Below about 60 km, the order 168 usually shows an unstable behavior, being deeply sensitive to the AOTF characterization due to the presence of spectrally saturated lines, while order 134 has a good response in this altitude range, with a good retrieval performance, that is, small residuals as shown in Figure 5.7 (bottom panels). Above 60 km, the absorption lines in order 134 begin to be very noisy, while those observed with the order 168 begin to be optically thin. This feature can also be observed in Figure 5.7 (top panels) where the residuals of the order 168 are better in this altitude range and the spectra observed with order 134 becomes too noisy with no visible absorption lines. For this reason, as a general criterium, we decide to use the order 134 to probe the atmosphere below 60 km and order 168 above where optically thin lines above noise are present in both orders. The value of 60 km has been assumed for simplicity, small changes in this transition altitude have little impact on our results. In some particular occultations where only observations from order 134 are available, a vertical extension of this criterium is applied to those altitudes where the retrieved averaging kernels (AvK) are larger than 0.03 (below that value we consider that the information in the retrieved profile mainly comes from the a priori climatology), allowing us to retrieve information up to 80-90 km. After some experimentation, we set this minimum value at 0.03; small changes around this value do not alter the results. There are other scans where the sensitivity in the order 134 drops at altitudes lower than 60 km, as shown by the AvK diagonals being lower than 0.03. In these cases, we maintain the general rule mentioned above for order 168, of considering only retrieved H_2O abundances above 60 km. Therefore, in these cases there is a gap between the upper altitude sounded in order 134 and that in order 168, where our retrieval results basically supply the climatological a priori H_2O. In the Figures that follow in Sections 5.4.1 and 5.4.2, we do not show those a priori values but focus on the purely NOMAD retrievals, that is, instead of adding the a priori values to form a full profile, we decide to leave an altitude gap between the two NOMAD orders to highlight the altitudes actually sounded.

Regarding the merging, first the retrieval using the order 134 is done for the full altitude altitude range, although the sensitivity to what happens above 90 km is very limited due to the noise in the measurements of this order. Then, we perform the retrieval of the order 168 for the full altitude range too but using the retrieved H_2O from order 134 as a priori instead of using the PCM climatology and applying a strong diagonal constrain in the the altitude range below 60 km with a smooth transition to a non-diagonalized region above that altitude. As a result, we obtain a profile merging information from order 134 below 60 km and from order 168 above. Note that we do not combine the two profiles by weighting them. We think that a combination of these two full profiles is risky and prone to errors due to the very different optical thickness between orders 134 and 168 and to any possible incompleteness in handling the error propagation in each of them. In Figure 5.8 we present an example of the order merging in two different occultations. Note that the difference between the combined profile and both 134 and 168 around 65 km is due to the global fit used, which tries to find the best match at all altitudes, although this effect is within errorbars.

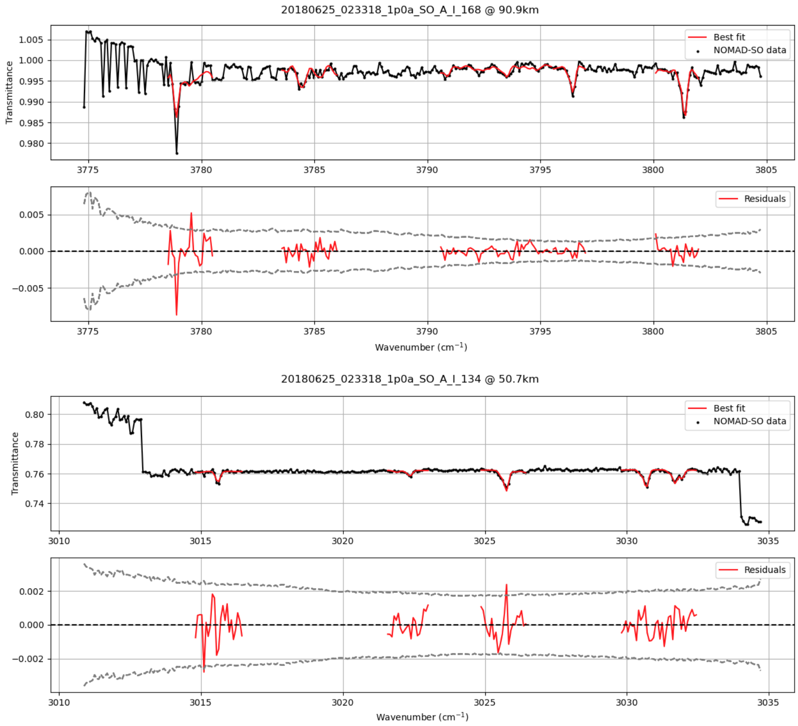

FIGURE 5.7: Example of the best fit and the residuals obtained after the retrieval. Two top panels show the data from order 168 at 90 km and two bottom panels the data from order 134 at 50 km.

5.3.3 Comparison and validation

Vertical profiles of H_2O abundance from the NOMAD SO channel have been previously presented in a couple of papers (Aoki et al., 2019; Villanueva et al., 2021) and also in a companion paper in this issue (Aoki et al., 2022). In Aoki et al., 2022 (A22) a comparison with ACS near-Infrared channel (NIR) retrievals (Fedorova et al., 2020) is performed, revealing that ACS H_2O abundances are 22% higher than their results. An important difference is that the ACS retrievals used measured temperatures in each scan by the same instrument, while A22 and co-workers used modeled temperatures. However, this result improves those presented in Aoki et al., 2019 (before the improvements in the AOTF/ILS characterization), where water vapor abundances were much higher than those in Fedorova et al., 2020. We have performed a first comparison with A22 for validation purposes, using data from diffraction order 134. Some caution is needed before comparing VMR, as this is a ratio of the H_2O abundance to the total abundance, and each team used a different reference PCM, and thus the atmospheric densities are not necessarily

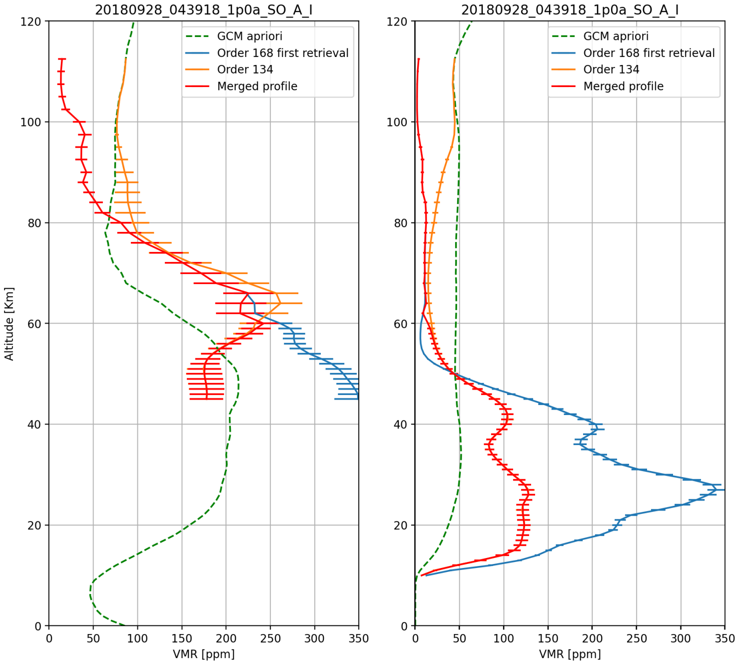

FIGURE 5.8: Two examples of the merging of vertical profiles from orders 134 and 168. Note that the merged profiles (red) overlaps the 134 order (orange) below 60 km whereas it overlaps the 168 order (blue) above.

similar. To eliminate this effect, the A22 profiles have to be corrected scaling the VMR by a density factor at all altitudes. We present the global comparison of the scaled results in Figure 5.9, showing a qualitative agreement between both retrievals. The linear weighted fitting of the data suggests that our retrievals are systematically higher than A22 by about 13%. In Figure 5.10 we present a direct comparison of eight individual vertical profiles from A22 with our retrievals. We observe a good agreement between most of the profiles (profiles with large discrepancy have been selected on purpose to highlight the necessity of a proper comparison work), despite using different methodologies with very different approaches. However, there are some discrepancies beyond the uncertainty range in some profiles, in particular in the altitude range between 10-20 km where no scientific conclusions have been drawn due the difficulty of obtaining results caused by the large dust opacity. The origin of this differences and its implication will be further investigated in future works with a proper and more detailed comparison that is beyond the scope of this work. Also a discussion on the global H_2O distribution has been held in Section 5.4 of this work with the results by Aoki et al., 2019, 2022 using NOMAD data and by Belyaev et al., 2021; Fedorova et al., 2020 and Alday et al., 2021 with ACS data, showing that the seasonal variation maps along with the latitudinal maps and the saturation ratio maps that we present here reveal similar structures and features as those previously presented.

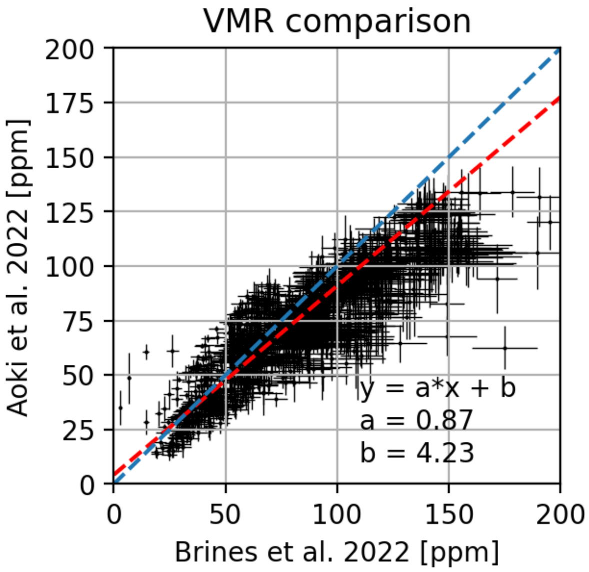

FIGURE 5.9: Comparison of the water vapor volume mixing ratio retrieved by Brines et al., 2023e and Aoki et al., 2022. The blue dashed line shows the curve $y = x$ and the red dashed line represents the linear weighted fitting of the scattered data.

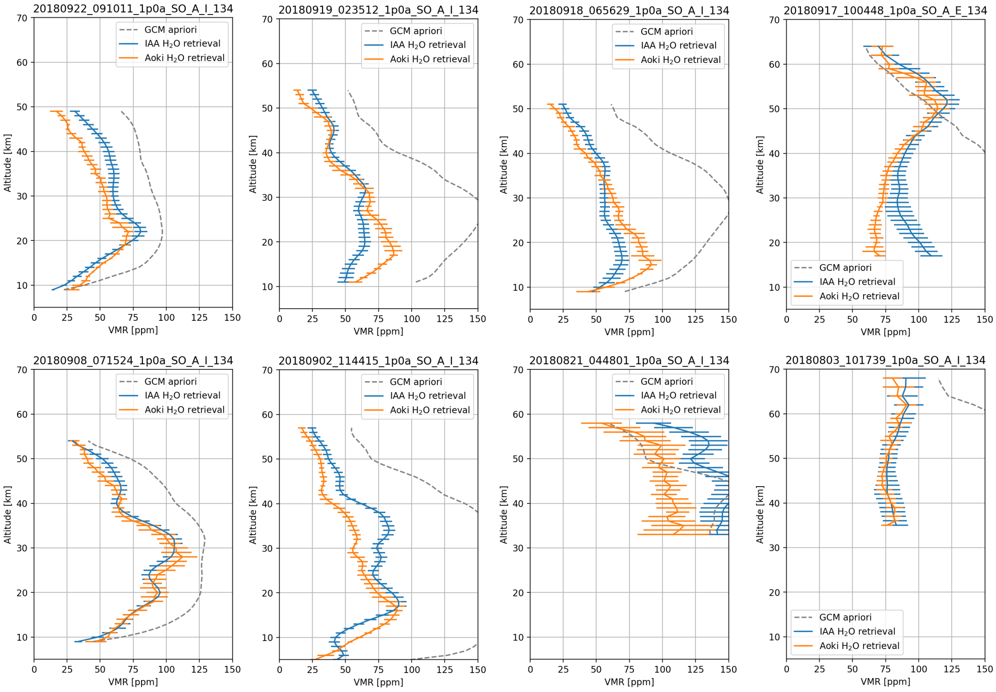

FIGURE 5.10: Examples of eight water vapor vertical profiles retrieved by Brines et al., 2023e (blue) and Aoki et al., 2022 (orange) using observations from diffraction order 134. Gray dashed line shows the Mars Planetary Climate Model a priori used for (Brines et al., 2023e) retrievals.

5.4 Results and discussion

Water vapor vertical profiles obtained after the inversion process allow us to generate different subproducts and study different aspects of the Martian atmosphere. Here we present detailed vertical distribution maps of the same seasonal period in two different MYs. The data analyzed covers a solar longitude range of 90°, form $L_S \sim 180°$ to $L_S \sim 270°$. This selected range allow us to study the water vapor distribution during the same season with and without the MY 34's GDS.

5.4.1 Martian Year 34

Seasonal variation

The growth and maturation phase of the 2018 GDS took place during the period covering a solar longitude range from $L_S \sim 190°$ to $L_S \sim 210°$ and with a long decay phase that extended until $L_S \sim 270°$ (Guzewich et al., 2019; Kass et al., 2020). This period corresponds with the northern autumn (southern spring) in Mars, which spans from $L_S = 180°$ to $L_S = 270°$. During this period, following the global seasonal trend as it was understood prior to 2018 observations, the northern hemisphere gradually starts to be colder at high latitudes as the northern autumn progresses (Smith et al., 2017). After $L_S = 170°$, water vapor abundances decrease in the north polar regions followed by an increase moving southward and reaching a maximum between 30°N and the equator that remains during the whole northern winter (Montmessin et al., 2017). In the southern hemisphere, water vapor progressively increases due to the southward transport and the temperature increase, leading to the southern polar cap sublimation at late southern spring (Montmessin et al., 2017). Southern spring and summer are warmer and wetter than the analog northern seasons, in particular at mid-low latitudes. The reason for this behavior is that the southern summer coincides with the perihelion of the Martian orbit so the radiation influencing the planet increases, and compared with the northern summer, the southern summer is noticeable warmer (Smith et al., 2017), and more water vapor from water ice sources can sublimate and ascend to the atmosphere (Montmessin et al., 2017). This classical description is under revision by recent detailed views of the vertical structure of temperature and water vapor that TGO instruments are providing (Aoki et al., 2019, 2022; Belyaev et al., 2021; Fedorova et al., 2020; López-Valverde et al., 2023; Villanueva et al., 2021), showing a distinct warming and moistening of the atmosphere in both hemispheres by $L_S \sim 200°$. During the GDS in MY 34, due to the huge amounts of dust, the atmosphere temperature in both hemispheres increased as a consequence of the absorption of the solar radiation by the dust particles (Montabone et al., 2020; Neary et al., 2020).

The seasonal variation maps are presented in Figure 5.11 for the northern (left panels) and southern (right panels) for MY 34. We present in Figure 5.12 a detailed

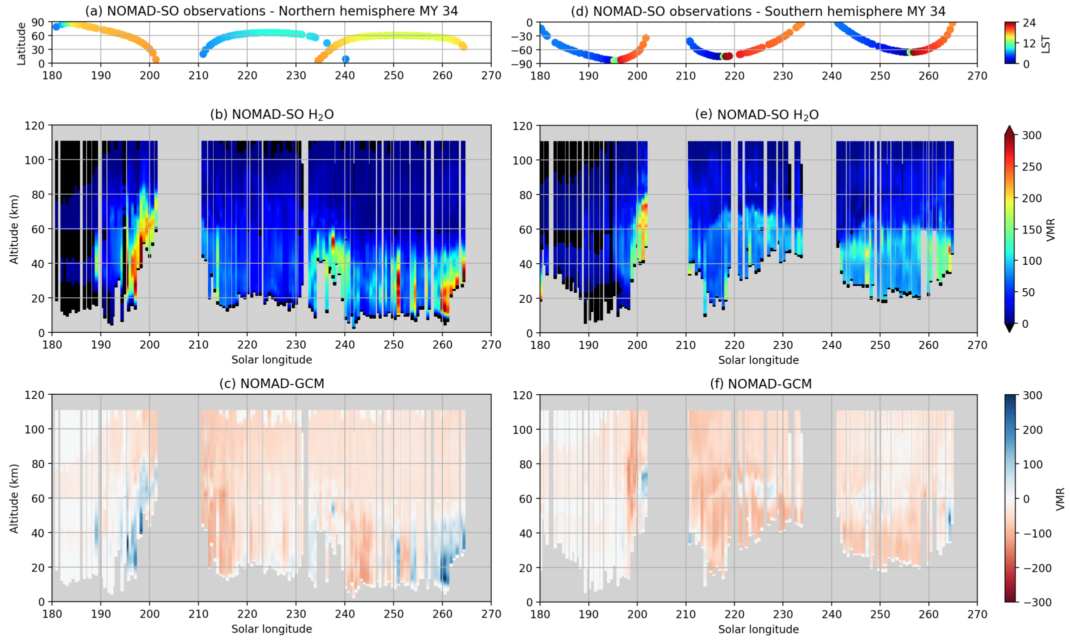

FIGURE 5.11: Seasonal vertical distribution maps of the retrieved water vapor (b,e) and the differences between the NOMAD SO retrievals and the Planetary Climate Model climatology (c and f) during the MY 34 in the Northern (left panels) and the Southern (right panels) hemispheres. Top panels (a and d) show the latitudes and the Local Solar Time of the observations analyzed. Black regions in panels (b and f) are masked due to the low averaging kernels obtained during the retrievals.

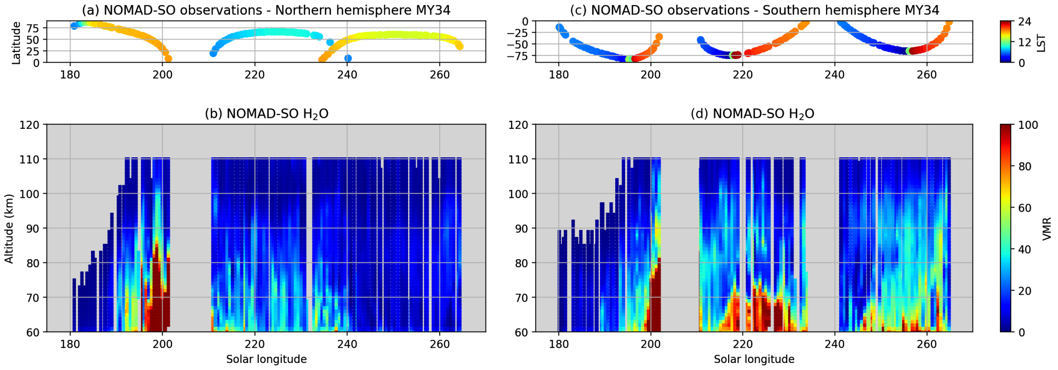

FIGURE 5.12: Seasonal vertical distribution maps of the retrieved water vapor at the upper atmosphere above 60 km during the MY 34 in the northern (b) and the Southern (d) hemispheres. Top panels (a and c) show the latitudes and the Local Solar Time of the observations analyzed.

insight of the water vapor in the upper atmosphere in order to highlight features below 100 ppmv. For the representation of both Figures, we have filtered the profiles to those altitudes where the averaging kernels of the retrievals are larger than 0.03 in order to exclude those regions where there is not enough information in the spectra to retrieve water vapor and hence, the profile would be purely mimicking PCM climatology. Those low information regions have been colored black. As shown in

Figure 5.11, during the mature of the GDS, we observe an intense peak in the water vapor volume mixing ratio, showing water abundances of ~150 ppmv at 80 km and ~30 ppmv up to 100 km in both hemispheres followed by a decrease of the water abundances to ~50 ppmv below 60 km just after the strong activity of the storm at $L_S \sim 210°$, shown in Figure 5.12. A possible explanation for this phenomenon is that due to the increased temperatures as a consequence of the dust enhancement, water vapor is not able to condense into ice as it ascends in the atmosphere, preventing the sedimentation of ice particles and due to the enhanced global circulation, allowing the water vapor to reach high altitudes (Neary et al., 2020). This increase is thought to be due to the intensification of the upward branch of the Hadley cell (Fedorova et al., 2020; Heavens et al., 2018). This same feature is presented in (Belyaev et al., 2021), observing water vapor abundances about 10-30 ppmv at 100 km during the perihelion of MYs 34 and 35. We also observe a peak in the water vapor VMR in the northern hemisphere at $L_S \sim 235°$ corresponding to observations at low-mid latitudes and near the equator where higher temperatures and hence higher amounts of water vapor are expected. In this case, the water vapor is mostly confined within an altitude range between 30-60 km.

In the southern hemisphere, we observe a progressive increase in the water vapor abundances at $L_S > 220°$, with a clear propagation up to 100 km of water vapor abundances larger than 40 ppmv as can be seen in Figure 5.12. This occurs because at this period of time, deep into the southern spring, the temperature increases gradually and the sublimation of the southern polar cap releases huge amounts of water vapor into the atmosphere. Then, due to the Hadley circulation intensification during this season and the eddy diffusion, water vapor can be distributed to lower latitudes (Smith, 2002). The intensification of the Hadley cell during the perihelion of MY 34 is directly observed by Olsen et al., 2021c, suggested to be the reason for the rapid increase in the observed CO VMR above 80 km instead of the 60 km predicted by the PCM.

Our H_2O distribution has many similarities with previous results from recent TGO publications (Alday et al., 2021; Aoki et al., 2019, 2022; Belyaev et al., 2021; Fedorova et al., 2020; Villanueva et al., 2021). Focusing on the works by Fedorova et al., 2020, who measured atmospheric temperatures using ACS NIR, and by (Aoki et al., 2019, 2022) using NOMAD SO, which are cited as F2020 and A2022 hereafter, we confirm the following five features: (a) both F2020 and A2022 also found a water vapor peak at 80 km/in the lower mesosphere during the mature phase of the GDS ($L_S = 195 - 205°$) (b) both works also reported the decline in VMR after $L_S \sim 210°$ (c) the peak at $L_S \sim 235°$ in the northern hemisphere that we reported was also observed by both works and discussed by A2022.(d) Significant water vapor abundances up to 100 km around $L_S \sim 260°$ in the southern hemisphere were also reported by F2020, but not by A2022 due to its limitation in altitude coverage. (e) The lowermost altitude of the H_2O profiles varies with latitude and season, as it is very dependent on the amount of aerosols in the lower atmosphere, and this variation is entirely similar to F2020 and A2022, although perhaps we are using a slightly more conservative criterion (our lowermost retrieved altitudes are a little bit higher). We also observe a few quantitative differences with those works, like these two main features: (a) F2020 shows overall larger water vapor abundances above 60 km in the southern hemisphere than those presented in this work at $L_S = 210 - 220°$ and $L_S = 250 - 260°$. This discrepancy is also found at $L_S = 210°$ in the northern hemisphere in A2022 too. (b) Comparing with Villanueva et al., 2021 we observe a discrepancy at $L_S = 240°$ in the northern hemisphere, showing water vapor abundances about 10-20 ppmv larger in this work than in (Villanueva et al., 2021).

Hygropause

On Earth, the region of the atmosphere near the tropopause where the water vapor reaches its minimum value is called the hygropause and can be found at ~20 km (Kley et al., 1979). On Mars, the absence of stratosphere and the vertical variability of the water vapor makes it difficult to fix an altitude for the hygropause. Different definitions of this atmospheric layer can be found in several works (a cold layer at 40-50 km altitude at which H_2O condenses (Stone et al., 2020); the altitude where the water vapor volume mixing ratio drops below 70 ppmv (Holmes et al., 2021), or where water content rapidly decreases to effectively zero (Heavens et al., 2018)). For this work we use a simple definition for this layer: the altitude where the water vapor volume mixing ratio starts to be lower than 50 ppmv.

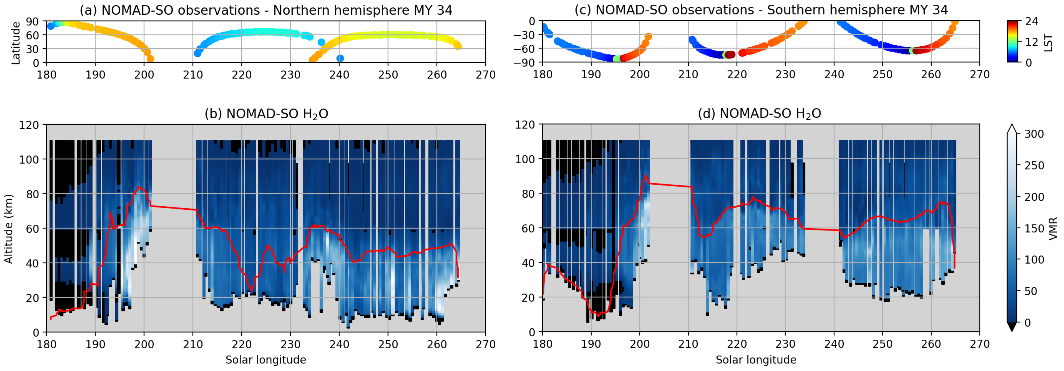

FIGURE 5.13: Seasonal vertical distribution maps of the retrieved water vapor (b and d) during the MY 34 in the northern (left panels) and the southern (right panels) hemispheres. The red line indicates the hygropause level. Top panels (a and c) show the latitudes and the Local Solar Time of the observations analyzed.

Figure 5.13 shows the altitude level of the hygropause (as defined above in this Section). We observe a clear increase in both hemispheres at $L_S \sim 200°$ as a result of the water vapor injection due to the GDS (Aoki et al., 2019; Belyaev et al., 2021; Chaffin et al., 2017; Fedorova et al., 2020). Fedorova et al., 2020 found comparable hygropause altitudes in both hemispheres and we confirm this result, although we find that after the intense activity of the dust storm, overall the hygropause level in the northern hemisphere with a mean altitude about 50 km, is lower compared to the southern hygropause observed at 60-70 km. This is expected since northern autumn is drier at lower altitudes near the troposphere according to Smith, 2002, 2004. This rising of the southern hygropuse also being noticeable at mid-low northern latitudes is due to the expansion of the lower atmosphere caused by the temperature increase. Also in the southern hemisphere, we observe peaks in the hygropause level at $L_S \sim 220^\circ$ and $L_S \sim 260^\circ$ corresponding to observations at ∼60-50°S. We attribute these peaks to two factors: (a) an enhancement of water vapor occurs due to the Hadley cell circulation, whose upwelling branch moves to mid southern latitudes during this period rising water vapor and transporting it northwards across the equator (Steele et al., 2014) and (b) an increase of the temperatures at 50-60 km observed by (López-Valverde et al., 2023) preventing water vapor from condensing.

Latitudinal variation

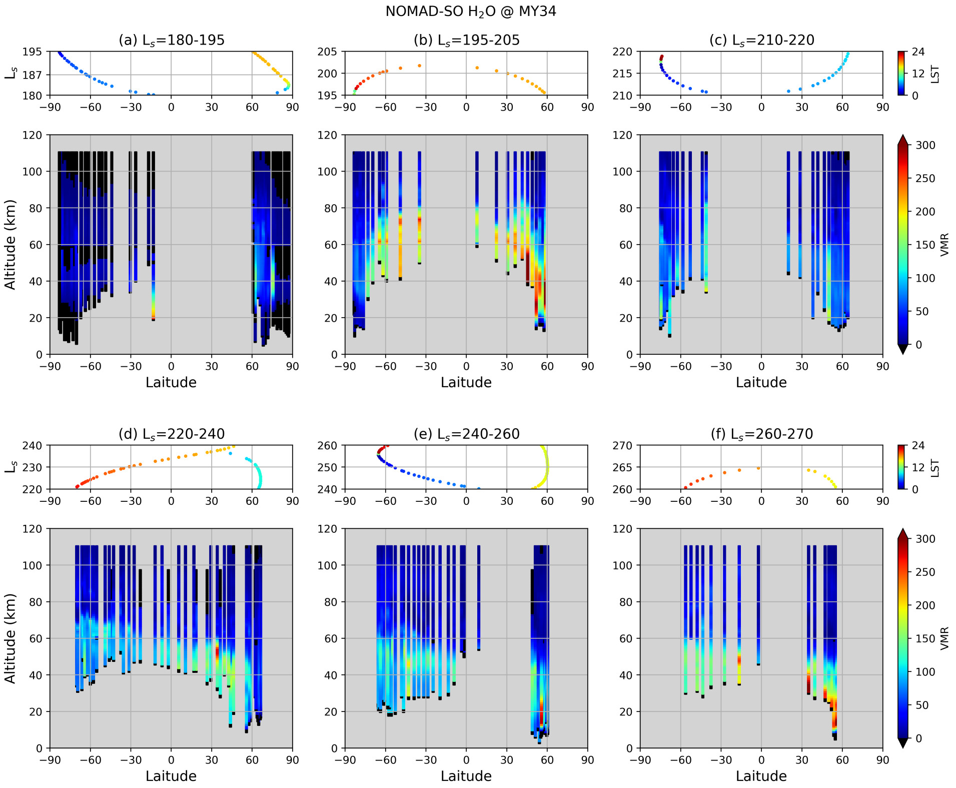

FIGURE 5.14: Latitudinal variation of the water vapor during the southern spring (northern autumn) of MY 34 for the growth (a-c) ad decay(d-f) phase of the GDS. Black regions are masked due to the low averaging kernels obtained during the retrievals.

In Figure 5.14, we show the latitudinal variation of the water vapor for the analyzed period of the MY 34. Panel 5.14a shows the period just before the GDS. We observe a dry atmosphere in both hemispheres with small amounts of water vapor

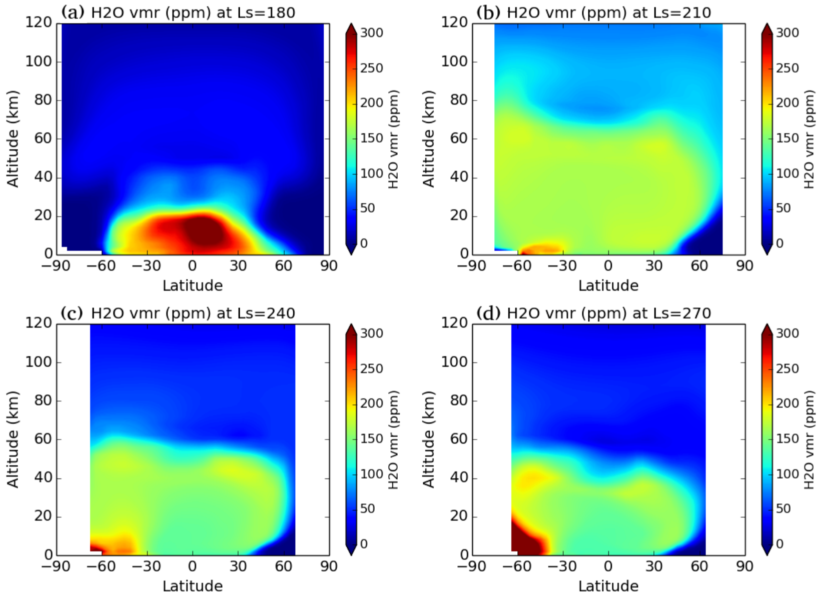

FIGURE 5.15: Latitudinal variation of the water vapor calculated with Mars Planetary Climate Model simulated for the evening terminator for MY 34 at $L_S = 180°$ (a), $210°$ (b), $240°$ (c) and $270°$ (d).

about ∼50 ppmv for the southern hemisphere and ∼100 ppmv present at very high latitudes. In Figure 5.14b, during the period of strong activity of the GDS, we observe a clear increase of the water vapor VMR with the water confined mostly between 60°N and 75°S and reaching altitudes up to 80 km at mid latitudes with abundances about 150 ppmv. After the peak of the GDS, the amount of H_2O in the atmosphere reduces again as shown in Figure 5.14c. Figures 5.14d and 5.14e correspond to the seasonal period deep into the southern spring during $L_S = 220° - 260°$. Here, we observe the effects on the progressive increase of the upper atmosphere temperature, allowing more water vapor be present in the atmosphere. Also more water is progressively available in the atmosphere due to sublimation of the southern polar cap (Villanueva et al., 2022a). We also observe high amounts of water vapor at northern mid latitudes extending up to 50°N with the H_2O confined below 50-60 km, corresponding to the global expansion of the lower atmosphere and the transport northwards by the main equator-crossing Hadley cell (Barnes et al., 2017; Steele et al., 2014). Finally, Figure 5.14f shows the period close to the southern summer, hence temperature in southern hemisphere is expected to increase. Here, we observe the same structure as in Figures 5.14d and 5.14e but presenting larger VMR values and showing overall a wetter atmosphere and revealing an increase in the water being released into the atmosphere. Figure 5.15 shows the latitudinal distribution of water vapor obtained with the Mars PCM at different L_S during the progress of the GDS and noticeably reproduces features observed by NOMAD, although abundances in the model are overestimated particularly during the early decay of the storm.

The results we find here are in line with the conclusions in Aoki et al., 2019, 2022 where an increase in the water vapor abundance in the middle atmosphere was observed at 60°N-60°S during the peak of the GDS. During the decay phase of the GDS Aoki et al., 2019, 2022 found that the water vapor in the middle atmosphere has peaks at latitudes greater than 60°S, which is also observed in this work.

Supersaturation and water ice

The saturation ratio expresses the ratio between the water vapor content present in the atmosphere ($\mu_{\mathrm{H_2O}}$), that is, the retrieved H_2O VMR, over the saturated water vapor (μ_{sat}) as equation 5.3 shows. To calculate the saturated H_2O VMR we use the expression equation 5.4 for the saturation pressure over water ice (since in Mars water vapor condenses solely into ice) by Murphy and Koop, 2005. The uncertainty associated to the saturation ratio (σ_S) showed in equation 5.5 can be obtained through error propagation taking into account the uncertainties of the retrieved H_2O VMR ($\sigma_{\mu_{H_2O}}$) and temperature (σ_T).

$$S = \frac{\mu_{\mathrm{H_2O}}}{\mu_{\mathrm{sat}}} = \mu_{\mathrm{H_2O}} \frac{P_{\mathrm{tot}}}{P_{\mathrm{sat}}} \tag{5.3}$$

$$P_{\mathrm{sat}}(T) = \exp\left(9.550426 - \frac{5723.265}{T} + 3.53068 \cdot \ln(T) - 0.00728332T\right);\ 110 < T < 273\,\mathrm{K} \tag{5.4}$$

$$\sigma_S = \frac{P_{tot}}{P_{sat}} \sqrt{\sigma^2_{\mu_{H_2O}} + \mu^2_{H_2O}\left(\frac{5723.265}{T^2} + \frac{3.53068}{T} - 0.00728332\right)^2 \sigma^2_T} \tag{5.5}$$

In Figures 5.16b-5.16e we present the first maps saturation ratio computed using the retrieved NOMAD SO temperatures for some occultations during MY34 when coincidences with orders 134-168 occur with order 149 López-Valverde et al., 2023. Although the number of processed occultations do not allow a detailed analysis, some structures can be identified. In the northern hemisphere, during the main activity of the GDS at $L_S \sim 200°$ we observe a clear region with supersaturation ($S > 10$) above 60 km up to 100 km. Later at $L_S \sim 230°$ a saturated layer appears at 80-100 km, decreasing in altitude to 60-80 km at $Ł_S \sim 240° - 260°$. In the southern hemisphere, at $L_S \sim 220°$ we observe a clear supersaturated layer at 60-80 km that increases in altitude and thickness as the location of the observations decrease in latitude. The structures described above were also observed by Fedorova et al., 2020 with ACS data. A rough comparison with maps obtained with PCM temperatures (shown in Figures 5.16c-5.16f) can be done. Note that a detailed description of the PCM and NOMAD SO temperatures is presented in (López-Valverde et al., 2023). The main differences we observe appear in: (a) $L_S \sim 230°$ at 90 km and (b) $L_S = 250° - 260°$ at 70 km, both in the northern hemisphere. This supersaturation layers observed with the NOMAD temperatures are not present in the map with PCM temperatures. This layers were also observed by Fedorova et al., 2020 with ACS data and supports the temperature results from (López-Valverde et al., 2023). These features underline the necessity of using measured temperatures for these kind of studies. In future works we will extend the number of occultations with simultaneous H_2O and temperature observations in order to further investigate these and other features which may appear.

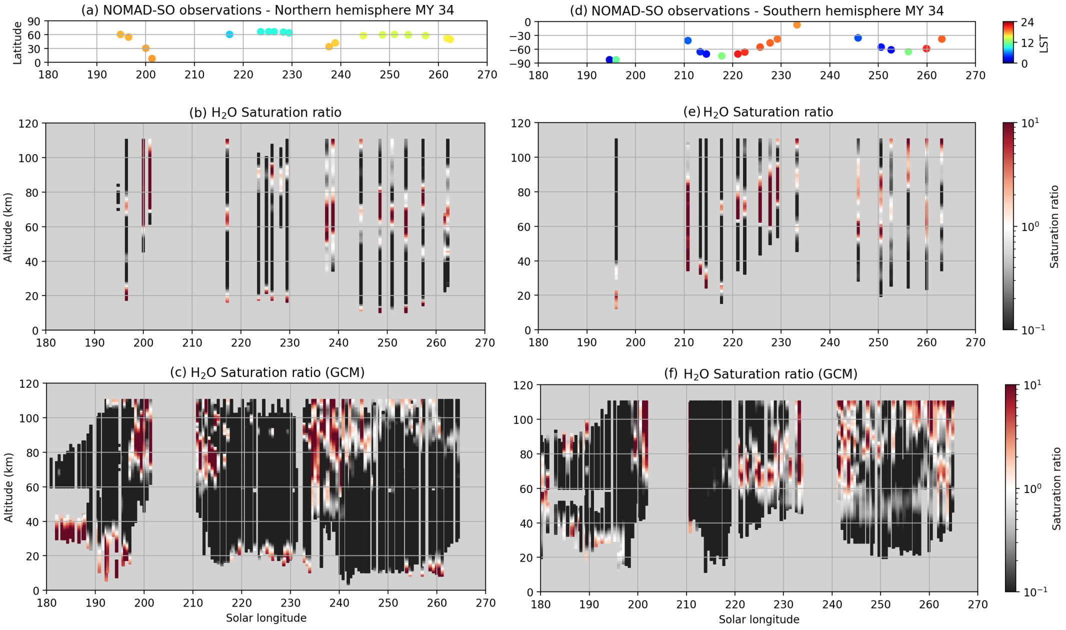

FIGURE 5.16: Saturation ratio calculated using retrieved Nadir and Occultation for MArs Discovery (NOMAD) Solar Occultation (SO) temperatures (middle panels) from López-Valverde et al., 2023 for MY 34 at northern (b) and southern (e) hemispheres. Bottom panels show the saturation ratio obtained from the Planetary Climate Model temperatures for the northern (c) and southern (f) hemispheres. Top panels show the latitudes and the Local Solar Time of the observations analyzed for the northern (a) and southern (d) hemispheres.

Also we analyze the coincidences between estimated supersaturation and water ice detections by Stolzenbach et al., 2023, where a detailed description and characterization of the nature of the Martian aerosols is presented. Here, we use their results on the water ice. In this limited study analyzing the observations with collocated H_2O, temperature and aerosols measurements we have identified a total of 156 supersaturation events, in which about 16% of the events show an H_2O ice mass loading exceeding 10^{-13}g·cm^{-3}. Moreover, we find that most of the coincidences occur at the upper atmosphere between 50-90 km and more than 40% of the cases are confined at 70-80 km. In addition, we observe a few cases where supersaturation occurs towards the top of a cloud layer, as it is shown in the schematic model proposed by Poncin et al., 2022 for the saturation state of the atmosphere in the presence of cloud occurrence. The reduced number of the analyzed profiles for this study does not allow us to draw further conclusions. Four saturation ratio profiles are shown in Figure 5.17. Supersaturated layers can be observed at 80-100 km in Figure 5.17a and at 70 km in Figures 5.17b and 5.17c, all of them coincident with H_2O ice detections and with atmospheric temperatures below the water vapor condensation limit. Figure 5.17d shows an example of a supersaturated layer at 70 km just above an ice cloud at 50 km. This finding with NOMAD SO observations suggests the presence of water ice clouds in a supersaturated atmosphere. Maltagliati et al., 2011a proposed the "scavenging" effect (falling ice cleaning the atmosphere from dust) as the main reason for the existence of supersaturated atmosphere, which would prevent the formation of water ice due to the absence of condensation nuclei. The water ice detected by (Stolzenbach et al., 2023) and the coincidence with supersaturated layers found in this work suggests that this mechanism is not the only reason for the supersaturation on Mars and supports the results by Fedorova et al., 2020 found with ACS who also observed supersaturation in presence of water ice. A specific study on supersaturation with an extended data set will be presented in future works.

5.4.2 Martian Year 35

Seasonal variation

As done in Section 5.4.1, here we present seasonal variation maps the Figure 5.18 for the northern (left panels) and southern (right panels) for MY 35 and an insight on the upper atmosphere in Figure 5.19.

During this year, no GDS took place in the planet, so the usual seasonal trend is expected to be observed. Compared with MY 34, in Figure 5.18 we observe noticeably less water vapor in the atmosphere at the solar longitude range between $L_S = 190° - 230°$ in the northern hemisphere. During this period, we observe a peak in the water vapor abundance at $L_S \sim 205°$ in the southern hemisphere. This feature was also present during the same period in MY 34 but remarkably enhanced by the GDS. It is interesting to point out that the feature observed in the northern hemisphere also at this L_S is no longer present in MY 35. However, the reason of this absence is not only the non-GDS conditions during MY 35 but also the latitudinal coverage of the observations with measurements mostly at high latitudes (+75°N) near the northern polar cap. Similarly to what we observe during MY 34, as the southern spring progresses and southern summer kicks in, the water vapor present in the southern hemisphere increases revealing high abundances in the period between $L_S = 230° - 270°$ due to seasonal dust activity. Comparing the same period of these two Martian years, we notice larger abundances in the southern hemisphere during the last one, with water vapor reaching volume mixing ratios about 100 ppmv up to 80 km at at high latitudes during the perihelion, even reaching abundances >50 ppmv at 100 km at $L_S \sim 260°$ as shown in Figure 5.19, also reported by Belyaev et al., 2021. In contrast, northern hemisphere shows a similar seasonal trend in both Martian years, with the water vapor mostly confined below 50 km at midlatitudes.

(a) 20180628_051615_1p0a_SO_A_I | L_s = 201.0° | Lat = 8.0°

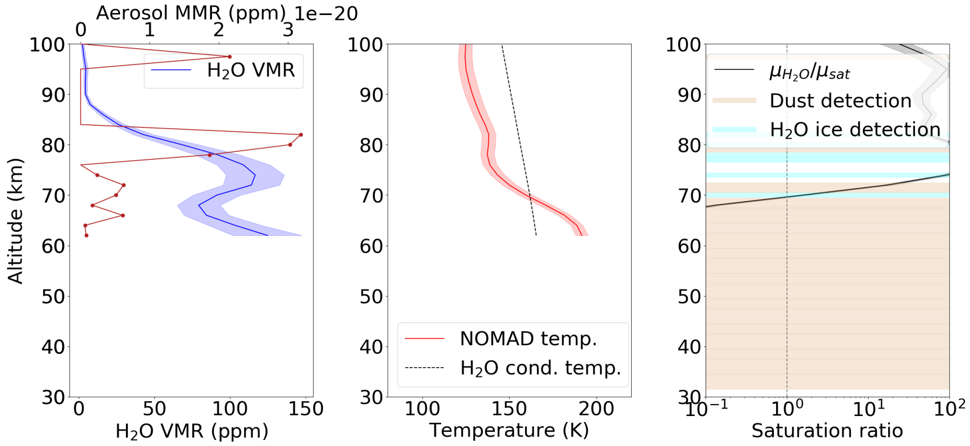

(b) 20180826_005011_1p0a_SO_A_I | L_s = 238.0° | Lat = 34.0°

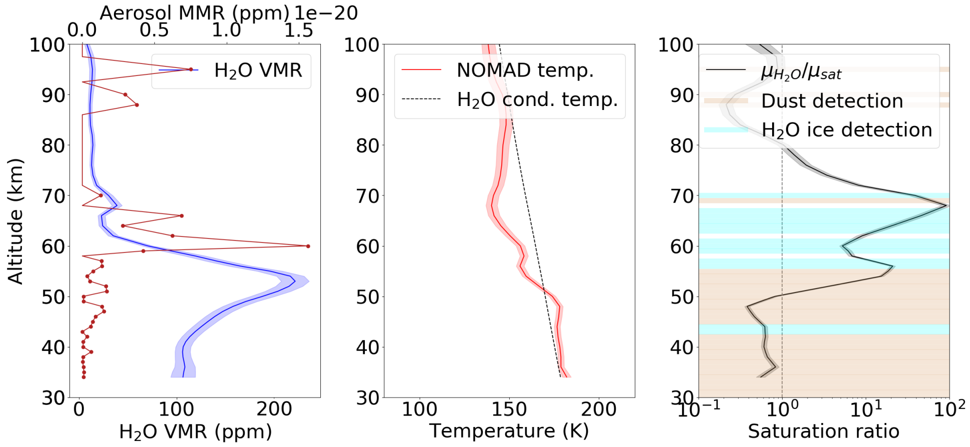

FIGURE 5.17: Profiles of water vapor, aerosols mass mixing ratio (MMR), temperature and water saturation ratio for four Nadir and Occultation for MArs Discovery (NOMAD) Solar Occultation (SO) observations. Left subpanel: Water vapor VMR (blue) and aerosol MMR (dark red). Center subpanel: NOMAD temperature (red) and water vapor condensation temperature (dashed). Right subpanel: Water saturation ratio (black), water ice detections (light blue) and dust detections (light brown). Vertical dashed line shows saturation ratio equal 1.

Hygropause

Figure 5.20 shows that the hygropause in the northern hemisphere is mostly confined below 30 km at high latitudes. However, at midlatitudes and low latitudes close to the equator, the hygropause level ascends up to 50-60 km. Compared to MY 34, during the period between $L_S = 190^\circ - 210^\circ$, the effects of the GDS are clearly visible, when hygropause near the equator reached an altitude about 80 km. The second part of the season is similar in both Martian years due to the similar dust conditions. In the southern hemisphere, looking at high latitudes we clearly observe how the hygropause increases in altitude as the spring progresses. With the water vapor mostly confined in the lower atmosphere at the beginning of the season, the hygropause level starts rising reaching an altitude of ~80 km at the end of the spring.

(c) 20180807_004441_1p0a_SO_A_I | L_s = 226.0° | Lat = -55.0°

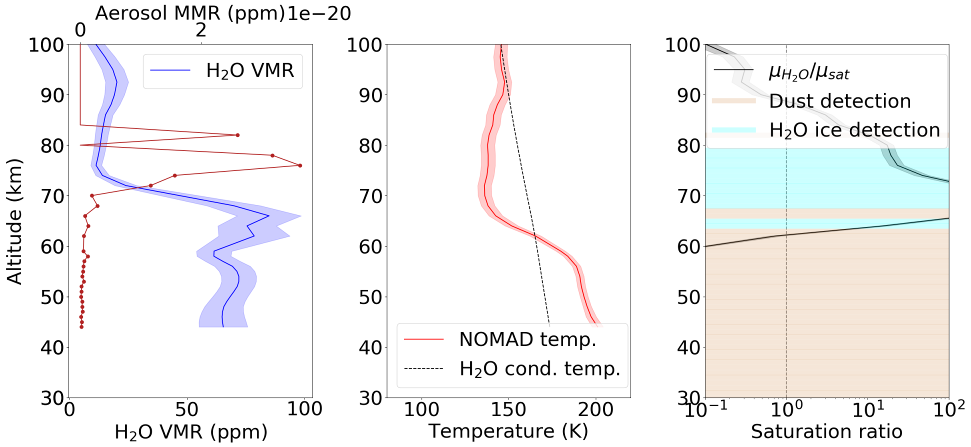

(d) 20180920_135655_1p0a_SO_A_I | L_s = 254.0° | Lat = 60.0°

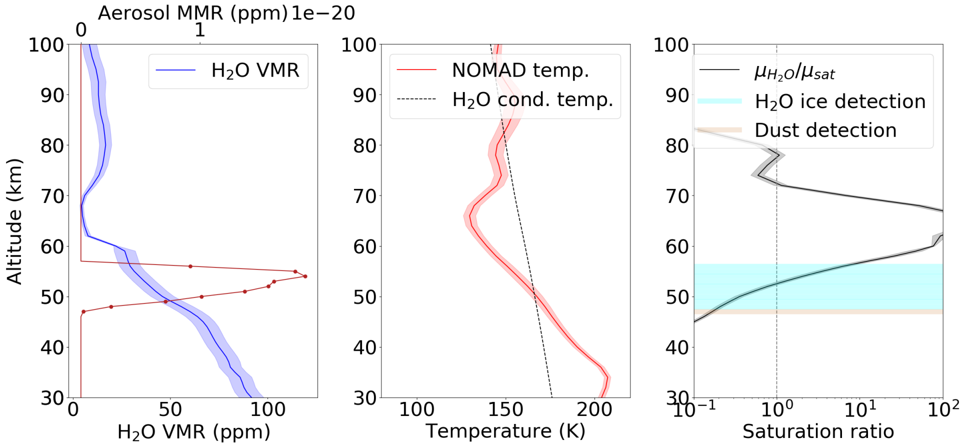

FIGURE 5.17: (continued)

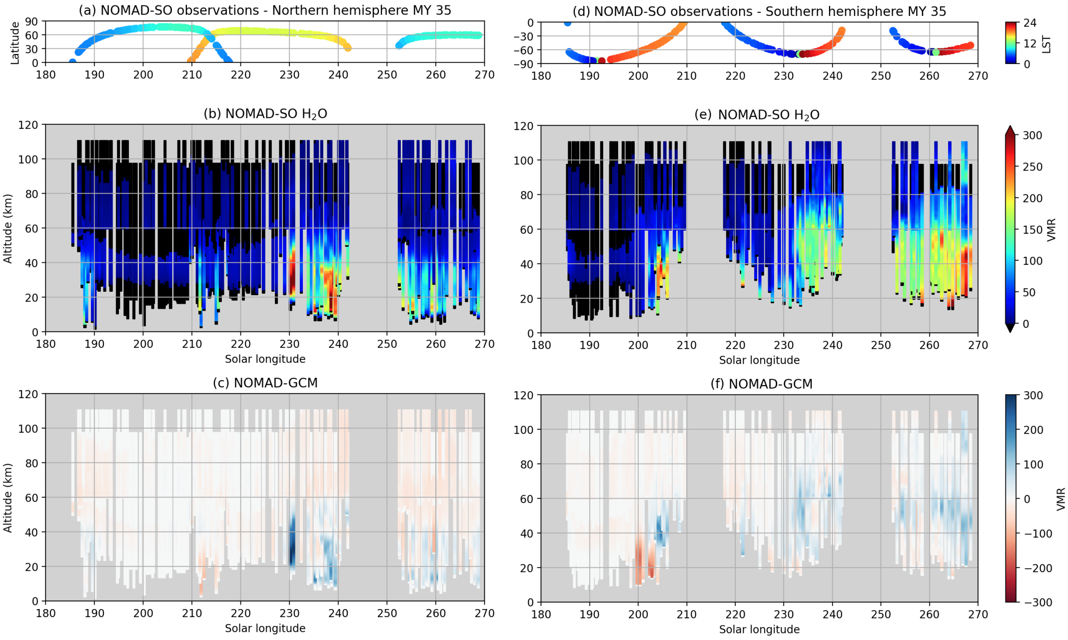

FIGURE 5.18: Seasonal vertical distribution maps of the retrieved water vapor (b and e) and the differences between the Nadir and Occultation for MArs Discovery (NOMAD) Solar Occultation (SO) retrievals and the Planetary Climate Model climatology (c and f) during the MY 35 in the northern (left panels) and the southern (right panels) hemispheres. Top panels (a and d) show the latitudes and the Local Solar Time of the observations analyzed. Black regions in panels (b and f) are masked due to the low averaging kernels obtained during the retrievals.

It is interesting to remark that in this year without a GDS, the topmost altitude we observe for the hygropause at $L_S = 240° - 260°$ is 10 km higher than in the same period of MY 34, although the temperature observed by ACS shows a similar trend in both MYs at this period Alday et al., 2021; Belyaev et al., 2021. Therefore, differences in the latitudinal sampling could be a possible explanation of this feature (Aoki et al., 2022).

Latitudinal variation

In Figure 5.21 we show the latitudinal maps of the water vapor distribution during the analyzed period of MY 35, covering the same L_S ranges as in Figure 5.14 for a direct comparison between both MYs. Regardless of the poor coverage of the northern hemisphere, panel 5.21b clearly show differences with the same panel in Figure 5.14 revealing that in this period water vapor is mostly confined below 45 km and in latitudes lower than 50°S. This observation agrees with the expected climatology according to the Mars PCM. Figure 5.22 shows the modeled latitudinal variation of the water vapor VMR by the PCM, and it proves again the strong effects of the GDS with noticeable differences between panels 5.15b and 5.22b. As spring develops, we observe the expected seasonal trend in Figures 5.21d-5.21f, showing the same structure observed during in MY 34 due to the increase of the atmospheric

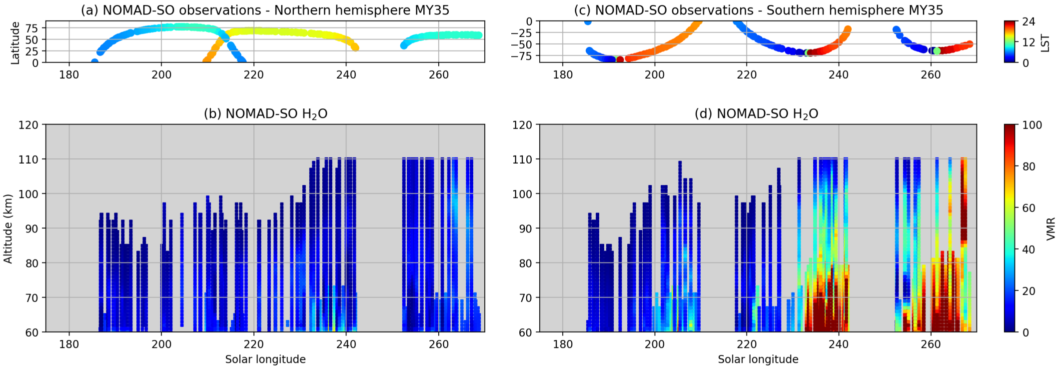

FIGURE 5.19: Seasonal vertical distribution maps of the retrieved water vapor at the upper atmosphere above 60 km during the MY 35 in the northern (b) and the southern (d) hemispheres. Top panels (a and c) show the latitudes and the Local Solar Time of the observations analyzed.

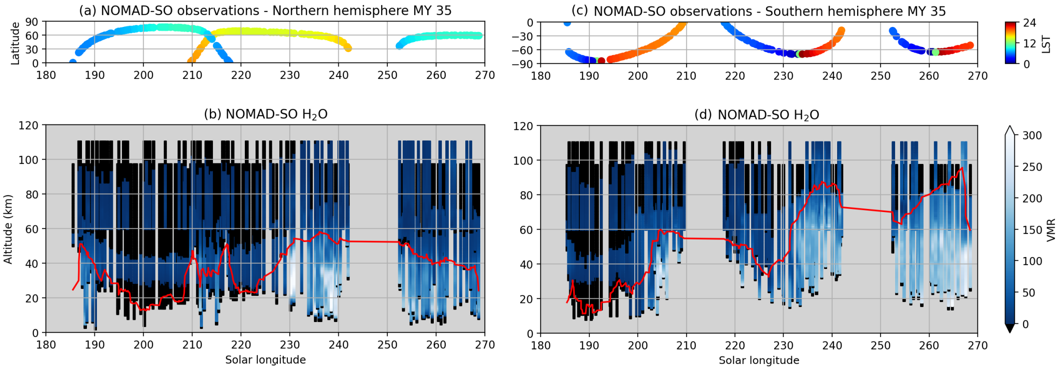

FIGURE 5.20: Seasonal vertical distribution maps of the retrieved water vapor (b,d) during the MY 35 in the Northern (left panels) and the Southern (right panels) hemispheres. The red line indicates the hygropause level. Top panels (a and c) show the latitudes and the Local Solar Time of the observations analyzed.

temperature and the regular dust activity. Also, the observed water vapor in this period in both years agree with the expected climatology simulated by the PCM as shown in Figure 5.15.

5.5 Summary and conclusions

In this work we have presented the water vapor vertical distributions obtained for the first half of the perihelion season during Martian years 34 and 35, covering the GDS event of 2018 and hence characterizing the water vapor under GDS and non-GDS conditions. The direct comparison of the same season with different dust configurations during $L_S \sim 180^\circ - 210^\circ$ allowed us to confirm the strong impact of a global dust event in the water distribution previously reported by MCS (Heavens et al., 2018), ACS (Alday et al., 2021; Belyaev et al., 2021; Fedorova et al., 2020) and NOMAD (Aoki et al., 2019; Liuzzi et al., 2020; Villanueva et al., 2021) observations.

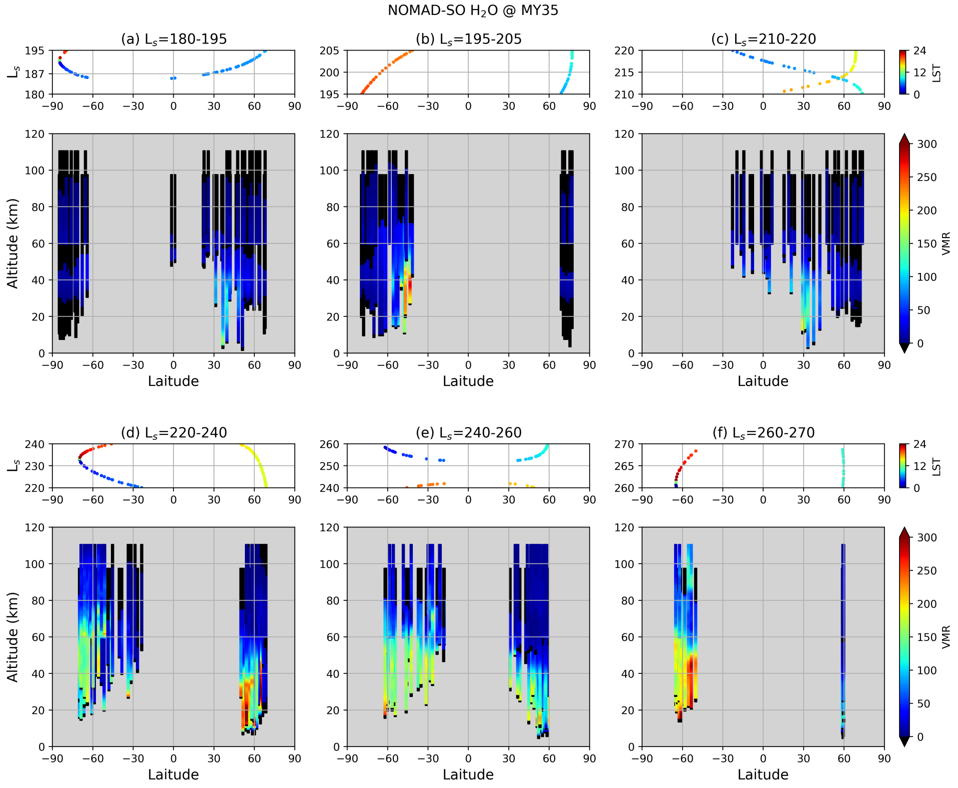

FIGURE 5.21: Latitudinal variation of the water vapor during the southern spring (northern autumn) of MY 35. Panels (a-f) show the same solar longitud ranges as in Figure 5.14. Black regions in panels b and f are masked due to the low averaging kernels obtained during the retrievals.

The vertical profiles presented here have been obtained retrieving data from the NOMAD SO diffraction orders 134 and 168 and using the a priori density and temperature profiles from the Mars PCM (Forget et al., 1999; Lefèvre et al., 2021), being the assumed profiles of minor importance for H_2O. The main findings we report are as follows:

- During the strong activity of the GDS, we observe an intense peak in the water vapor showing abundances about 150 ppmv at 80 km in both hemisphere. After this short period, the abundance reduces to 50 ppmv in northern hemisphere and the high water vapor is only visible again at high southern latitudes. In contrast, during MY 35, water vapor does not exceed abundances of 50 ppmv above 50 km in the northern hemisphere.
- Due to the GDS peak, water vapor is mostly confined between 60°N and 75°S and revealing high abundances up to 80 km at midlatitudes and low latitudes close to the equator. This distribution is not observed during the same period of MY 35.
- At high southern latitudes, we observe large water vapor abundances up to altitudes as high as 60 km, indicative of a warmer atmosphere during the

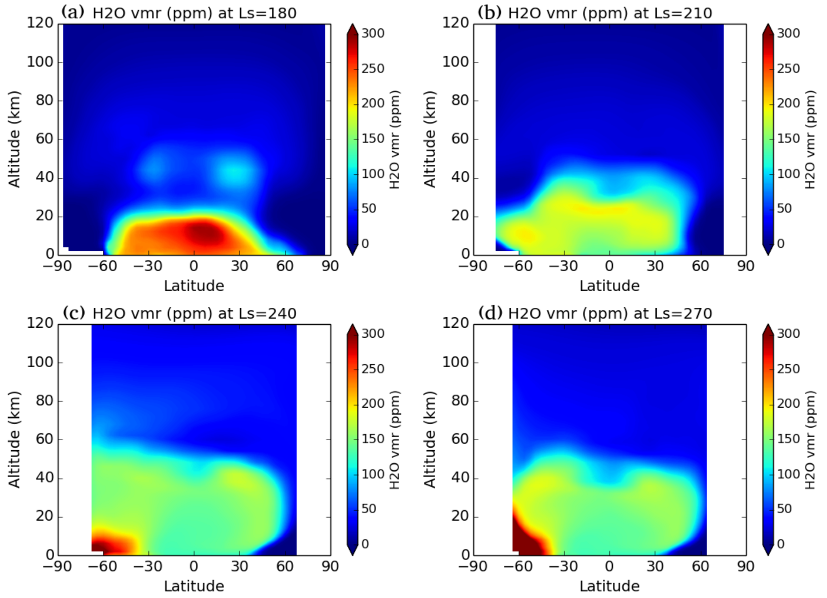

FIGURE 5.22: Latitudinal variation of the water vapor calculated with Mars Mars Planetary Climate Model simulated for the evening terminator for MY 35 at $L_S = 180°$ (a), 210° (b), 240° (c) and 270° (d).

period close to the southern summer solstice ($L_S = 220° - 270°$). This feature is observed in both MYs possibly due to similar dust conditions after the GDS.

- We report an estimation of the saturation ratio calculated using NOMAD SO temperatures, revealing multiple layers of supersaturation for MY 34. During the GDS, a clear region is observed above 60 km in both hemispheres where saturation ratio is greater than 10. Similar features are observed during the decay phase of the storm, revealing supersaturation layers above regions with high water vapor abundances in the middle atmosphere.

- We identify supersaturated layers in the presence of water ice, indicative of a condensation process going on at the terminator at the precise moment and local time of the NOMAD observations.

- The comparison of H_2O distributions derived from TGO SO data with other teams shows a qualitative agreement, although some discrepancies can be observed in the altitude range between 10-20 km, the origin of which needs to be further investigated in future works.

We plan to extend the data set analyzed here to explore the later half of the perihelion season and further, to study the whole NOMAD SO data set available to date. We also plan to revisit the saturation maps presented here using NOMAD temperatures and also to extend and gain more insight into correlation between water ice and supersaturation.

Chapter 6

High Altitude Water Vapor During the Perihelion Season

This Chapter is based on the publication: "Strong localized pumping of water vapor to high altitudes on Mars during the perihelion seasons"
Accepted in Geophysical Research Letters, July 2024

This Chapter is based on the publication: "Strong localized pumping of water vapor to high altitudes on Mars during the perihelion seasons" Accepted in Geophysical Research Letters, July 2024

Abstract

Here we present water vapor vertical profiles observed with the ExoMars TGO/NOMAD instrument during the perihelion and Southern summer solstice season (L_S =240°-300°) in three consecutive Martian Years 34, 35 and 36. We show the detailed latitudinal distribution of H_2O at tangent altitudes from 10 to 120 km, revealing a vertical plume at 60°S - 50°S injecting H_2O upward, reaching abundance of about 50 ppmv at 100 km. We have observed this event repeatedly in the three Martian years analyzed, appearing at $L_S = 260^\circ - 280^\circ$ and showing inter-annual variations in the magnitude and timing due to long term effects of the MY 34 Global Dust Storm. We provide a rough estimate of projected hydrogen escape of 3.2×10^9 $cm^{-2}s^{-1}$ associated to these plumes, adding further evidence of the key role played by the perihelion season in the long term evolution of the planet's climate.

6.1 Introduction

The thin atmosphere we observe at Mars nowadays makes the planet cold and dry. In an atmosphere dominated by CO_2, water vapor only represents a small fraction of the total atmospheric composition (∼0.03 %). Spacecraft observations have provided valuable insights into the H_2O behavior on Mars. In the current Martian climate, H_2O shows a large variability throughout the year, involving sublimation and condensation processes affected by dust and atmospheric transport (Montmessin et al., 2017). This cycle is also known to present strong latitudinal gradients, as reported by the Thermal Emission Spectrometer (TES) by using column densities (Smith, 2002). However, until the last decade, the knowledge about the water vapor vertical structure and the latitudinal variations at high altitudes was limited. Solar occultation (SO) observations allowed to explore the atmospheric vertical distribution in unprecedented detail. A few instruments, the Spectroscopy for the Investigation of the Characteristics of the Atmosphere of Mars (SPICAM) onboard

Mars Express (MEX) and Auguste onboard the Phobos-2, have provided vertical profiles of the martian atmosphere using SO observations (Fedorova et al., 2009, 2018b, 2021; Maltagliati et al., 2011a, 2013) and others, the Compact Reconnaissance Imaging Spectrometer for Mars (CRISM) and the Mars Climate Sounder (MCS), both on board Mars Reconnaissance Orbiter (MRO) used limb observations for indirect information on H_2O abundance (Clancy et al., 2012, 2017b; Heavens et al., 2018).

The first SO and water vapor vertical profiles on Mars were obtained with the Auguste spectrometer (Rodin et al., 1997). With SPICAM and mostly limited to an altitude below 70 km, some of the first dedicated studies on H_2O vertical profiles were done by Fedorova et al., 2009. Later, Maltagliati et al., 2011a, 2013 reported evidence of H_2O present in excess of saturation (supersaturation) during the Northern summer and showed for the first time H_2O vertical profiles during a full Martian Year (MY). They found a strong variability of the profiles and reported discrepancies with General Circulation Models (GCMs). More recently, Fedorova et al., 2021 presented the first multiyear survey of water vapor vertical distribution obtained from SPICAM observations.

Similarly, Clancy et al., 2017b analyzed the seasonal and global variability of H_2O profiles which were derived from CRISM O_2 emission rates. They claimed difficulties in the accuracy of modeling cloud microphysics in Mars GCM simulations. Later, Fedorova et al., 2018b reported an enhancement of the H_2O abundance in the middle atmosphere during the 2007 dust storm and Chaffin et al., 2017 showed how this led to an increase of the escape rates of hydrogen. This was also studied by Heavens et al., 2018 using estimates of middle atmospheric water vapor and ice content from the distribution of water ice clouds and temperature observed with MCS. This phenomenon was observed again during the 2018 Global Dust Storm (GDS) with the Nadir and Occultation for MArs Discovery (NOMAD) and Atmospheric Chemistry Suite (ACS) instruments, both onboard the ExoMars Trace Gas Orbiter (TGO) (Alday et al., 2021; Aoki et al., 2019, 2022; Belyaev et al., 2021; Brines et al., 2023e; Fedorova et al., 2020, 2023; Vandaele et al., 2019; Villanueva et al., 2021) and also with the SPICAM instrument, whose observations were compared to the GDS of MY 28 (Fedorova et al., 2021). These recent works analyzed H_2O vertical distribution up to 100 km thanks to the high sensitivity of the instruments.

Aoki et al., 2019; Vandaele et al., 2019 and Fedorova et al., 2020 reported an increase in the H_2O abundance between 40-80 km during the GDS, the latter showing dust playing a significant role in altering atmospheric dynamics during dust storms. These events lift dust particles into the atmosphere modifying the temperature profiles due to the dust radiative heating Neary et al., 2020 and preventing H_2O condensation even at high altitudes, enhancing hydrogen escape (Heavens et al., 2018). Belyaev et al., 2021 presented profiles in the upper mesosphere reporting similar water abundance during the GDS and perihelion periods. Brines et al., 2023e showed the effects of the GDS comparing the southern spring season during MYs 34 and 35 and reported supersaturation events in presence of water ice, a phenomenon also found by (Fedorova et al., 2020, 2023) at high altitudes. This is in line with the study presented by Poncin et al., 2022, in which, on average, large parts of the atmosphere were observed to be close to saturation, although typically at lower altitudes than those observed by Fedorova et al., 2023. Villanueva et al., 2021 reported an increase of the H_2O in both abundance and altitude during the beginning of the Southern summer, but they only retrieved H_2O up to 100 km for one MY and did not focus the analysis on this feature, as done in this paper. This localized phenomenon was studied by Shaposhnikov et al., 2019, who modeled mechanisms responsible for the upward water transport at high southern latitudes during the perihelion season. The injection of water during this season was previously noticed by SPICAM during multi-annual monitoring (Fedorova et al., 2021), where they observed H_2O at high altitudes repeatedly during the southern summer, confirming a seasonal impact on the hydrogen escape rate.

Here, building upon previous NOMAD water vapor retrievals from Brines et al., 2023e, we introduced several improvements which provide H_2O with an optimal vertical resolution from about 10 to 120 km. This work analyzes with an unprecedented detail the vertical distribution of H_2O during the perihelion (L_S~250°) and southern summer solstice (L_S~270°) of three consecutive MYs, which besides the dust storms, is claimed to be the season driving the escape of hydrogen to space (Jakosky, 2021; Mayyasi et al., 2023). We focused the analysis on the upper mesosphere, showing for the first time latitudinal structures from 60 to 120 km.

The NOMAD instrument and the data analysis are described in Section 6.2. In Section 2.3.1 we provide information about the parameterization of the NOMAD SO characterization. Details about the methodology used during the data analysis are presented in A.1. The main results are presented in Section 6.3. Extended interpretation of the observations and conclusion are given in Sections 6.4 and 6.5 respectively. In A.2 we show a comparison of three Forward Models (FMs), used to perform an internal validation of the NOMAD characterization and its implementation into the simulations.

6.2 Data analysis

The NOMAD instrument is a suite of three spectrometers (channels) covering spectral regions between 0.2 to 4.3 µm. It observes the Martian atmosphere with three channels in different geometries: Solar Occultation (SO) and limb/nadir observation (LNO). A third channel observes the atmosphere in both configurations (UVIS). Each channel is equipped with its own set of optics and detectors (Vandaele et al.,

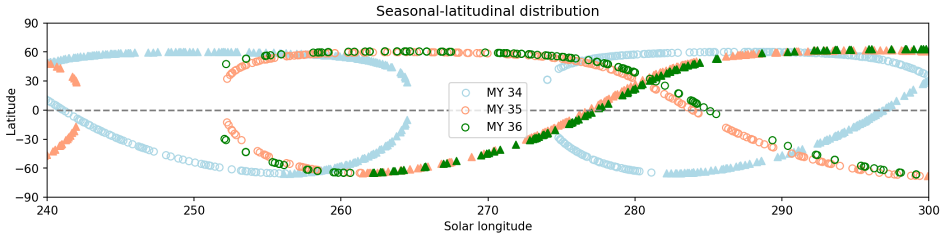

FIGURE 6.1: Latitude of the analyzed NOMAD SO observations over solar longitude for MYs 34 (blue), 35 (orange) and 36 (green). Horizontal dashed line indicates the equator. Morning and evening terminator occultations are indicated with circles and triangles respectively.

2018). The SO channel operates in the infrared covering a spectral range between 2.3 to 4.3 μm (2320 - 4350 cm^{-1}) using an echelle grating in Littrow configuration with a resolving power around 17000. NOMAD uses an Acousto-Optical Tunable Filter (AOTF) to separate diffraction orders on the detector plane. In addition, the dispersion and diffraction effects of the light throughout the whole optical system affects the signal reaching the detector introducing an instrumental effect to the spectral lines. Typically, the Instrumental Line Shape (ILS) can be modeled by convolving the monochromatic spectrum with a Gaussian kernel. However, the NOMAD data exhibits an asymmetric ILS with an extended left wing of the Gaussian. This feature can be instead reproduced with a double Gaussian whose separation varies with frequency and diffraction order (Thomas et al., 2022; Villanueva et al., 2022a). More details about the NOMAD AOTF and ILS characterization are summarized in 2.3.1.

For this study we selected 1065 occultations taken with the NOMAD SO channel. The selected observations cover the perihelion and the southern summer solstice season of three consecutive MYs (34, 35 and 36) with Solar Longitude (L_S) ranging from $L_S = 240°$ to $L_S = 300°$. The seasonal-latitudinal distribution of the occultations is shown in Figure 6.1.

We used Level 1 calibrated transmittances processed by the Belgian Institute for Space Aeronomy (BIRA-IASB) (Trompet et al., 2023), which were revised by our in-house pipeline to clean them from residual spectral shifts and bending at each altitude. The IAA-preprocessing includes the latest NOMAD instrument characterization (Villanueva et al., 2022a) and uses the state-of-the-art line-by-line Karlsruhe Optimized Radiative transfer Algorithm (KOPRA) during the cleaning (Brines et al., 2023e; López-Valverde et al., 2023).

For the inversions we selected spectra from the NOMAD diffraction orders 134 (3011-3035 cm^{-1}) and 136 (3056-3081 cm^{-1}) both containing lines with intensities of about 10^{-21} cm^{-1}/(molecule · cm^{-2}), and from orders 168 (3775-3805 cm^{-1}) and 169 (3798-3828 cm^{-1}), these two with stronger line intensities of about 10^{-19}

$cm^{-1}/(molecule \cdot cm^{-2})$ from the ν_3 fundamental band. These line intensities and their broadening coefficients used in this study are defined for the standard HITRAN atmosphere (1 atm, 296 K) Gordon et al., 2022. Although those coefficients are given for air (Earth atmosphere), we performed sensitivity tests comparing KOPRA simulations using the default HITRAN linelist and the list provided by (Gamache et al., 2016) for its application to CO_2-rich atmospheres. Our results showed that at the optically thin region of the diffraction orders used in this work, the differences in transmittance between both simulations was below the measurement noise ($< 10^{-4}$). Therefore, we decided to use the latest linelist available from Gordon et al., 2022 with standard H_2O line parameters.

Considering this, we used spectra from orders 134 and 136 for the lower atmosphere and from orders 168 and 169 for the upper atmosphere, typically covering an altitude range from 0 to 60 km and from 60 to 120 km respectively. This way, following a similar approach as in Brines et al., 2023e we extended their methodology from two to four diffraction orders using different orders for different altitude ranges in order to avoid optically thick (saturated) absorption lines present in orders 168 and 169 at low altitudes. We improved our retrieval scheme in three ways.

First, we optimized our pipeline in order to handle two diffraction orders simultaneously. Before we were combining two separate inversions, one for each diffraction order, as if they were different measurements. Now, we perform a common global fit of the spectra in the two diffraction orders at once. The selected occultations contain pairs of diffraction orders with at least one of the low altitude orders (134, 136) and one of the high altitude orders (168, 169). This is the optimal way to combine diffraction orders which sample different altitude ranges, avoiding artifacts and ad-hoc assumptions in the transition regions. Details about the combination of orders are presented in 4.4.

Second, and in support of the previous point, we introduced an automatic selection of the transition region for the merging of the low/high altitude diffraction orders. This is based on a computation of the altitude where the H_2O lines become optically thick, analyzing how the shape of the absorption lines observed by NOMAD changes with altitude in orders 168 and 169. A typical H_2O profile in Figure 6.2-A shows how orders 134 (red) and 168 (orange) were combined during the inversion of the solar occultation 20200828_130241_1p0a_SO_A_E. Dashed line shows the transition altitude and gray shaded area indicates the transition range where spectra from both orders do contribute at the same time during the retrieval.

And third, we developed an in-house tool to improve the characterization of the NOMAD SO measurement noise. This is necessary because our retrieval scheme is

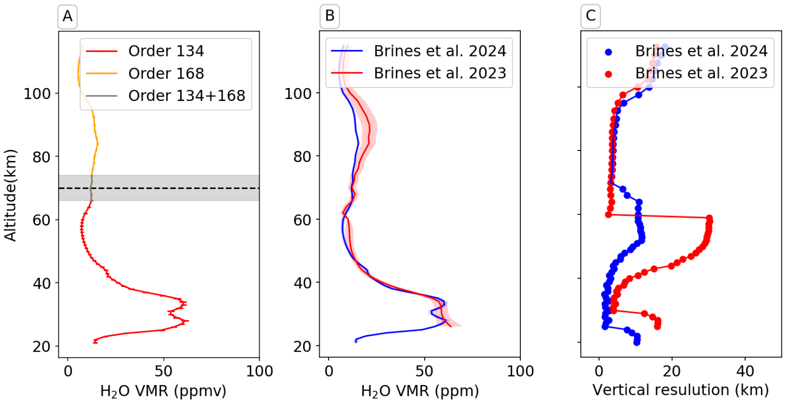

FIGURE 6.2: Water vapor vertical profiles retrieved from the occultation 20200828_130241_1p0a_SO_A_E. Panel A shows a typical H_2O vertical profile retrieved combining orders 134 (red) and 168 (orange). Horizontal dashed line indicates the transition altitude z^0 between the orders and gray shaded area shows the transition range where spectra of both orders were used during the inversion. Panels B and C show a side by side comparison of a water vapor profile and its vertical resolution respectively using the retrieval scheme presented here (blue) with Brines et al., 2023e (red). Vertical resolution in panel C at 30 km is about 2 km (blue).

optimized to assume the measurement uncertainties as pure uncorrelated random noise. However, the uncertainties provided within the Level 1 calibrated data (Thomas et al., 2022) do not differentiate between systematic and random noise. In order to quantify and correct for the systematic component, we performed an analysis of the spectra at every SO using covariance matrices, allowing us to characterize the random noise of the data. As a result, we are improving the sensitivity and performance of the inversions in the upper atmosphere (90-120 km). A description of the measurement noise characterization is presented in 4.3.

Using the modification previously described we managed to improve the retrieved water vapor, obtaining continuous vertical profiles with better vertical resolution compared to the results from Brines et al., 2023e, typically ∼2 km (larger than the NOMAD field of view (Vandaele et al., 2018)). Specifically, as shown in Figure 6.2 (panels B and C), this improvement can be seen around the transition region from the lower to the upper atmosphere (50-70 km). We performed the inversion of the selected data set following the convergence criteria presented in Brines et al., 2023e. The retrievals were performed using the Retrieval Control Program (RCP) developed at the Institut für Meteorologie und Klimaforschung (IMK) which incorporates KOPRA as FM. For the a priori atmosphere we followed the same approach presented in Brines et al., 2023e. That is, during the retrieval process we used total atmospheric densities and temperature-pressure profiles derived from specific runs of the Mars Planetary Climate Model (Forget et al., 1999) developed at the Laboratoire de Météorologie Dynamique (LMD Mars PCM) at the exact location and time of the NOMAD observations. As discussed in Brines et al., 2023e, our H_2O retrieval scheme has low sensitivity to changes in temperature profiles. We performed several sensitivity tests in order to estimate the expected errors due to our PCM assumption. Performing retrievals changing the apriori temperature profile by ±5 K had an impact of 2% on the retrieved water vapor VMR while introducing an oscillation in the pressure profile with an amplitude of 10% had an overall impact of less than 4% in the retrieved water vapor number density. During the inversion, we used a first order Tikhonov-type regularization optimized for each diffraction order.

A precise FM requires a precise characterization of the instrumental response. Since Brines et al., 2023e, we are implementing the latest description of the NOMAD SO (Villanueva et al., 2022a). With the objective of validating this implementation and to unify the criteria used by other teams within the NOMAD consortium, we performed an extensive comparison of the FMs used by the main groups actively analyzing H_2O on Mars with NOMAD SO data. These teams are: Instituto de Astrofísica de Andalucía (IAA-CSIC), Tokyo University, Royal Belgian Institute for Space Aeronomy (ISAB-BIRA), and NASA Goddard Spaceflight Center. This work revealed a remarkable agreement between the FM used by the teams, showing discrepancies below 0.2% when comparing high resolution simulations. A summary is presented in A.2.

6.3 Results

6.3.1 Latitudinal variation

The eccentricity of the Martian orbit is known to significantly enhance the solar flux reaching the planet during the perihelion season (Smith et al., 2017), enhancing the wind stress near the surface and the lifting of dust, which in turn absorbs more solar radiation and heats the atmosphere, making the southern summer ($L_S = 270° - 360°$) the warmest and most humid season on Mars. This affects the meridional circulation and vertical transport of water vapor, both being intensified during this season. As mentioned in Section 6.1, during the perihelion season there are strong gradients in the latitudinal distribution of water column abundance. In order to explore its vertical structure, we studied different L_S periods through the southern spring and summer seasons. We selected observations during and after the perihelion season, covering L_S ranges $L_S = 240° - 260°$, $L_S = 260° - 280°$ and $L_S = 280° - 300°$ (denoted L_S^1, L_S^2 and L_S^3 respectively) of MYs 34, 35 and 36. The latitudinal distribution of H_2O is presented in Figure 6.3. We have binned the retrieved profiles in 5° latitude intervals. The bins were calculated with a weighted average of all the profiles within the interval, according to its retrieved uncertainty. Due to the TGO orbital configuration, the L_S^2 range of MY 34 observations is different from the range selected for MYs 35 and 36. The selected ranges optimize the latitudinal coverage. During these L_S periods, we observed a vertical column of H_2O (denoted as "plume") with abundance of about 50 ppmv at 60°S-30°S reaching altitudes up to 100 km during L_S^2 in MYs

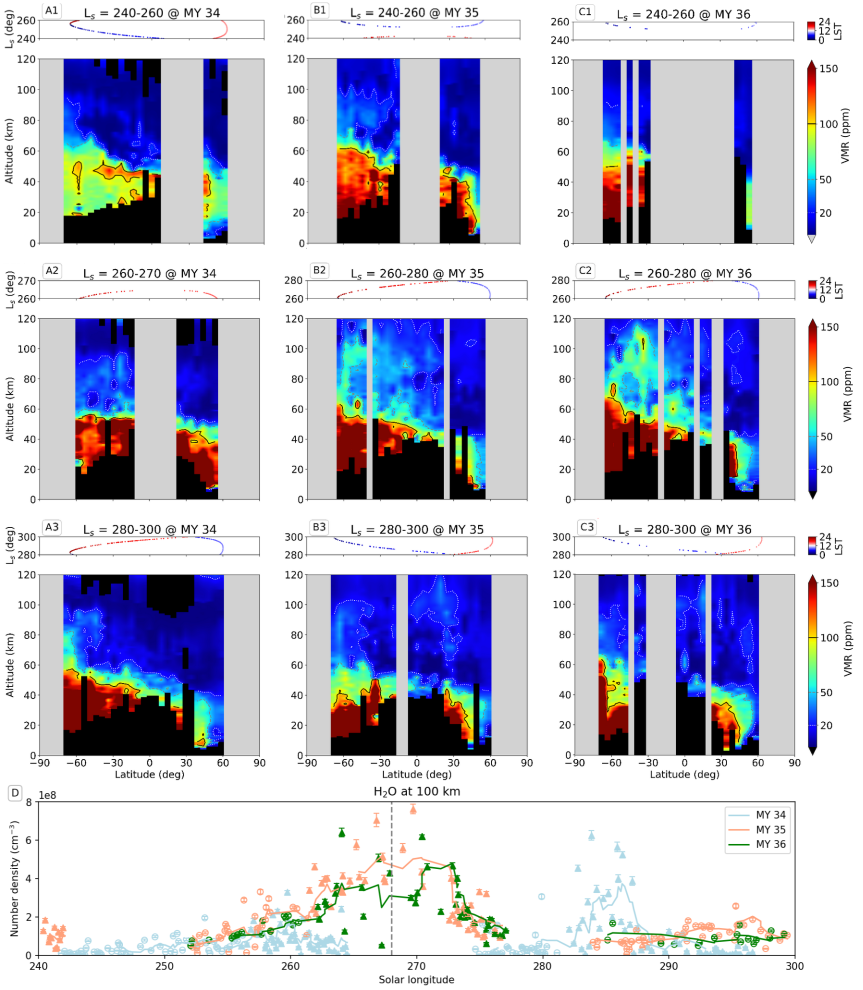

FIGURE 6.3: Water vapor latitudinal variation during L_S^1=240°-260° (A1, B1, C1), L_S^2=260°-280° (A2, B2, C2) and L_S^3=280°-300° (A3, B3, C3) for MYs 34 (left), 35 (middle) and 36 (right). Lines show VMR contours at 100 (black), 50 (gray) and 20 (white) ppmv. Dots in panels A1-A3, B1-B3, C1-C3 indicate the latitude, Solar Longitude and Local Solar Time of the observations. Panel D shows the seasonal variation of water vapor number density (cm^{-3}) in the southern hemisphere at 100 km for L_S = 240°-300° during MYs 34 (blue), 35 (orange) and 36 (green). Vertical dashed line indicates the peak of the plume observed at 100 km during MYs 35 and 36 at L_S = 268°. Solid lines show the seasonal average. In panel D, morning and evening terminator occultations are indicated with circles and triangles respectively

35 and 36 (Figures 6.3B2 and 6.3C2). MY 34 also showed a similar structure but with reduced abundance and with a peak showing up later in time (Figures 6.3A3 and 6.3D). In the three MYs, NOMAD observations do not reveal any significant water injection above 80 km prior to L_S~260° (Figures 6.3A1, 6.3B1 and 6.3C1). In the Northern hemisphere, the H_2O obtained is mostly confined below 40 km and at low-mid latitudes, as expected during the winter season (Montmessin et al., 2017).

We compared our H_2O results with data derived from ACS MIR observations

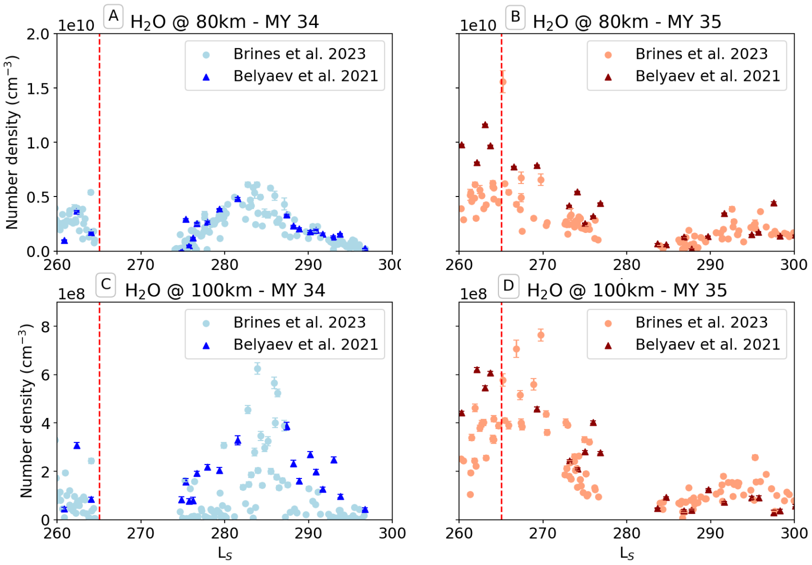

FIGURE 6.4: Seasonal variation of water vapor number density (cm^{-3}) in the southern hemisphere at 80 km for $L_S = 260° - 300°$ during MYs 34 and 35 (panels A and B) and at 100 km for the same period (panels C and D). Circles represent the observations presented in this work and triangles show data from Belyaev et al., 2021. Vertical red dashed line indicates $L_S = 265°$.

obtained during L_S^2 and L_S^3 in MYs 34 and 35 (Belyaev et al., 2021), revealing a good agreement between both instruments. This is presented in Figure 6.4, showing the H_2O number density seasonal variation observed with NOMAD and ACS at 80 and 100 km.

6.3.2 Interannual variability

Although we found a strong injection of water vapor to high altitudes in the three MYs, we observed some differences between them. In order to evaluate the contribution of the injection and its interannual variability, we averaged the retrieved profiles within the solar longitude ranges L_S^1, L_S^2 and L_S^3 for each analyzed MY, excluding observations from latitudes below 45° in order to capture vertical profiles representative of the observed plume. The average H_2O profiles for each L_S range in the southern hemisphere are presented in Figures 6.5A, 6.5B and 6.5C for MYs 34, 35 and 36 respectively. The difference in ppmv between L_S^2 and L_S^3 profiles is shown in Figure 6.5D. We observed a clear enhancement of the water abundance above 80 km of about 30 ppmv during L_S^2 in MYs 35 and 36 (orange and green lines), showing a similar vertical structure in both years. In contrast, MY 34 shows an enhancement of about 15 ppm during L_S^3 due to the peak observed around L_S~285°. The vertical profiles observed during the period L_S^1 (green line) prior to the plume detection show a similar trend in the three MYs.

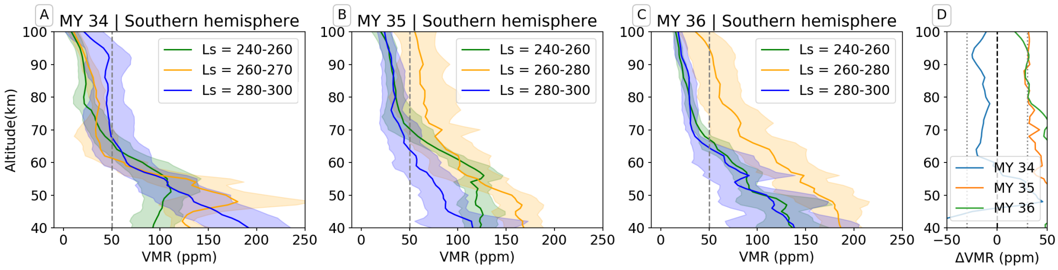

FIGURE 6.5: Averaged water vapor VMR profiles at southern hemisphere during solar longitude ranges $L_S^1 = 240^\circ - 260^\circ$ (green), $L_S^2 = 260^\circ - 280^\circ$ (yellow) and $L_S^3 = 280 - 300^\circ$ (blue) for MYs 34(A), 35(B), and 36(C). Profiles from latitudes below 45° have been excluded in the average. Shaded areas represent the standard deviation of the average. Vertical dashed lines indicate abundance of 50 ppmv. Panel D shows the averaged profiles difference L_S^2-L_S^3 for MYs 34 (blue), 35 (orange) and 36 (green). Vertical dotted lines indicate abundance of ±30 ppmv (dotted) and 0 ppmv (dashed) for reference.

6.4 Discussion

Recent works reporting TGO SO measurements found high water vapor abundance during the season analyzed here. Belyaev et al., 2021 using the ACS MIR channel found peaks of about 10-30 ppmv of H_2O at 100-120 km around Mars perihelion in MYs 34 and 35; as well as Fedorova et al., 2023, where the maximum was found up to 100 km. Using NOMAD SO data, Aoki et al., 2022 observed a maximum H_2O density at $L_S = 265^\circ$ in MY 35; Brines et al., 2023e using NOMAD SO observations showed H_2O abundance about 50 ppmv at high altitudes around $L_S \sim 260^\circ$ in MY 35 and Villanueva et al., 2021, again exploiting NOMAD SO measurements during MYs 34 and 35 denominated this feature as "Aspirator". We report here a detailed latitudinal structure of this phenomenon during three consecutive MYs for the first time, with a robust characterization of the observations in the upper mesosphere (>100 km) and revealing a large H_2O column located at 60°S reaching altitudes up to 110 km. This plume appears during MYs 34, 35 and 36 (Figures 6.3A, 6.3B and 6.3C respectively), suggesting a large water injection of about 50 ppmv into the upper atmosphere repeatedly every year during a specific period of time (L_S^2). Observations prior to $L_S = 260^\circ$ (L_S^1) do not show any significant injection but a gradual increase in water vapor in southern latitudes starting around $L_S = 250^\circ$, specially during MYs 35 and 36 (Figure 6.3D). However, in MY 34, this phenomenon is observed later in time (L_S^3) and presents a lower abundance plume with 50 ppmv at 80 km and <20 ppmv at 100 km (Fig. 6.3A3). This feature, reaching altitudes close to the mesopause (∼120 km), can not be simulated by the current LMD Mars PCM (Forget et al., 1999), which was used to generate the apriori climatology used during the retrievals presented here. However, it seems to coincide in time and location with an upward H_2O flux branch in the model by Shaposhnikov et al., 2019. Nonetheless, simulations using data assimilation (DA) Holmes et al., 2022 showed the presence of the plume during L_S^2 of MY 35. The assimilation combined the Mars PCM Uk-spectral

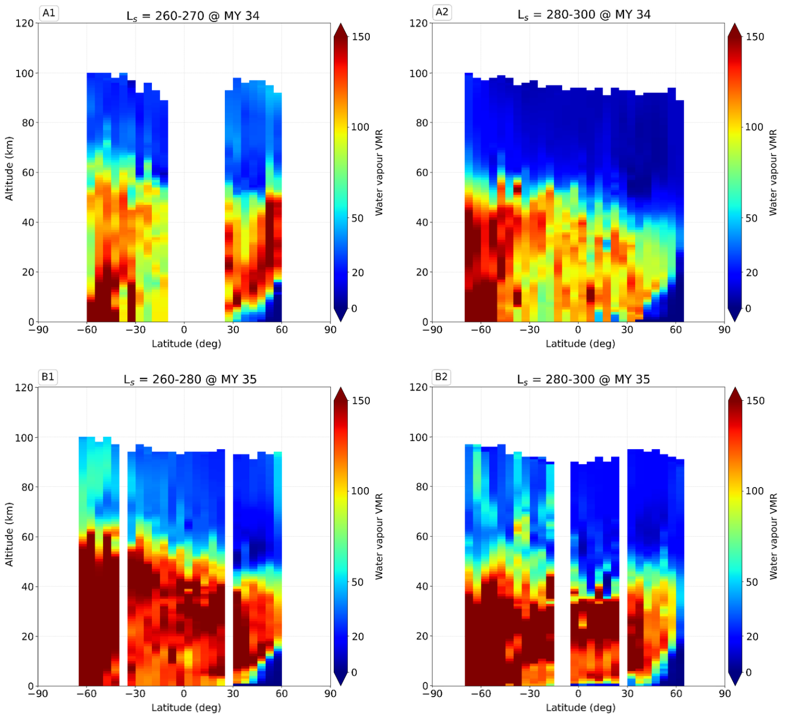

FIGURE 6.6: Simulated water vapor latitudinal variation during $L_S^1 = 260° - 280°$ (A1, B1) and $L_S^2 = 280° - 300°$ (A2, B2) for MYs 34 (top) and 35 (bottom) for the NOMAD SO observations using assimilated data. The Open access to Mars Assimilated Remote Soundings (OpenMARS) assimilation combines the Mars Planetary Climate Model (PCM) Uk-spectral with several spacecraft data sets to provide a global reconstruction of the evolving water cycle constrained by several sets of temperature profiles, water vapor columns and profiles and dust column. Full details can be found in Holmes et al., 2022.

with several spacecraft datasets, including NOMAD water vapor column abundance Crismani et al., 2021 and NOMAD+ACS water vapor profiles (Alday et al., 2021; Aoki et al., 2019; Fedorova et al., 2020; Villanueva et al., 2021), proving the advantages of combining GCM models with observations. Regardless of this result, firm conclusions about the nature of this feature cannot be drawn solely from DA studies. Future studies with a free GCM focusing on exploring its response to diverse parameters' perturbations shall provide valuable information about the drivers of this unique feature. DA profiles are shown in Figure 6.6.

The discrepancy between MYs 35, 36 and MY 34 might be attributed to several reasons. One is related to the NOMAD sampling and its orbital configuration. The TGO coverage during MY 34 is different compared to the sampling during MYs 35 and 36, this is, TGO sampled the same latitudes at different L_S. If the plume had a preferential latitude to appear every year, NOMAD would not observe it at the same L_S during MY 34 than during MYs 35 and 36. This suggests the H_2O injection observed here to be a local and a short duration phenomenon taking place in a specific time and location. This difference between MY 34 and the following Mars

Years is observed in Figure 6.3D, where the peak of the plume in MYs 35 and 36 occurs at $L_S \sim 268°$, a period of time which was not sampled by TGO during MY 34. Aoki et al., 2022 also reported a H_2O peak at $L_S = 265°$ during MY 35 but not in MY 34, attributing this to differences in the NOMAD sampling.

Another possible cause of the interannual variability may be the alteration of the atmospheric dynamics and transport caused by the MY 34 GDS and its slow decay phase in southern extratropic latitudes at $L_S \sim 255°$ (Kass et al., 2020). The water vapor abundance peak observed later in time at $L_S \sim 285°$ suggests a delay in the appearance of the plume during MY 34. In addition, the abundance below 60 km during MY 34 in the southern hemisphere prior to $L_S = 260°$ show smaller values than in MYs 35 and 36. This circumstance can be observed also in Aoki et al., 2022 (see their Figures 8 and 9), although they did not discuss this interannual difference. Fedorova et al., 2023 also reported much higher water vapor saturation during the perihelion of MY 35 compared to MY 34 and our observations are also compatible with Pankine et al., 2023. They studied the water vapor in the Southern Polar Region (SPR), analyzing observations of several instruments during years with and without global dust events claiming that water vapor column abundance decreased following the GDS, when compared to years without a GDS. During the period L_S^1, the temperature (Fedorova et al., 2023) and the column dust optical depth (Martín-Rubio et al., 2024) at high southern latitudes where similar in both MY 34 and 35 (see their Figure 7 and Figure 2 respectively), which may exclude the possibility of an enhanced water vapor condensation during the GDS year. Hence, the cause of the water abundance deficit during MY 34 may be related to a lower water vapor production rate by sublimation of the H_2O ice reservoirs. Due to the GDS, the southern polar vortex diminished its intensity during $L_S = 200° - 220°$, providing a weaker barrier to transport into the SPR and onto the surface (Streeter et al., 2021). This phenomena, could have increased the deposition of dust over H_2O ice during the GDS peak activity, leading to a reduction of the water vapor production rate (Gundlach et al., 2011). Pankine et al., 2023 also suggested the disruption of the southward transport of vapor by the atmospheric circulation as a potential cause of the observed differences between GDS and non-GDS years.

These observations may suggest that, in addition to the strong upward branch of the meridional circulation Shaposhnikov et al., 2019, the mechanisms driving the formation of the plume require a sufficiently high tropospheric (< 50 km) water vapor abundance at least larger than 100 ppm. In MY 34 this condition is fulfilled during L_S^2, leading to the delayed plume observed during L_S^3. This hypothesis should be explored in future studies with the help of observations from multiple instruments combined with GCMs Holmes et al., 2022.

Note that the measurements during L_S^2 of MYs 35 and 36 correspond to the evening terminator, whereas the measurements during L_S^3 of these same years correspond the morning terminator. This can be observed in Figure 6.3D, where the peak in H_2O density at L_S~285° only in MY 34 appears during evening observations. At present, we can not exclude local time effects as partially responsible for the plume origin and variability.

In addition to the vertical transport of H_2O in the plume, effects of the meridional transport towards Northern latitudes at high altitudes can also be observed in Figures 6.3B2 and 6.3C2, showing a layer of H_2O at 100 km with abundance >20 ppmv reaching latitudes of about 30°N. As the southern summer advances and the vertical transport around 60°S weakens, the ascending plume vanishes and the vertical and meridional injections of water diminishes. This effect is observed in Figures 6.3B3 and 6.3C3, where abundance at high altitudes decrease in both hemispheres suggesting a less efficient northward transport.

Average H_2O profiles in Figure 6.5 present an enhancement of water above 50 km in the southern hemisphere during L_S^2 of MYs 35 and 36. As seen in Figures 6.5B and Figure 6.5C, it appears repeatedly in both years, showing a difference of 20-30 ppmv at 100 km between the two analyzed L_S periods. In contrast, in Figure 6.5A this difference is smaller during MY 34, with larger abundance during L_S^3 and showing a variation of about 15 ppmv above 80 km between both L_S ranges. We can use these averaged profiles to estimate the atomic hydrogen escape flux associated to the plumes studied here. Applying the model by Chaffin et al., 2017 and assuming that the water injection from Figure 6.5B and 6.5C is sustained during the whole period when the plume is observed (~20° in L_S, i.e. 10^6 s), we obtained an integral escape flux about $\sim 3.2 \pm 0.5 \times 10^9$ $cm^{-2}s^{-1}$, which is in similar range as previous results (Belyaev et al., 2021; Bhattacharyya et al., 2017; Holmes et al., 2021). Repeating this exercise for the period when the plume was not observed, we obtained an estimation of $\sim 2.5 \pm 0.3 \times 10^9$ $cm^{-2}s^{-1}$. Taking into account the uncertainties introduced in the estimation of the escape (~15%) and the possible bias due to the uncertainties of the thermal structure within the region where the profiles where averaged (~5% as a conservative value obtained from our sensitivity tests), we estimate a rough increase by $\sim 30 \pm 25\%$ in the hydrogen escape over the period without the plume, which represents a modest but not negligible increase marginally above our uncertainties. Details about the method used for the estimation are presented in A.1. This estimation contains several uncertainties and the calculation presented here is only suitable to provide a rough order of magnitude estimate. Testing the known or unknown approximations in Chaffin et al., 2017 photochemical model was not a target of the present work. More recently, Montmessin et al., 2022 used a hybrid photochemistry-transport model combined with ACS observations from Belyaev et al., 2021 to compare the hydrogen escape rate during the perihelion season of MYs 34 and 35, suggesting this season to dominate the long term escape.

6.5 Summary and conclusions

During perihelion, suspended dust particles alter the thermal structure and consequently the atmospheric dynamics. This directly affects the atmospheric composition by strong vertical transport of minor species like H_2O. This work provides an insight into the water vapor vertical distribution during the perihelion and Southern summer solstice season. We have presented detailed latitudinal variation of the H_2O showing a strong pumping of water into the upper atmosphere and revealing abundance with volume mixing ratios about 50 ppmv at 100 km. The water vapor plume is observed to be confined to the southern hemisphere at latitudes between 60° and 50°. In addition, we have observed this feature only during a short period of time (20° in L_S) but repeated during the three MYs analyzed here. During non-GDS years we observe the injection to occur at $L_S = 260° - 280°$. However, during MY 34 the plume appears shifted towards southern latitudes and appears later in time, showing lower abundance above 80 km. We attributed these differences to variations in the latitudinal and seasonal sampling of the TGO spacecraft and to possible long term effects of the MY 34 GDS weakening the southern polar vortex and allowing the dust to deposit over water ice reservoirs, leading to a reduced water vapor production rate during the perihelion. In order to answer these questions, more observations of this phenomenon will be necessary. Increasing the number of H_2O dedicated observations with TGO during the perihelion season could help to provide a better temporal and latitudinal sampling of this short term and local event. We are planning to learn about possible drivers of this phenomenon by exploring the response of the Mars PCM to diverse parameters' perturbations, study that will be presented in future works. Finally, we provided a rough estimation of the hydrogen escape flux associated to the strong plumes in MY35 and 36 of about $\sim 3.2 \pm 0.5 \times 10^9$ $cm^{-2}s^{-1}$, which adds to the importance of the perihelion season to the global budget of hydrogen escape on Mars. The accumulation of more MYs of observations may give us a good estimate of the importance of these plumes over the global and annual hydrogen escape on Mars. Our results are in line with those presented in previous similar analysis. A comparison with Belyaev et al., 2021 shows a good agreement in the H_2O abundance retrieved with NOMAD and ACS instruments, complementing and confirming many of Belyaev et al., 2021 findings with a different instrument and retrieval approach.

Chapter 7

Four Martian Years of Water Vapor from NOMAD

This Chapter is based on the publication: "Four Martian Years of water vapor from NOMAD/TGO observations"
In preparation for Journal of Geophysical Research: Planets, 2024

Abstract

The study of water vapor in the Martian atmosphere is an open research field as it is crucial for understanding Mars' climate and its transition from a once warmer and wetter environment to its current cold and dry state. Although water vapor is nowadays relatively scarce on Mars, it influences many surface and atmospheric processes, contributing to the planet's complex water cycle. In April 2018, the Trace Gas Orbiter (TGO), equipped with the Nadir and Occultation for Mars Discovery (NOMAD) instrument, commenced its science operations allowing for the monitoring of the Martian atmosphere and providing comprehensive data on its seasonal, latitudinal, and local time variability. This study presents the most extended data set of water vapor measurements from the NOMAD instrument to date, covering four consecutive Martian Years. Building upon previous researches primarily focused on the perihelion season, this analysis now includes the aphelion season, offering a comprehensive view of Mars' water cycle. Observations from April 2018 to December 2023 were analyzed, covering perihelion of Mars Year (MY) 34 to aphelion of MY 37 and presenting water vapor vertical profiles from approximately 5-10 km to 110-120 km in altitude. This study reveals consistent seasonal and latitudinal water vapor patterns, showing water vapor systematically more vertically extended during the perihelion season than during the aphelion. We present an extensive analysis of the water vapor local time variability, confirming overall larger abundances during the evenings than during mornings. The extensive data set analyzed here also enabled robust comparisons with other NOMAD and ACS results and the novel application of cluster analysis techniques to Martian water vapor vertical profiles providing a simplified water vapor climatology.

7.1 Introduction

Among many other open research fields, the presence of water vapor in the Martian atmosphere stands out as a particularly engaging topic of study. This species on Mars, despite its relative low abundance, provides valuable clues about the planet's climate. Water vapor participates actively on many surface and atmospheric processes such as regolith-atmosphere interactions, chemistry and photochemistry, nucleation, sublimation and transport. Its distribution throughout the planet depends, directly or indirectly, on those processes resulting in a complex water cycle also strongly coupled with temperature variations, and therefore, on the atmospheric dynamics at local and global scales. Understanding the dynamics, sources, and variability of water vapor in the Martian atmosphere nowadays and through time is essential for piecing together the planet's geological and atmospheric evolution, which has driven Mars from a more humid and warmer past to the colder and dryer planet we observe today. Despite its importance, the knowledge about the vertical distribution of water vapor in the Martian atmosphere was limited until recent years. The thin atmosphere of Mars (its surface pressure is about 1% of that on Earth) makes detecting and measuring trace gases rather difficult, being observations on integrated column abundances from nadir-looking orbiters (Smith, 2002) and models (Forget et al., 1999; Haberle et al., 2019), the main source of available information. Extending the solar occultation technique, widely used on Earth for atmospheric sounding, to Mars has allowed us to achieve sensitivities high enough to study the precise distribution of water vapor, among other trace species, at different altitudes.

The first Solar occultations on Mars focused on water vapor were performed by the Auguste experiment during the Phobos mission (Rodin et al., 1997). They reported vertical profiles during northern spring equinox, showing a sharp decrease in abundance above 25 km and confirming the presence of an hygropause at 30 km. Mars experiences significant and largely unpredictable changes in temperature and pressure with latitude and season, which affects the sublimation-condensation of water ice and the vertical and meridional transport of water vapor. This variability means that a comprehensive understanding of the water cycle requires continuous and systematic monitoring over extended periods, a milestone that could not be achieved with sporadic missions.

The Spectroscopy for the Investigation of the Characteristics of the Atmosphere of Mars (SPICAM) onboard Mars Express (MEX) was the first instrument in orbit around Mars with the ability to use the solar occultation technique. It provided water vapor vertical profiles from 15 to 50 km which were used as an indicator of an atmosphere of about 5 K warmer than predictions by Global Circulation Models (GCMs) at those altitudes (Fedorova et al., 2009). In addition, SPICAM found that supersaturation (saturation ratio exceeding 1) was persistent in the martian atmosphere during the northern spring-summer seasons, precisely during solar longitudes (L_S) ranging from 50° to 120° (Maltagliati et al., 2011a). It also revealed data-GCM discrepancies in the abundance of water above 30 km. Similar studies carried out for the full Martian Year (MY) showed the importance of the vertical distribution on the water water cycle. SPICAM also reported for the first time larger abundances and more vertically extended profiles during the perihelion than during the aphelion season, which were unexpected based on the previous knowledge of column density measurements (Maltagliati et al., 2013). In addition, the analysis of observations during the global dust storm in 2007 showed that water vapor was present at altitudes up to 80 km with abundances larger than 100 ppm (Fedorova et al., 2018a). More recently, Fedorova et al., 2021 presented another relevant SPICAM result, showing water vapor density profiles for MYs 28 to 34 and confirming the impact of dust storms on water vapor vertical distribution at middle and high altitudes, adding to the impact of the perihelion season on the hydrogen escape rates.

In April 2018, the Trace Gas Orbiter (TGO) started its regular science operations. With several solar occultation instruments onboard, such as the Nadir and Occultation for MArs Discovery (NOMAD, (Vandaele et al., 2018)) and the Atmospheric Chemistry Suite (ACS, (Korablev et al., 2018)), the orbital configuration of TGO makes this spacecraft suitable to monitor the martian atmosphere, with an excellent sampling in the vertical and a good latitudinal and seasonal coverage. To date, many studies have been carried out with NOMAD and ACS, reporting outstanding results since the beginning of the mission revealing valuable information about the vertical structure and variability of the Martian atmosphere. To mention a few, the 2018 Global Dust Storm (GDS) was extensively discussed by several teams, confirming to have a strong impact on the the water vertical distribution (Aoki et al., 2019; Brines et al., 2023e; Fedorova et al., 2020; Vandaele et al., 2019). Global dust storms allow water vapor to be present at high altitudes and prevent its condensation due to the enhanced radiative heating (Neary et al., 2020). The high sensitivity of those instruments allowed for the study of water isotopic fractionation (Villanueva et al., 2022a), which revealed the prevalence of the perihelion season for the formation of atomic H and D at high altitudes (Alday et al., 2021). Also, a few recent studies devoted to the perihelion season characterized the upper atmosphere water distribution, reporting water vapor abundances for the first time at altitudes as high as $\sim 100 - 120$ km (Belyaev et al., 2021; Brines et al., 2024b).

Here, we present the largest NOMAD water vapor data set studied up to date. Building upon our previous water vapor retrievals mainly focused on the perihelion season (Brines et al., 2023e, 2024b), we extended the analysis to the aphelion season providing a complete view of the martian water cycle throughout 3 complete Martian years. We have also improved our water vapor retrieval scheme in several directions as detailed below. We analyzed NOMAD observations from April 2018 to December 2023, covering from the perihelion season of MY 34 ($L_S = 160°$) to the aphelion season of MY 37 ($L_S = 160°$). This data set allowed us to explore the seasonal and latitudinal variability of water vapor for four consecutive MYs, revealing distinct patterns that repeat every year in addition to features observed only during specific years. Although a solar occultation experiment is not ideal for local time studies, we show below how the TGO orbit permits local time analysis at some latitudes and seasons. The high sensitivity of the NOMAD instrument allowed us to obtain water vapor abundances from $\sim 5 - 10$ km up to $\sim 110 - 120$ km altitude. In addition, the extensive data set used in this work permitted a robust comparison between other NOMAD and ACS results and, for the first time, we applied of cluster analysis techniques to martian water vapor vertical profiles.

The structure of this paper is as follows: In Section 7.2 we describe the details about the NOMAD instrument and the data analysis. The results about the seasonal and latitudinal variability of water vapor profiles are presented in Sections 7.3 and 7.4 respectively. A brief discussion about water vapor local time variability is presented in 7.5. The comparison with NOMAD and ACS is shown in Section 7.6 and the cluster analysis in Section 7.7. Finally, Section 7.8 summarizes the results.

7.2 Data set and analysis

7.2.1 The NOMAD instrument

The NOMAD instrument is a suit of three spectrometers able to sample the Martian atmosphere in different viewing geometries and at different spectral ranges operating between 0.2 to 4.3 μm covering the UV, visible and infrared (IR) regions of the spectrum Vandaele et al., 2018. Those spectrometers are (i) the Solar Occultation (SO) channel dedicated for solar occultation measurements in the IR (2.3-4.3 μm), (ii) the Limb Nadir and solar Occultation (LNO) covering a slightly smaller spectral range than SO (2.3-3.8 μm) but, in contrast to the SO channel, able to sound the atmosphere with nadir and limb geometries, and (iii) the Ultraviolet and Visible Spectrometer (UVIS) sampling the spectral region between 200 and 650 nm and also very versatile regarding observational geometries. Focusing on the SO channel, its design is based upon the Solar Occultation in the Infrared (SOIR) instrument onboard Venus Express (Bertaux et al., 2007). It uses an echelle grating in Littrow configuration (the incident and reflected are equal) allowing for a spectral resolution of about $\lambda/\Delta\lambda \sim 17000$ (Neefs et al., 2015). During a typical solar occultation, NOMAD is able to sample the atmosphere every second, acquiring sets of spectra at about 1 km tangent height step. An Acousto Optical Tunable Filter (AOTF) in the optical path of the instrument is used to select up to six diffraction orders, which are measured quasi-simultaneously at every altitude. This feature is particularly useful to sample different spectral regions at different altitude ranges. By selecting proper combinations of orders, we are able to avoid optically thick spectral lines or to combine different target species, allowing flexibility and making the NOMAD instrument an excellent asset to build vertical profiles of diverse science contents with an unprecedented vertical resolution. An extended description of the NOMAD instrument was presented by Neefs et al., 2015 and the most recent instrumental characterization, in which IAA-CSIC participated actively, is summarized in Villanueva et al., 2022a where major updates with respect to the early in-flight calibrations (Liuzzi et al., 2019; Thomas et al., 2022) were done, particularly in the AOTF and instrumental line shape (ILS) characterization. The first of these, the AOTF, resulted to be best described by an asymmetric sinc-squared function with order-dependent parameters. The main issue of these kind of instruments is that, due to the wings of the sinc, the flux coming from adjacent orders propagates to the central target order. In the end, the flux measured by the detector resulted to be a combination of the main diffraction order plus an undetermined number of adjacent orders. The second key parameter, the ILS, was found to be a double Gaussian function whose widths and separation were also varying through the diffraction order. The AOTF and ILS parameters used in this work are those provided by Villanueva et al., 2022a, assuming that the observed radiance contains flux from the central diffraction order and also from its first ± four adjacent orders.

The data processing and analysis performed at IAA-CSIC with NOMAD SO measurements have been extensively described in previous works (López-Valverde et al., 2023). In addition, at IAA-CSIC we follow a sequential inversion pipeline where other species such as CO (Modak et al., 2023), aerosols (Stolzenbach et al., 2023) and temperature and densities (López-Valverde et al., 2023) are also retrieved using NOMAD SO spectra. The work presented here is focused on the distribution and variability of water vapor and builds upon two previous studies of water vapor (Brines et al., 2023e, 2024b), but extending the data set and improving the data processing and retrieval scheme in several aspects, as discussed in the following Section.

7.2.2 Data analysis

For this work we used Level 1 calibrated transmittances (Trompet et al., 2023) from the latest pipeline processing at the Belgian Institute for Space Aeronomy (BIRA-IASB) and available at ESA, 2024. This data, however, contains some residual systematics which need to be addressed before retrieving the vertical profiles. With that goal, at IAA-CSIC we have developed a variety of pre-processing tools designed to identify and correct for the major systematics still present in the data. In particular, two of them are: (i) the bending of the spectral continuum (baseline) and (ii) the spectral shift.

The residual bending, which varies from scan to scan, sometimes present variations of the transmittance through the diffraction order at a single altitude of up to about 0.1. This large oscillation is not caused by dust or water ice particles or by molecular absorption bands, but by quasi-random variations on the temperature of the detector during the start-end of each atmospheric scan. In order to characterize its spectral shape and following a similar approach to those presented in other works analyzing NOMAD SO data (Aoki et al., 2019), we used a fourth order polynomial to fit the baseline of each spectrum. This correction, however, needs to be done carefully since the presence of absorption lines may introduce a bias during the baseline characterization. To handle this situation we used line-by-line forward model calculations carried out with the Karlsruhe OPtimized Radiative transfer Algorithm (KOPRA) (Stiller, 2000). This forward model has been adapted for the Martian atmosphere and more recently, updated with the NOMAD SO instrument characterization (AOTF and ILS) mentioned above. During the bending correction, the spectral shift is characterized simultaneously and eventually also corrected. The cleaning of the NOMAD SO data has been extensively described in López-Valverde et al., 2023 and Brines et al., 2023e. The advantage of our methodology is that when using the KOPRA simulations we are taking into account any instrumental effects introduced into the spectra. These cautions are especially relevant for the analysis at high altitudes, where a poor characterization of the continuum can lead to large biases affecting the line depths, or for other purposes like the binning of spectra at different altitudes.

Despite this cleaning, we noticed that a fourth order polynomial fitting for the bending characterization was not enough for some purposes, like looking for trace species or retrieving water vapor at the highest altitudes. In some scans we found a residual low frequency oscillation after the cleaning which was present at all the tangent heights. The amplitude of this oscillation was found to be about $\sim 5 \times 10^{-4}$ in transmittance, a value close to the random measurement noise. Hence, taking advantage of this fact, for each scan and we averaged a dozen of spectra a the top of the atmosphere (TOA), where molecular absorption lines are undetected, thus, characterizing the oscillation. Then, we removed this oscillation from each tangent height.

In addition to the cleaning, our pre-processing pipeline also provides an in-house characterization of the random component of the measurement noise using covariance matrices (C-matrix). Those matrices were computed for each solar occultation using dozens of spectra from TOA. Their diagonals, containing the random oscillations in the measurements (C-noise). This C-noise resulted to be about 2-4 times smaller than the nominal measurement noise provided by Thomas et al., 2022 at high altitudes. The largest component of this nominal value is a systematic spectrally correlated component that can be addressed during the inversion. Hence, using a much smaller random noise allowed us to improve the sensitivity of our inversions at the uppermost atmosphere.

Here we applied the IAA-CSIC processing pipeline to an extended NOMAD SO data set for water vapor, as an improved follow-up study of the work presented by Brines et al., 2023e, 2024b. We selected a total of 7558 occultations taken during Martian Years (MY) 34, 35, 36 and 37. These observations cover a Solar Longitude range from $L_S \sim 160°$ of MY 34 to $L_S \sim 160°$ of MY 37, being the most extensive

NOMAD SO data set up to date. In Figure 7.1 we show the seasonal-latitudinal distribution of all the occultations indicating the morning (blue) and evening (red) terminator observations.

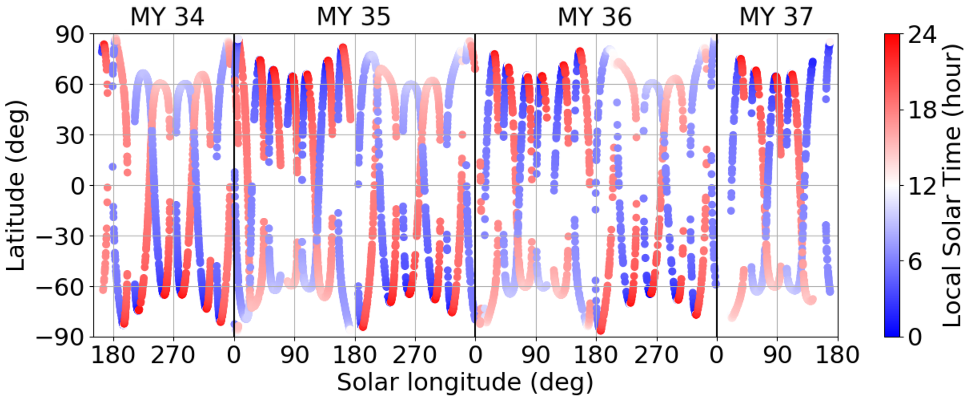

FIGURE 7.1: Latitude of the analyzed NOMAD SO observations over solar longitude for MY 34, 35, 36 and 37. Color indicates local solar time of the measurements, blue and red for morning and evening observations respectively. Vertical black lines indicate the beginning of each Martian Year.

We analyzed all the NOMAD data available in four different diffraction orders: 134 (3011-3035 cm^{-1}), 136 (3056-3081 cm^{-1}), 168 (3775-3805 cm^{-1}) and 169 (3798-3828 cm^{-1}). The first two contain relatively weak absorption lines ($S \sim 10^{-21}$ $\mathrm{cm}^{-1}/(\mathrm{molecule}\cdot\mathrm{cm}^{-2})$ whereas the others show much stronger lines from the spectral region close to the ν_3 fundamental band which saturate at low altitudes (optical depth > 1). Since the AOTF allows for simultaneous measurement of different diffraction orders at each tangent height, for each occultation we can select the most convenient order at every altitude. This way we developed a strategy to combine upto four different pairs of orders, 134 or 136 with 168 or 169, using them at different altitude ranges. This methodology is possible only when both orders have been measured during the same solar occultation, and although it limits the number of occultations available, it is necessary in order to obtain reliable vertical profiles from the bottom to the top of the atmosphere. Typically, we used low altitude orders (134/136) below 60 km and high altitude orders (168/169) above 60 km. This transition altitude, however, is not fixed. We used KOPRA simulations to calculate the curve of growth (variation of the line equivalent width with number of absorbents) of the strongest lines in orders 168 and 169 to estimate the water vapor partial pressure where those lines became optically thick. Then, using a first, approximate estimation of the water vapor volume mixing ratio (VMR) for each scan, obtained during the pre-processing (based on the linedepth of the KOPRA simulations used during the bending and shift correction) we determined the optimal transition altitude for each occultation. With all of this cleaning and pre-processing, the data are ready for the retrievals.

The water vapor profiles were obtained using the Retrieval Control Program (RCP) von Clarmann et al., 2003b, a multi-parameter non-linear least squares fitting of measured and modeled spectra, which incorporates KOPRA as its Forward Model. We followed the same methodology from our previous works (Brines et al., 2023e), although with the improvements previously described in the measurement noise characterization and modifying the retrieval setup to permit the combination of orders, conducting a single global fit to data from two different diffraction orders. These improvements allowed us to obtain consistent vertical profiles for an extended vertical range from ∼5 to ∼120 km altitude. The lowermost altitude limit is due to the presence of aerosols, mostly suspended dust in the lower atmosphere, and varies a lot depending on the season and location of the occultation. This bottom altitude for the inversion was determined during the pre-processing using an estimation of the slant opacity, cutting those altitudes with values of total optical depth along the line of sight larger than 2.0 (∼0.1 in transmittance) and avoiding steep gradients larger than 0.08 km^{-1}. On the other hand, the upper altitude layer for the inversion is also variable with season and location and was set during the inversion using the averaging kernels computed during the retrieval. Low values of averaging kernels were filtered, i.e. excluded, as they are indicative of results biased toward a priori/climatological values due to weak absorption lines (below measurement noise). During the inversions, the key inputs for to RCP are: (i) the NOMAD data, (ii) the a priori information and (iii) the retrieval constraints. The first were provided after the cleaning described above. For the a priori atmosphere, we used pressure and temperature profiles extracted from specific runs of the Mars Planetary Climate Model (Mars-PCM) (Forget et al., 1999) at the exact time and location of each solar occultation. The PCM runs where performed taking into account the best estimate of the dust optical depths from Montabone et al., 2020 for each MY, including the GDS in MY 34. Due to the lack of measured data, for MY 37, we used the same dust climatology than for MY 36. Since only the aphelion season of MY 37($L_S < 160°$) is analyzed here, which is a period of low dust activity, we expect this climatology and Mars-PCM simulation to have a negligible impact on our results. Regarding the retrieval constrains, we used a first order Tikhonov regularization optimized for each diffraction order. It was first determined by performing synthetic retrievals and then fine tuned with a subset of actual inversions, which allowed us to select a regularization as a trade off between error propagation, vertical resolution and convergence rate. In order to avoid border effects and to improve the stability of the retrievals we imposed a strong diagonal constraint at the bottom/top most altitudes of the retrieved vector, in addition to a strong regularization in those altitude ranges where the measurements were not available (low altitudes with large dust opacity).

Besides the propagation of the uncertainty in the measured transmittance during the inversion, we need to take into account and quantify other sources of errors: (i) the uncertainty in the reference atmosphere and (ii) uncertainty in the NOMAD instrumental calibration. As previously described we used temperature and pressure profiles from the Mars-PCM assuming the simulated atmosphere to be the real one. We performed several sensitivity tests introducing modification on those a priori. Varying the temperature by ±5 K (estimated accuracy of our dedicated runs of the Mars-PCM) and introducing wave functions to simulate extreme ±10% oscillations in the pressure gave an uncertainty in the retrieved water vapor of about 5%. Regarding the instrumental calibration, the major uncertainty comes from the AOTF characterization. We performed retrievals varying the AOTF parameters by 1σ, which resulted in impacts of about ±10% in the retrieved water vapor VMR. These uncertainties have to be taken into account when analyzing the results and during the comparisons with other teams.

7.3 Seasonal variability

The results of all our retrievals are presented in Figure 7.2. We show the vertical variation of the water vapor profiles during the four MYs analyzed in the middle and bottom panels for the northern and southern hemispheres respectively. For visualization purposes, we performed a weighted average of the profiles within bins of 1° in solar longitude. The latitude where each solar occultation was performed is shown in the top panel and exhibits a relatively quick variation from low to high latitudes (and vice versa). This peculiarity of the TGO orbit makes these maps difficult to analyze due to the fact that season, latitude and local time are changing at the same time. Nevertheless, this representation allows for the identification of several climatological patterns, repeated year after year, and it allows to highlight specific distinct events. Hereafter, and for the benefit of the reader, we will use the notation L_S^X when referring to the solar longitude of the MY X.

7.3.1 Northern hemisphere

When looking at the Northern hemisphere we observe that water vapor is more abundant at two altitude ranges depending on the season. During the perihelion season of each martian year ($L_S{\sim}180^\circ - 360^\circ$), water vapor is present at an extended altitude range from about 10 km or below, up to 60 km (middle atmosphere). In particular, during $L_S^{34}{\sim}190^\circ - 210^\circ$ we observe a distinct enhancement of the water abundance of about 150 ppm at 80 km. The ultimate source of this feature during MY 34 was the GDS, and this abundances are not again with such intensity during the rest of the data set. The large dust abundance present in the atmosphere during that period lead to an increase of the temperature in the 40-60 km altitude range (Neary et al., 2020) which prevented the condensation of water vapor at those altitudes. As a consequence, water vapor was able to be present in form of vapor at higher altitudes than usual. This topic was extensively discussed by previous works analyzing NOMAD data such as Aoki et al., 2019; Brines et al., 2023e and also by other TGO instruments like ACS NIR (Fedorova et al., 2020). At the end of each Martian year,

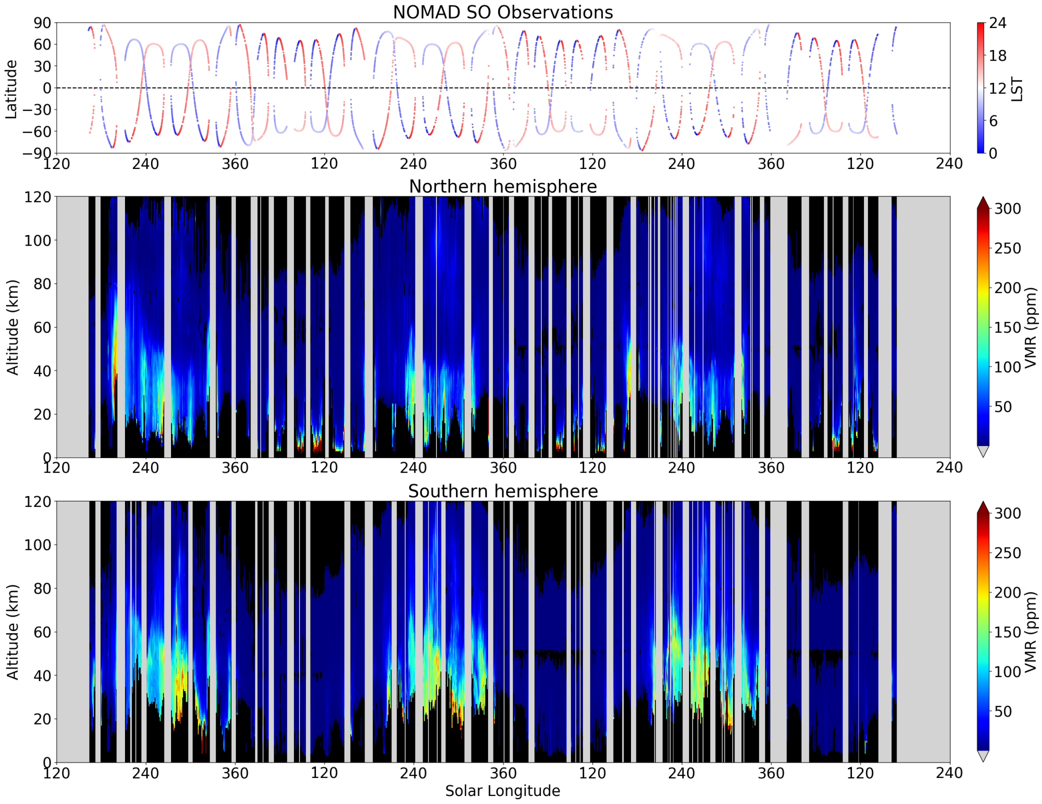

FIGURE 7.2: Vertical distribution of water vapor volume mixing ratio (VMR) over Solar Longitude during MYs 34, 35, 36 and 37 for the Northern (middle panel) and Southern (bottom panel) hemispheres. Top panel indicates the Latitude and Local Solar Time of the observations.

a regional dust storm usually occurs, and is known as C-storm (Kass et al., 2016). Although with a more moderate intensity, its effects on the water vapor were similar to those of the GDS, showing an increased abundance in the middle atmosphere ($L_S^{34}{\sim}330°$, $L_S^{35}{\sim}320°$).

On the other hand, during the aphelion season ($L_S{\sim}0° - 180°$) water seems to be more confined to low altitudes, from 5 km to 10 km (lower atmosphere) showing a sharp decrease at 20 km. In addition, the top most altitude where water was detected during this period falls to a tangent height of about 80 km. This period corresponds to the northern summer so the large abundance observed in the lower atmosphere corresponds to the well known summer season's water release from the sublimation of the northern polar cap due to the increase of the temperature in this hemisphere (Villanueva et al., 2022a).

7.3.2 Southern hemisphere

The Southern hemisphere also shows distinct climatological patterns. Water is present in larger abundance and in a more extended vertical range during the perihelion season, coinciding with the southern spring and summer. During this period, also known as the "dusty season", local/regional dust storm events are frequent and the abundance of aerosols (dust) in the atmosphere is significantly larger than during other seasons. Due to its orbital eccentricity, Mars receives an enhanced solar flux at perihelion leading to a warmer southern summer (Smith et al., 2017) and an intense single cell meridional circulation, transporting species like water vapor from the south to the north. This effect is also affected by the topographic asymmetry between hemispheres, where the higher southern surface elevation results in a more intense thermal forcing of the mean circulation (Barnes et al., 2017). Close to the summer solstice, around $L_S \sim 270^\circ$ a strong injection of water vapor to the mesopause (~100 km) is repeated every year. This feature has been discussed in previous works (Aoki et al., 2022; Belyaev et al., 2021; Brines et al., 2024b; Fedorova et al., 2021; Villanueva et al., 2022a) and in addition to the global dust storms, revealed to be a driving factor on the injection of water vapor to thermospheric altitudes and for the hydrogen escape from Mars.

The southern autumn and winter seasons ($L_S \sim 0^\circ - 180^\circ$) show a clear contrast compared to the local summer. During the aphelion season, above 70-80 km the water vapor abundance is extremely low, below our detection limits and only abundances about 50 ppm are observed in the lower atmosphere at equatorial latitudes.

7.4 Latitudinal variability

Although the interhemispheric asymmetry is evident in Fig. 7.2, the large seasonal variation complicates other studies, like detailed latitudinal analysis. Hence, another representation of the profiles with a careful selection of appropriate occultations is required in order to properly identify and characterize variations of water vapor abundance with latitude.

Here we selected different subsets of observations taken during relatively small ranges of L_S ($\Delta L_S = 30^\circ$), which show a significant the latitudinal sampling. For a given latitude, in order to avoid mixing observations made at different local times, we split the sets considering occultations from only one terminator (morning or evening). Representing the vertical profiles within those L_S windows with latitude-altitude maps, we assume that the observed water vapor distribution is caused only by the latitudinal variability. These cautions are also needed in order to analyze effects of the local time variations, discussed in the next Section.

7.4.1 Aphelion season

In Figures 7.3 and 7.4 we show the latitudinal distribution of water vapor at the morning and evening terminators respectively for the aphelion season (from $L_S = 0^\circ$

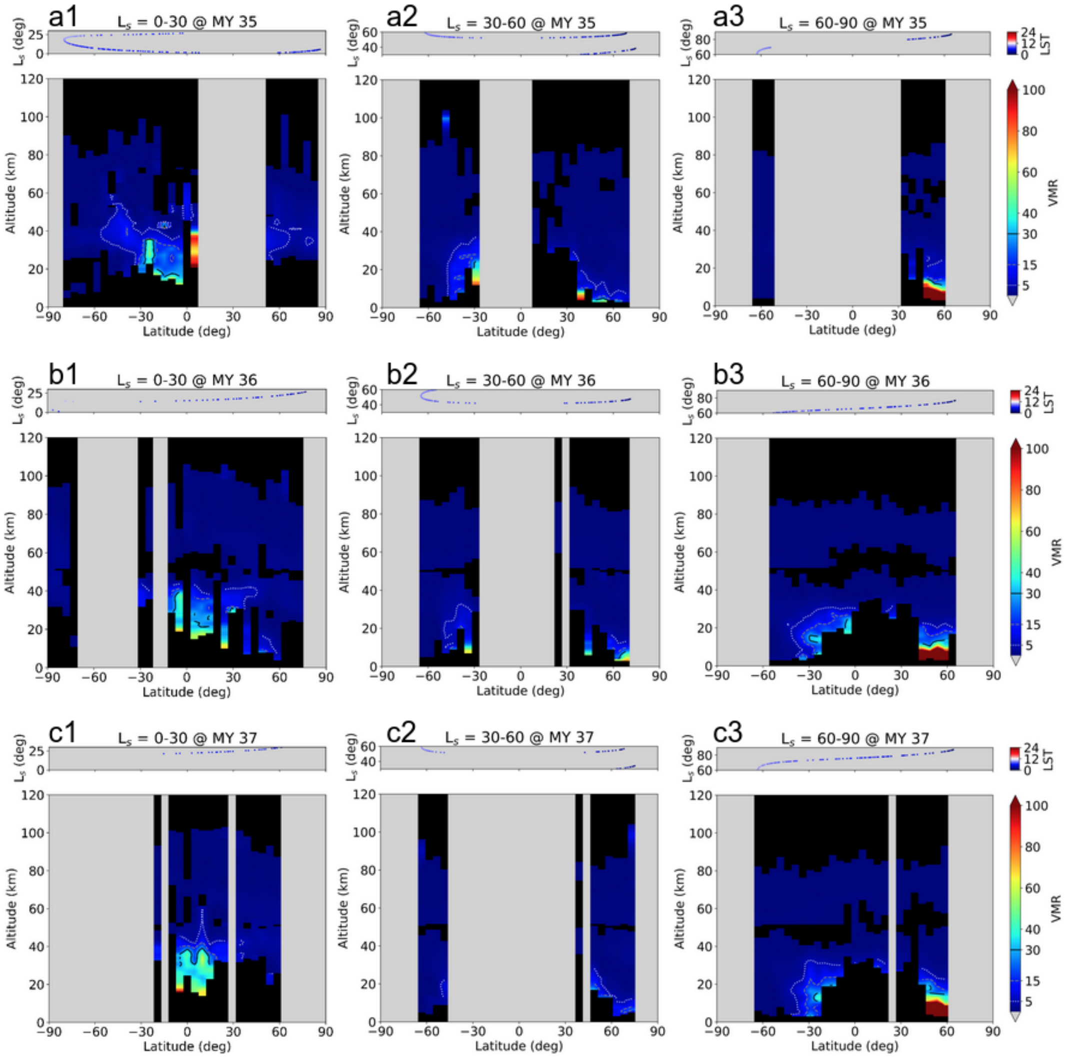

FIGURE 7.3: Latitudinal distribution of water vapor profiles during the aphelion season of MYs 35 (top), 36 (middle) and 37 (bottom panels) from observations at the morning terminator. Latitude and local solar time of the observations are indicated with dots above each panel.

to $L_S = 180°$) of MYs 35, 36 and 37. Here, the vertical profiles were averaged in 5° latitude bins. In order to ease the interannual comparison, each panel covers the same solar longitude with $\Delta L_S = 30°$.

During both the aphelion season and the periods close to the equinoxes ($L_S = 0°$ and $L_S = 180°$), most of the water vapor is confined to low altitudes and at low latitudes, close to the equator. In Figures 7.4-a1, 7.4-a2, 7.4-b1, 7.4-b2 and 7.4-c2, we observe abundances below 20 ppm above 40 km during the evenings, whereas during mornings (same panels of Figure 7.3), this limit is observed at 20-30 km and presents large altitude gradients at high northern latitudes. All Martian years show a similar structure, mostly symmetric respect to the equator and with the larger abundances appearing between 30°S-30°N. During this period of the year, close to the northern spring equinox, the global meridional transport induces a polar

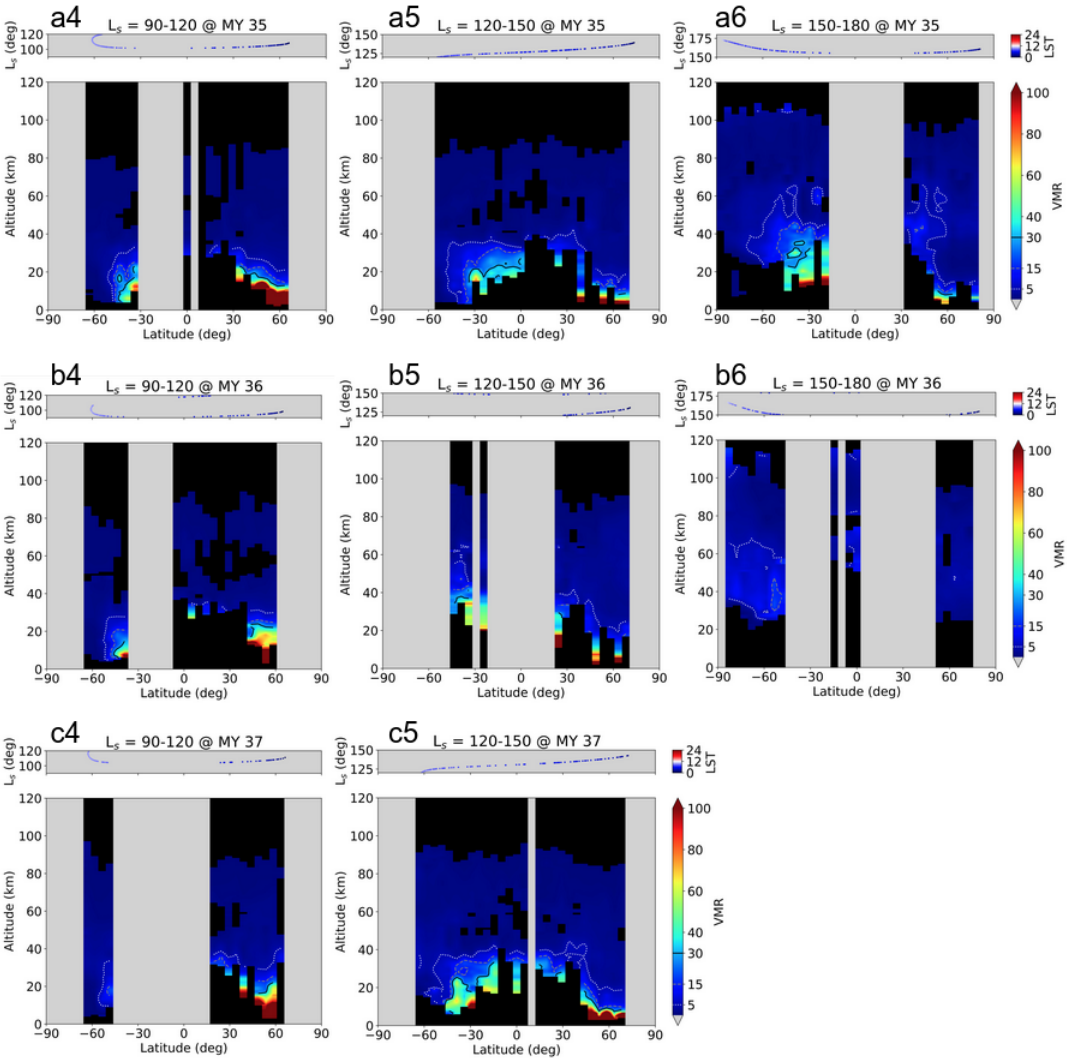

FIGURE 7.3: (continued)

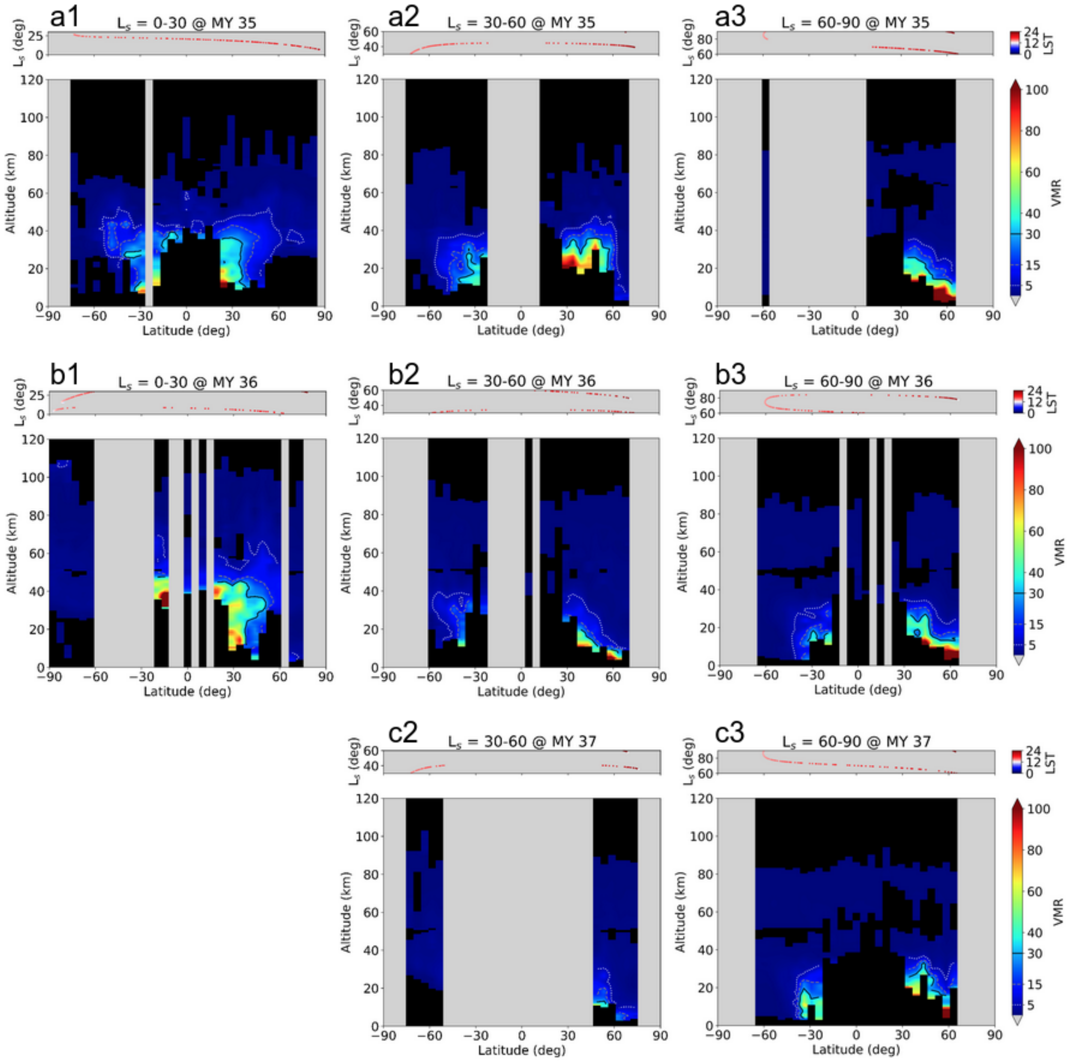

FIGURE 7.4: Latitudinal distribution of water vapor profiles during the aphelion season of MYs 35 (top), 36 (middle) and 37 (bottom panels) from observations at the evening terminator. Latitude and local solar time of the observations are indicated with dots above each panel.

warming in the middle atmosphere as the downward branch of the cross-equatorial circulation descends at high latitudes (Medvedev & Hartogh, 2007). This effect occurs at both hemispheres since the warmest surface temperatures at the equator lead to a two-cell Hadley circulation with a low latitude upwelling branch (Smith et al., 2017) and a descent branch at high latitudes causing an adiabatic warming. These warmer polar temperatures were also reported by ACS (Belyaev et al., 2022; Fedorova et al., 2023) and could be responsible for the layer of water vapor observed at ∼40 km in the southern hemisphere (∼60°S), as shown in Figures 7.3-a1 and 7.4-a1, 7.4-a2 and 7.4-b2. Below this layer, water vapor abundance falls, and this seems to be associated to the formation of water ice clouds (Fedorova et al., 2023; Stolzenbach et al., 2023). The enhancement of water vapor abundance in the middle atmosphere at high latitudes is observed again during the period close to the northern autumn equinox, as shown in Figures 7.3-a5, 7.3-b5, 7.3-a6, 7.3-b6 for the morning and

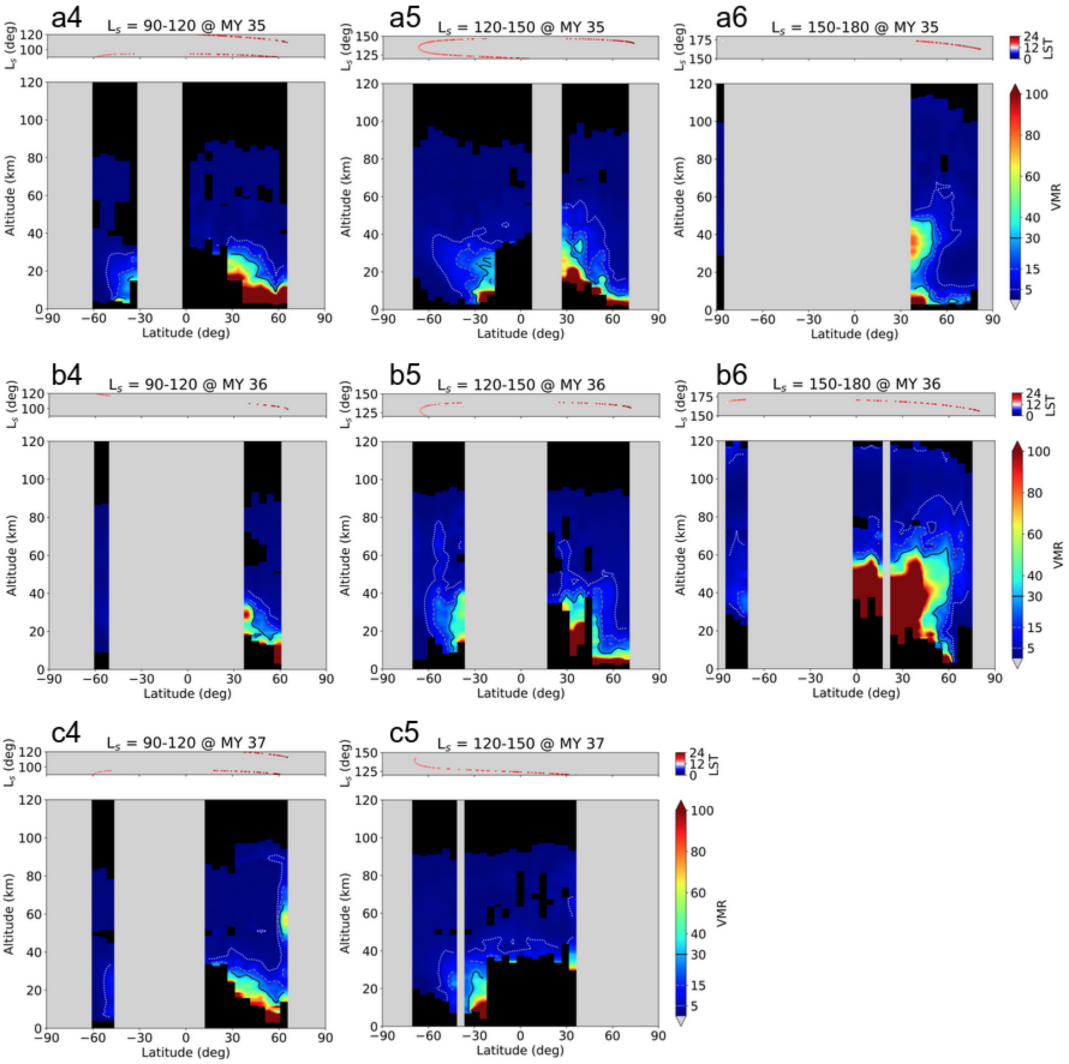

FIGURE 7.4: (continued)

7.4-a5,7.4-b5,7.4-a6 and 7.4-b6 for the evening terminator, which coincides with warm layers at polar latitudes, also observed by ACS MIR (Belyaev et al., 2022) and ACS NIR data (Fedorova et al., 2023).

Close to the northern summer solstice ($L_S = 90°$), the equatorial symmetric pattern previously described disappears, revealing an asymmetric structure between both hemispheres, very repetitive and similar during the three MYs. As shown in Figures 7.3-a3, 7.3-a4, 7.3-b3,7.3-b4, 7.3-c3 and 7.3-c4 for the morning and 7.4-a3, 7.4-a4 7.4-b3, 7.4-c3 and 7.4-c4 for the evening terminator, the distribution of water vapor is shifted towards the northern hemisphere. The increase of the temperatures at high northern latitudes leads to the sublimation of the polar cap in the summer hemisphere, releasing large amounts of water resulting in low altitude VMRs > 100 ppm at high latitudes $> 60°$N. These large abundances in the northern hemisphere are confined to lower altitudes during the mornings (below 10 km) than during the evenings, possibly due to temperature differences and to the formation of nighttime ice clouds, whose precipitation results in downward transport of water vapor toward the surface (Daerden et al., 2010).

At the end of this first half of the year, close to the northern autumn equinox, the vertical extent of the observed water vapor abundances during MYs 35 and 36 are significantly larger than during the spring equinox, specifically during evenings (Figures 7.4-a6 and 7.4-b6), where VMRs $>$ 100ppm are present at $\sim$50 km altitude in the northern hemisphere. Evening temperatures observed by ACS were larger during this period than during the northern spring equinox (Belyaev et al., 2022), possibly increasing the altitude where water ice clouds form. This is also suggested by Aoki et al., 2022 based on GEM-Mars simulations, who found this late aphelion water vapor enhancement in the northern hemisphere related to a lower rate of cloud formation during daytime.

7.4.2 Perihelion season

In Figures 7.5 and 7.6 we show the latitudinal distribution of water vapor at the morning and evening terminators respectively for the perihelion season (from $L_S = 180°$ to $L_S = 360°$) of MYs 34, 35 and 36. Similarly to what is shown for the aphelion season, profiles were averaged in bins of 5° latitude and in order to ease the interannual comparison, each panel covers the same solar longitude with $\Delta L_S = 30°$.

First, the effects of the GDS are noticeable in the set of profiles of Figure 7.6-a1, during $L_S^{34} = 180 - 210$. The mature phase of the GDS took place at $L_S^{34} = 198$ and the peak on the temperature increase due to the large dust abundance was registered around $L_S^{34} = 207$ (Kass et al., 2020). During this period, the effects of the storm can only be observed for the evening terminator due to the sampling location and timing of NOMAD measurements, capturing the GDS during the evenings. Nevertheless, the interannual variability between MY 34 and the following years is evident. In MY 34 we observe water abundance of about 100 ppm even at 70-80 km altitude in the southern hemisphere at ∼60° latitude, showing a sharp decrease towards polar latitudes at $>$ 80°S. In the northern hemisphere, the distribution is similar, with large abundance of about 200 ppm below 40 km and again, a sharp decrease at $>$ 65°N. The larger abundances at high southern latitudes are possibly due to the weakening of the Southern Polar Vortex induced by the storm (Streeter et al., 2021). During non-GDS years the abundance at latitudes $>$ 60°S was not larger than 20 ppm as shown in Figures 7.6-b1 and 7.6-c1.

After the GDS, during its decay phase at $L_S^{34} = 213 - 230°$ (Kass et al., 2020), the interannual variability is more noticeable in the northern hemisphere. In Figures 7.5-a2 and 7.6-a2, for both terminators at latitudes 0°N-30°N, we observe water abundance of about 100 ppm at 50 km during MY 34, whereas in the following years this values are observed only below 20-30 km. In contrast, in the southern hemisphere at latitudes $>$ 60°S we notice larger abundances below 60 km at the evening terminator during the years without GDS, with at least 100 ppm. These differences between years with and without global dust storms were reported by Brines et al., 2024b, and Pankine et al., 2023 found systematically lower water vapor abundance at high southern latitudes during the years with storms compared to the years with regular dust activity.

For the following sets between $L_S = 240° - 300°$, the distribution and abundance of water below 60 km is similar in all the three MYs, although MY 34 shows slightly lower abundances at the evening terminator. In Figures 7.5-a3, 7.5-b3, 7.5-c3, 7.5-a4, 7.5-b4, 7.5-c4 for the morning, and 7.6-a3, 7.6-b3, 7.6-c3, 7.6-a4, 7.6-b4, 7.6-c4 for the evening terminator, we observe an asymmetric pattern with more vertically extended abundance in the southern hemisphere. This is possibly due as a result of the vertical transport produced by the upwelling branch of the Hadley cell, which intensifies during southern summer. The intensification of the circulation is due not only to the enhancement of the solar flux produced by the orbital eccentricity of Mars but also to the north-south topography dichotomy (Richardson & Wilson, 2002). Above 60 km, however, some interannual differences arise. MYs 35 and 36 present a large injection of water vapor to the upper atmosphere particularly intense at the evening terminator. We observe abundances of about 50 ppm up to 100 km as shown in Figures 7.6-b3, and 7.6-c3, feature which appears later and with reduced intensity in MY 34 (Figure 7.6-a4). This observed plume, reported by ACS (Belyaev et al., 2021) and NOMAD (Aoki et al., 2022; Villanueva et al., 2022a), was recently deeply analyzed by Brines et al., 2024b, who presented an extended discussion about the nature of this phenomena and suggested the long term effects of the GDS to be responsible of its weak and delayed appearance during MY 34. Looking at the northern hemisphere, we observe a layer of low water vapor abundance below 20

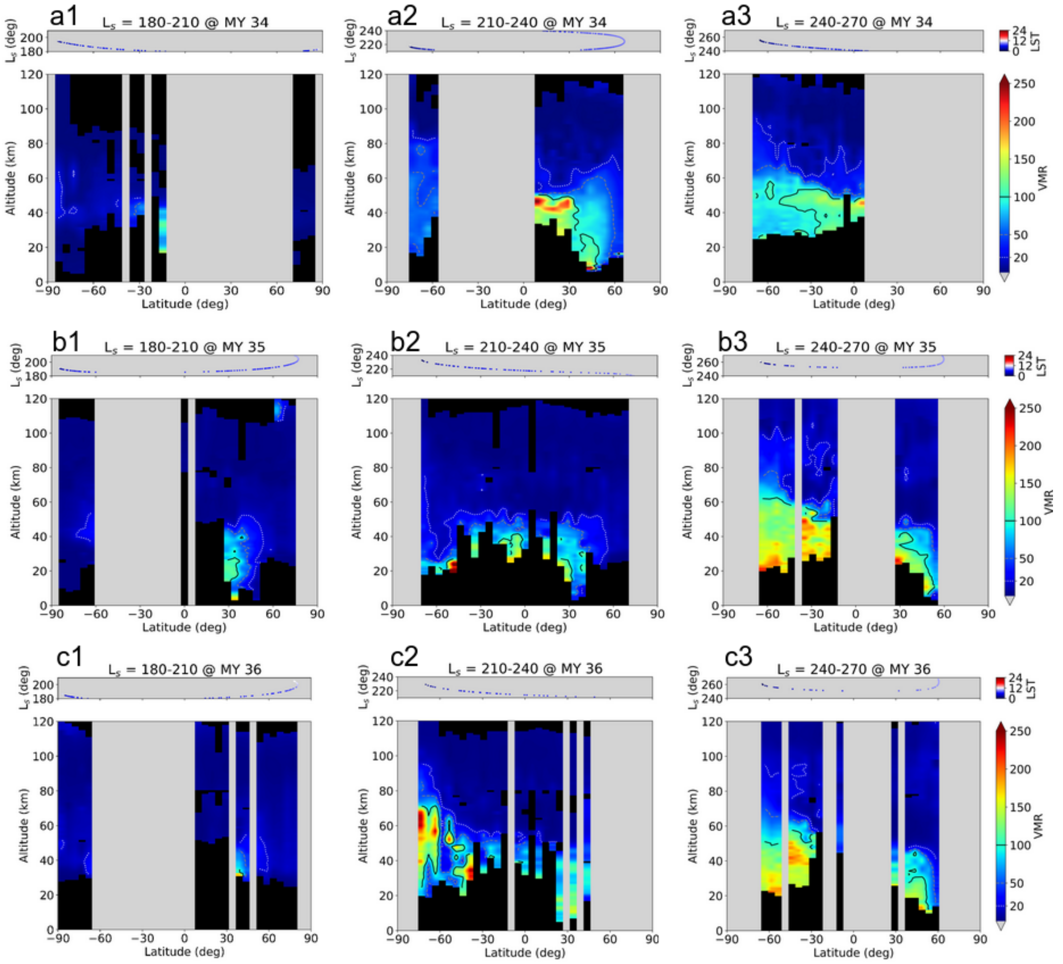

FIGURE 7.5: Latitudinal distribution of water vapor profiles during the perihelion season of MYs 34 (top), 35 (middle) and 36 (bottom panels) from observations at the morning terminator. Latitude and local solar time of the observations are indicated with dots above each panel.

ppm at 40-60 km. This depletion of water seems to be present at both terminators although is particularly noticeable in Figures 7.5-b4 and 7.5-c4 at the morning terminator, where water increases again above the depletion, forming another layer of $>$ 20ppm visible at ∼100 km. These layers of depleted water vapor coincide with regions where water ice clouds were observed by Fedorova et al., 2023 and the presence of larger abundance above suggests that water is being transported through the meridional circulation at high altitudes from the southern hemisphere towards high northern latitudes.

The last part of the year is particularly interesting due to the frequent occurrence of local dust storms, also called C-Storms (Kass et al., 2016), which occurred at $L_S^{34}{\sim}320°$ and $L_S^{35}{\sim}330$ (Liuzzi et al., 2020). These storms warmed up the atmosphere and their effects can be observed more clearly at the evening terminator in Figures 7.6-a5 and 7.6-b6, where MYs 34 and 35 show larger abundance in a more extended vertical range (up to 60-70 km) at high southern latitudes (∼60°). In addition, these effects

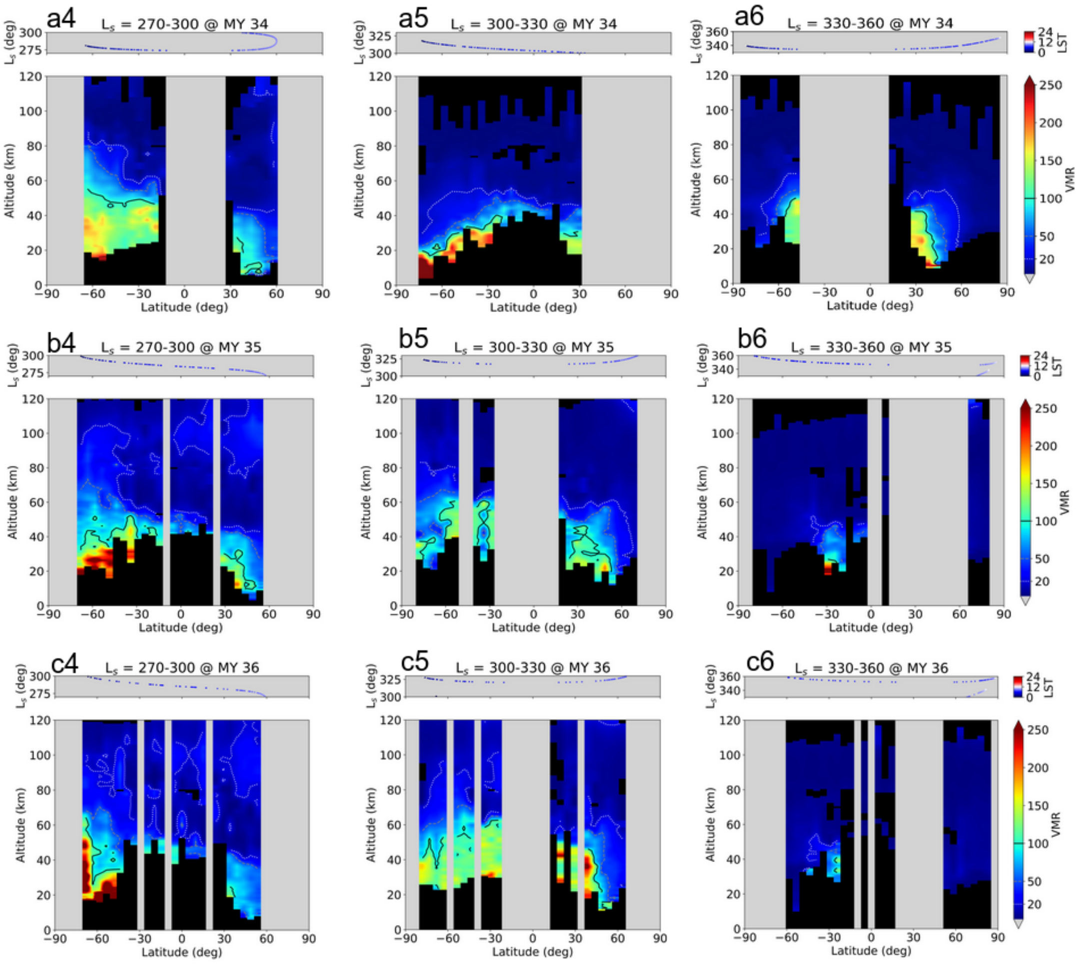

FIGURE 7.5: (continued)

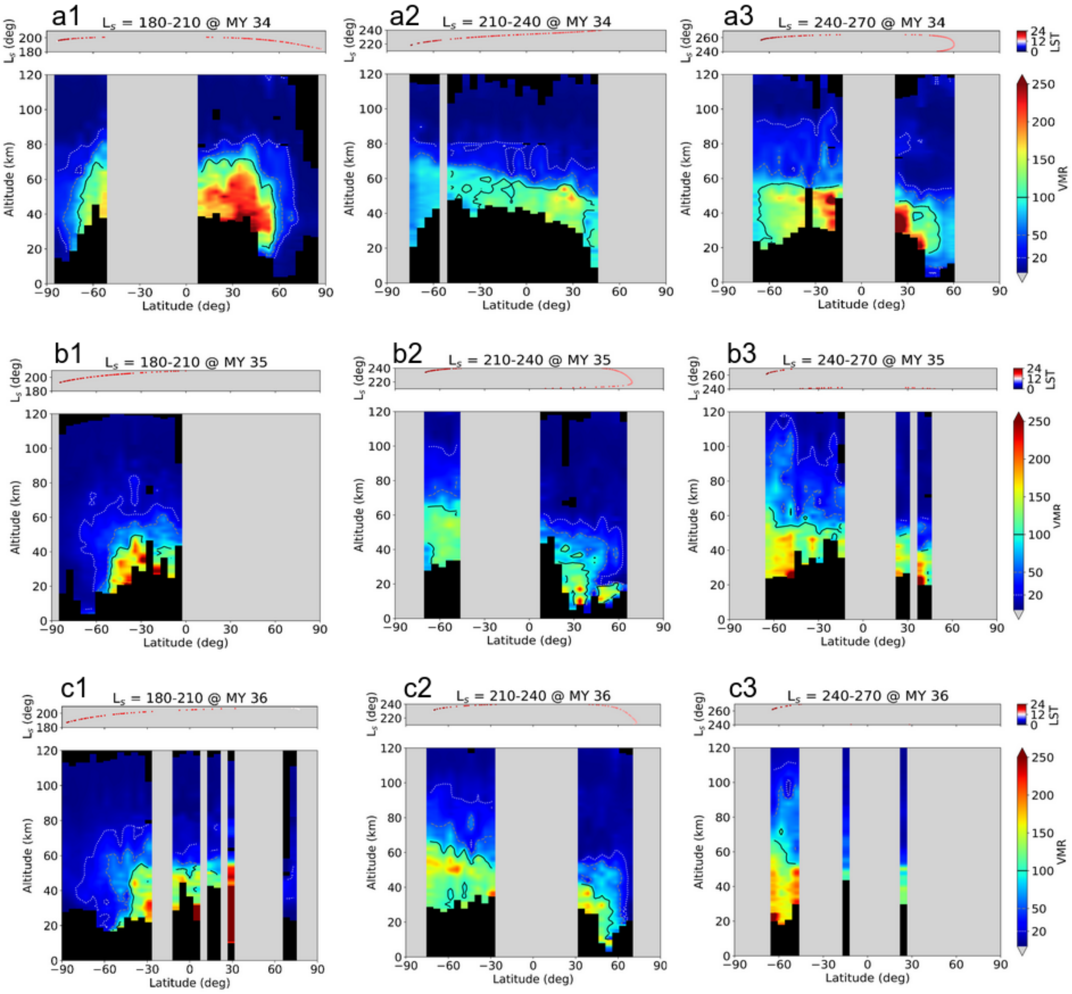

FIGURE 7.6: Latitudinal distribution of water vapor profiles during the perihelion season of MYs 34 (top), 35 (middle) and 36 (bottom panels) from observations at the evening terminator. Latitude and local solar time of the observations are indicated with dots above each panel.

are also noticeable in the morning terminator, as shown in Figures 7.5-b5 and 7.5-c5, where MYs 35 and 36 show abundances of about 100 ppm at 60 km, whereas in MY 34 these values only appear below 40 km. From a general point of view and ignoring the effects of the storms, during this period all MYs show a comparable pattern, recovering an interhemispheric symmetry with the water vapor mostly confined at mid-low latitudes below 40-50 km as a result of the progressively cooling down of the atmosphere.

7.5 Diurnal variability

The selection of the L_S ranges for Figures 7.5, 7.6, 7.3 and 7.4 was made in order to allow for the interannual comparison throughout different seasons. Although morning and evening terminators are clearly differentiated, not all latitudes were sampled at both terminators for all the profile sets. For each TGO orbit, typically

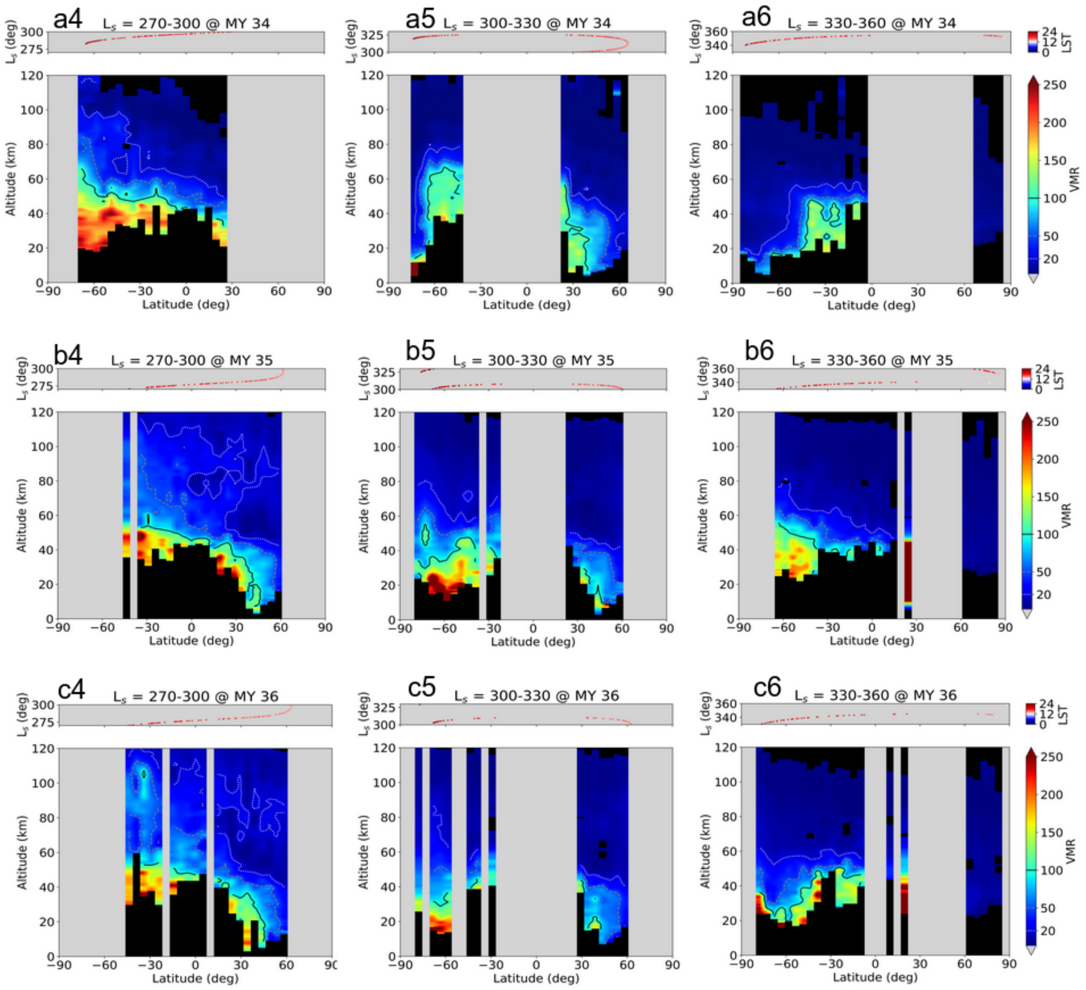

FIGURE 7.6: (continued)

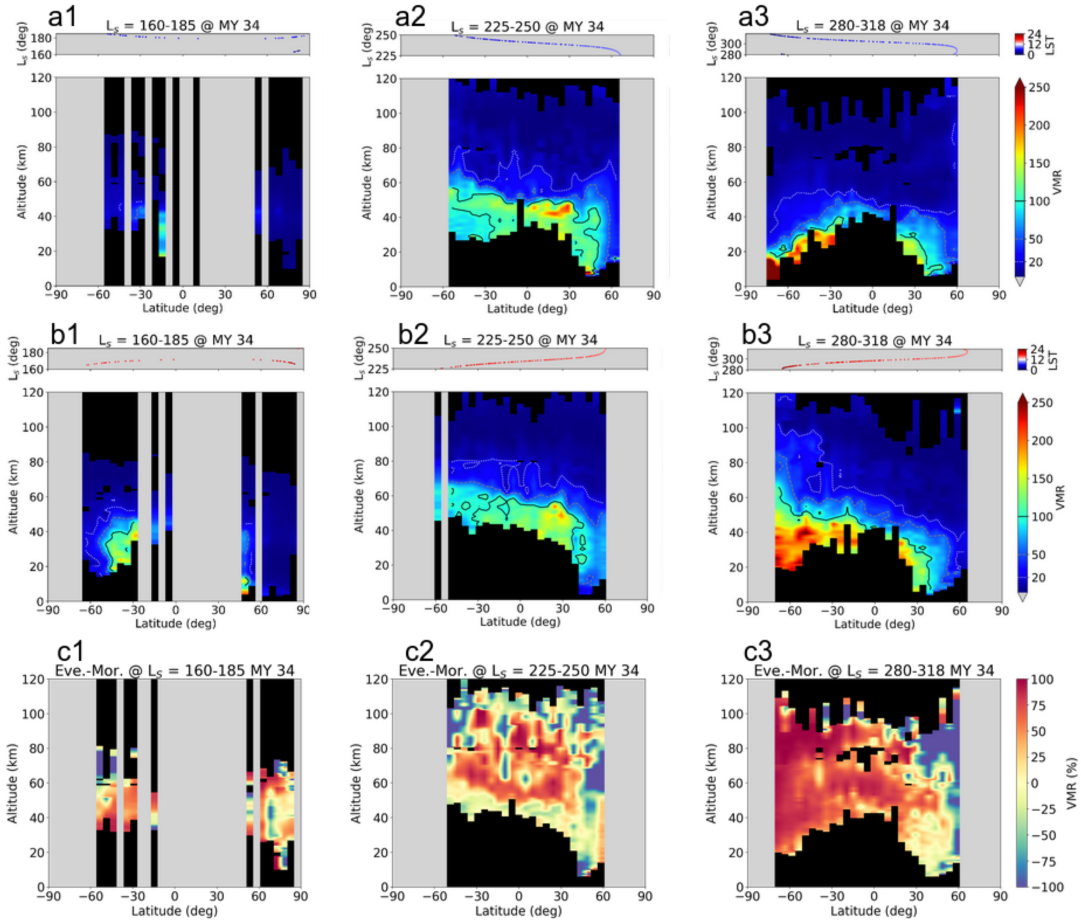

FIGURE 7.7: Latitudinal distribution of water vapor profiles at different Solar Longitude ranges during MY 34 for the morning (top) and evening (middle) terminators. Bottom panels show the relative difference between evening and morning observations. Latitude and local solar time of the observations are indicated with dots above each panel.

NOMAD measures a sunrise and a sunset at each hemisphere, thus making the analysis of local time variations complicated. Despite this limitation, the TGO orbital geometry allows for the sampling of nearby latitudes at both terminators during a few L_S ranges throughout the Martian year. For this Section we selected another subset of profiles in some L_S intervals, short enough to avoid seasonal variability effects.

In Figures 7.7, 7.8, 7.9 and 7.10 we show the water vapor latitudinal distribution for different L_S ranges optimized in order to allow for a comprehensive analysis of local time variations for MYs 34, 35, 36 and 37 respectively. For these Figures, the top and middle rows show the latitudinal maps for the morning and evening terminators respectively, whereas the bottom row illustrates the relative difference evening-morning. We define morning/evening profiles as those retrieved from observations taken before/after 11am, excluding mid-day observations from the analysis. Typically, most of the occultations occur at 6am or 6pm for low-mid latitudes, whereas a reduced number of scans at high latitudes (> 80°) sample the atmosphere also between 12am to 12pm, although local time at polar latitudes is less meaningful.

Looking at the bottom row of all these Figures, we observe overall reddish tones indicating the tendency of the atmosphere to be more humid during the evenings, at least within the sampled altitude range above 20 km. During the aphelion, in Figures 7.8-c1, 7.9-c1 and 7.10-c1 those diurnal differences appear more intense in the northern hemisphere, with the southern hemisphere showing a state of low abundance below 40 km at both terminators during MYS 35 and 37. The location of this water vapor enhancement during the northern evenings coincide with regions where 5-10 K warmer temperatures were measured by ACS (Fedorova et al., 2023).

Before the winter autumn equinox, the meridional transport is dominated by a Hadley cell with the upper branch located at high northern latitudes. The vertical transport enhanced during daytime leads to the larger water vapor abundances observed during the northern evenings up to 40 km in Figures 7.8-c2 and 7.9-c2 for MYs 35 and 36 respectively. However, during MY 37 this transport is observed to be particularly intense during $L_S \sim 112°$, as shown in Figure 7.10-b2 during the evenings. This feature does not appear with such intensity during the previous MYs. Figure 7.10-c2 reveals a layer with larger abundances during the evenings at ∼80km, decreasing to lower altitudes (∼60km) at latitudes > 60°S. This is also observed in Figure 7.9-c2 and suggests a more efficient southward transport at those altitudes during the evenings, although modest during this period of the year (Kahre et al., 2020).

Just before the solstice, in Figures 7.7-c2, 7.8-c4 and 7.9-c3 we observe a distinct layer between 40-60 km showing abundances ∼100 ppm larger during the evenings. This layer extends horizontally along 50°S-50°N suggesting the presence of diurnal waves in the middle atmosphere as the hygropause expands during the day and contracts during the night.

During the perihelion, in Figures 7.7-c3, 7.8-c5 and 7.9-c4 the interhemispheric assymmetry not only reveals larger and more vertically extended abundances in the southern hemisphere, but also that those large abundances are even more intense during the southern evenings, with differences of about 100 ppm and 50 ppm in the middle and upper atmospheres respectively. All this suggests a more intense vertical transport during the daytime. Nonetheless the northern middle atmosphere does not show such contrast but an enhancement of water vapor during the morning terminator at ∼100 km. This feature can be observed also in Fedorova et al., 2023 (see their Figure 9). A tentative explanation for the presence of this layer at ∼60°N could be the following: water vapor is lifted up to the mesosphere at the

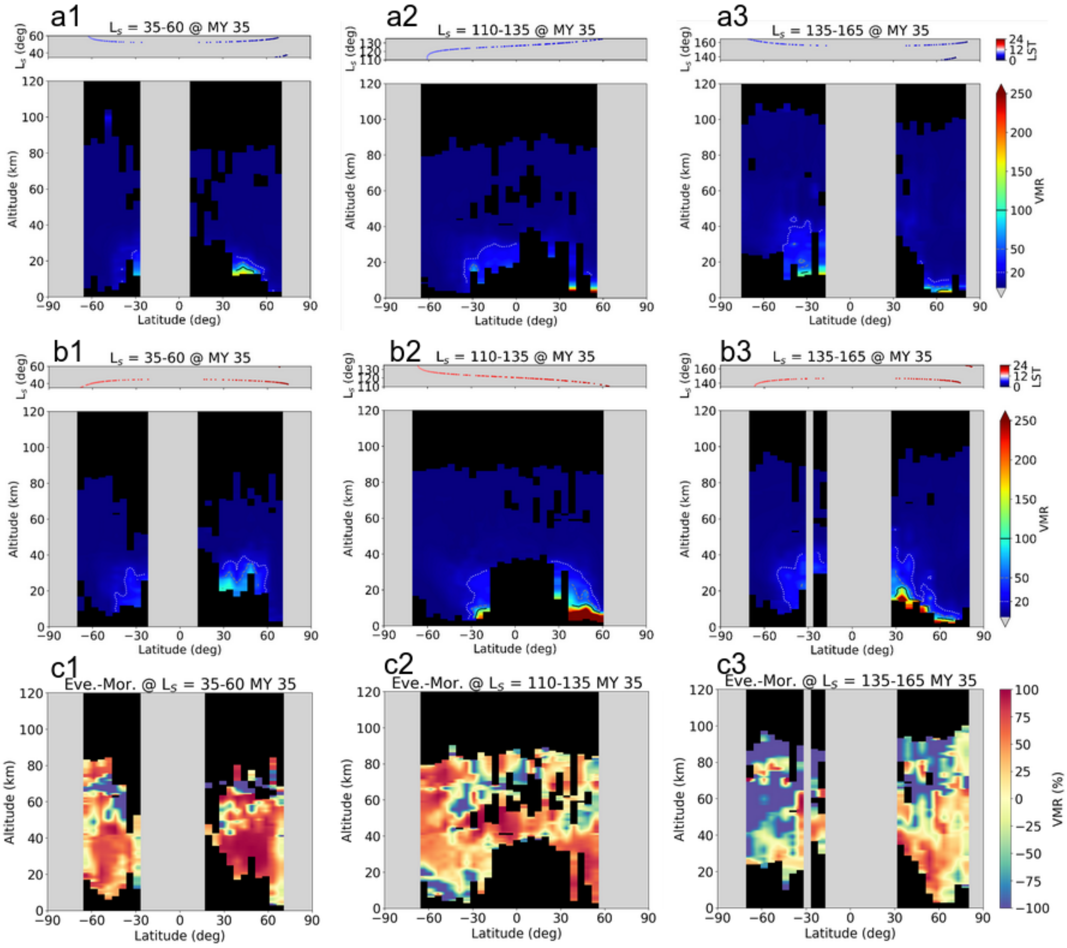

FIGURE 7.8: Latitudinal distribution of water vapor profiles at different Solar Longitude ranges during MY 35 for the morning (top) and evening (middle) terminators. Bottom panels show the relative difference between evening and morning observations. Latitude and local solar time of the observations are indicated with dots above each panel.

southern hemisphere and transported northward with the meridional circulation. In absence of solar light during nighttime, water accumulates at high altitudes as it is being transported toward the northern hemisphere, showing a maximum abundance during mornings at high northern latitudes. Then, during daytime, photo-dissociation reduces the amount of water at high altitudes, hence, producing the observed water vapor deficit at the evenings. This explanation may suggest the delicate balance between vertical and meridional transports and photo-dissociation. At high altitudes in the southern hemisphere, the evening's enhanced vertical transport appears to be more significant than photo-dissociation. Conversely, in the northern hemisphere, the daytime meridional transport is insufficient to compensate for the water lost through photolysis. The high sensitivity of the NOMAD instrument allowed for the first time to systematically explore the distribution of water at these high altitudes. The current lack of similar measurements and the reduced number of similar studies about local time water vapor variability make difficult to confirm or

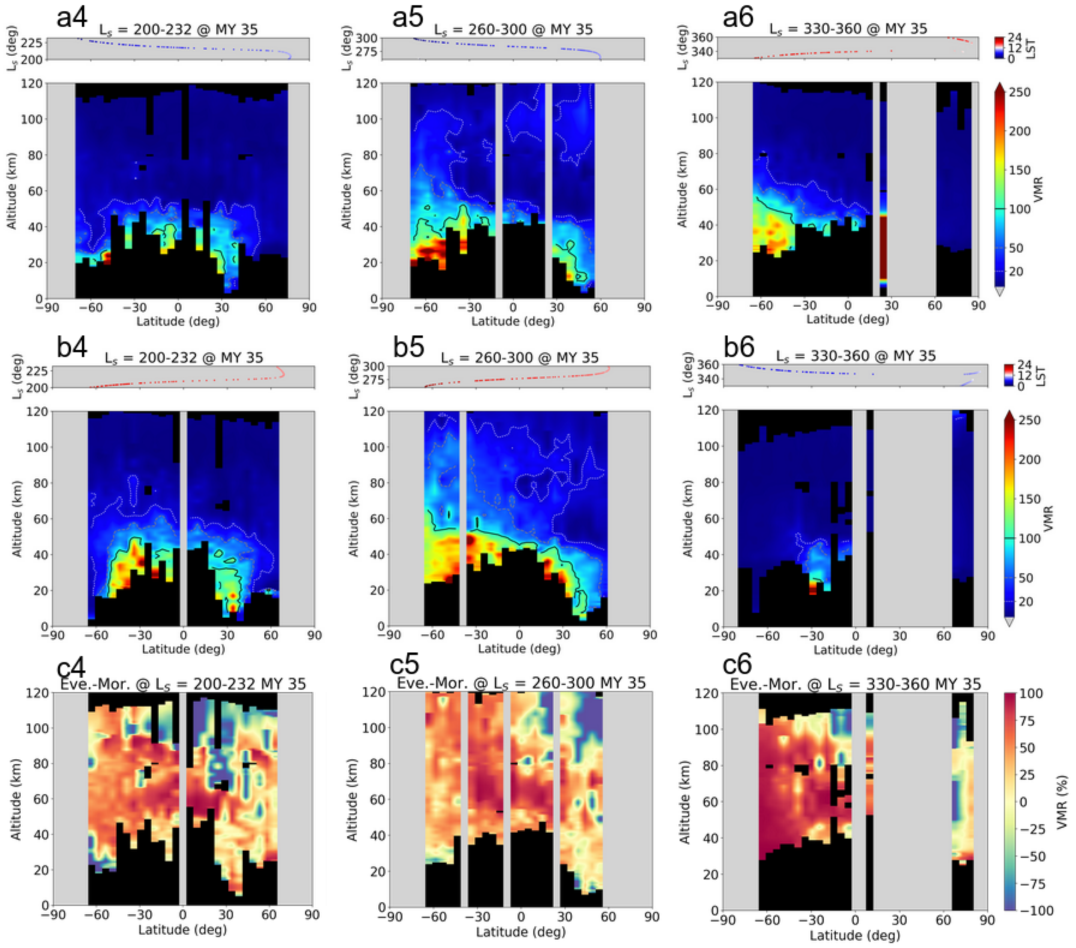

FIGURE 7.8: (continued)

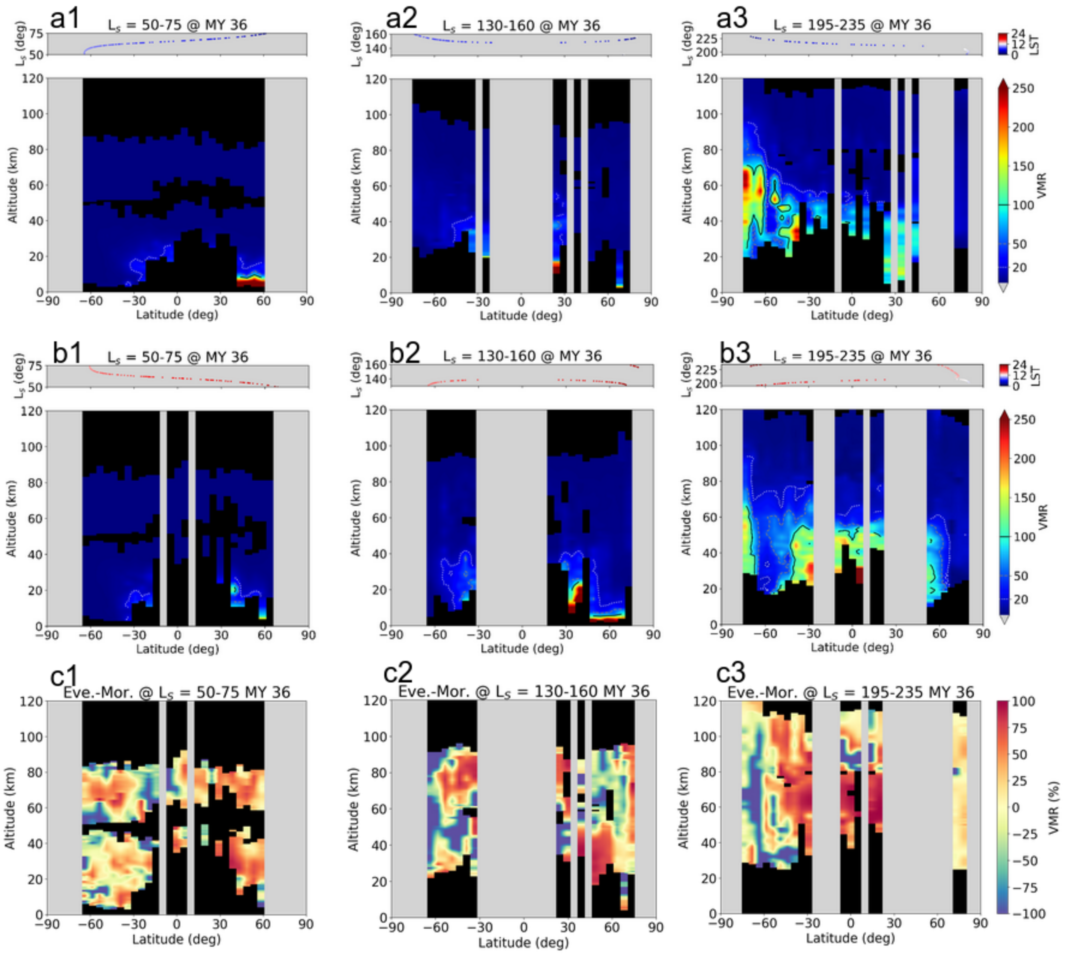

FIGURE 7.9: Latitudinal distribution of water vapor profiles at different Solar Longitude ranges during MY 36 for the morning (top) and evening (middle) terminators. Bottom panels show the relative difference between evening and morning observations. Latitude and local solar time of the observations are indicated with dots above each panel.

discard this hypothesis, hence, more observations are needed to provide more insight on this phenomena.

By the end of the year, as shown in Figures 7.8-c6 and 7.9-c5 the effects of the C-storms reveal a pronounced increase of water vapor during the southern evenings at 30°S-60°S below 40-60 km, while the northern hemisphere does not show such strong local time variations.

All these results confirm and complement some of the previous studies on water vapor latitudinal and local time variability carried out with other TGO instruments such as Belyaev et al., 2021; Fedorova et al., 2023, extending the altitude coverage and adding for the first time TGO observations for the MY 37. They analyzed ACS measurements and reported overall larger water vapor abundance during evenings than during the mornings. In addition, they also revealed thermal tides modulating

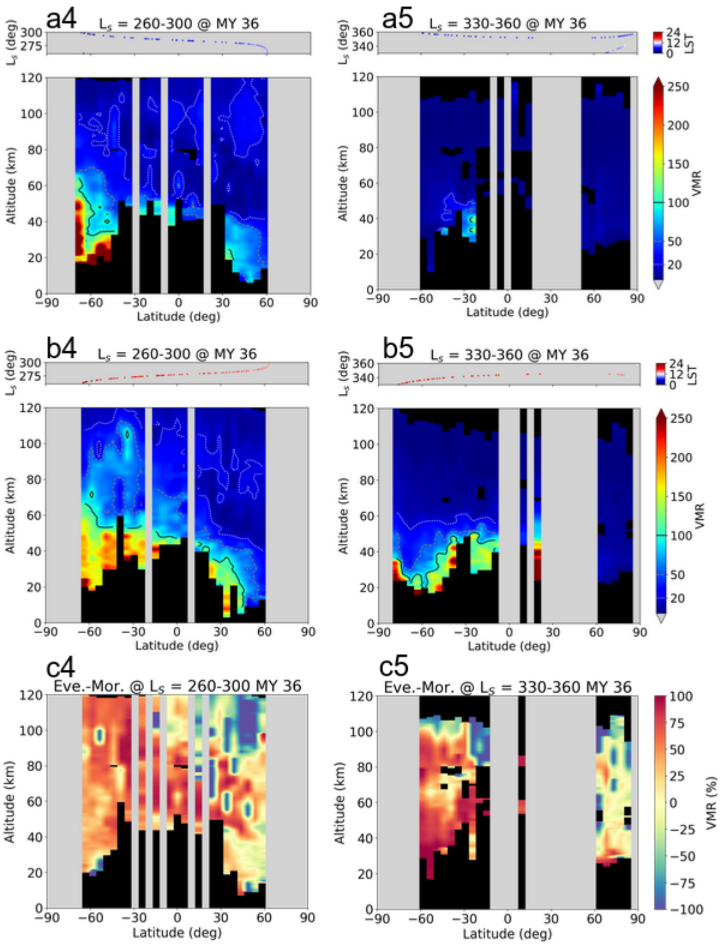

FIGURE 7.9: (continued)

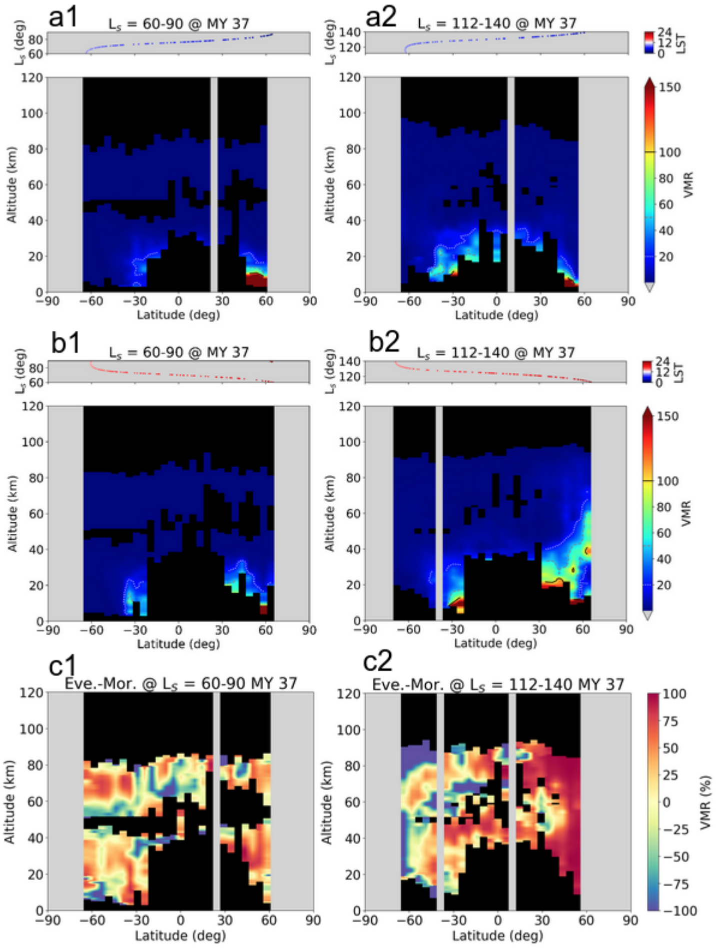

FIGURE 7.10: Latitudinal distribution of water vapor profiles at different Solar Longitude ranges during MY 37 for the morning (top) and evening (middle) terminators. Bottom panels show the relative difference between evening and morning observations. Latitude and local solar time of the observations are indicated with dots above each panel.

water vapor variations between morning and evening terminators. Our results are also in line with those presented by Aoki et al., 2022, who analyzed NOMAD observations using a completely different retrieval scheme.

7.6 Comparison and validation with previous works

The orbital geometry and the high sensitivity achieved with the solar occultation observation technique make TGO an ideal asset for the systematic search and characterization of trace species in the martian atmosphere. Water vapor, despite being in relatively low abundance in Mars (∼0.03 % of the total atmospheric composition), is a crucial factor in the planet's climate. For that reason, several teams within the TGO consortium are studying this species with different instruments onboard the spacecraft, characterizing topics such as the water at high altitudes (Belyaev et al., 2021; Brines et al., 2024b), isotopic fractionation (Alday et al., 2021;

Villanueva et al., 2022a), water vapor saturation ratios (Fedorova et al., 2023) or its seasonal variability (Aoki et al., 2022). In this Section we show a comparison of the results presented here (hereafter referred to as NOMAD-B) with the results obtained from two of the most recent and extensive studies on water vapor performed with NOMAD (Aoki et al., 2022) (hereafter referred to as NOMAD-A) and ACS (Fedorova et al., 2023) (hereafter referred to as ACS-F). ACS, also onboard TGO, is a suite of three high resolution spectrometers: (i) the near-infrared channel (NIR), (ii) the middle-infrared channel (MIR) and (iii) the thermal infra-red channel in honor of Professor Vassily Ivanovich Moroz (TIRVIM). This instrument operates in the spectral range from 0.65 to 17 µm (Korablev et al., 2018) and like NOMAD, was designed to observe the atmosphere in solar occultation, nadir and limb geometries. The NIR channel, operetaing in the spectral range 0.73-1.6 µm, follows the design of the SPICAM-IR instrument, this is, based on an AOTF filter and an echelle-grating, entirely similar to the NOMAD SO channel. Although both NOMAD SO and ACS NIR sample the atmosphere in solar occultations, due to difference in the pointing alignment of the instruments, not all their observations are collocated or match well in latitude and longitude. Hence, in order to avoid climatological variability effects during the comparison, we selected a subset of measurements imposing a co-location criterion. This is, we only considered as co-located those ACS and NOMAD occultations within a latitude-longitude box of 5°. Since both NOMAD and ACS follow the same orbit, for almost every occultation the solar longitude and local time are identical. With this restriction, we selected a subset of measurements during MYs 34, 35 and 36, resulting in a total of 903 vertical profiles common in this work and in Fedorova et al., 2023, making a total of 28825 coincident water vapor measurements. On the other hand, the profiles presented in Aoki et al., 2022 were measured with NOMAD SO, so the co-location criterion is granted. The number of common occultations available for the comparison between this work and Aoki et al., 2022 during MYs 34, 35 and 36 is 4193, making a total of 89901 coincident water vapor measurements. The data analysis and inversion methods performed by each team are described in Aoki et al., 2022 and Fedorova et al., 2023 for the NOMAD-A and ACS-F retrievals respectively.

Aoki et al., 2022 retrieved the water vapor column density along the line of sight (LOS) using the optimal estimation method (Rodgers, 2000), processing the spectrum at each altitude as an independent measurement assuming a constant volume mixing ratio along the LOS. The VMRs are expressed for a given reference atmosphere. So, in order to eliminate the effect of using different atmospheric densities in both retrieval schemes (GEM-Mars in the case of NOMAD-A, and the Mars-PCM in our inversion), the VMR from the NOMAD-A data set were scaled by the factor $s = \rho^A/\rho^B$, where ρ^A and ρ^B are the total atmospheric densities used in NOMAD-A and NOMAD-B retrievals respectively.

The profiles from ACS-F were obtained using a global fit method, similar to what it is done in this study, where the spectra at all altitudes are processed simultaneously (Fedorova et al., 2020). For the ACS-F retrievals, the total atmospheric densities are not included in the publication and therefore, they were not available at the time of the publication of this Thesis, so the scaling of the VMRs to a common reference atmosphere was not possible. Nevertheless, ACS-F uses during the inversions the temperature and pressure profiles from the European Martian Climate Database (EMCD), which is based on the Mars-PCM used for our retrievals. Hence, the bias introduced by the discrepancy on the reference atmospheres between ACS-F and NOMAD-B are possibly small.

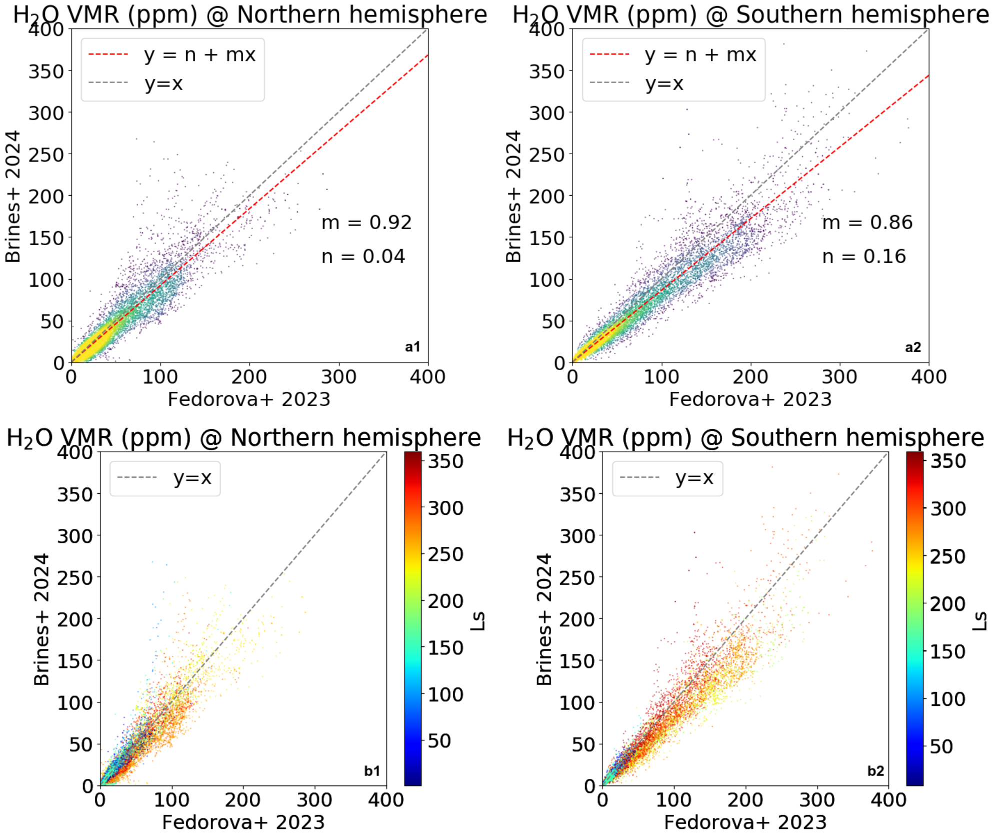

FIGURE 7.11: Comparison of our water vapor abundances (y-axis) with those obtained by Fedorova et al., 2023 (x-axis). Colors indicate point density (top panels) and Solar Longitude (bottom panels). Red dashed line in top panels show the linear fitting. Gray dashed line indicates $y = x$.

The procedures and retrieval methodology used in NOMAD-B and those described above used in NOMAD-A and ACS-F are all different, each one of them requiring specific assumptions to consider during the inversions. Therefore, the comparison presented here must be taken with caution. In Figures 7.11 and 7.12 we show correlograms with the comparison between the results obtained in this Thesis (y-axis) and those from ACS-F and NOMAD-A respectively (x-axis).

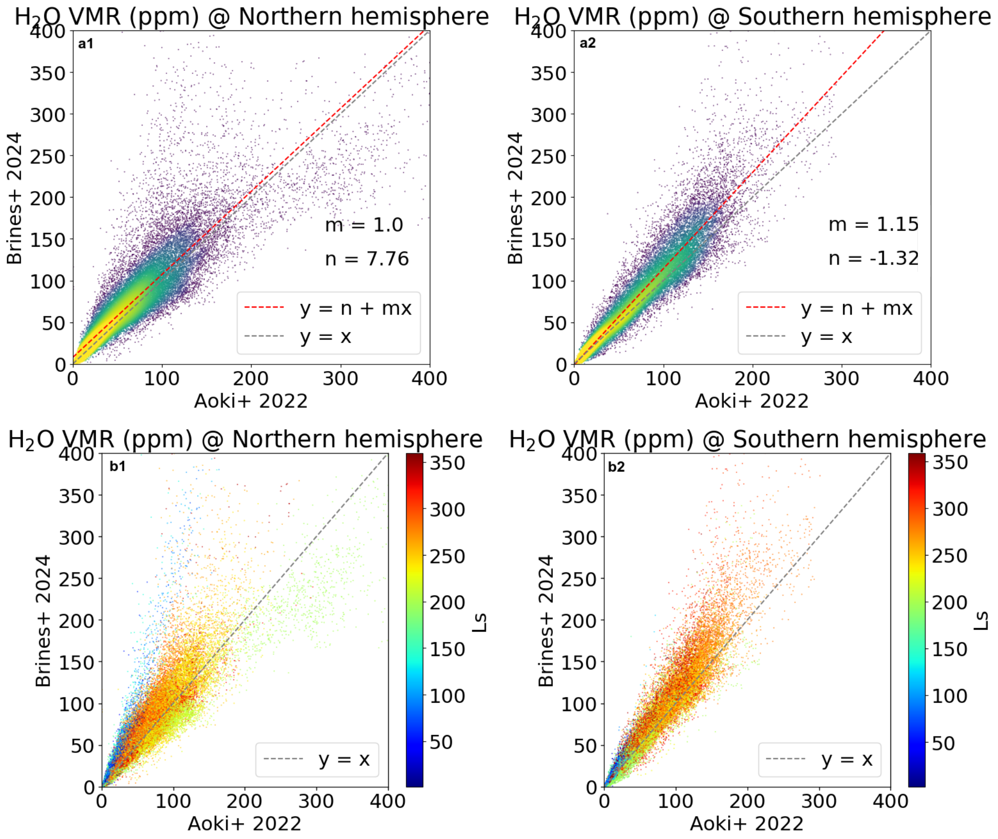

FIGURE 7.12: Comparison of our water vapor abundances (y-axis) with those obtained by Aoki et al., 2022 (x-axis). Colors indicate point density (top panels) and Solar Longitude (bottom panels). Red dashed line in top panels show the linear fitting. Gray dashed line indicates $y = x$.

Left and right panels indicate measurements taken for the northern and southern hemispheres respectively. For both Figures, colors in top panels show the point density distribution (the more yellowish, the larger number of points) whereas the colors in the bottom panels represent different seasons throughout the Martian year. Overall the agreement is good in both comparisons, with mean correlation factors of 0.91 for the comparison with ACS-F and 0.83 in the case of NOMAD-A. Considering the large differences in the retrieval approaches, the linear fit of the comparison also shows an excellent agreement between the three sets of retrievals. We notice, however, that the results presented in this work are globally about ∼7.5% larger than NOMAD-A and about ∼11% systematically smaller than ACS-F, which falls within the retrieval's uncertainties of both NOMAD and ACS. Despite the overall good agreement, some profiles show systematic bias, particularly in the northern hemisphere. The comparison with NOMAD-A reveals a diverging branch towards higher VMR values in NOMAD-B results. As shown in Figure 7.12-b1, this branch corresponds with profiles measured during the aphelion season and specifically, at low altitudes (below 20-30 km). The reason of this bias could be related to several factors. At those altitudes the constraints imposed during the inversion, i.e. regularization, play a significant role and values obtained at the lowermost edge of the retrieved altitude grid might be affected by the a priori climatology. Other possible reason for the bias could be the retrieval method itself. In the case of NOMAD-A, the assumption of a constant VMR along the LOS and not considering the contribution of the spectra from the layers above the observation shall introduce biases under conditions of strong vertical gradients, which are common at low altitudes during the northern summer (Brines et al., 2024b).

A selection of 32 profiles, 16 for each hemisphere, measured during different seasons are presented in Figures B.1 and B.2 for the northern and southern hemispheres respectively. This set was selected because it captures a variety of representative features observed in the water vapor profiles, covering different atmospheric conditions. Each panel shows the retrieved profiles from NOMAD-B (blue, this work), NOMAD-A (green) and ACS-F (red). Overall, as discussed above in this Section, the agreement between the three retrievals is good, with all three profiles capturing the same vertical structure. However, some discrepancies arise regarding the amplitude of those structures, with more pronounced features appearing in NOMAD-B. The reason of this bias might be due to the different vertical resolution obtained during the inversions, i.e. the averaging kernels, which is directly related with the information content. Our retirevals seem optimal in terms of vertical resolution. Also, the noise propagation in comparable or better than in the other inversions, and the altitude coverage that can be studied is also larger.

7.7 Cluster analysis

As discussed in Sections 7.3 and 7.4, the water vapor distribution on Mars has a strong variability with season and latitude, although following repeated patterns and similar vertical structures every Martian year. Therefore, a characterization by means of a small set of representative profiles could be very useful to characterize the water vapor climatology. In this Section we present the results obtained after the application of cluster analysis techniques to our retrieved data set of profiles in order to identify the most relevant vertical structures associated to different times and locations. Cluster analysis is a statistical method used to categorize similar objects into subsets, or "clusters," ensuring that objects within the same cluster are more similar to each other than to those in different clusters. The main objective of cluster analysis is to reveal the inherent groupings in a data set without any prior knowledge about the groups. There are several techniques for clustering, each with distinct advantages and limitations.

For this work, and based on previous similar studies on Martian temperature vertical profiles (Cala Hurtado, 2016), we used the K-means algorithm. This is an iterative method which clusters data minimizing the distance between data points while maximizing the mean distance between clusters. First, a number of clusters is provided. Then, a representative vertical profile for each cluster is randomly defined, i.e. centroid, and the retrieved NOMAD profiles are assigned to each one of those clusters in a way that the mean euclidean distance between each profile and the cluster's centroid is minimum. After that, the centroids are recalculated for the new clusters and the assignation process is done again. These two steps are repeated until convergence, that is, until the difference between the new centroids and the previous one is less than a certain value. Here we explored different initial configurations and several numbers of clusters, from 2 to 20, in order to evaluate the impact of the random initialization of centroids and the sensitivity to different levels of clustering. We studied several quality metrics commonly used in this kind of studies such as the Silhouette coefficient (Rousseeuw, 1987), the Davies-Bouldin index (Davies & Bouldin, 1979) or the Calinski-Harabasz index (Caliński & Harabasz, 1974). All these metrics try to evaluate and compare the between-cluster separation with the within-cluster dispersion, where the larger the first and the smaller the second, the better. After these test and based on visual inspections, we decided to use $K = 6$ clusters to provide a simplified view of the water vapor climatology, describing the seasonal and latitudinal inter-annual variability with 6 distinct representative profiles. We applied the clustering to the whole data set at once, including the four MYs and both southern and northern hemisphere measurements during the cluster assignation.

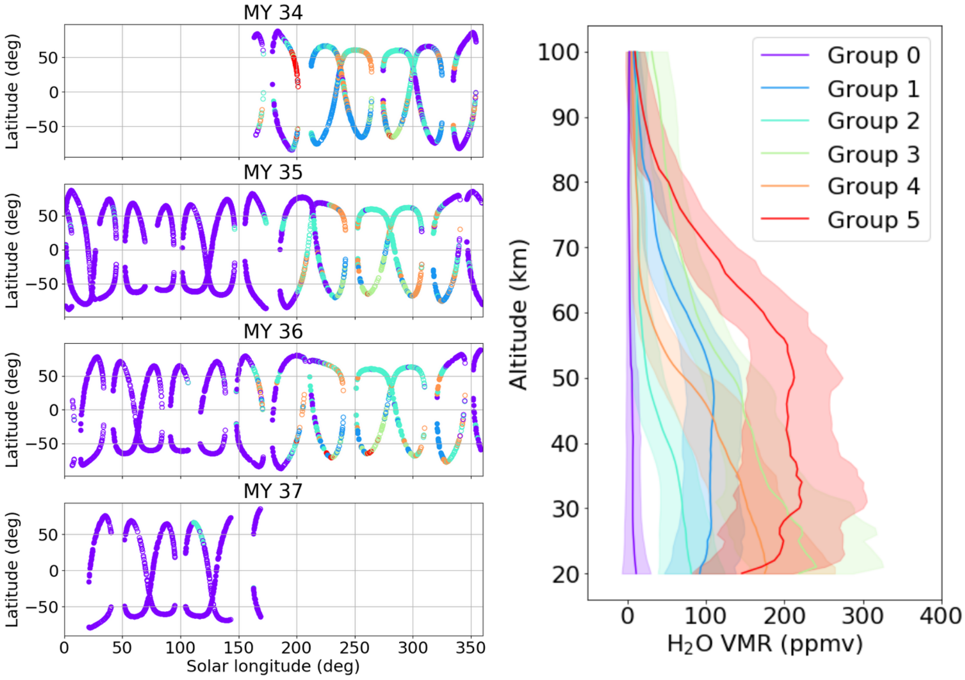

FIGURE 7.13: Left panels show the seasonal-latitudinal distribution of the retrieved NOMAD SO water vapor vertical profiles for MYs 34, 35, 36 and 37 (from top to bottom respectively). Colors indicate the groups where profiles were assigned. Right panel shows the representative profile of each cluster.

In Figure 7.13, we show the results of the clustering for MYs 34, 35, 36 and 37. Left panels indicate the latitude and solar longitude of each identified group, identified by colors for every MY. The representative profiles of each cluster are presented in the right hand side panel. From Figure 7.13 we can identify different features represented by distinct groups.

- First, Group 0 is observed during $L_S{\sim}0^\circ - 180^\circ$ and $L_S{\sim}340^\circ - 360^\circ$ and includes all the profiles representative for the aphelion season and the northern spring equinox. It shows low and nearly constant water vapor abundance at all altitudes and is common during this period in all MYs. On the other hand, groups 1 to 5 are used to describe the variability during the perihelion season.
- Group 1, characterized by abundances about 100 ppm below 50 km, appears scattered during the second half of the year, although seems to be more common in the southern hemisphere. It is particularly frequent during $L_S{\sim}200^\circ - 250^\circ$ in MY 34, period which coincides with the decay phase of the GDS. It is also common around $L_S{\sim}320^\circ$ in MYs 34,35,36 coinciding with the appearance of the C-storm.
- Group 2, with abundances between 50 to 100 ppm below 40 km, is common at mid-high northern latitudes below 70°. Unlike any other year, this profile appears also during the aphelion of MY 37 at $L_S{\sim}110^\circ - 120^\circ$.
- Group 3 shows abundances ranging between 100 to 200 ppm below 50 km and about 50 ppm above 80 km. It appears only in the southern hemisphere (mid latitudes) and is common during $L_S{\sim}250^\circ - 280^\circ$ in MYs 34,35,36. This period corresponds with the perihelion and its time and location of appearance coincides with the detection of high water vapor abundance in the upper atmosphere, as discussed by Belyaev et al., 2021, and more recently by Brines et al., 2024b.
- Group 4, with abundances above 100 ppm below 45 km and with a sharp decrease above, appears scattered in both hemispheres, usually acting as a transition between groups 1, 2 and 3.
- Finally, Group 5 represent water vapor profiles with abundances of about 200 ppm below 60 km and about 50 ppm at 80 km, decreasing with altitude. This type of profiles appears at $L_S{\sim}180^\circ - 210^\circ$ in MY 34 and are representative of the peak activity of the GDS during that year. This group is also briefly observed during the perihelion at $L_S{\sim}260^\circ$ in MYs 35 and 36 and $L_S{\sim}280^\circ$ in MY 34, between observations of the Group 3.

These results show that seasonal variability is overall more relevant than the latitudinal or local time variations. However, some groups may have a preference to appear in the northern or southern hemispheres, and similarly, a few groups were observed more frequently during specific local times.

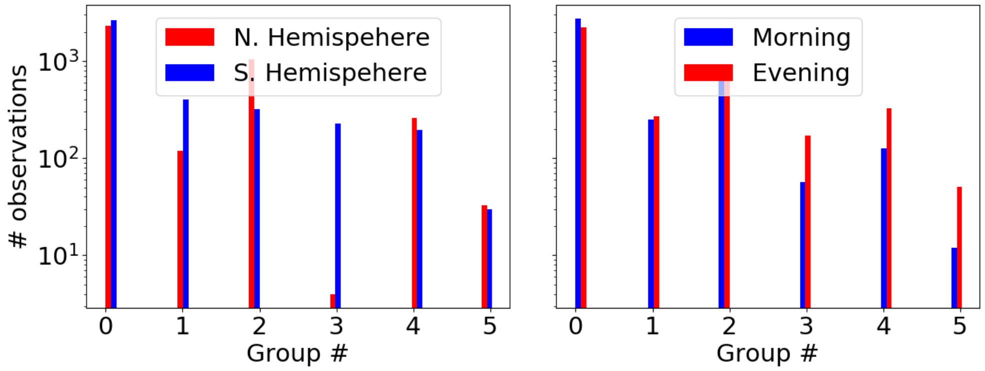

FIGURE 7.14: Left panel shows the number of profiles measured at the northern (red) and southern (blue) hemisphere for each group. Right panel shows the same but for profiles measured during mornings (blue) and evenings (red).

In Figure 7.14 we show the number of observations grouped in each cluster, indicating if the profiles within the group correspond to measurements taken at the northern or southern hemisphere (left panel) and if the observations correspond to the morning or evening terminators (right panel). Although some of these groups were observed with a slightly larger frequency in one hemisphere than in the other, only Groups 1 and 3 stand out clearly to be representative for the southern hemisphere. While the first corresponds to the observations during the decay phase of the GDS, the second represents profiles showing the largest abundance of water vapor at high altitudes. On the other hand, Group 2 seem to be more frequent in the northern hemisphere during the winter solstice. Regarding the local time, profiles from Groups 3 and 4 appear more repeatedly during evening observations. However, the larger amount of evening profiles in Group 5, which contains mostly profiles observed during the GDS, is due to the fact that this event was observed only during evenings indicating a bias in the sample rather than a true feature.

Improving the assignation method and focusing the analysis on specific periods could help to highlight some of the interhemispheric and local time variations discussed here and in previous Sections. The goal of this analysis was to provide a complete and simplified view of the water vapor climatology, settling the framework for future studies on clustering of Martian water vapor vertical profiles, possibly focused on more specific times and locations.

7.8 Summary and conclusions

For this work, we analyzed NOMAD SO spectra from more than 7000 occultations collected over MYs 34 to 37, covering four diffraction orders and combining them in order to avoid optically thick absorption lines. Our pre-processing pipeline significantly improved the correction of systematic errors in the NOMAD SO data, particularly for high-altitude measurements where accurate baseline characterization is crucial. This permitted the retrieval of extended water vapor vertical profiles from approximately 5 km to 120 km altitude in a single consistent inversion. In this study we presented the seasonal and latitudinal variability of water vapor in the Martian atmosphere providing the most extensive water vapor climatology up to date based on NOMAD observations. In addition, our large data set allowed us to perform a robust comparison with other teams and instruments also analyzing water vapor on Mars and a novel statistical technique based on cluster analysis was applied for the first time to Martian water vapor vertical profiles. Our main conclusions can be summarized as follows:

- We observed strong seasonal variations in water vapor distribution on Mars, with distinct differences between perihelion and aphelion seasons in both hemispheres, with the southern hemisphere experiencing more intense and extended water vapor presence during its summer. These variations and interhemispheric asymmetry are influenced by factors such as dust storms, polar cap sublimation, Martian orbital eccentricity and topographic differences.

- During equinoxes, water vapor is mostly confined to low altitudes and at low latitudes, showing abundances below 20 ppm above 30 km during the mornings and above 40 km during the evenings. However, the vertical extension of this water vapor layers and its peak abundances are larger during the northern autumn then during the spring equinox. The latitudinal distribution is symmetric with respect to the equator, repeatedly during all MYs. In addition, our observations reveal a 40 km altitude layer of abundances of about 20 ppm at ±60° latitude as a consequence of the polar warming.

- The effects of injecting water vapor at high altitudes during the GDS were visible after the northern autumn equinox during MY 34, which presented abundances of about 100 ppm at 80 km altitude. In the period corresponding to the decay phase of the storm, and at altitudes below 60 km, we observed larger abundances during MYs 35 and 36 than during MY 34 (the GDS year).

- During the perihelion, all MYs show a similar asymmetric distribution, with larger and more vertically extended abundances at the southern hemisphere. However, MY 35 and 36 show a more intense vertical transport at 60°S, injecting abundances of about 50 ppm at 100 km altitude. During this period, we observed hints of the presence of water ice clouds in the form of depletion layers of water vapor in the northern hemisphere between 40 and 60 km altitude.

- Overall water vapor profiles show larger abundances and more vertically extended structures during the evening than during the morning systematically throughout the whole MY due to enhanced vertical transport. Typically this dynamical effect is more intense during the aphelion season, however MY 37 shows also an intense upward transport in the northern hemisphere at $L_S \sim 112°$

which was not observed during other MYs. In addition, a distinct enhancement of abundances during the morning at 100 km suggests the photolysis of water vapor in the mesosphere and above to play a key role on the distribution and transport of water vapor at high altitudes.

- We presented for the first time an application of cluster analysis techniques to NOMAD SO water vapor vertical profiles. We identified at least 6 distinct type of profiles representative of different atmospheric conditions. This purely statistical tool, blind to physics, revealed meaningful distributions and provided a simplified water vapor climatology. The clustering successfully captured the water vapor strong seasonal variability above other variations due to latitude or local time, with the exception of the peak of the MY 34 GDS which already stands out as a separate vertical profile.
- All the results presented in this work extend and complement some of previous recent studies on water vapor vertical profiles. Here we presented a comparison with other two teams retrieving water vapor from observations NOMAD and ACS observations. This comparison, taking into account the instrumental uncertainties and the difference in the data processing, retrieval methods, and vertical resolution/information content revealed an overall good agreement between the three teams.

Chapter 8

Conclusions and Future Work

In this Chapter we provide a summary of the research conducted during the development of this Thesis. The work presented here focused on the detection, mapping and scientific description of the water vapor abundance and distribution in the Martian atmosphere using solar occultation measurements with the NOMAD/TGO spectrometer.

8.1 Goals and methods

A collaborative effort among the European Space Agency and Russia's Roscosmos led to the development of the ExoMars mission. Since 2018, the Trace Gas Orbiter (TGO) has been probing the Martian atmosphere in different observation geometries with several instruments, including the Nadir and Occultation for Mars Discovery (NOMAD). NOMAD's Solar Occultation channel, based on the Venus Express's SOIR spectrometer, uses an echelle grating with an Acousto-Optical Tunable Filter (AOTF) in Litrow geometry to separate diffraction orders. This, enables quasi-simultaneous atmospheric probing with about 1 km vertical sampling, allowing systematic observations of the vertical structure of the Martian atmosphere with an unprecedented vertical resolution. Recent collaborative efforts within the NOMAD consortium have provided the best characterization of the AOTF and ILS, in which we participated actively as part of the work done for this Thesis.

This Thesis has been supported by and developed under a pre-doctoral contract, funded by the Spanish Ministry of Science and Innovation (MCIU) from the grant PRE2019-088355 and by 'ESF Investing in your future'. With financial support by FEdER funds, and associated to a Research Project (PGC2018-101836-B-100) lead by the IAA, devoted to the scientific exploitation of NOMAD data.

The research presented in this Thesis was carried out in the Grupo de Atmospferas Planetarias Terrestres (GAPT) of the IAA, as an active collaboration with other international research groups within the NOMAD consortium. The original plan, development of the research and the results obtained have been presented regularly in all the NOMAD Science Working Team meetings over the last 4 years. Also in a series of contributions on national an international conferences, as listed in Apendix

C. And also in a number of publications in top journals in the field, some of them lead by myself and some others where I appear as co-author. They are also listed in Appendix C. Chapters 5, 6 and 7 of this Thesis contain articles lead by me, the first two already published and the third one in preparation.

This research has made extensive use of a number of research tools developed over the years at the GAPT/IAA and other research laboratories, like the TGO pre-processing (IAA), the forward model KOPRA (IMK/IAA) and the inversion processor RCP (IMK, Karlsruhe Institute of Technology, Germany). In turn, this Thesis has contributed to improve and extend the IAA pre-processing scheme with new modules (codes in Python) in several directions. The data set used in this Thesis are Level 1 calibrated atmospheric transmittances in limb/solar occultation geometry supplied by the NOMAD PI's laboratory (BIRA, Brussels, Belgium). After downloading the data, my proper research started with a revision of the calibrated data, with the double goal of (i) first, the characterization of the NOMAD instrument response and its actual random noise levels, and (ii) second, the correction of systematics and residual defects present in the data. This study included the generation of synthetic spectra for better understanding the capabilities of our inversion scheme and the impact of the different uncertainties. Then I proceeded to perform the actual inversions of water vapor abundances, to carry out studies of internal consistency, and to perform detailed comparison and validation exercises with other data sets. These, together with comparisons with state-of-the-art climate models of Mars, allowed scientific interpretation of the water vapor abundances and their variability, sources, and links to other geophysical parameters.

The major scientific results obtained in this This include the vertical distribution of water vapor on Mars during the southern spring-summer seasons in Martian years (MY) 34 and 35, covering the 2018 GDS in MY 34. By comparing the same season with different dust conditions, we were able to analyze the significant impact of global dust events on the water vapor vertical distribution. This is the topic of my first scientific publication and was included in Chapter 5. After proving the reliability of our retrieval setup and improving the data analysis techniques, we decided to perform a specific study focused on the study on high altitude water vapor during the southern summer solstice of MYs 34, 35 and 36. During this season, a strong localized vertical transport in the southern hemisphere revealed a notable increase in water vapor reaching the upper atmosphere, emphasizing the need for more water vapor observations during perihelion to better understand this event. This was presented in my second publication and included here in Chapter 6. Finally, we extended the analysis to over 7000 NOMAD SO occultations from MYs 34 to 37, basically all the NOMAD SO data available up to the date of publication of this work. The main goal was to create the most extensive climatology of water vapor vertical profiles on Mars based on NOMAD observations. Further improvements in the pre-processing pipeline allowed for retrieving accurate vertical profiles of water vapor from 5 km to 120 km altitude and the large size of the data set permitted the identification of regular patterns and interannual changes in the water vapor distribution, as well as the application of statistical tools such as the cluster analysis.

8.2 Programmatic achievements

The most relevant conclusion of the Thesis can be summarized as follows:

1. This thesis presents an extensive description of the vertical profiles of water vapor on Mars and their variability from solar occultation data by NOMAD/SO, after a successful combination of pre-processing/cleaning tools developed at IAA and an state-of-the-art retrieval suite (KOPRA+RCP) adapted to solar occultations for the first time.

2. The work presented in this Thesis addressed some if the main objectives planed for the ExoMars 2016 mission such as: (i) the investigation of the chemical composition of the Martian atmosphere, in particular the water vapor variability and characterization of its distribution in the atmosphere, (ii) the study of the atmospheric escape by analyzing water vapor in the upper atmosphere, (iii) extending the Mars water vapor climatology and seasonal cycles, and (iv) the study of sources and sinks for water vapor in the Martian atmosphere.

3. In this Thesis we have carried out an analysis of the NOMAD SO ILS and AOTF with independent tools developed for this purpose. These results were combined with those obtained independently by other teams within the NOMAD consortium, provide a consensual recipe for the instrument's characterization.

4. Specific software tools, developed for the processing of NOMAD SO calibrated transmittances for the analysis of water vapor were incorporated into the IAA Pre-Processing, which have contributed to improve parallel studies in the GAPT/IAA. These are: (i) the IAA-PreProcessing's module designed to correct for bendings in the baseline of the spectra and shifts in the position of the absorption lines, optimized with the implementation of a jump-search algorithm, (ii) a precise characterization of the spectral shift by selecting optimal altitude ranges, (iii) a precise fine tune correction of the bending based on averaging spectra at high altitudes, (iv) a precise characterization of the random component of the measurement noise by the use of covariance matrices, method which has been recently implemented in the official NOMAD calibration pipeline, (v) a novel retrieval technique within the NOMAD consortium based on the combination of different diffraction orders sampling different altitude ranges during a single inversion, (vi) the implementation of module devoted to the cluster analysis of the NOMAD data, and (vii)

visualization tools to examine pre-processing, inversion and post-processing data.

5. An extensive error analysis and sensitivity tests were conducted and presented. By simulating spectra for different atmospheric conditions and taking into account the instrumental characterization of NOMAD we were able to determine an optimal regularization for each diffraction order to use during the inversions. In addition, synthetic retrievals were used to demonstrate the reliability of our setup, proving its independence from the water vapor a prior profile used, and revealing a 2% uncertainty propagated to the retrieved profiles from possible errors in the reference temperature and pressure. An estimated uncertainty of about 10 % in the retrieved water vapor profiles from the uncertainty in the AOTF characterization was also reported.
6. In addition, we presented a summary of an extensive comparison of the forward models used by several teams within the NOMAD consortium, testing the correct implementation of the NOMAD SO characterization recipe in all of them.This work was done at the University of Tokyo and NASA Goddard Space Flight Center during a total of 3.5 months of stay abroad.

8.3 Scientific conclusions

1. The analysis of the 2018 GDS revealed water vapor abundances peaking at 150 ppmv at 80 km in both hemispheres during the strong activity of the storm before dropping to 50 ppmv in the northern hemisphere with high levels persisting at high southern latitudes, contrasting with MY 35 where water vapor did not exceed 50 ppmv above 50 km. We observed that during the GDS, water vapor was mostly present at latitudes between 60°N and 75°S, with high abundances up to 80 km at mid and low latitudes.
2. Estimations of the saturation ratio using NOMAD SO temperatures were performed for MY 34, revealing multiple layers of supersaturation, with a clear region above 60 km in both hemispheres during the GDS. In addition we identified sporadic supersaturated layers in the presence of water ice suggesting condensation processes at the terminator.
3. Detailed analysis of the observations during the perihelion season revealed a strong vertical transport of water vapor to the upper atmosphere, particularly localized at the southern hemisphere, with significant plumes reaching 50 ppmv at 100 km, observable for short periods and repeated across different MYs showing some interannual variability. These variations influenced by the MY 34 GDS, suggest a weakened southern polar vortex and reduced water vapor production rates during years with dust storms.

4. Estimations of the hydrogen escape to space during at the perihelion revealed an enhancement of 30% compared to other periods with weaker vertical transport.
5. We presented the analysis of the whole water vapor climatology available from NOMAD SO observations including over 7000 occultations taken during four MYs which, together with the retrievals by companion spectrometer AXS/MIR, provided the most extended data set of water vapor vertical profiles on Mars up to this date.
6. We observed strong seasonal and interhemispheric variations in water vapor distribution on Mars repeated every year, with the southern hemisphere experiencing more intense and vertically extended water vapor presence during its summer, influenced by factors such as dust storms, polar cap sublimation, orbital eccentricity, and topographic differences. Overall, water vapor profiles showed larger abundances during evening terminator observations.
7. The large number of profiles in the analyzed data set allowed us for the first time to perform a cluster analysis to Martian water vapor profiles, identifying six distinct atmospheric conditions and providing a simplified water vapor climatology.
8. An extensive number of comparisons exercises was conducted and presented, validating many of the results obtained during the elaboration of this Thesis. Comparisons of the results presented here with water vapor profiles and seasonal variability of water vapor number density at high altitudes obtained from the same (NOMAD) and other instruments (ACS) revealed a good agreement within instrument uncertainties between different teams, in spite of performing retrievals using different methods.

8.4 Future Work

The work done for this Thesis and the results obtained, although complete and interesting in themselves, raise a series of new questions and paves new paths for improving and extending the studies presented here. Both technical and scientific improvements are foreseen:

1. *Regularization improvements.* Atmospheric retrievals, are on their own, handcrafted works. Every time we launch a retrieval, it improves the results and performance of the previous one. As discussed throughout this work, one of the main drivers/user decisions affecting the inversions is the regularization. In favor of automation of large scale computations, we decided to use a common regularization, acceptable for all of the observations analyzed here. Although it was optimized for each diffraction order, the extreme variability of the Martian atmosphere led to some retrieved profiles to be highly or poorly regularized. Hence, based on the a prior information from the model (which

is expected to be close to the reality), we propose in the future to adapt the regularization for each observation, taking into account its season, location and local time. This way we expect not only to improve the ratio of convergence and numerical stability during the inversion, but also to provide profiles with more meaningful and reliable retrieval uncertainties.

2. *Extension of combined orders*. One of the main contributions of this work to the NOMAD community is the combination of two different diffraction orders in one single retrieval. The success proved on water vapor encouraged us to extend this methodology to other species. We already did some steps in that direction. Preliminary results on CO retrievals indicate a good performance of the method and we are now extending it to CO_2 and temperature retrievals. In addition, we are working on combining not only two but three or more orders. We expect this improvement to have a positive impact on temperature retrievals, where the strong saturation of the CO_2 lines required for the inversion impose strong limitations on the available altitude range of meaningful inversions.

3. *Improved performance at low altitudes*. The sampling of the lower atmosphere is limited by the presence of aerosols, mostly dust. Our retrieval scheme imposes a strong constrain in the lowermost altitudes, cutting the vertical profiles and filtering observations below regions with large aerosol opacity. In addition, the comparisons with water vapor profiles from other teams revealed some biases at those low altitudes. By studying in detail those cases, relaxing the filtering conditions, using an optimized regularization for these conditions, performing dedicated aerosol retrievals at those altitudes, and mainly, adding CO_2 as a joint target along with the water vapor, we expect to improve the performance and reliability below 10-20 km, currently a caveat in our retrieval scheme.

4. *Temperature and supersaturation*. One of the topics addressed in this Thesis is the saturation state of the atmosphere. This study imposes the limitation of having simultaneous observations of water vapor and temperature. We provided a first study of supersaturation during MY 34, where reliable NOMAD temperatures were available. Current difficulties involved with the temperature retrievals limited the extension of this study. However, major improvements have been achieved since then, increasing our confidence in the retrieved temperatures. We expect that extending most of the upgrades discussed above to the temperature inversion scheme will solve most of the difficulties in the temperature inversions. This will allow the extension of the saturation study to the complete NOMAD data set. In addition, by extending the aerosol analysis presented in Stolzenbach et al., 2023, which is an ongoing work in our team, will allow for a more complete view of the relationship between dust, water ice and water vapor.

5. *Cluster analysis*. For this Thesis we introduced a statistical analysis tool based on data clustering, applied for the first time to Martian water vapor vertical

profiles. Our first results paved the way to improve this analysis. Focusing on specific seasons or locations may provide more precise cluster assignation, and implementing the upgrades mentioned above will help to eliminate biases and outliers which may affect the clustering process. These improvements will help to identify rare profiles or issues during the inversions that may have been overlooked so far.

6. *Extension to other trace species*.HCl has recently been detected by two instruments onboard TGO: the Atmospheric Chemistry Suite (ACS) Korablev et al., 2021 and more recently NOMAD Aoki et al., 2021. Multiple ongoing studies are trying to characterize the climatology of HCl on Mars, currently not completely understood, looking for possible relationships between temperature and other atmospheric species such as dust or water vapor. The processing pipeline presented in this Thesis proved to be successful for water vapor retrievals and its extension to other trace species such as HCl might be almost straightforward. We already did some steps in this direction and HCl retrievals are currently underway, which will be presented in the upcoming EPSC Meeting 2024 in Granada.

Appendix A

Supplementary Material for Ch. 6

A.1 Estimation of hydrogen escape

We present here a method for estimating the hydrogen escape flux by the water vapor plume which is based on the approximated method by Chaffin et al. (2017). During its application we have also evaluated the uncertainties associated to several assumptions, as explained next.

In order to estimate the H escape flux induced by the observed water vapor plume, we have averaged all the vertical profiles in the southern hemisphere for latitudes above 45 degrees during the three LS periods ($L_S^1 = 240° - 260°$, $L_S^2 = 260° - 280°$ and $L_S^3 = 280° - 300°$) for each MY. They are shown the nine panels (A to C) of Figure A.1. The model presented by Chaffin et al., 2017 provides a total flux calculated by taking into account the water vapor abundance at different tangent altitudes (from 20 to 120). They assumed vertical profiles of Gaussian parcels with a width of 12.5 km centered at different altitudes. Each parcel has a concentration peak of 20, 40, 60 or 80 ppmv for each altitude which correlates to a specific hydrogen escape flux contribution. We fit of our average vertical profiles with modeled profiles generated using a predefined set of combination of parcels. For each combination we compute its χ^2. The best combination of parcels is the one that provides the minimum value of χ^2. The uncertainty of the fitting has been estimated with the difference between the fitted profile and the closest combination of Gaussian parcels available. We obtain a deficient fitting below 50 km which is due to the limit of 80 ppmv in the H2O abundance imposed by the model. However this does not have a strong effect on the total estimated escape flux. With a linear extrapolation of the model and increasing the limit from 80 to 100 ppmv, the contribution to the total flux of the parcel at 40 km increases only by 3.5%. The increase in the contribution of the parcel at 20 km is negligible. The obtained profile provides the total hydrogen escape flux. The fittings of the average profiles and the estimated hydrogen escape fluxes for L_S^1, L_S^2 and L_S^3 during MYs 34, 35 and 36 are shown in Figure A.1. Applying this model to an arbitrary atmosphere, different from that used to generate the model, introduces uncertainties in the absolute values of the escape flux that are difficult to estimate although the variations between them, in which we are focused, are valid. Nevertheless, these results are in line with the estimation by Belyaev et al., 2021 obtained with the same approach and with the escape flux observed by the Hubble Space Telescope during the perihelion season (Bhattacharyya et al., 2017).

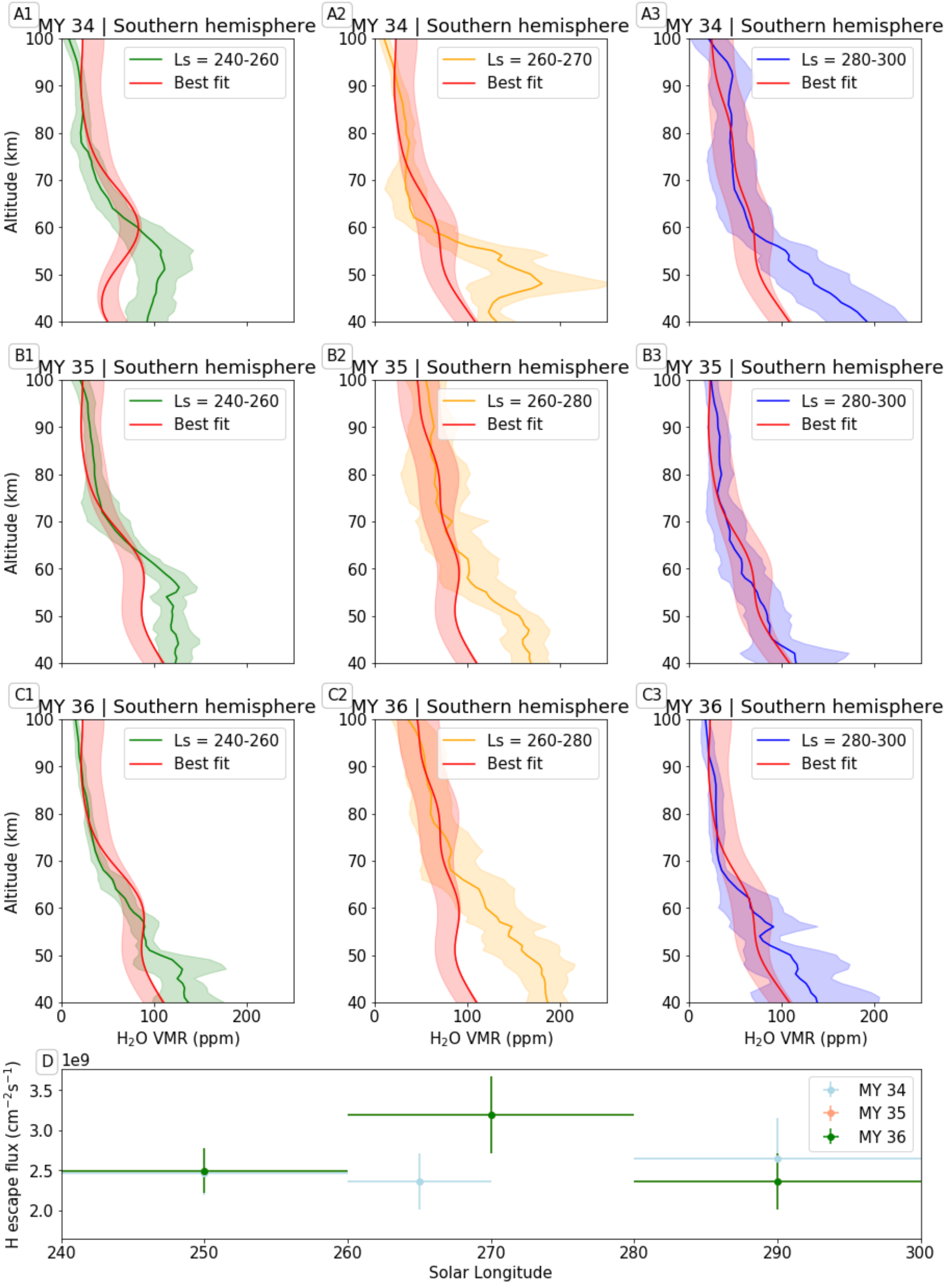

FIGURE A.1: Fitting (red line) of the average profiles at $L_S^1 = 240° - 260°$ (top panels), $L_S^2 = 260° - 280°$ (middle panels) and $L_S^3 = 280° - 300°$ (bottom panels) for MYs 34, 35 and 36 (panels A, B and C respectively) using the model from Chaffin et al., 2017. Shaded area of averaged profiles indicate the standard deviation of the average. Shaded area of the fitting profiles show the uncertainty of the fitting. The bad fitting below 50 km is due to the limitations of the model (see text for details). Panel D shows the estimated hydrogen flux for MYs 34 (light blue), 35 (orange) and 36 (green). Note that orange and green points are overlapped.

A.2 Comparison and validation

The objective of this Section is to compare different Forward Models (FM) used by different teams in the NOMAD consortium in order to verify the correct implementation of the NOMAD SO calibration into such FM. Characterizing these instrument's features is crucial for the data analysis and its parameterization needs to be correctly implemented. We performed a comparison of the FMs used by the four main groups in the NOMAD consortium analyzing H_2O on Mars with NOMAD SO data. These teams are: Instituto de Astrofísica de Andalucía (IAA), Tokyo University (UTokyo), Royal Belgian Institute for Space Aeronomy (BIRA), and NASA Goddard Spaceflight Center. A brief description of each radiative transfer algorithm involved in the comparison and details about the parameters used for the simulations are presented here, along with a summary of the results. We compare simulations from three radiative transfer algorithms: KOPRA used by the IAA, the Atmospheric Spectra Inversion Modular Utility Tools (ASIMUT) used by BIRA and UTokyo, and the Planet Spectrum Generator (PSG) used by NASA-Goddard. The results presented in Section 3 of this paper have been obtained from retrievals based on the KOPRA forward model.

- Karlsruhe Optimized and Precise Radiative transfer Algorithm (KOPRA). This algorithm, originally developed for data analysis of the Michelson Interferometer for Passive Atmospheric Sounding (MIPAS) has been already tested on multiple Earth atmosphere remote sounding projects and recently adapted for the Martian atmosphere (Jiménez-Monferrer et al., 2021). KOPRA is a forward line-by-line and layer-by-layer model for calculation of the infra-red radiative transfer through the atmosphere and integrates the radiative transfer equation along the line of sight with a Curtis-Gordon approach, taking into account refraction effects in a ellipsoidal surface (Stiller et al., 2002). The line-by-line modeling includes accurate evaluation of the Voigt line shape function using an optimized implementation of the Humlicek's algorithm (Kuntz, 1997; Ruyten, 2004). Line coupling effects, pressure shift, self- and air-broadening of the Doppler and Lorentzian line shapes and continuum emission caused by gases and aerosols are also taken into account during the calculations.

- Atmospheric Spectra Inversion Modular Utility Tools (ASIMUT). The ASIMUT software was originally developed to model the Earth atmosphere and simulate measurements under different observation geometries and instrument configurations. It has been adapted to simulate the atmosphere of Venus (Vandaele et al., 2008) and recently, the Martian atmosphere (Vandaele et al., 2018). Similarly to other algorithms, ASIMUT computes the radiative transfer calculations in each layer following the radiation path and using the Curtis-Gordon approximations. For the absorption coefficients calculation, the single line and broadband absorptions are taken into account along with the

Rayleigh scattering. The code allows the user to select different line shape profiles, the Voigt function being the default one and estimated with different methods, including the Humlicek algorithm approximation (Vandaele et al., 2006).

- Planet Spectrum Generator (PSG). The PSG is a state-of-the-art radiative transfer model developed in order to generate planetary spectra for a broad variety of instrumental configurations and observation geometries. As the previous mentioned codes, PSG computes the line-by-line calculations considering the Curtis-Gordon ray-trace temperature at every layer. For the line shape calculation, PSG uses a Faddeeva function as originally implemented by Humlicek, 1982 with improvements suggested by Wells 1999 to estimate the Voigt profile. It takes into account the pressure shift and its dependence with temperature, and the thermal kinetic and collisional broadening effects affecting the Gaussian and Lorentzian line widths (Villanueva et al., 2018; Villanueva et al., 2022b).

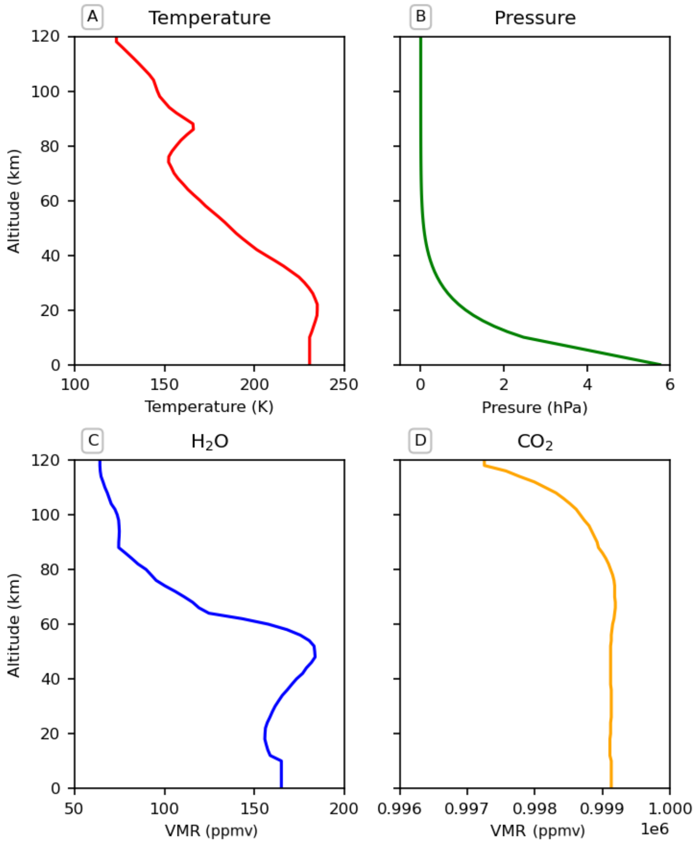

FIGURE A.2: Vertical profiles of the reference atmosphere used to generate the simulations for the forward model comparison. Profiles of temperature, pressure, H_2O and CO_2 Volume Mixing Ratios (VMR) are shown in panels A, B, C and D respectively. The profiles have been obtained from the Mars Planetary Climate Model for the location of the NOMAD observation 20180803_101739_1p0a_SO_A_I.

In order to ease the comparison of the forward models, a common reference atmosphere has been selected to generate the simulated spectra using the same pressure, temperature and gas abundances in the three codes. This reference atmosphere has been generated with the Mars Planetary Climate Model (PCM) to be representative of the Martian atmosphere during the NOMAD SO observation 20180803_101739_1p0a_SO_A_I (latitude = -64.2°, longitude = -26.5°, Ls = 223.09°, local time = 20.7h). Vertical profiles of the reference atmosphere are shown in Figure A.2. In addition, the list containing the line parameters (line position, intensity, broadening coefficients...) used during the comparison have been set to the latest HITRAN 2020 linelists (Gordon et al., 2022), although isotopes $^{13}C^{18}O_2$ and $^{18}O^{13}C^{17}O$ have not been considered in the KOPRA and ASIMUT simulations. Typically, the NOMAD forward model is generated as follows:

1. A high resolution spectrum is generated in a wide spectral range covering the desired adjacent orders.
2. The blaze function is applied, scaling the radiance and differentiating the limits of the diffraction orders.
3. The AOTF filter scales the main and the adjacent orders with a squared-sinc function.
4. The flux of the adjacent orders is added to the main order signal. The ILS convolution is also applied.
5. Finally, the high resolution spectrum is interpolated to the NOMAD data spectral grid.

The parameters involved in this comparison are: the blaze center frequency (FSR), blaze width (FSR_0), AOTF center wavenumber (ν_0), AOTF width (w), AOTF sidelobe factor (S) and AOTF asymmetry factor (A), which are described in 2.3.1. We have selected arbitrary blaze and AOTF parameters (labeled as "test" parameters in Figure A.3) during the high resolution comparison and values from Villanueva et al., 2022a characterization for the retrievals (labeled as "NOMAD" parameters in Figure A.3).

For the high resolution simulation we have selected a spectral range corresponding to the NOMAD diffraction order 170 (3390-3410 cm^{-1}) and extended to 3370 and 3430 cm^{-1} in order to simulate the closest adjacent orders. The number of adjacent orders has been set to ± 1 during the high resolution and AOTF comparisons, and to ± 4 during the NOMAD retrievals. The mean spectral resolution of the simulations are $5 \cdot 10^{-4}$ cm^{-1} for KOPRA, $3 \cdot 10^{-4}$ cm^{-1} for PSG and $2 \cdot 10^{-3}$ cm^{-1} for ASIMUT. In order to compare the three models, the simulations have been interpolated to a constant spectral grid with a resolution of $2 \cdot 10^{-3}$ cm^{-1}. The comparisons have been done with the simulated transmittance of an altitude of 10 km in order to test the models under a strong absorption condition. For the AOTF

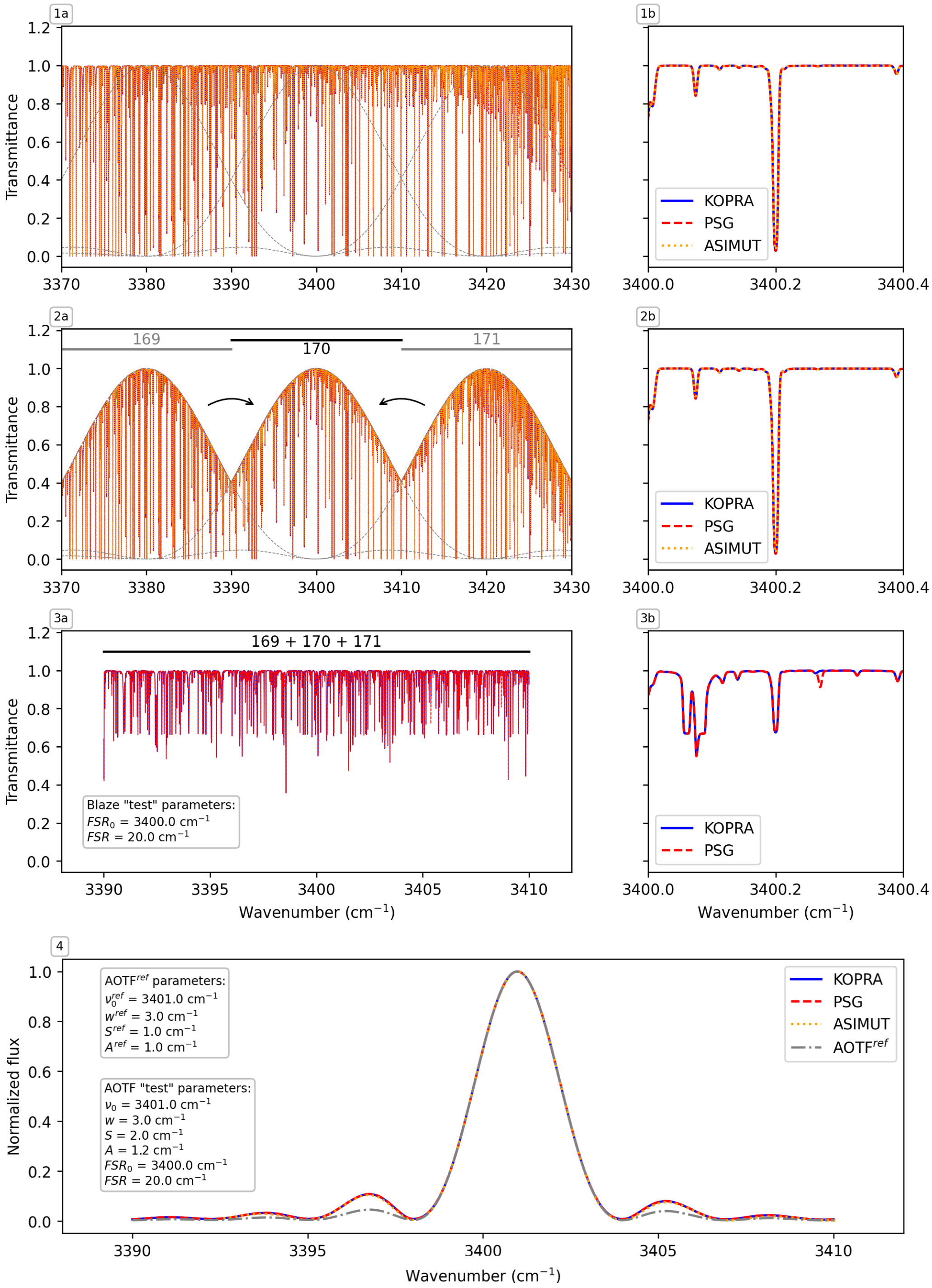

FIGURE A.3: Simulated spectra generated with KOPRA (blue), PSG (red) and ASIMUT (yellow) during different stages of the NOMAD forward modeling. Panels 1a to 3a show the high resolution transmittance at 10 km without any filter function, after the grating function and after the order addition without AOTF respectively. Panels 1b to 3b show the same within a narrower spectral range. Panel 4 shows the normalized radiance at 100 km simulated with the AOTF filter (blue, red and yellow) and with a symmetric AOTFref (gray). Simulations in panels 1 to 4 were generated using arbitrary blaze and AOTF parameters (labeled as "test" parameters).

comparison, a radiance without absorption lines is required to properly analyze the shape of the sinc-squared function. For that, simulated radiances at 100 km have been used. Since each simulation uses a different solar flux, the resulted total flux of the radiances are different, so, in order to proceed with the comparison we normalized each radiance.

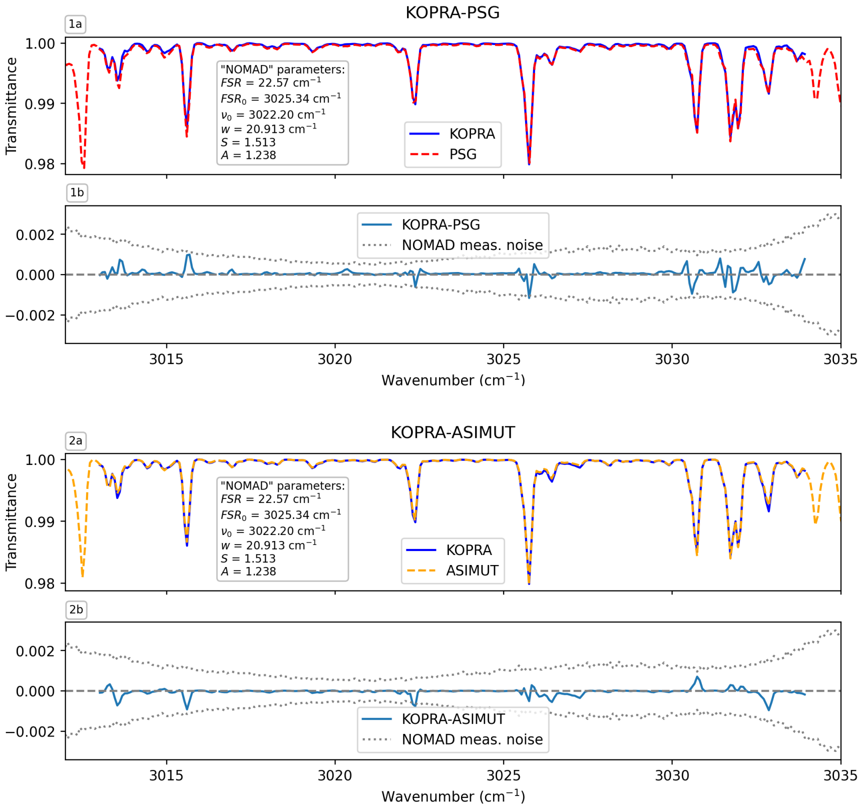

FIGURE A.4: Panels 1a and 2a show the normalized forward model used for the fitting during a NOMAD data retrieval at 30 km for the diffraction order 134. The residuals between KOPRA, PSG and ASIMUT are shown in panels 1b and 2b. Forward models in panels 1 and 2 use the NOMAD characterization (labeled as "NOMAD" parameters).

As shown in panels panels 1b-3b of Figure A.3, the agreement between KOPRA, PSG and ASIMUT is remarkable. Focusing the analysis on the absorption line at 3400.2 cm^{-1}, the discrepancy between KOPRA-PSG is about ∼0.05% and about ∼0.2% between KOPRA-ASIMUT. We do not observe any spectral shift between simulations in panel 3, meaning that the addition of the adjacent orders was equally reproduced in the KOPRA and PSG models. Some lines appear only on the PSG simulation corresponding to isotopes $^{13}C^{18}O_2$ and $^{18}O^{13}C^{17}O$ which were not included in the KOPRA simulation. Regarding the AOTF comparison shown in panel 4 of Figure A.3, we proved the asymmetric sinc-squared function to be properly implemented in KOPRA, PSG and ASIMUT, with discrepancies below 0.1% due to numerical approximations during normalization and interpolation processes. These differences between KOPRA, ASIMUT and PSG are due to the complexities of the NOMAD instrumental features and all the subtle differences in the implementation of the radiative transfer calculations and numerical approximations. Being smaller than the measurement noise and the instrument characterization ambiguity, which are the most relevant uncertainties, do not have any significant impact during the data processing. Hence, the goal of having the same forward model generated by three independent algorithms has been successfully achieved, proving the same implementation of the NOMAD SO characterization into the radiative transfer codes. As shown in panels 1a and 2b of Figure A.4, the overall agreement of the FM used in the retrievals is good, with the main spectral features such as the adjacent order addition and ILS convolution equally represented in all the simulations. The differences between these simulations are below the Level 1 NOMAD SO measurement noise with a mean ratio of the differences to the noise of $\sim$0.05. In addition, the slant H2O column density values at 30 km obtained by PSG and KOPRA retrievals when using the same temperature and pressure shows relative differences below 0.07%.

The differences found in the FMs obtained from the fittings during the retrievals might be due to the different approaches used by the teams. In PSG and ASIMUT, the inversion is solved with the optimal estimation approach. Each spectrum (i.e. each tangent altitude) is considered as an independent measurement and a constant vertical profile representative of the exact location of the tangential observation is used as apriori (Vandaele et al., 2006; Villanueva et al., 2018). On the other hand, the RCP-KOPRA performs a global fit taking into account all the observations during the atmospheric scan to produce the vertical profiles (von Clarmann et al., 2003b). Both approaches have costs and benefits depending on the type of observations to analyze (fast sampling with low latitudinal and longitudinal drifting or slow sampling with large latitudinal and longitudinal drifting on the planet's surface). In the case of RCP-KOPRA, the global fit allows a robust characterization of the profile, being sensitive to strong vertical gradients. However, the a priori used during the retrievals are profiles representative of the full atmospheric scan, and the pressure and temperature profiles must be under hydrostatic equilibrium. This way, possible horizontal inhomogeneities due to differences in the geographical location of the measurements during the scan are not taken into account. On the other hand, since PSG and ASIMUT consider each observation independently, they select the pressure and temperature representative for the exact location, although using a constant vertical profile during the inversion. Not considering the contribution of the spectra from the layers above the observation does introduce uncertainties under conditions of strong vertical gradients, and some of the largest differences in the water vapor profiles among the teams are due to this approximation.

Appendix B

Supplementary Material for Ch. 7

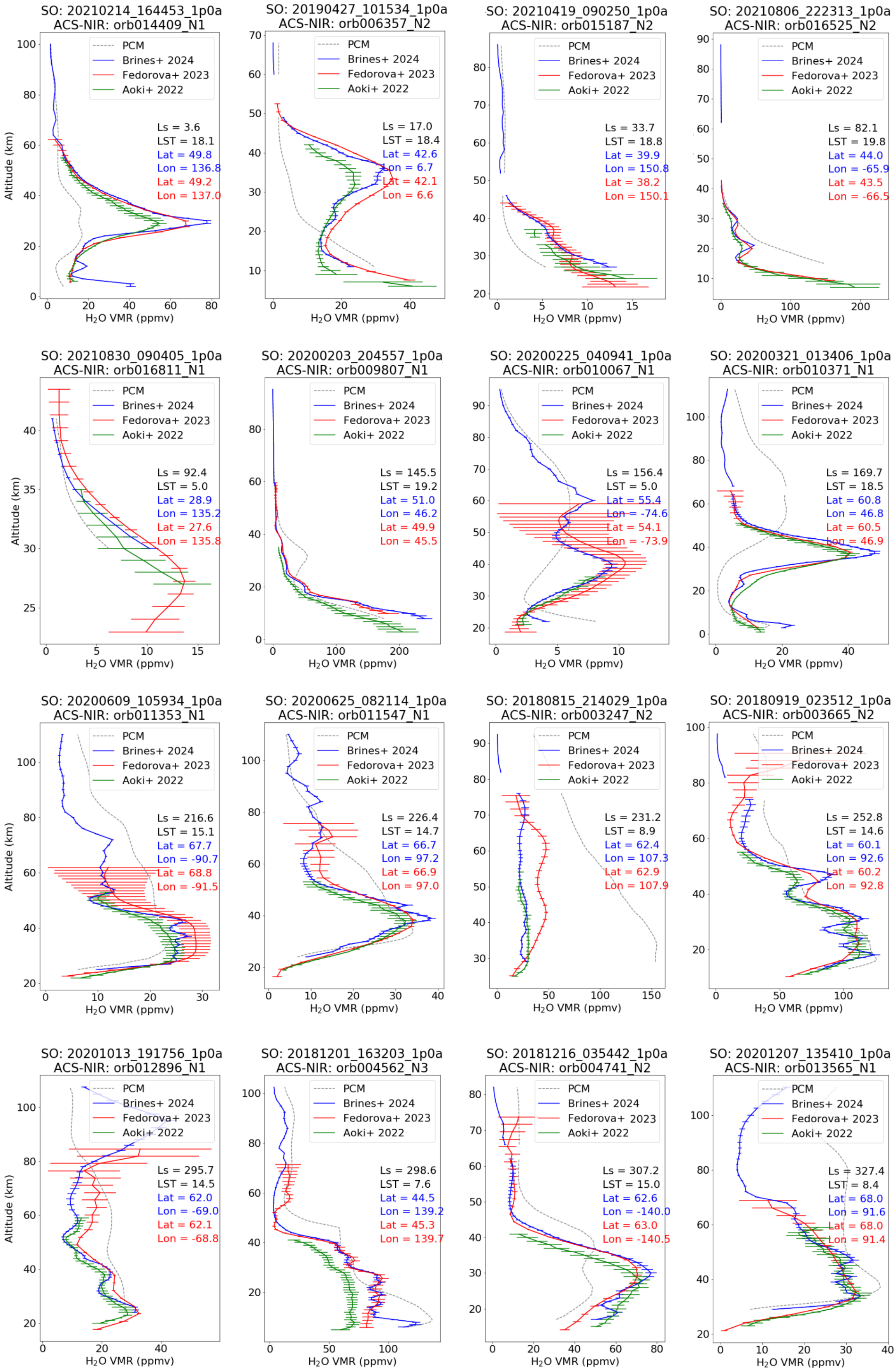

FIGURE B.1: Comparison of water vapor vertical profiles at the northern hemisphere retrieved from NOMAD and ACS observations.

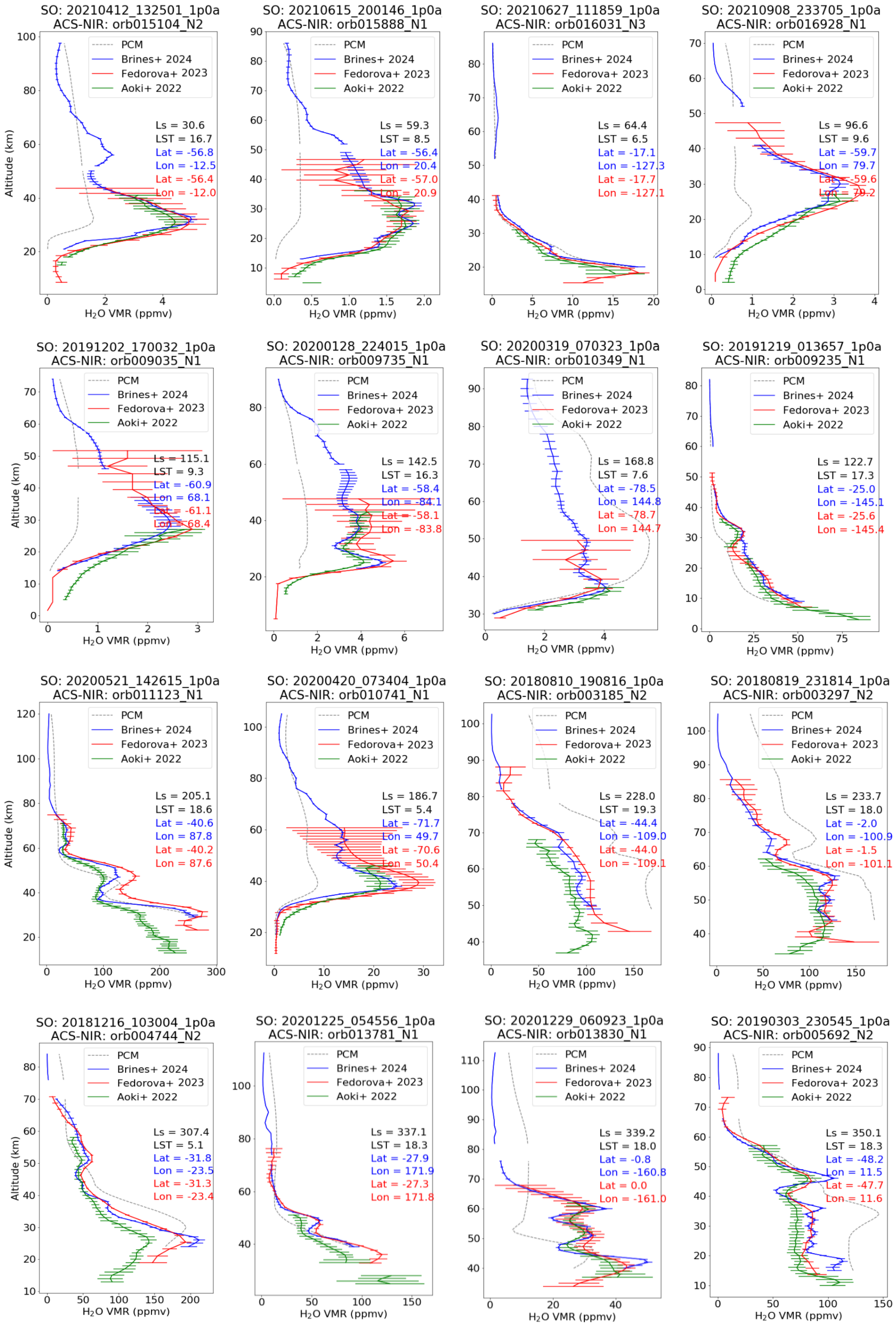

FIGURE B.2: Comparison of water vapor vertical profiles at the southern hemisphere retrieved from NOMAD and ACS observations.

Appendix C

Contributions to Conferences and Peer-Reviewed Publications

C.1 National and international conferences

Brines, A., Lopez-Valverde, M., Stolzenbach, A., Modak, A., Funke, B., Gonzalez-Galindo, F., Lopez-Moreno, J., Hill, B., Aoki, S., Vandaele, A. C., et al. (2021c). Water vapor distributions in the Martian atmosphere from NOMAD solar occultation observations. *AGU Fall Meeting Abstracts*, *2021*, P35F–2195

Brines, A., Lopez-Valverde, M. A., Stolzenbach, A., Modak, A., Hill, B., Funke, B., González-Galindo, F., Moreno, J. J. L., Aoki, S., Vandaele, A. C., et al. (2021d). *Martian water vapor vertical profiles from solar occultation measurements by NOMAD onboard TGO/ExoMars: H2O-temperature retrievals with the IAA-KOPRA forward model* (tech. rep.). Copernicus Meetings

Brines, A., López-Valverde, M., Sotlzenbach, A., Modak, A., Funke, B., & González Galindo, F. (2021a). Retrievals of H2O vertical profiles from NOMAD SO channel. *NOMAD Science Working Team*

Brines, A., López-Valverde, M., Sotlzenbach, A., Modak, A., Funke, B., & González Galindo, F. (2021b). Update on water vapor profiles with the IAA retrieval scheme. *NOMAD Science Working Team*

Brines, A., Ángel Lopez Valverde, M., Stolzenbach, A., Modak, A., Funke, B., Gonzalez Galindo, F., Juan Lopez Moreno, J., Aoki, S., Carine Vandaele, A., Daerden, F., et al. (2022d). Mars water vapor vertical distributions from the troposphere to the mesosphere from NOMAD solar occultation for Martian years 34 and 35. *European Planetary Science Congress*, EPSC2022–504

Brines, A., López-Valverde, M., Stolzenbach, A., Modak, A., Funke, B., Galindo, F., Lopez-Moreno, J., Aoki, S., Villanueva, G., Liuzzi, G., et al. (2022c). Water vapor vertical distribution during perihelion season of Martian years 34 and 35 observed with NOMAD-SO. *Seventh International Workshop on the Mars Atmosphere: Modelling* *and Observations*, 2402

Brines, A., López-Valverde, M., Sotlzenbach, A., Modak, A., Funke, B., & González Galindo, F. (2022b). Water vapor vertical distribution on Mars during perihelion season of MY 34 and MY 35 with ExoMars-TGO/NOMAD observations. *NOMAD Science Working Team*

Brines, A., López-Valverde, M., Sotlzenbach, A., Modak, A., Funke, B., & González Galindo, F. (2022a). Update on improvements and extension of the H2O retrievals carried out at IAA. *NOMAD Science Working Team*

Brines, A., López-Valverde, M., Sotlzenbach, A., Modak, A., Funke, B., González Galindo, F., Aoki, S., Villanueva, G., Luizzi, G., Thomas, I., et al. (2023d). Water vapor vertical distribution in the Martian atmosphere from TGO/NOMAD observations. *Highlights of Spanish Astrophysics XI*, 449

Brines, A., López-Valverde, M., Sotlzenbach, A., Modak, A., Funke, B., & González Galindo, F. (2023c). Water vapor vertical distribution on mars during 5 years of ExoMars-TGO/NOMAD observations. *VII Reunión de Ciencias Planetarias y Exploración del Sistema Solar*

Brines, A., López-Valverde, M., Sotlzenbach, A., Modak, A., Funke, B., & González Galindo, F. (2023b). Update on H2O retrievals combining orders and using measurement noise from covariance matrices. *NOMAD Science Working Team*

Brines, A., López-Valverde, M., Sotlzenbach, A., Modak, A., Funke, B., & González Galindo, F. (2023a). High altitude water vapor during the perihelion season. *NOMAD Science Working Team*

Brines, A., López-Valverde, M., Sotlzenbach, A., Modak, A., Funke, B., & González Galindo, F. (2024a). Update on the NOMAD/SO water vapor climatology. *NOMAD Science Working Team*

C.2 Publications

Brines, A., López-Valverde, M., Stolzenbach, A., Modak, A., Funke, B., Galindo, F., Aoki, S., Villanueva, G., Liuzzi, G., Thomas, I., et al. (2023e). Water vapor vertical distribution on Mars during perihelion season of MY 34 and MY 35 with ExoMars-TGO/NOMAD observations. *Journal of Geophysical Research: Planets*, *128*(11), e2022JE007273

Brines, A., López-Valverde, M., Funke, B., Galindo, F., Aoki, S., Villanueva, G., Liuzzi, G., Thomas, I., et al. (2024b). Strong localized pumping of water vapor to high altitudes on Mars during the perihelion season. *Geophysical Research Letters (accepted)*

Aoki, S., Daerden, F., Viscardy, S., Thomas, I. R., Erwin, J. T., Robert, S., Trompet, L., Neary, L., Villanueva, G. L., Liuzzi, G., et al. (2021). Annual appearance of hydrogen chloride on Mars and a striking similarity with the water vapor vertical distribution observed by TGO/NOMAD. *Geophysical Research Letters*, *48*(11), e2021GL092506

Villanueva, G. L., Liuzzi, G., Aoki, S., Stone, S. W., Brines, A., Thomas, I. R., Lopez-Valverde, M. A., Trompet, L., Erwin, J., Daerden, F., et al. (2022a). The deuterium isotopic ratio of water released from the Martian caps as measured with TGO/NOMAD. *Geophysical Research Letters*, *49*(12), e2022GL098161

Yoshida, N., Nakagawa, H., Aoki, S., Erwin, J., Vandaele, A. C., Daerden, F., Thomas, I., Trompet, L., Koyama, S., Terada, N., et al. (2022). Variations in vertical CO/CO2 profiles in the Martian mesosphere and lower thermosphere measured by the ExoMars TGO/NOMAD: Implications of variations in eddy diffusion coefficient. *Geophysical Research Letters*, *49*(10), e2022GL098485

López-Valverde, M. A., Funke, B., Brines, A., Stolzenbach, A., Modak, A., Hill, B., González-Galindo, F., Thomas, I., Trompet, L., Aoki, S., et al. (2023). Martian atmospheric temperature and density profiles during the first year of NOMAD/TGO solar occultation measurements. *Journal of Geophysical Research: Planets*, *128*(2), e2022JE007278

Stolzenbach, A., López Valverde, M.-A., Brines, A., Modak, A., Funke, B., González-Galindo, F., Thomas, I., Liuzzi, G., Villanueva, G., Luginin, M., et al. (2023). Martian atmospheric aerosols composition and distribution retrievals during the first martian year of NOMAD/TGO solar occultation measurements: 1. methodology and application to the my 34 global dust storm. *Journal of Geophysical Research: Planets*, *128*(11), e2022JE007276

Modak, A., López-Valverde, M. A., Brines, A., Stolzenbach, A., Funke, B., González-Galindo, F., Hill, B., Aoki, S., Thomas, I., Liuzzi, G., et al. (2023). Retrieval of Martian atmospheric CO vertical profiles from NOMAD observations during the first year of TGO operations. *Journal of Geophysical Research: Planets*, *128*(3), e2022JE007282

Aoki, S., Shiobara, K., Yoshida, N., Trompet, L., Yoshida, T., Terada, N., Nakagawa, H., Liuzzi, G., Vandaele, A., Thomas, I., et al. (2023). Depletion of 13c in co in the atmosphere of mars suggested by exomars-tgo/nomad observations. *The Planetary Science Journal*, *4*(5), 97

Trompet, L., Vandaele, A., Thomas, I., Aoki, S., Daerden, F., Erwin, J., Flimon, Z., Mahieux, A., Neary, L., Robert, S., Vilanueva, G., G, L., Lopez-Valverde, M., Brines, A., Bellucci, G., Lopez-Moreno, J., & Patel, M. (2023). Carbon dioxide retrievals from NOMAD-SO on ESA's ExoMars Trace Gas Orbiter and temperature profiles retrievals with the hydrostatic equilibrium equation: 1. description of the method. *Journal of Geophysical Research: Planets*, *128*(3), e2022JE007277

Bibliography

Acton Jr, C. H. (1996). Ancillary data services of NASA's navigation and ancillary information facility. *Planetary and Space Science*, *44*(1), 65–70.

Alday, J., Trokhimovskiy, A., Irwin, P. G., Wilson, C. F., Montmessin, F., Lefèvre, F., Fedorova, A., Belyaev, D. A., Olsen, K. S., Korablev, O., et al. (2021). Isotopic fractionation of water and its photolytic products in the atmosphere of Mars. *Nature Astronomy*, *5*(9), 943–950.

Aoki, S., Shiobara, K., Yoshida, N., Trompet, L., Yoshida, T., Terada, N., Nakagawa, H., Liuzzi, G., Vandaele, A., Thomas, I., et al. (2023). Depletion of 13c in co in the atmosphere of mars suggested by exomars-tgo/nomad observations. *The Planetary Science Journal*, *4*(5), 97.

Aoki, S., Daerden, F., Viscardy, S., Thomas, I. R., Erwin, J. T., Robert, S., Trompet, L., Neary, L., Villanueva, G. L., Liuzzi, G., et al. (2021). Annual appearance of hydrogen chloride on Mars and a striking similarity with the water vapor vertical distribution observed by TGO/NOMAD. *Geophysical Research Letters*, *48*(11), e2021GL092506.

Aoki, S., Vandaele, A., Daerden, F., Villanueva, G. L., Liuzzi, G., Clancy, R., Lopez-Valverde, M., Brines, A., Thomas, I., Trompet, L., et al. (2022). Global vertical distribution of water vapor on Mars: Results from 3.5 years of ExoMars-TGO/NOMAD science operations. *Journal of Geophysical Research: Planets*, *127*(9), e2022JE007231.

Aoki, S., Vandaele, A. C., Daerden, F., Villanueva, G. L., Liuzzi, G., Thomas, I. R., Erwin, J. T., Trompet, L., Robert, S., Neary, L., et al. (2019). Water vapor vertical profiles on Mars in dust storms observed by TGO/NOMAD. *Journal of Geophysical Research: Planets*, *124*(12), 3482–3497.

Arthur, D., Vassilvitskii, S., & Gabow, H. (2007). Proceedings of the eighteenth annual ACM-SIAM symposium on discrete algorithms. *Society for Industrial and Applied Mathematics*.

Ashman, M., Aberasturi Vega, M., Cardesin Moinelo, A., Costa, M., Frew, D., Garcia Beteta, J. J., Geiger, B., Metcalfe, L., Muñoz, C., Muñoz, M., et al. (2018). Science planning implementation and challenges for the Exomars Trace Gas Orbiter. *2018 SpaceOps Conference*, 2580.

Banwell, C. (1972). *Fundamentals of molecular spectroscopy: By CN Banwell*. New York, McGraw-Hill.

Barnes, J. R., Haberle, R. M., Wilson, R. J., Lewis, S., Murphy, J. R., & Read, P. L. (2017). The Global Circulation.

Belyaev, D. A., Fedorova, A., Trokhimovskiy, A., Alday, J., Montmessin, F., Korablev, O. I., Lefèvre, F., Patrakeev, A. S., Olsen, K. S., & Shakun, A. V. (2021). Revealing a high water abundance in the upper mesosphere of Mars with ACS onboard TGO. *Geophysical Research Letters*, *48*(10), e2021GL093411.

Belyaev, D. A., Fedorova, A. A., Trokhimovskiy, A., Alday, J., Korablev, O. I., Montmessin, F., Starichenko, E. D., Olsen, K. S., & Patrakeev, A. (2022). Thermal structure of the middle and upper atmosphere of Mars from ACS/TGO CO2 spectroscopy. *Journal of Geophysical Research: Planets*, *127*(10), e2022JE007286.

Bertaux, J.-L., Nevejans, D., Korablev, O., Villard, E., Quémerais, E., Neefs, E., Montmessin, F., Leblanc, F., Dubois, J.-P., Dimarellis, E., et al. (2007). SPICAV on Venus Express: Three spectrometers to study the global structure and composition of the Venus atmosphere. *Planetary and Space Science*, *55*(12), 1673–1700.

Bhattacharyya, D., Clarke, J., Chaufray, J.-Y., Mayyasi, M., Bertaux, J.-L., Chaffin, M., Schneider, N., & Villanueva, G. (2017). Seasonal changes in hydrogen escape from Mars through analysis of HST observations of the Martian exosphere near perihelion. *Journal of Geophysical Research: Space Physics*, *122*(11), 11–756.

Bonev, B. P., Hansen, G. B., Glenar, D. A., James, P. B., & Bjorkman, J. E. (2008). Albedo models for the residual south polar cap on Mars: Implications for the stability of the cap under near-perihelion global dust storm conditions. *Planetary and Space Science*, *56*(2), 181–193.

Brines, A., López-Valverde, M., Sotlzenbach, A., Modak, A., Funke, B., & González Galindo, F. (2021a). Retrievals of H2O vertical profiles from NOMAD SO channel. *NOMAD Science Working Team*.

Brines, A., López-Valverde, M., Sotlzenbach, A., Modak, A., Funke, B., & González Galindo, F. (2021b). Update on water vapor profiles with the IAA retrieval scheme. *NOMAD Science Working Team*.

Brines, A., López-Valverde, M., Sotlzenbach, A., Modak, A., Funke, B., & González Galindo, F. (2022a). Update on improvements and extension of the H2O retrievals carried out at IAA. *NOMAD Science Working Team*.

Brines, A., López-Valverde, M., Sotlzenbach, A., Modak, A., Funke, B., & González Galindo, F. (2022b). Water vapor vertical distribution on Mars during perihelion season of MY 34 and MY 35 with ExoMars-TGO/NOMAD observations. *NOMAD Science Working Team*.

Brines, A., López-Valverde, M., Sotlzenbach, A., Modak, A., Funke, B., & González Galindo, F. (2023a). High altitude water vapor during the perihelion season. *NOMAD Science Working Team*.

Brines, A., López-Valverde, M., Sotlzenbach, A., Modak, A., Funke, B., & González Galindo, F. (2023b). Update on H2O retrievals combining orders and using measurement noise from covariance matrices. *NOMAD Science Working Team*.

Brines, A., López-Valverde, M., Sotlzenbach, A., Modak, A., Funke, B., & González Galindo, F. (2023c). Water vapor vertical distribution on mars during 5 years of ExoMars-TGO/NOMAD observations. *VII Reunión de Ciencias Planetarias y Exploración del Sistema Solar*.

Brines, A., López-Valverde, M., Sotlzenbach, A., Modak, A., Funke, B., & González Galindo, F. (2024a). Update on the NOMAD/SO water vapor climatology. *NOMAD Science Working Team*.

Brines, A., López-Valverde, M., Sotlzenbach, A., Modak, A., Funke, B., González Galindo, F., Aoki, S., Villanueva, G., Luizzi, G., Thomas, I., et al. (2023d). Water vapor vertical distribution in the Martian atmosphere from TGO/NOMAD observations. *Highlights of Spanish Astrophysics XI*, 449.

Brines, A., López-Valverde, M., Stolzenbach, A., Modak, A., Funke, B., Galindo, F., Lopez-Moreno, J., Aoki, S., Villanueva, G., Liuzzi, G., et al. (2022c). Water vapor vertical distribution during perihelion season of Martian years 34 and 35 observed with NOMAD-SO. *Seventh International Workshop on the Mars Atmosphere: Modelling and Observations*, 2402.

Brines, A., Ángel Lopez Valverde, M., Stolzenbach, A., Modak, A., Funke, B., Gonzalez Galindo, F., Juan Lopez Moreno, J., Aoki, S., Carine Vandaele, A., Daerden, F., et al. (2022d). Mars water vapor vertical distributions from the troposphere to the mesosphere from NOMAD solar occultation for Martian years 34 and 35. *European Planetary Science Congress*, EPSC2022–504.

Brines, A., Lopez-Valverde, M., Stolzenbach, A., Modak, A., Funke, B., Gonzalez-Galindo, F., Lopez-Moreno, J., Hill, B., Aoki, S., Vandaele, A. C., et al. (2021c). Water vapor distributions in the Martian atmosphere from NOMAD solar occultation observations. *AGU Fall Meeting Abstracts*, *2021*, P35F–2195.

Brines, A., Lopez-Valverde, M. A., Stolzenbach, A., Modak, A., Hill, B., Funke, B., González-Galindo, F., Moreno, J. J. L., Aoki, S., Vandaele, A. C., et al. (2021d). *Martian water vapor vertical profiles from solar occultation measurements by NOMAD onboard TGO/ExoMars: H2O-temperature retrievals with the IAA-KOPRA forward model* (tech. rep.). Copernicus Meetings.

Brines, A., López-Valverde, M., Funke, B., Galindo, F., Aoki, S., Villanueva, G., Liuzzi, G., Thomas, I., et al. (2024b). Strong localized pumping of water vapor to high altitudes on Mars during the perihelion season. *Geophysical Research Letters (accepted)*.

Brines, A., López-Valverde, M., Stolzenbach, A., Modak, A., Funke, B., Galindo, F., Aoki, S., Villanueva, G., Liuzzi, G., Thomas, I., et al. (2023e). Water vapor vertical distribution on Mars during perihelion season of MY 34 and MY 35 with ExoMars-TGO/NOMAD observations. *Journal of Geophysical Research: Planets*, *128*(11), e2022JE007273.

Cala Hurtado, A. (2016). Aplicación novedosa de técnicas de clustering a medidas infrarrojas y a simulaciones físicas de la atmósfera de Marte. In *Master Thesis in computational engineering and intelligent systems*. Universidad del Pais Vasco.

Caliński, T., & Harabasz, J. (1974). A dendrite method for cluster analysis. *Communications in Statistics-theory and Methods*, *3*(1), 1–27.

Chaffin, M., Deighan, J., Schneider, N., & Stewart, A. (2017). Elevated atmospheric escape of atomic hydrogen from Mars induced by high-altitude water. *Nature geoscience*, *10*(3), 174–178.

Chaffin, M., Kass, D., Aoki, S., Fedorova, A., Deighan, J., Connour, K., Heavens, N., Kleinböhl, A., Jain, S., Chaufray, J.-Y., et al. (2021). Martian water loss to space enhanced by regional dust storms. *Nature Astronomy*, *5*(10), 1036–1042.

Clancy, R. T., Montmessin, F., Benson, J., Daerden, F., Anthony, C., & Wolf, M. J. (2017a). Mars clouds. *The atmosphere and climate of Mars*, *18*, 295.

Clancy, R. T., Sandor, B. J., Wolff, M. J., Smith, M. D., Lefèvre, F., Madeleine, J.-B., Forget, F., Murchie, S. L., Seelos, F. P., Seelos, K. D., et al. (2012). Extensive MRO CRISM observations of 1.27 μm o2 airglow in Mars polar night and their comparison to MRO MCS temperature profiles and LMD GCM simulations. *Journal of Geophysical Research: Planets*, *117*(E11).

Clancy, R. T., Smith, M. D., Lefèvre, F., McConnochie, T. H., Sandor, B. J., Wolff, M. J., Lee, S. W., Murchie, S. L., Toigo, A. D., Nair, H., et al. (2017b). Vertical profiles of Mars 1.27 μm O2 dayglow from MRO CRISM limb spectra: Seasonal/global behaviors, comparisons to LMD-GCM simulations, and a global definition for Mars water vapor profiles. *Icarus*, *293*, 132–156.

Clancy, R., Grossman, A., Wolff, M., James, P., Rudy, D., Billawala, Y., Sandor, B., Lee, S., & Muhleman, D. (1996). Water vapor saturation at low altitudes around Mars aphelion: A key to Mars climate? *Icarus*, *122*(1), 36–62.

Clancy, R., Sandor, B., Wolff, M., Christensen, P., Smith, M., Pearl, J., Conrath, B., & Wilson, R. (2000). An intercomparison of ground-based millimeter, MGS TES, and Viking atmospheric temperature measurements: Seasonal and interannual variability of temperatures and dust loading in the global Mars atmosphere. *Journal of Geophysical Research: Planets*, *105*(E4), 9553–9571.

Conrath, B., Curran, R., Hanel, R., Kunde, V., Maguire, W., Pearl, J., Pirraglia, J., Welker, J., & Burke, T. (1973). Atmospheric and surface properties of Mars obtained by infrared spectroscopy on Mariner 9. *Journal of Geophysical Research*, *78*(20), 4267–4278.

Crismani, M., Villanueva, G., Liuzzi, G., Smith, M., Knutsen, E., Daerden, F., Neary, L., Mumma, M., Aoki, S., Trompet, L., et al. (2021). A global and seasonal perspective of martian water vapor from ExoMars/NOMAD. *Journal of Geophysical Research: Planets*, *126*(11), e2021JE006878.

Curtis, A. (1952). A statistical model for water vapour absorption. *QJ Roy. Met. Soc.*, *78*, 639–640.

Daerden, F., Whiteway, J., Davy, R., Verhoeven, C., Komguem, L., Dickinson, C., Taylor, P., & Larsen, N. (2010). Simulating observed boundary layer clouds on Mars. *Geophysical Research Letters*, *37*(4).

Davies, D. L., & Bouldin, D. W. (1979). A cluster separation measure. *IEEE transactions on pattern analysis and machine intelligence*, (2), 224–227.

Encrenaz, T., Melchiorri, R., Fouchet, T., Drossart, P., Lellouch, E., Gondet, B., Bibring, J.-P., Langevin, Y., Titov, D., Ignatiev, N., et al. (2005). A mapping of martian water sublimation during early northern summer using OMEGA/Mars Express. *Astronomy & Astrophysics*, *441*(3), L9–L12.

Eriksson, P. (2000). Analysis and comparison of two linear regularization methods for passive atmospheric observations. *Journal of Geophysical Research: Atmospheres*, *105*(D14), 18157–18167.

ESA. (2024). PSA [https://archives.esac.esa.int/psa/].

Escudero-Jiménez, M., López-Valverde, M., Peralta, J., Moya, T., Belmonte, A., Brines, A., Modak, A., Funke, B., GonzálezGalindo, F., Thomas, I., López-Moreno, J., Patel, M., Bellucci, G., & A.C., V. (n.d.). Upper limits of CH4 and OCS in the Martian atmosphere from averaging of solar occultation spectra by NOMAD/Trace Gas Orbiter. *Icarus (submitted)*.

Farmer, C., Davies, D., Holland, A., LaPorte, D., & Doms, P. (1977). Mars: Water vapor observations from the Viking orbiters. *Journal of Geophysical Research*, *82*(28), 4225–4248.

Fedorova, A., Bertaux, J.-L., Betsis, D., Montmessin, F., Korablev, O., Maltagliati, L., & Clarke, J. (2018a). Water vapor in the middle atmosphere of Mars during the 2007 global dust storm. *Icarus*, *300*, 440–457.

Fedorova, A., Bertaux, J.-L., Betsis, D., Montmessin, F., Korablev, O., Maltagliati, L., & Clarke, J. (2018b). Water vapor in the middle atmosphere of Mars during the 2007 global dust storm. *Icarus*, *300*, 440–457.

Fedorova, A., Korablev, O., Bertaux, J.-L., Rodin, A., Montmessin, F., Belyaev, D., & Reberac, A. (2009). Solar infrared occultation observations by SPICAM experiment on Mars-Express: Simultaneous measurements of the vertical distributions of H2O, CO2 and aerosol. *Icarus*, *200*(1), 96–117.

Fedorova, A., Korablev, O., Bertaux, J.-L., Rodin, A., Kiselev, A., & Perrier, S. (2006). Mars water vapor abundance from SPICAM IR spectrometer: Seasonal and geographic distributions. *Journal of Geophysical Research: Planets*, *111*(E9).

Fedorova, A., Montmessin, F., Korablev, O., Lefèvre, F., Trokhimovskiy, A., & Bertaux, J.-L. (2021). Multi-annual monitoring of the water vapor vertical distribution on Mars by SPICAM on Mars Express. *Journal of Geophysical Research: Planets*, *126*(1), e2020JE006616.

Fedorova, A., Montmessin, F., Korablev, O., Luginin, M., Trokhimovskiy, A., Belyaev, D. A., Ignatiev, N. I., Lefèvre, F., Alday, J., Irwin, P. G., et al. (2020). Stormy water on Mars: The distribution and saturation of atmospheric water during the dusty season. *Science*, *367*(6475), 297–300.

Fedorova, A., Montmessin, F., Trokhimovskiy, A., Luginin, M., Korablev, O., Alday, J., Belyaev, D., Holmes, J., Lefevre, F., Olsen, K., et al. (2023). A two-martian years survey of the water vapor saturation state on Mars based on ACS NIR/TGO occultations. *Journal of Geophysical Research: Planets*, *128*(1), e2022JE007348.

Fedorova, A. A., Montmessin, F., Rodin, A. V., Korablev, O. I., Määttänen, A., Maltagliati, L., & Bertaux, J.-L. (2014). Evidence for a bimodal size distribution for the suspended aerosol particles on Mars. *Icarus*, *231*, 239–260.

Forget, F., Millour, E., Pierron, T., Bierjon, A., & the MCD team. (2022). Mars Climate Databes v6.1 validation document. *The Mars Climate Database*.

Forget, F., Montmessin, F., Bertaux, J.-L., González-Galindo, F., Lebonnois, S., Quemerais, E., Reberac, A., Dimarellis, E., & López-Valverde, M. A. (2009). Density and temperatures of the upper Martian atmosphere measured by stellar occultations with Mars Express SPICAM. *Journal of Geophysical Research: Planets*, *114*(E1).

Forget, F., Hourdin, F., Fournier, R., Hourdin, C., Talagrand, O., Collins, M., Lewis, S. R., Read, P. L., & Huot, J.-P. (1999). Improved general circulation models of the Martian atmosphere from the surface to above 80 km. *Journal of Geophysical Research: Planets*, *104*(E10), 24155–24175.

Forget, F., Hourdin, F., & Talagrand, O. (1998). CO2 snowfall on Mars: Simulation with a General Circulation Model. *Icarus*, *131*(2), 302–316.

Forgy, E. W. (1965). Cluster analysis of multivariate data: Efficiency versus interpretability of classifications. *biometrics*, *21*, 768–769.

Formisano, V., Atreya, S., Encrenaz, T., Ignatiev, N., & Giuranna, M. (2004). Detection of methane in the atmosphere of Mars. *science*, *306*(5702), 1758–1761.

Franz, H. B., Trainer, M. G., Malespin, C. A., Mahaffy, P. R., Atreya, S. K., Becker, R. H., Benna, M., Conrad, P. G., Eigenbrode, J. L., Freissinet, C., et al. (2017). Initial SAM calibration gas experiments on Mars: Quadrupole mass spectrometer results and implications. *Planetary and Space Science*, *138*, 44–54.

Gamache, R. R., Farese, M., & Renaud, C. L. (2016). A spectral line list for water isotopologues in the 1100-4100 cm-1 region for application to CO2-rich planetary atmospheres. *Journal of Molecular Spectroscopy*, *326*, 144–150.

Gérard, J.-C., Aoki, S., Willame, Y., Gkouvelis, L., Depiesse, C., Thomas, I. R., Ristic, B., Vandaele, A. C., Daerden, F., Hubert, B., et al. (2020). Detection of green line emission in the dayside atmosphere of Mars from NOMAD-TGO observations. *Nature Astronomy*, *4*(11), 1049–1052.

Gérard, J.-C., Soret, L., Thomas, I., Ristic, B., Willame, Y., Depiesse, C., Vandaele, A., Daerden, F., Hubert, B., Mason, J., et al. (2024). Observation of the Mars O2 visible nightglow by the nomad spectrometer onboard the Trace Gas Orbiter. *Nature Astronomy*, *8*(1), 77–81.

Gierasch, P. J., & Goody, R. M. (1972). The effect of dust on the temperature of the Martian atmosphere. *Journal of the Atmospheric Sciences*, *29*(2), 400–402.

Glatthor, N., Hoepfner, M., Stiller, G. P., von Clarmann, T., Dudhia, A., Echle, G., Funke, B., & Hase, F. (1999). Intercomparison of the KOPRA and the RFM radiative transfer codes. *3867*, 348–363.

Glavin, D. P., Freissinet, C., Miller, K. E., Eigenbrode, J. L., Brunner, A. E., Buch, A., Sutter, B., Archer Jr, P. D., Atreya, S. K., Brinckerhoff, W. B., et al. (2013). Evidence for perchlorates and the origin of chlorinated hydrocarbons detected by SAM at the Rocknest aeolian deposit in Gale Crater. *Journal of Geophysical Research: Planets*, *118*(10), 1955–1973.

Godson, W. (1953). The evaluation of infra-red radiative fluxes due to atmospheric water vapour. *Quarterly Journal of the Royal Meteorological Society*, *79*(341), 367–379.

González-Galindo, F., Chaufray, J.-Y., López-Valverde, M., Gilli, G., Forget, F., Leblanc, F., Modolo, R., Hess, S., & Yagi, M. (2013). Three-dimensional Martian ionosphere model: I. the photochemical ionosphere below 180 km. *Journal of Geophysical Research: Planets*, *118*(10), 2105–2123.

González-Galindo, F., López-Valverde, M., Forget, F., García-Comas, M., Millour, E., & Montabone, L. (2015). Variability of the Martian thermosphere during eight Martian years as simulated by a ground-to-exosphere global circulation model. *Journal of Geophysical Research: Planets*, *120*(11), 2020–2035.

Goody, R. M., & Yung, Y. L. (1995). *Atmospheric radiation: Theoretical basis*. Oxford university press.

Goody, R., & Yung, Y. (1989). Vibration-rotation spectra of gaseous molecules. In *Atmospheric radiation*. Oxford University Press.

Gordon, I. E., Rothman, L. S., Hargreaves, R., Hashemi, R., Karlovets, E. V., Skinner, F., Conway, E. K., Hill, C., Kochanov, R. V., Tan, Y., et al. (2022). The HITRAN2020 molecular spectroscopic database. *Journal of quantitFative spectroscopy and radiative transfer*, *277*, 107949.

Gordon, I. E., Rothman, L. S., Hill, C., Kochanov, R. V., Tan, Y., Bernath, P. F., Birk, M., Boudon, V., Campargue, A., Chance, K., et al. (2017). The HITRAN2016 molecular spectroscopic database. *Journal of Quantitative Spectroscopy and Radiative Transfer*, *203*, 3–69.

Graedel, T., & Keene, W. (1995). Tropospheric budget of reactive chlorine. *Global Biogeochemical Cycles*, *9*(1), 47–77.

Gundlach, B., Skorov, Y. V., & Blum, J. (2011). Outgassing of icy bodies in the Solar System–i. the sublimation of hexagonal water ice through dust layers. *Icarus*, *213*(2), 710–719.

Gurwell, M. A., Bergin, E. A., Melnick, G. J., & Tolls, V. (2005). Mars surface and atmospheric temperature during the 2001 global dust storm. *Icarus*, *175*(1), 23–31.

Guzewich, S. D., Lemmon, M., Smith, C., Martínez, G., de Vicente-Retortillo, Á., Newman, C., Baker, M., Campbell, C., Cooper, B., Gómez-Elvira, J., et al. (2019). Mars Science Laboratory observations of the 2018/Mars year 34 global dust storm. *Geophysical Research Letters*, *46*(1), 71–79.

Haberle, R. M., Kahre, M. A., Hollingsworth, J. L., Montmessin, F., Wilson, R. J., Urata, R. A., Brecht, A. S., Wolff, M. J., Kling, A. M., & Schaeffer, J. R.

(2019). Documentation of the nasa/ames legacy mars global climate model: Simulations of the present seasonal water cycle. *Icarus*, *333*, 130–164.

Haberle, R. M., Leovy, C. B., & Pollack, J. B. (1982). Some effects of global dust storms on the atmospheric circulation of Mars. *Icarus*, *50*(2-3), 322–367.

Hartmann, W. K. (1973). Martian cratering, 4, Mariner 9 initial analysis of cratering chronology. *Journal of Geophysical Research*, *78*(20), 4096–4116.

Hartogh, P., Jarchow, C., Lellouch, E., de Val-Borro, M., Rengel, M., Moreno, R., Medvedev, A., Sagawa, H., Swinyard, B., Cavalié, T., et al. (2010). Herschel/HIFI observations of Mars: First detection of O2 at submillimetre wavelengths and upper limits on HCl and H2O2. *Astronomy & Astrophysics*, *521*, L49.

Heavens, N., Benson, J., Kass, D., Kleinböhl, A., Abdou, W., McCleese, D., Richardson, M., Schofield, J., Shirley, J., & Wolkenberg, P. (2010). Water ice clouds over the Martian tropics during northern summer. *Geophysical Research Letters*, *37*(18).

Heavens, N. G., Kleinböhl, A., Chaffin, M. S., Halekas, J. S., Kass, D. M., Hayne, P. O., McCleese, D. J., Piqueux, S., Shirley, J. H., & Schofield, J. T. (2018). Hydrogen escape from Mars enhanced by deep convection in dust storms. *Nature Astronomy*, *2*(2), 126–132.

Hollingsworth, J. L., Haberle, R. M., Barnes, J. R., Bridger, A. F., Pollack, J. B., Lee, H., & Schaeffer, J. (1996). Orographic control of storm zones on Mars. *Nature*, *380*(6573), 413–416.

Holmes, J., Lewis, S., Patel, M., Alday, J., Aoki, S., Liuzzi, G., Villanueva, G., Crismani, M., Fedorova, A., Olsen, K., et al. (2022). Global variations in water vapor and saturation state throughout the Mars year 34 dusty season. *Journal of Geophysical Research: Planets*, *127*(10), e2022JE007203.

Holmes, J., Lewis, S., Patel, M., Chaffin, M., Cangi, E., Deighan, J., Schneider, N., Aoki, S., Fedorova, A., Kass, D., et al. (2021). Enhanced water loss from the martian atmosphere during a regional-scale dust storm and implications for long-term water loss. *Earth and Planetary Science Letters*, *571*, 117109.

Honerkamp, J., & Weese, J. (1990). Tikhonovs regularization method for ill-posed problems: A comparison of different methods for the determination of the regularization parameter. *Continuum Mechanics and Thermodynamics*, *2*, 17–30.

Hourdin, F., Van, P., Forget, F., & Talagrand, O. (1993). Meteorological variability and the annual surface pressure cycle on Mars. *Journal of the atmospheric sciences*, *50*(21), 11.

Jakosky, B. M. (2021). Atmospheric loss to space and the history of water on Mars. *Annual Review of Earth and Planetary Sciences*, *49*, 71–93.

Jakosky, B. M., & Farmer, C. B. (1982). The seasonal and global behavior of water vapor in the Mars atmosphere: Complete global results of the Viking atmospheric water detector experiment. *Journal of Geophysical Research: Solid Earth*, *87*(B4), 2999–3019.

James, P. B., Bell III, J. F., Clancy, R. T., Lee, S. W., Martin, L. J., & Wolff, M. J. (1996). Global imaging of Mars by Hubble Space Telescope during the 1995 opposition. *Journal of Geophysical Research: Planets*, *101*(E8), 18883–18890.

Jiménez Monferrer, S. (2019). CO2 retrievals in the Mars daylight thermosphere from 4.3 um limb emissions. In *Doctoral Thesis in physics*. Universidad de Granada.

Jiménez-Monferrer, S., López-Valverde, M. Á., Funke, B., González-Galindo, F., Piccialli, A., García-Comas, M., López-Puertas, M., Gondet, B., & Bibring, J.-P. (2021). CO2 retrievals in the Mars daylight thermosphere from its 4.3 μm limb emission measured by OMEGA/MEx. *Icarus*, *353*, 113830.

Jurado Navarro, Á. A., et al. (2016). Retrieval of CO2 and collisional parameters from the MIPAS spectra in the earth atmosphere.

Kahre, M., Haberle, R., Hollingsworth, J., & Wolff, M. (2020). MARCI-observed clouds in the Hellas Basin during northern hemisphere summer on Mars: Interpretation with the NASA/Ames legacy Mars Global Climate Model. *Icarus*, *338*, 113512.

Kahre, M. A., Murphy, J. R., & Haberle, R. M. (2006). Modeling the Martian dust cycle and surface dust reservoirs with the NASA Ames general circulation model. *Journal of Geophysical Research: Planets*, *111*(E6).

Kahre, M. A., Murphy, J. R., Newman, C. E., Wilson, R. J., Cantor, B. A., Lemmon, M. T., & Wolff, M. J. (2017). The Mars dust cycle. *The atmosphere and climate of Mars*, *18*, 76.

Kass, D., Kleinböhl, A., McCleese, D., Schofield, J., & Smith, M. (2016). Interannual similarity in the Martian atmosphere during the dust storm season. *Geophysical Research Letters*, *43*(12), 6111–6118.

Kass, D., Schofield, J., Kleinböhl, A., McCleese, D., Heavens, N., Shirley, J., & Steele, L. (2020). Mars Climate Sounder observation of Mars' 2018 global dust storm. *Geophysical Research Letters*, *47*(23), e2019GL083931.

Keating, G., Bougher, S., Zurek, R., Tolson, R., Cancro, G., Noll, S., Parker, J., Schellenberg, T., Shane, R., Wilkerson, B., et al. (1998). The structure of the upper atmosphere of Mars: In situ accelerometer measurements from Mars Global Surveyor. *Science*, *279*(5357), 1672–1676.

Khayat, A. S., Smith, M. D., & Guzewich, S. D. (2019). Understanding the water cycle above the north polar cap on mars using MRO CRISM retrievals of water vapor. *Icarus*, *321*, 722–735.

Kleinböhl, A., John Wilson, R., Kass, D., Schofield, J. T., & McCleese, D. J. (2013). The semidiurnal tide in the middle atmosphere of Mars. *Geophysical Research Letters*, *40*(10), 1952–1959.

Kleinböhl, A., Schofield, J. T., Kass, D. M., Abdou, W. A., Backus, C. R., Sen, B., Shirley, J. H., Lawson, W. G., Richardson, M. I., Taylor, F. W., et al. (2009). Mars Climate Sounder limb profile retrieval of atmospheric temperature, pressure, and dust and water ice opacity. *Journal of Geophysical Research: Planets*, *114*(E10).

Kley, D., Stone, E., Henderson, W., Drummond, J., Harrop, W., Schmeltekopf, A., Thompson, T., & Winkler, R. (1979). In situ measurements of the mixing ratio of water vapor in the stratosphere. *Journal of the Atmospheric Sciences*, *36*(12), 2513–2524.

Knutsen, E. W., Villanueva, G. L., Liuzzi, G., Crismani, M. M., Mumma, M. J., Smith, M. D., Vandaele, A. C., Aoki, S., Thomas, I. R., Daerden, F., et al. (2021). Comprehensive investigation of Mars methane and organics with ExoMars/NOMAD. *Icarus*, *357*, 114266.

Korablev, O., Montmessin, F., Trokhimovskiy, A., Fedorova, A. A., Shakun, A., Grigoriev, A., Moshkin, B., Ignatiev, N., Forget, F., Lefèvre, F., et al. (2018). The atmospheric chemistry suite (ACS) of three spectrometers for the ExoMars 2016 trace gas orbiter. *Space Science Reviews*, *214*, 1–62.

Korablev, O., Olsen, K. S., Trokhimovskiy, A., Lefèvre, F., Montmessin, F., Fedorova, A. A., Toplis, M. J., Alday, J., Belyaev, D. A., Patrakeev, A., et al. (2021). Transient HCl in the atmosphere of Mars. *Science Advances*, *7*(7), eabe4386.

Korablev, O., Vandaele, A. C., Montmessin, F., Fedorova, A. A., Trokhimovskiy, A., Forget, F., Lefèvre, F., Daerden, F., Thomas, I. R., Trompet, L., et al. (2019). No detection of methane on Mars from early ExoMars Trace Gas Orbiter observations. *Nature*, *568*(7753), 517–520.

Krasnopolsky, V. A., & Feldman, P. D. (2001). Detection of molecular hydrogen in the atmosphere of Mars. *Science*, *294*(5548), 1914–1917.

Krasnopolsky, V. A., Maillard, J. P., & Owen, T. C. (2004). Detection of methane in the Martian atmosphere: Evidence for life? *Icarus*, *172*(2), 537–547.

Kuiper, G. P. (1952). The atmospheres of the earth and planets. *Chicago*.

Kuntz, M. (1997). A new implementation of the Humlicek algorithm for the calculation of the Voigt profile function. *Journal of Quantitative Spectroscopy and Radiative Transfer*, *57*(6), 819–824.

Lange, L., Forget, F., Banfield, D., Wolff, M., Spiga, A., Millour, E., Viúdez-Moreiras, D., Bierjon, A., Piqueux, S., Newman, C., et al. (2022). InSight pressure data recalibration, and its application to the study of long-term pressure changes on Mars. *Journal of Geophysical Research: Planets*, *127*(5), e2022JE007190.

Lefevre, F., & Forget, F. (2009). Observed variations of methane on Mars unexplained by known atmospheric chemistry and physics. *Nature*, *460*(7256), 720–723.

Lefèvre, F., Trokhimovskiy, A., Fedorova, A., Baggio, L., Lacombe, G., Määttänen, A., Bertaux, J.-L., Forget, F., Millour, E., Venot, O., et al. (2021). Relationship between the ozone and water vapor columns on Mars as observed by SPICAM and calculated by a global climate model. *Journal of Geophysical Research: Planets*, *126*(4), e2021JE006838.

Levenberg, K. (1944). A method for the solution of certain non-linear problems in least squares. *Quarterly of applied mathematics*, *2*(2), 164–168.

Liu, J., Richardson, M. I., & Wilson, R. (2003). An assessment of the global, seasonal, and interannual spacecraft record of Martian climate in the thermal infrared. *Journal of Geophysical Research: Planets*, *108*(E8).

Liuzzi, G., Villanueva, G. L., Crismani, M. M., Smith, M. D., Mumma, M. J., Daerden, F., Aoki, S., Vandaele, A. C., Clancy, R. T., Erwin, J., et al. (2020). Strong variability of Martian water ice clouds during dust storms revealed from ExoMars Trace Gas Orbiter/NOMAD. *Journal of Geophysical Research: Planets*, *125*(4), e2019JE006250.

Liuzzi, G., Villanueva, G. L., Mumma, M. J., Smith, M. D., Daerden, F., Ristic, B., Thomas, I., Vandaele, A. C., Patel, M. R., Lopez-Moreno, J.-J., et al. (2019). Methane on Mars: New insights into the sensitivity of CH4 with the NOMAD/ExoMars spectrometer through its first in-flight calibration. *Icarus*, *321*, 671–690.

Liuzzi, G., Villanueva, G. L., Trompet, L., Crismani, M. M., Piccialli, A., Aoki, S., Lopez-Valverde, M. A., Stolzenbach, A., Daerden, F., Neary, L., et al. (2021). First detection and thermal characterization of terminator CO2 ice clouds with ExoMars/NOMAD. *Geophysical Research Letters*, *48*(22), e2021GL095895.

Lommel, E. (1887). Die photometrie der diffusen zurückwerfung. *Sitzber. Acad. Wissensch. München*, *17*, 95–124.

López-Valverde, M., & López-Puertas, M. (1994). A non-local thermodynamic equilibrium radiative transfer model for infrared emissions in the atmosphere of Mars: 1. theoretical basis and nighttime populations of vibrational levels. *Journal of Geophysical Research: Planets*, *99*(E6), 13093–13115.

López-Valverde, M. A., Gerard, J.-C., González-Galindo, F., Vandaele, A.-C., Thomas, I., Korablev, O., Ignatiev, N., Fedorova, A., Montmessin, F., Määttänen, A., Guilbon, S., Lefevre, F., Patel, M. R., Jiménez-Monferrer, S., García-Comas, M., Cardesin, A., Wilson, C. F., Clancy, R. T., Kleinböhl, A., … Rodríguez, J. (2018). Investigations of the Mars upper atmosphere with ExoMars Trace Gas Orbiter. *Space Science Reviews*, *214*(1), 29.

López-Valverde, M. A., Funke, B., Brines, A., Stolzenbach, A., Modak, A., Hill, B., González-Galindo, F., Thomas, I., Trompet, L., Aoki, S., et al. (2023). Martian atmospheric temperature and density profiles during the first year of NOMAD/TGO solar occultation measurements. *Journal of Geophysical Research: Planets*, *128*(2), e2022JE007278.

Madeleine, J.-B., Forget, F., Millour, E., Montabone, L., & Wolff, M. (2011). Revisiting the radiative impact of dust on Mars using the LMD Global Climate Model. *Journal of Geophysical Research: Planets*, *116*(E11).

Mahaffy, P. R., Webster, C. R., Atreya, S. K., Franz, H., Wong, M., Conrad, P. G., Harpold, D., Jones, J. J., Leshin, L. A., Manning, H., et al. (2013). Abundance and isotopic composition of gases in the Martian atmosphere from the Curiosity rover. *Science*, *341*(6143), 263–266.

Maltagliati, L., Montmessin, F., Fedorova, A., Korablev, O., Forget, F., & Bertaux, J.-L. (2011a). Evidence of water vapor in excess of saturation in the atmosphere of Mars. *science*, *333*(6051), 1868–1871.

Maltagliati, L., Montmessin, F., Korablev, O., Fedorova, A., Forget, F., Määttänen, A., Lefèvre, F., & Bertaux, J.-L. (2013). Annual survey of water vapor vertical distribution and water–aerosol coupling in the martian atmosphere observed by SPICAM/MEx solar occultations. *Icarus*, *223*(2), 942–962.

Maltagliati, L., Titov, D. V., Encrenaz, T., Melchiorri, R., Forget, F., Keller, H. U., & Bibring, J.-P. (2011b). Annual survey of water vapor behavior from the OMEGA mapping spectrometer onboard Mars Express. *Icarus*, *213*(2), 480–495.

Maltagliati, L., Titov, D. V., Encrenaz, T., Melchiorri, R., Forget, F., Garcia-Comas, M., Keller, H. U., Langevin, Y., & Bibring, J.-P. (2008). Observations of atmospheric water vapor above the Tharsis volcanoes on Mars with the OMEGA/MEx imaging spectrometer. *Icarus*, *194*(1), 53–64.

Marquardt, D. W. (1963). An algorithm for least-squares estimation of nonlinear parameters. *Journal of the society for Industrial and Applied Mathematics*, *11*(2), 431–441.

Martín-Rubio, C., Vicente-Retortillo, A., Gómez, F., & Rodríguez-Manfredi, J. (2024). Interannual variability of regional dust storms between Mars years 24 and 36. *Icarus*, *412*, 115982.

Marzo, G. A., Lopez-Valverde, M. A., & Gonzalez-Galindo, F. (2008). Cluster analysis of martian atmospheric temperature profiles. *37th COSPAR Scientific Assembly*, *37*, 1937.

Mayyasi, M., Clarke, J., Chaufray, J.-Y., Kass, D., Bougher, S., Bhattacharyya, D., Deighan, J., Jain, S., Schneider, N., Villanueva, G., et al. (2023). Solar cycle and seasonal variability of H in the upper atmosphere of Mars. *Icarus*, *393*, 115293.

MCD. (2024). *Mars Climate Database*. Retrieved June 19, 2024, from https://www-mars.lmd.jussieu.fr/

Medvedev, A. S., & Hartogh, P. (2007). Winter polar warmings and the meridional transport on Mars simulated with a general circulation model. *Icarus*, *186*(1), 97–110.

Melchiorri, R., Encrenaz, T., Fouchet, T., Drossart, P., Lellouch, E., Gondet, B., Bibring, J.-P., Langevin, Y., Schmitt, B., Titov, D., et al. (2007). Water vapor mapping on Mars using OMEGA/Mars Express. *Planetary and Space Science*, *55*(3), 333–342.

Millour, E., Forget, F., Spiga, A., Pierron, T., Bierjon, A., Montabone, L., Vals, M., Lefèvre, F., Chaufray, J.-Y., Lopez-Valverde, M., et al. (2022). The Mars Climate Database (Version 6.1). *Europlanet Science Congress 2022*, *16*, EPSC2022–786.

Mitrofanov, I., Malakhov, A., Bakhtin, B., Golovin, D., Kozyrev, A., Litvak, M., Mokrousov, M., Sanin, A., Tretyakov, V., Vostrukhin, A., et al. (2018). Fine resolution epithermal neutron detector (FREND) onboard the ExoMars trace gas orbiter. *Space Science Reviews*, *214*, 1–26.

Modak, A., López-Valverde, M. A., Brines, A., Stolzenbach, A., Funke, B., González-Galindo, F., Hill, B., Aoki, S., Thomas, I., Liuzzi, G., et al. (2023). Retrieval of Martian atmospheric CO vertical profiles from NOMAD observations during the first year of TGO operations. *Journal of Geophysical Research: Planets*, *128*(3), e2022JE007282.

Montabone, L., Forget, F., Millour, E., Wilson, R., Lewis, S., Cantor, B., Kass, D., Kleinböhl, A., Lemmon, M., Smith, M., et al. (2015). Eight-year climatology of dust optical depth on Mars. *Icarus*, *251*, 65–95.

Montabone, L., Spiga, A., Kass, D. M., Kleinböhl, A., Forget, F., & Millour, E. (2020). Martian year 34 column dust climatology from Mars climate sounder observations: Reconstructed maps and model simulations. *Journal of Geophysical Research: Planets*, *125*(8), e2019JE006111.

Montmessin, F., Belyaev, D. A., Lefèvre, F., Alday, J., Vals, M., Fedorova, A., Korablev, O. I., Trokhimovskiy, A., Chaffin, M. S., & Schneider, N. M. (2022). Reappraising the production and transfer of hydrogen atoms from the middle to the upper atmosphere of Mars at times of elevated water vapor. *Journal of Geophysical Research: Planets*, *127*(5), e2022JE007217.

Montmessin, F., Forget, F., Rannou, P., Cabane, M., & Haberle, R. M. (2004). Origin and role of water ice clouds in the Martian water cycle as inferred from a general circulation model. *Journal of Geophysical Research: Planets*, *109*(E10).

Montmessin, F., Korablev, O., Trokhimovskiy, A., Lefèvre, F., Fedorova, A., Baggio, L., Irbah, A., Lacombe, G., Olsen, K., Braude, A., et al. (2021). A stringent upper limit of 20 pptv for methane on Mars and constraints on its dispersion outside gale crater. *Astronomy & Astrophysics*, *650*, A140.

Montmessin, F., Rannou, P., & Cabane, M. (2002). New insights into martian dust distribution and water-ice cloud microphysics. *Journal of Geophysical Research: Planets*, *107*(E6), 4–1.

Montmessin, F., Smith, M. D., Langevin, Y., Mellon, M. T., & Fedorova, A. (2017). The water cycle. *The atmosphere and climate of Mars*, *18*, 338.

Mumma, M. J., Villanueva, G. L., Novak, R. E., Hewagama, T., Bonev, B. P., DiSanti, M. A., Mandell, A. M., & Smith, M. D. (2009). Strong release of methane on Mars in northern summer 2003. *Science*, *323*(5917), 1041–1045.

Murphy, D. M., & Koop, T. (2005). Review of the vapour pressures of ice and supercooled water for atmospheric applications. *Quarterly Journal of the Royal Meteorological Society: A journal of the atmospheric sciences, applied meteorology and physical oceanography*, *131*(608), 1539–1565.

Nakagawa, H., Terada, N., Jain, S. K., Schneider, N. M., Montmessin, F., Yelle, R. V., Jiang, F., Verdier, L., England, S. L., Seki, K., et al. (2020). Vertical propagation of wave perturbations in the middle atmosphere on Mars by MAVEN/IUVS. *Journal of Geophysical Research: Planets*, *125*(9), e2020JE006481.

Navarro, T., Madeleine, J.-B., Forget, F., Spiga, A., Millour, E., Montmessin, F., & Määttänen, A. (2014a). Global climate modeling of the Martian water cycle with improved microphysics and radiatively active water ice clouds. *Journal of Geophysical Research: Planets*, *119*(7), 1479–1495.

Navarro, T., Madeleine, J.-B., Forget, F., Spiga, A., Millour, E., Montmessin, F., & Määttänen, A. (2014b). Global climate modeling of the Martian water cycle with improved microphysics and radiatively active water ice clouds. *Journal of Geophysical Research: Planets*, *119*(7), 1479–1495.

Neary, L., Daerden, F., Aoki, S., Whiteway, J., Clancy, R. T., Smith, M., Viscardy, S., Erwin, J., Thomas, I., Villanueva, G., et al. (2020). Explanation for the increase in high-altitude water on Mars observed by NOMAD during the 2018 global dust storm. *Geophysical Research Letters*, *47*(7), e2019GL084354.

Neefs, E., Vandaele, A. C., Drummond, R., Thomas, I. R., Berkenbosch, S., Clairquin, R., Delanoye, S., Ristic, B., Maes, J., Bonnewijn, S., et al. (2015). NOMAD spectrometer on the ExoMars trace gas orbiter mission: Part 1—design, manufacturing and testing of the infrared channels. *Applied optics*, *54*(28), 8494–8520.

Nier, A., & McElroy, M. B. (1977). Composition and structure of Mars' upper atmosphere: Results from the neutral mass spectrometers on Viking 1 and 2. *Journal of Geophysical Research*, *82*(28), 4341–4349.

Olsen, K. S., Trokhimovskiy, A., Montabone, L., Fedorova, A. A., Luginin, M., Lefèvre, F., Korablev, O. I., Montmessin, F., Forget, F., Millour, E., Bierjon, A., Baggio, L., Alday, J., Wilson, C. F., Irwin, P. G. J., Belyaev, D. A., Patrakeev, A., & Shakun, A. (2021a). Seasonal reappearance of HCl in the atmosphere of Mars during the Mars year 35 dusty season. *Astronomy & Astrophysics*, *647*, A161.

Olsen, K. S., Fedorova, A., Trokhimovskiy, A., Montmessin, F., Lefèvre, F., Korablev, O., Baggio, L., Forget, F., Millour, E., Bierjon, A., et al. (2022). Seasonal changes in the vertical structure of ozone in the Martian lower atmosphere and its relationship to water vapor. *Journal of Geophysical Research: Planets*, *127*(10), e2022JE007213.

Olsen, K., Lefèvre, F., Montmessin, F., Fedorova, A., Trokhimovskiy, A., Baggio, L., Korablev, O., Alday, J., Wilson, C., Forget, F., et al. (2021b). The vertical structure of CO in the martian atmosphere from the ExoMars Trace Gas Orbiter. *Nature Geoscience*, *14*(2), 67–71.

Olsen, K., Lefèvre, F., Montmessin, F., Fedorova, A., Trokhimovskiy, A., Baggio, L., Korablev, O., Alday, J., Wilson, C., Forget, F., et al. (2021c). The vertical structure of CO in the martian atmosphere from the ExoMars Trace Gas Orbiter. *Nature Geoscience*, *14*(2), 67–71.

Owen, T., Biemann, K., Rushneck, D., Biller, J., Howarth, D., & Lafleur, A. (1977). The composition of the atmosphere at the surface of Mars. *Journal of Geophysical research*, *82*(28), 4635–4639.

Pankine, A. A., Leung, C., Tamppari, L., Martinez, G., Giuranna, M., Piqueux, S., Smith, M., & Trokhimovskiy, A. (2023). Effects of global dust storms on water vapor in the southern polar region of Mars. *Journal of Geophysical Research: Planets*, *128*(12), e2023JE008016.

Patel, M. R., Antoine, P., Mason, J., Leese, M., Hathi, B., Stevens, A. H., Dawson, D., Gow, J., Ringrose, T., Holmes, J., et al. (2017). NOMAD spectrometer on the ExoMars trace gas orbiter mission: Part 2—design, manufacturing, and testing of the ultraviolet and visible channel. *Applied optics*, *56*(10), 2771–2782.

Perrier, S., Bertaux, J.-L., Lefèvre, F., Lebonnois, S., Korablev, O., Fedorova, A., & Montmessin, F. (2006). Global distribution of total ozone on Mars from SPICAM/MEX UV measurements. *Journal of Geophysical Research: Planets*, *111*(E9).

Piqueux, S., Byrne, S., Kieffer, H. H., Titus, T. N., & Hansen, C. J. (2015). Enumeration of Mars years and seasons since the beginning of telescopic exploration. *Icarus*, *251*, 332–338.

Poncin, L., Kleinböhl, A., Kass, D. M., Clancy, R. T., Aoki, S., & Vandaele, A. C. (2022). Water vapor saturation and ice cloud occurrence in the atmosphere of Mars. *Planetary and Space Science*, *212*, 105390.

Quémerais, E., Bertaux, J.-L., Korablev, O., Dimarellis, E., Cot, C., Sandel, B. R., & Fussen, D. (2006). Stellar occultations observed by SPICAM on Mars Express. *Journal of Geophysical Research: Planets*, *111*(E9).

Richardson, M. I., & Wilson, R. J. (2002). A topographically forced asymmetry in the Martian circulation and climate. *Nature*, *416*(6878), 298–301.

Rodgers, C. D. (2000). *Inverse methods for atmospheric sounding: Theory and practice* (Vol. 2). World scientific.

Rodin, A., Korablev, O., & Moroz, V. (1997). Vertical distribution of water in the near-equatorial troposphere of Mars: Water vapor and clouds. *Icarus*, *125*(1), 212–229.

Rousseeuw, P. J. (1987). Silhouettes: A graphical aid to the interpretation and validation of cluster analysis. *Journal of computational and applied mathematics*, *20*, 53–65.

Ruyten, W. (2004). Comment on "a new implementation of the Humlicek algorithm for the calculation of the Voigt profile function" by M. Kuntz [JQSRT 57 (6)(1997) 819–824]. *Journal of Quantitative Spectroscopy and Radiative Transfer*, *86*(2), 231–233.

Serio, C., Masiello, G., & Liuzzi, G. (2016). Demonstration of random projections applied to the retrieval problem of geophysical parameters from hyperspectral infrared observations. *Applied Optics*, *55*(24), 6576–6587.

Shaposhnikov, D. S., Medvedev, A. S., Rodin, A. V., & Hartogh, P. (2019). Seasonal water "pump" in the atmosphere of Mars: Vertical transport to the thermosphere. *Geophysical Research Letters*, *46*(8), 4161–4169.

Šimečková, M., Jacquemart, D., Rothman, L. S., Gamache, R. R., & Goldman, A. (2006). Einstein A-coefficients and statistical weights for molecular absorption transitions in the HITRAN database. *Journal of Quantitative Spectroscopy and Radiative Transfer*, *98*(1), 130–155.

Smith, D. E., Zuber, M. T., Solomon, S. C., Phillips, R. J., Head, J. W., Garvin, J. B., Banerdt, W. B., Muhleman, D. O., Pettengill, G. H., Neumann, G. A., et al. (1999). The global topography of Mars and implications for surface evolution. *science*, *284*(5419), 1495–1503.

Smith, M. D. (2002). The annual cycle of water vapor on Mars as observed by the Thermal Emission Spectrometer. *Journal of Geophysical Research: Planets*, *107*(E11), 25–1.

Smith, M. D. (2004). Interannual variability in TES atmospheric observations of Mars during 1999–2003. *Icarus*, *167*(1), 148–165.

Smith, M. D., Badri, K., Atwood, S. A., Edwards, C. S., Christensen, P. R., Wolff, M. J., Bertrand, T., Forget, F., Al Tunaiji, E., Wolfe, C., et al. (2022). EMIRS observations of the aphelion-season Mars atmosphere. *Geophysical Research Letters*, *49*(15), e2022GL099636.

Smith, M. D., Bougher, S. W., Encrenaz, T., Forget, F., & Kleinböhl, A. (2017). Thermal structure and composition. *The atmosphere and climate of Mars*, *18*, 42.

Smith, M. D., Pearl, J. C., Conrath, B. J., & Christensen, P. R. (2001). One Martian year of atmospheric observations by the Thermal Emission Spectrometer. *Geophysical Research Letters*, *28*(22), 4263–4266.

Smith, M. D., Wolff, M. J., Clancy, R. T., & Murchie, S. L. (2009). Compact Reconnaissance Imaging Spectrometer observations of water vapor and carbon monoxide. *Journal of Geophysical Research: Planets*, *114*(E2).

Smith, M. D., Wolff, M. J., Lemmon, M. T., Spanovich, N., Banfield, D., Budney, C. J., Clancy, R. T., Ghosh, A., Landis, G. A., Smith, P., et al. (2004). First atmospheric science results from the Mars Exploration Rovers Mini-TES. *Science*, *306*(5702), 1750–1753.

Spinrad, H., Münch, G., & Kaplan, L. D. (1963). The detection of water vapor on Mars. *Astrophysical Journal, vol. 137, p. 1319*, *137*, 1319.

Sprague, A., Boynton, W., Kerry, K., Janes, D., Hunten, D., Kim, K., Reedy, R., & Metzger, A. (2004). Mars' south polar ar enhancement: A tracer for south polar seasonal meridional mixing. *Science*, *306*(5700), 1364–1367.

Sprague, A. L., Boynton, W. V., Kerry, K. E., Janes, D. M., Kelly, N. J., Crombie, M. K., Nelli, S. M., Murphy, J. R., Reedy, R. C., & Metzger, A. E. (2007). Mars' atmospheric argon: Tracer for understanding Martian atmospheric circulation and dynamics. *Journal of Geophysical Research: Planets*, *112*(E3).

Steele, L. J., Lewis, S. R., Patel, M. R., Montmessin, F., Forget, F., & Smith, M. D. (2014). The seasonal cycle of water vapour on Mars from assimilation of Thermal Emission Spectrometer data. *Icarus*, *237*, 97–115.

Stiller, G. P. (2000). The Karlsruhe Optimized and Precise Radiative transfer Algorithm (KOPRA). -.

Stiller, G. P., von Clarmann, T., Funke, B., Glatthor, N., Hase, F., Höpfner, M., & Linden, A. (2002). Sensitivity of trace gas abundances retrievals from infrared limb emission spectra to simplifying approximations in radiative transfer modelling. *Journal of Quantitative Spectroscopy and Radiative Transfer*, *72*(3), 249–280.

Stolzenbach, A., López Valverde, M.-A., Brines, A., Modak, A., Funke, B., González-Galindo, F., Thomas, I., Liuzzi, G., Villanueva, G., Luginin, M., et al. (2023). Martian atmospheric aerosols composition and distribution retrievals during the first martian year of NOMAD/TGO solar occultation measurements: 1. methodology and application to the my 34 global dust storm. *Journal of Geophysical Research: Planets*, *128*(11), e2022JE007276.

Stone, S. W., Yelle, R. V., Benna, M., Lo, D. Y., Elrod, M. K., & Mahaffy, P. R. (2020). Hydrogen escape from Mars is driven by seasonal and dust storm transport of water. *Science*, *370*(6518), 824–831.

Streeter, P. M., Lewis, S. R., Patel, M. R., Holmes, J. A., Fedorova, A. A., Kass, D. M., & Kleinböhl, A. (2021). Asymmetric impacts on Mars' polar vortices from an equinoctial global dust storm. *Journal of Geophysical Research: Planets*, *126*(5), e2020JE006774.

Thomas, I. R., Aoki, S., Trompet, L., Robert, S., Depiesse, C., Willame, Y., Erwin, J. T., Vandaele, A. C., Daerden, F., Mahieux, A., et al. (2022). Calibration of NOMAD on ESA's ExoMars trace gas orbiter: Part 1–the solar occultation channel. *Planetary and Space Science*, *218*, 105411.

Thomas, I. R., Vandaele, A. C., Robert, S., Neefs, E., Drummond, R., Daerden, F., Delanoye, S., Ristic, B., Berkenbosch, S., Clairquin, R., et al. (2016). Optical and radiometric models of the NOMAD instrument part ii: The infrared channels-SO and LNO. *Optics Express*, *24*(4), 3790–3805.

Thomas, N., Cremonese, G., Ziethe, R., Gerber, M., Brändli, M., Bruno, G., Erismann, M., Gambicorti, L., Gerber, T., Ghose, K., et al. (2017). The colour and stereo surface imaging system (CaSSIS) for the ExoMars trace gas orbiter. *Space science reviews*, *212*, 1897–1944.

Trompet, L., Vandaele, A., Thomas, I., Aoki, S., Daerden, F., Erwin, J., Flimon, Z., Mahieux, A., Neary, L., Robert, S., Vilanueva, G., G, L., Lopez-Valverde, M., Brines, A., Bellucci, G., Lopez-Moreno, J., & Patel, M. (2023). Carbon dioxide retrievals from NOMAD-SO on ESA's ExoMars Trace Gas Orbiter and temperature profiles retrievals with the hydrostatic equilibrium equation: 1. description of the method. *Journal of Geophysical Research: Planets*, *128*(3), e2022JE007277.

Tschimmel, M., Ignatiev, N. I., Titov, D. V., Lellouch, E., Fouchet, T., Giuranna, M., & Formisano, V. (2008). Investigation of water vapor on Mars with PFS/SW of Mars Express. *Icarus*, *195*(2), 557–575.

Vandaele, A. C., De Mazière, M., Drummond, R., Mahieux, A., Neefs, E., Wilquet, V., Korablev, O., Fedorova, A., Belyaev, D., Montmessin, F., et al. (2008).

Composition of the Venus mesosphere measured by Solar Occultation at Infrared on board Venus Express. *Journal of Geophysical Research: Planets*, *113*(E5).

Vandaele, A. C., Korablev, O., Daerden, F., Aoki, S., Thomas, I. R., Altieri, F., López-Valverde, M., Villanueva, G., Liuzzi, G., Smith, M. D., et al. (2019). Martian dust storm impact on atmospheric H2O and D/H observed by ExoMars Trace Gas Orbiter. *Nature*, *568*(7753), 521–525.

Vandaele, A. C., Kruglanski, M., & De Mazière, M. (2006). Modeling and retrieval of atmospheric spectra using ASIMUT.

Vandaele, A. C., Lopez-Moreno, J.-J., Patel, M. R., Bellucci, G., Daerden, F., Ristic, B., Robert, S., Thomas, I., Wilquet, V., Allen, M., et al. (2018). NOMAD, an integrated suite of three spectrometers for the ExoMars trace gas mission: Technical description, science objectives and expected performance. *Space Science Reviews*, *214*(5), 1–47.

Vandaele, A. C., Neefs, E., Drummond, R., Thomas, I. R., Daerden, F., Lopez-Moreno, J.-J., Rodriguez, J., Patel, M. R., Bellucci, G., Allen, M., et al. (2015). Science objectives and performances of NOMAD, a spectrometer suite for the ExoMars TGO mission. *Planetary and Space Science*, *119*, 233–249.

Villanueva, G. L., Liuzzi, G., Aoki, S., Stone, S. W., Brines, A., Thomas, I. R., Lopez-Valverde, M. A., Trompet, L., Erwin, J., Daerden, F., et al. (2022a). The deuterium isotopic ratio of water released from the Martian caps as measured with TGO/NOMAD. *Geophysical Research Letters*, *49*(12), e2022GL098161.

Villanueva, G. L., Liuzzi, G., Crismani, M. M., Aoki, S., Vandaele, A. C., Daerden, F., Smith, M. D., Mumma, M. J., Knutsen, E. W., Neary, L., et al. (2021). Water heavily fractionated as it ascends on Mars as revealed by ExoMars/NOMAD. *Science Advances*, *7*(7), eabc8843.

Villanueva, G. L., Smith, M. D., Protopapa, S., Faggi, S., & Mandell, A. M. (2018). Planetary Spectrum Generator: An accurate online radiative transfer suite for atmospheres, comets, small bodies and exoplanets. *Journal of Quantitative Spectroscopy and Radiative Transfer*, *217*, 86–104.

Villanueva, G. L., Liuzzi, G., Faggi, S., Protopapa, S., Kofman, V., Fauchez, T., Stone, S. W., & Mandell, A. M. (2022b). Fundamentals of the Planetary Spectrum Generator. *Fundamentals of the Planetary Spectrum Generator. 2022 edition of the handbook by GL Villanueva et al. ISBN 978-0-578-36143-7*.

Villanueva, G., Mumma, M., Novak, R., Radeva, Y., Käufl, H., Smette, A., Tokunaga, A., Khayat, A., Encrenaz, T., & Hartogh, P. (2013). A sensitive search for organics (CH4, CH3OH, H2CO, C2H6, C2H2, C2H4), hydroperoxyl (HO2), nitrogen compounds (N2O, NH3, HCN) and chlorine species (HCl, CH3Cl) on Mars using ground-based high-resolution infrared spectroscopy. *Icarus*, *223*(1), 11–27.

von Clarmann, T., Glatthor, N., Grabowski, U., Höpfner, M., Kellmann, S., Kiefer, M., Linden, A., Tsidu, G. M., Milz, M., Steck, T., et al. (2003a). Retrieval of temperature and tangent altitude pointing from limb emission spectra recorded from space by the michelson interferometer for Passive Atmospheric Sounding (MIPAS). *Journal of Geophysical Research: Atmospheres*, *108*(D23).

von Clarmann, v., Glatthor, N., Grabowski, U., Höpfner, M., Kellmann, S., Kiefer, M., Linden, A., Tsidu, G. M., Milz, M., Steck, T., et al. (2003b). Retrieval of temperature and tangent altitude pointing from limb emission spectra recorded from space by the Michelson Interferometer for Passive Atmospheric Sounding (MIPAS). *Journal of Geophysical Research: Atmospheres*, *108*(D23).

Webster, C. R., Mahaffy, P. R., Atreya, S. K., Flesch, G. J., Mischna, M. A., Meslin, P.-Y., Farley, K. A., Conrad, P. G., Christensen, L. E., Pavlov, A. A., et al. (2015). Mars methane detection and variability at Gale crater. *Science*, *347*(6220), 415–417.

Wilson, R. J., & Richardson, M. I. (2000). The Martian atmosphere during the Viking mission, i: Infrared measurements of atmospheric temperatures revisited. *Icarus*, *145*(2), 555–579.

Yoshida, N., Nakagawa, H., Aoki, S., Erwin, J., Vandaele, A. C., Daerden, F., Thomas, I., Trompet, L., Koyama, S., Terada, N., et al. (2022). Variations in vertical CO/CO2 profiles in the Martian mesosphere and lower thermosphere measured by the ExoMars TGO/NOMAD: Implications of variations in eddy diffusion coefficient. *Geophysical Research Letters*, *49*(10), e2022GL098485.

Zurek, R. W., Chicarro, A., Allen, M. A., Bertaux, J.-L., Clancy, R. T., Daerden, F., Formisano, V., Garvin, J. B., Neukum, G., & Smith, M. D. (2011). Assessment of a 2016 mission concept: The search for trace gases in the atmosphere of Mars. *Planetary and Space Science*, *59*(2-3), 284–291.